NASA Contractor Report 4287

Static and Free-Vibrational Response of Semi-Circular Graphite-Epoxy Frames With Thin-Walled Open Sections

J. Scott Collins and Eric R. Johnson

GRANT NAG1-343
MARCH 1990

(NASA-CR-4287) STATIC AND FREE-VIBRATIONAL RESPONSE OF SEMI-CIRCULAR GRAPHITE-EPOXY FRAMES WITH THIN-WALLED OPEN SECTIONS Final Report (Virginia Polytechnic Inst. and State Univ.) 216 p CSCL 20K H1/39
N90-27122
Unclas
0280223

NASA Contractor Report 4287

Static and Free-Vibrational Response of Semi-Circular Graphite-Epoxy Frames With Thin-Walled Open Sections

J. Scott Collins and Eric R. Johnson
Virginia Polytechnic Institute & State University
Blacksburg, Virginia

Prepared for
Langley Research Center
under Grant NAG1-343

National Aeronautics and
Space Administration
Office of Management
Scientific and Technical
Information Division

1990

Static and Free-Vibrational Response of Semi-Circular Graphite-Epoxy Frames with Thin-Walled Open Sections

by

J. Scott Collins
Dr. Eric R. Johnson, Chairman
Aerospace and Ocean Engineering

(ABSTRACT)

Experiments were conducted to measure the three-dimensional static and free vibrational response of two graphite-epoxy, thin-walled, open section frames. The frames are semi-circular with a radius of three feet, and one specimen has an I cross section and the other has a channel cross section. The flexibility influence coefficients were measured in static tests for loads applied at midspan with the ends of the specimens clamped. Natural frequencies and modes were determined from vibrational tests for free and clamped end conditions. The experimental data is used to evaluate a new finite element which was developed specifically for the analysis of curved, thin-walled structures. The formulation of the element is based on a Vlasov-type, thin-walled, curved beam theory.

The predictions from the finite element program generally correlated well with the experimental data for the symmetric I-specimen. Discrepancies in some of the data were found to be due to flexibility in the 'clamped' end conditions. With respect to the data for the channel specimen, the correlation was less satisfactory. The finite element analysis predicted the out-of-plane response of the channel specimen reasonably well, but large discrepancies occurred between the predicted in-plane response and the experimental data. The analysis predicted a much more compliant in-plane response then was observed in the experiments.

PAGE ii INTENTIONALLY BLANK

PRECEDING PAGE BLANK NOT FILMED

Table of Contents

Introduction 1

Background 1

Objective 8

Literature Review 8

Dynamics 9

Statics 12

Summary 14

Test Specimens 15

Design and Fabrication 15

Specimen Characterization 20

Experimental Apparatus and Tests 28

Dynamic Tests 29

Free-Free Frame Tests 29

Clamped-Clamped Frame Tests 31

Static Tests 37

In-Plane Static Tests 39
Out of Plane Static Tests 44
Crush Test 49

Experimental Results **52**
Dynamic Test Data 52
Static Test Data 61
Load-Displacement Plots 63
Data Reduction 71
Flexibility Influence Coefficients 72
Crush Test 78

Analysis **83**
Thin-Walled Curved Beam Theory 84
Strain Energy 84
Kinetic Energy 97
Hamilton's Principle 100
Hooke's Law 102
Continuum Solutions 110
In-Plane Vibration Solution 111
In-Plane Static Solution 115
Out-of-Plane Vibration Solution 120
Finite Element Computer Program 124
Element Formulation 125
Application to Test Specimens 127

Correlation of Numerical and Experimental Results **134**

Correlation of Dynamic Data 134
Free-Free Data 135
Clamped-Clamped Tests 136
Correlation of Static Data 151
I-Specimen Results 155
Channel Specimen Results 159

Concluding Remarks 161
Future Work 164

REFERENCES 166

Vibrational Test Data 169
Frequency Response Data from Dynamic Tests 169
Mode Shapes 184

Static Test Data 193
Static Test Data Reduction 193
Reduced Static Data 197

Cross-Sectional Properties 203

List of Illustrations

Figure 1. Drop test of full scale fuselage section 3

Figure 2. Drop test of full scale fuselage section 4

Figure 3. Drop test of a composite fuselage subsection 6

Figure 4. Drop test of a composite fuselage subsection 7

Figure 5. Cross sections of the specimens 16

Figure 6. Specimen layup 18

Figure 7. Specimen dimensions 19

Figure 8. Ultrasound scan of the channel specimen 21

Figure 9. Three-point bend test configuration 22

Figure 10. Load-displacement data from three-point bend tests 23

Figure 11. Iosipescu shear test results 25

Figure 12. Tension test results 26

Figure 13. Free-free frame vibrational test setup 30

Figure 14. Structural analyzer test flowchart 32

Figure 15. Experimental apparatus for clamped-clamped dynamic tests 34

Figure 16. Experimental apparatus for clamped-clamped dynamic tests 35

Figure 17. Experimental apparatus for clamped-clamped dynamic tests 36

Figure 18. Frequency response plots for the I-section specimen 38

Figure 19. Load fixture and Coordinate system 40

Figure 20. Load fixture 42
Figure 21. In-plane test apparatus 43
Figure 22. Schematic of modified load fixture 45
Figure 23. Photograph of modified load fixture and dial indicators 47
Figure 24. Out of plane test apparatus 48
Figure 25. Crush test apparatus 50
Figure 26. First free-free in-plane mode of the channel specimen 54
Figure 27. Second free-free out-of-plane mode of the I-specimen 55
Figure 28. First free-free torsional mode of the I-specimen 57
Figure 29. Comparison of free-free natural frequencies 59
Figure 30. Comparison of clamped-clamped natural frequencies 62
Figure 31. Radial load versus radial displacement 64
Figure 32. Radial load versus lateral displacement 65
Figure 33. Radial load versus twist displacement 66
Figure 34. Lateral load versus radial displacement 68
Figure 35. Lateral load versus lateral displacement 69
Figure 36. Lateral load versus twist displacement 70
Figure 37. Crush test load displacement plot 80
Figure 38. Initial failures for crush test 82
Figure 39. Cylindrical and cross-sectional coordinates 85
Figure 40. General symmetric cross section 88
Figure 41. Loading for in-plane static solution 118
Figure 42. Strain energy distributions in vibrational modes for both specimens . . 129
Figure 43. Number of elements convergence study 130
Figure 44. Penalty parameter convergence study 132
Figure 45. Free-free in-plane mode shapes for the I-specimen 137

Figure 46. Clamped-clamped in-plane natural frequencies for the I-specimen 139
Figure 47. Effects of torsional spring end conditions 142
Figure 48. Clamped-clamped, in-plane natural frequencies for the channel specimen 143
Figure 49. Five noded, in-plane, clamped-clamped mode shape for both specimens 145
Figure 50. Six noded, in-plane, clamped-clamped mode shape for both specimens 146
Figure 51. Clamped-clamped out-of-plane natural frequencies for the I-specimen 147
Figure 52. Clamped-clamped out-of-plane natural frequencies for the channel specimen 149
Figure 53. Five noded, out-of-plane, clamped-clamped mode shape for both specimens 152
Figure 54. Six noded, out-of-plane, clamped-clamped mode shape for both specimens 153
Figure 55. Influence of torsional spring stiffness on 157
Figure 56. Proximity probe orientations for clamped-clamped vibrational tests .. 170
Figure 57. I-specimen frequency response plot for radial excitation; 11-111 Hz .. 171
Figure 58. I-specimen frequency response plot for radial excitation; 110-180 Hz . 172
Figure 59. I-specimen frequency response plot for radial excitation; 233-400 Hz . 173
Figure 60. I-specimen frequency response plot for lateral excitation; 6.8-15 Hz .. 174
Figure 61. I-specimen frequency response plot for lateral excitation; 20-260 Hz .. 175
Figure 62. Channel frequency response plot for radial excitation; 30-160 Hz 176
Figure 63. Channel frequency response plot for radial excitation; 142-240 Hz ... 177
Figure 64. Channel frequency response plot for radial excitation; 270-340 Hz ... 178
Figure 65. Channel frequency response plot for lateral excitation; 6.8-10 Hz 179
Figure 66. Channel frequency response plot for lateral excitation; 15-80 Hz 180
Figure 67. Channel frequency response plot for lateral excitation; 70-125 Hz 181
Figure 68. Channel frequency response plot for lateral excitation; 140-219 Hz ... 182
Figure 69. Channel frequency response plot for lateral excitation; 230-330 Hz ... 183

Figure 70. Two and three noded in-plane, free-free mode shapes 185
Figure 71. Three noded in-plane, clamped-clamped modes for both specimens . . . 186
Figure 72. Four noded in-plane, clamped-clamped modes for both specimens . . . 187
Figure 73. Seven noded in-plane, clamped-clamped modes for the I-specimen . . . 188
Figure 74. Two noded out-of-plane, clamped-clamped modes for both specimens 189
Figure 75. Three noded out-of-plane, clamped-clamped modes for both specimens 190
Figure 76. Four noded out-of-plane, clamped-clamped modes for both specimens 191
Figure 77. Seven noded out-of-plane, clamped-clamped mode for the I-specimen . 192
Figure 78. Schematic of rectangular block, coordinate system and dial indicators 194
Figure 79. Deformed cross section 195

List of Tables

Table 1. Nominal material properties for AS4/5208 from Narmco 17

Table 2. Engineering constants from quasi-isotropic coupon tests 27

Table 3. Natural frequencies and node locations of the free-free modes 58

Table 4. Natural frequencies and node locations of the clamped-clamped modes . 60

Table 5. Flexibility coefficients for the I-specimen from the in-plane tests 73

Table 6. Flexibility influence coefficients for the channel specimen from the in-plane tests 75

Table 7. Flexibility coefficients for the I-specimen from the out-of-plane tests . . . 77

Table 8. Flexibility influence coefficients for the channel specimen from the out-of-plane tests 79

Table 9. Correlation of the free-free in-plane natural frequencies of the I-specimen 136

Table 10. Correlation of clamped-clamped in-plane natural frequencies for the I-specimen 140

Table 11. Effects of boundary spring stiffness on the in-plane vibrational response of the I-specimen 141

Table 12. Correlation of clamped-clamped, in-plane natural frequencies for the channel specimen 144

Table 13. Correlation of clamped-clamped, out-of-plane natural frequencies for both specimens 150

Table 14. Correlation of flexibility coefficient for the I-specimen 155

Table 15. Correlation of the flexibility coefficients for the I-specimen 158

Table 16. Correlation of the flexibility coefficients for the channel specimen 160

Table 17. Static data from in-plane tests for 20 pound radial load 198

Table 18. Static data from in-plane tests for 40 pound radial load 199

Table 19. Static data from in-plane tests for 60 pound radial load 200

Table 20. Static data from out-of-plane tests 201

Table 21. Static data from out-of-plane tests 202

Table 22. Cross-sectional Properties of both test specimens 203

Chapter 1

Introduction

Background

Fiber reinforced composite materials are used increasingly in the primary structural components of military aircraft. Use of composites in civilian transport aircraft is generally limited to secondary structural components. However, the well documented advantages of composites are motivating designers to use composites more extensively. Using composites in primary structural components of civilian aircraft raises the issue of crashworthiness. Research has revealed deficiencies in the energy absorbing capabilities of fiber reinforced composite materials. Though composites are poor energy absorbers on a material level, it may be possible to design composite structures which absorb energy efficiently. Thus, the challenge to the engineering community is to design composite structural components which carry the flight loads and perform satisfactorily in a crash situation.

Crashworthiness is a complicated issue, but arguably the primary concerns in a crash are to maintain a protective shell around the passengers and to keep decelerations at a survivable level. Aluminum fails in a ductile manner, thus it absorbs energy when it yields and fails. Fiber reinforced composites tend to fail in a brittle fashion which inhibits their ability to absorb energy. It has been found under certain special circumstances (e.g., tubes in axial compression) composite structures are able to efficiently absorb energy via a stable axial crush (Ref. 1). Though crushable composites are an encouraging development, application of this technology to aircraft design is not imminent.

Before further discussion of the crashworthiness of composite materials, it is informative to review some of the research that has been conducted on the impact response of aluminum structural components. Drop tests of full scale aluminum transport fuselage sections have been conducted at the NASA Langley Research Center (Refs. 2, 3, and 4). The results of drop tests of two fuselage sections are shown in Figs. 1 and 2. The fuselage section which includes the wing spar (Fig. 1) shows no structural damage, however, very high inertial loads were transferred to the passenger level. The fuselage section without the wing spar (Fig. 2) suffered extensive structural damage resulting in lower inertial loads at the passenger level. Extensive bending failures of the fuselage frames helped reduce the inertial loads transmitted to the passenger level indicating that the fuselage frame is an important component in the impact response of a conventional aircraft.

If aluminum frames play a significant role in energy absorption, then composite frames may have to behave similarly to obtain acceptable energy absorption. Tests comparing the impact response of composite and aluminum frames (Ref. 5) showed that the frames fail in distinctly different fashions. The aluminum frames formed plastic

ORIGINAL PAGE
BLACK AND WHITE PHOTOGRAPH

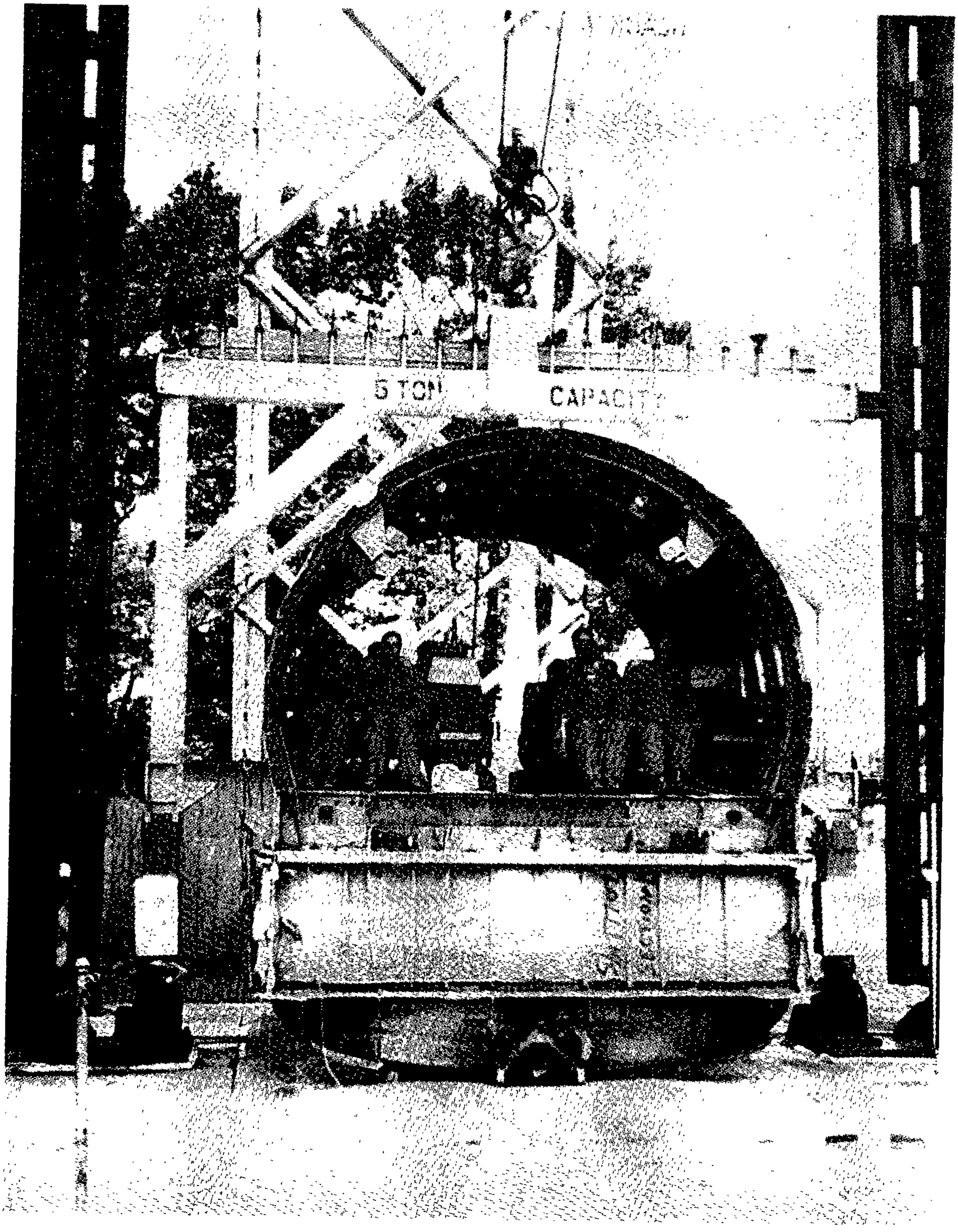

Figure 1. **Drop test of full scale fuselage section:** Fuselage section including the wing spars suffers little structural damage during drop test, resulting in high inertial loads at the passenger level. The section was dropped from a height of six feet resulting in an impact velocity of twenty feet per second.

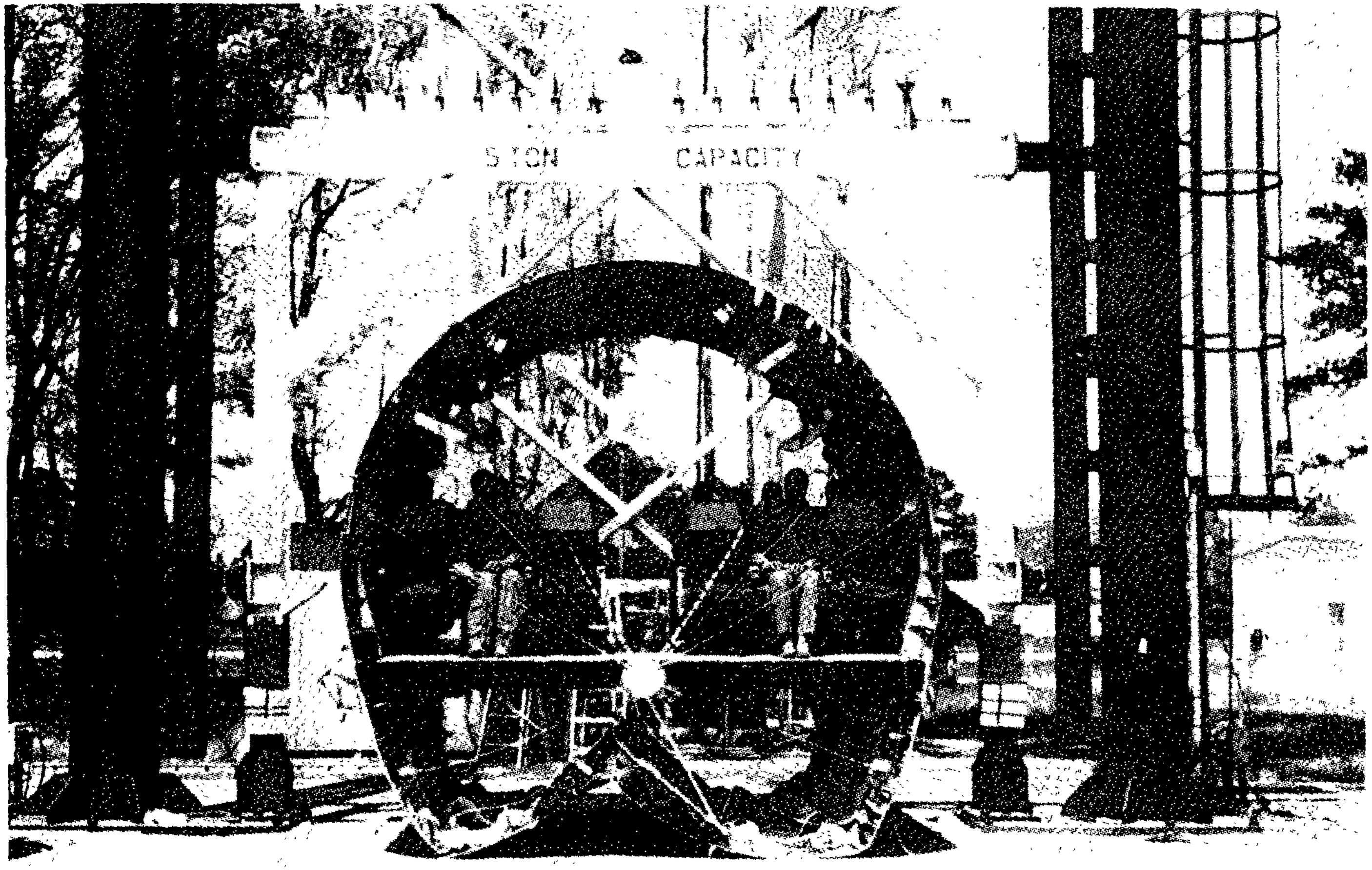

Figure 2. **Drop test of full scale fuselage section:** Fuselage sections located fore and aft of the wing suffered extensive structural damage, resulting in lower accelerations at the passenger level. The section was dropped from a height of six feet resulting in an impact velocity of twenty feet per second.

ORIGINAL PAGE
BLACK AND WHITE PHOTOGRAPH

hinges at several locations around the frame without fracturing, thus maintaining structural integrity. Failure of the composite frames involved a complete fracture of the cross section near the impact point. Complete fracturing of the frame is an undesirable failure since loss of structural integrity implies an uncrashworthy design.

Tests of built-up composite fuselage subsections (Ref. 6) further demonstrated the tendency of composite frames to fail in a brittle manner. The photographs in Figs. 3 and 4 show a skeleton subsection before and after the drop test, respectively. The frames of the subsection suffered numerous localized brittle fractures resulting in loss of structural integrity and minimal energy absorption. A drop test of another subsection which had a layer of skin attached to the outside of the frames resulted in a single brittle fracture of each frame at the impact point. The skin helped the subsection maintain structural integrity. However, in both cases, very high inertial pulses were transmitted to the 'passenger level'.

These test results indicate that conventional designs for composite fuselage frames fail to provide satisfactory impact behavior. The structural design of a composite frame must complement the material system such that crashworthiness is achieved. Since unconventional designs are necessary to utilize composites while maintaining crashworthiness, it is important to develop reliable analytical tools which can predict the response of these designs. The reliability of the analyses should be established by comparisons with experimental data. This research attempts to provide some of this data and to evaluate a new finite element computer code. The finite element evaluated here is expected to be incorporated in the crash analysis finite element program DYCAST.

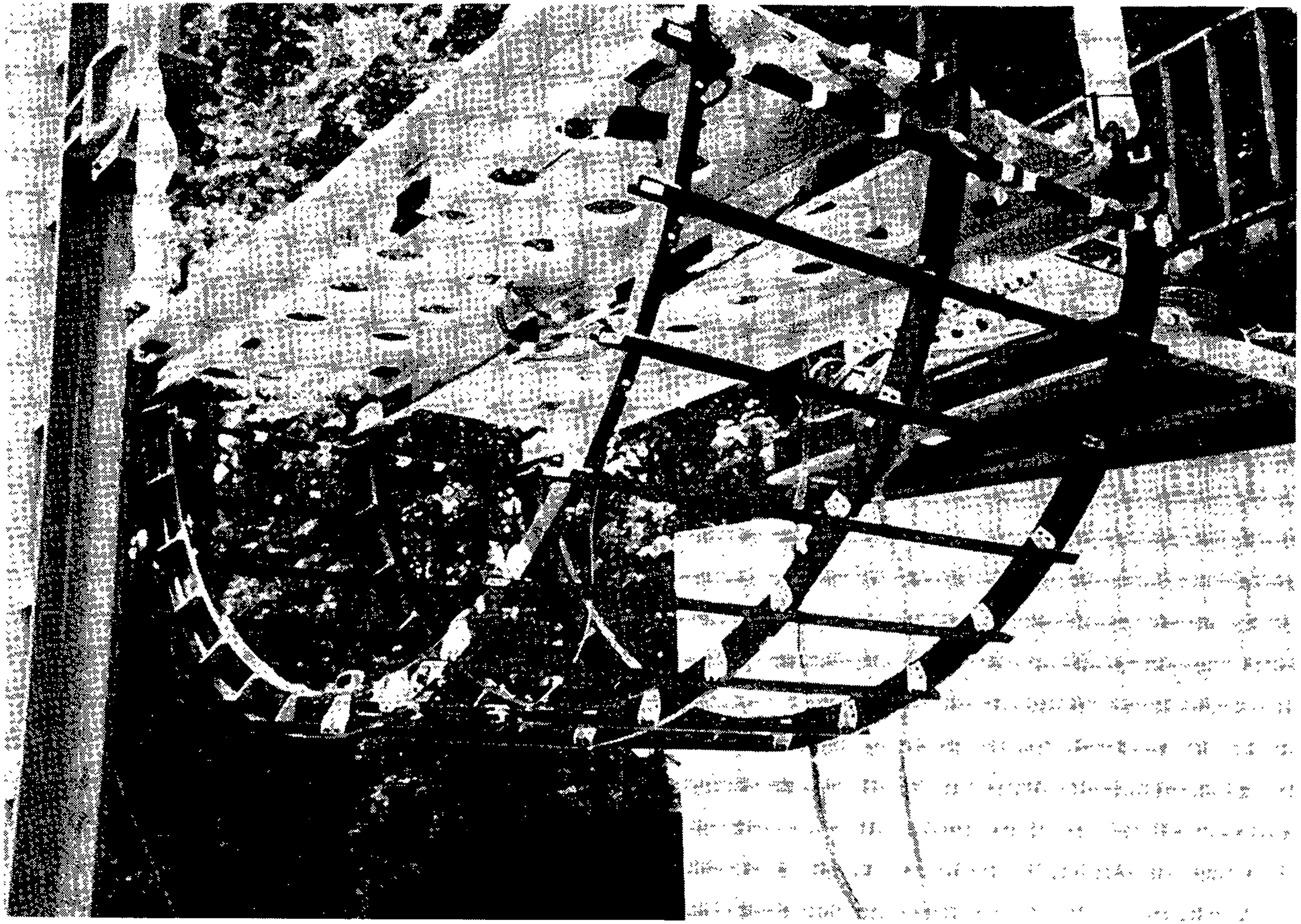

Figure 3. Drop test of a composite fuselage subsection: The photograph shows an all composite fuselage skeleton subsection prior to drop test.

ORIGINAL PAGE
BLACK AND WHITE PHOTOGRAPH

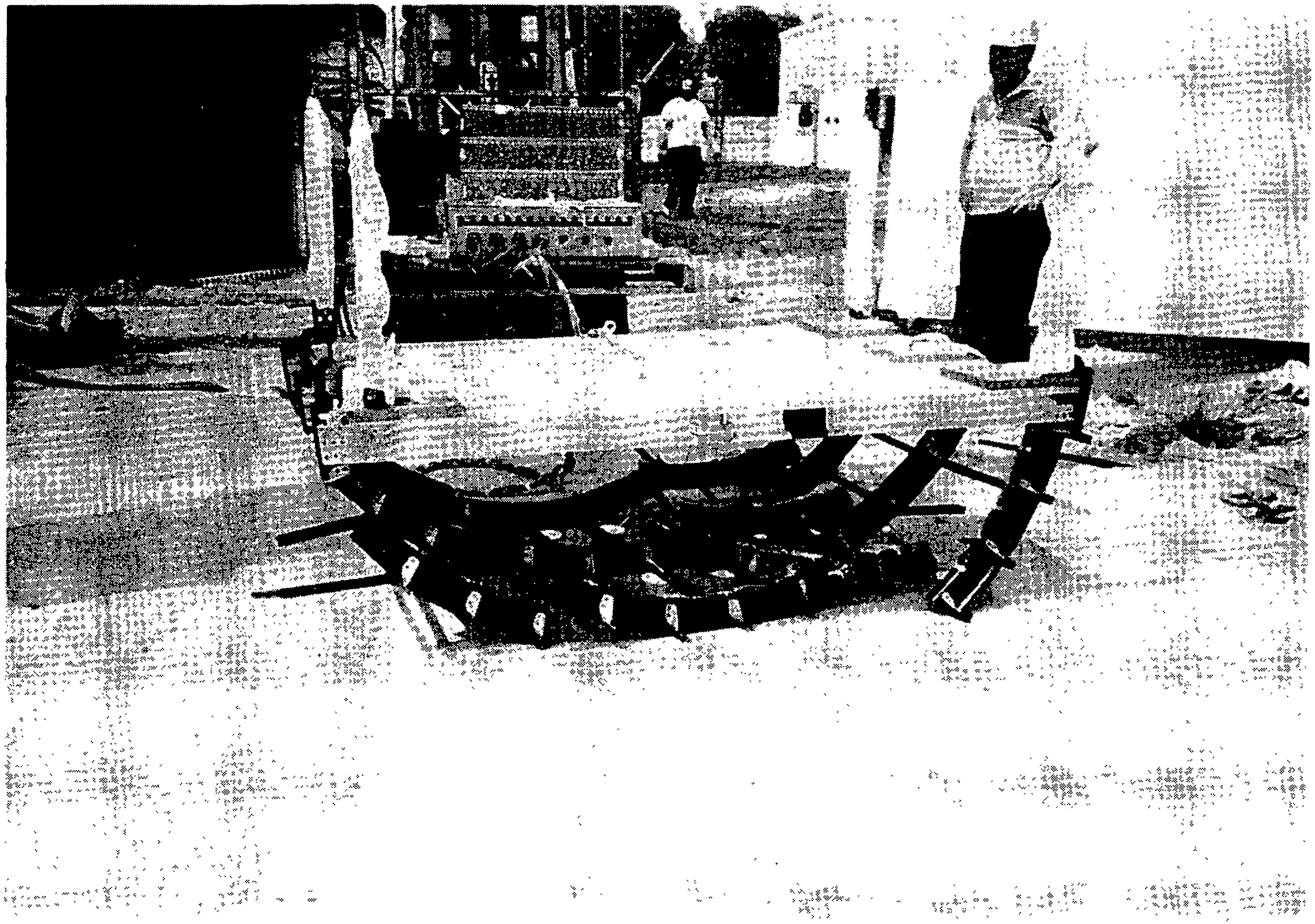

Figure 4. Drop test of a composite fuselage subsection: Subsection was dropped such that the impact velocity was twenty feet per second. The photograph of the impacted subsection shows numerous localized brittle failures.

ORIGINAL PAGE
BLACK AND WHITE PHOTOGRAPH

Objective

The objectives of this research are to measure the three-dimensional static and vibratory response of two graphite-epoxy frame specimens, and to correlate the experimentally measured response with predictions from a computer program which uses a newly developed finite element. The test specimens are thin-walled, open section, semicircular frames with a nominal radius of three feet. One specimen has an I cross section and the other has an asymmetric channel cross section. The finite element was recently developed by Noor et al. (Ref. 7), for the analysis of curved thin-walled beams with open sections. The flexibility influence coefficients were measured in static tests for loads applied at the midspan with the ends of the frames clamped in supports. Dynamic tests provided the natural frequencies and mode shapes of the frames for free-free and clamped-clamped end conditions. It is important to validate the analysis for the linear response of these frames before attempting the nonlinear analysis of frame collapse.

Literature Review

The scope of this research includes both the static and dynamic response of semicircular frames. Since few researchers choose to address both topics in a single document, it is convenient to divide the literature review accordingly.

Dynamics

The vibrations of curved beams and rings is an old and recurring topic in the literature. In general, the vibratory response of a curved beam or ring encompasses in-plane modes (deformations within the plane of curvature) and out-of-plane modes (deformations out of the plane of curvature). If the curved beam has a plane of symmetry coinciding with the plane of curvature, then the in-plane and out-of-plane modes decouple and can be treated separately. Many early researchers took advantage of this. Only relatively recently have researchers addressed the coupled vibrational problem of a curved beam with an asymmetric cross section.

The first published paper addressing the dynamic response of a circular ring was written by Hoppe (Ref. 8) in 1871. In 1888, Lamb (Ref. 9) determined the in-plane natural frequencies for a shallow ring segment with free-free end conditions. In 1892, Love (Ref. 10) generated the differential equations governing the vibration of a complete ring, solved the equations approximately, and presented frequency equations for the in-plane and out-of-plane modes of a complete ring.

In 1928, Den Hartog (Ref. 11) used a Rayleigh solution to solve for the first in-plane natural frequency for ring segments with clamped and pinned boundary conditions. Den Hartog found that if the arc length of the ring segment was sufficiently small, the fundamental in-plane mode was extensional in nature possessing only two nodes similar to the fundamental mode of a straight beam. Generally, if the opening angle was greater than 80°, then the fundamental mode had three nodes and was flexural. For a semi-circular ring segment with clamped boundary conditions, Den Hartog's solution for the frequency ω in Hertz reduces to

$$\omega = \frac{0.6971}{a^2}\left(\frac{EI_{yy}}{\gamma}\right)^{\frac{1}{2}} \tag{1.1}$$

where EI_{yy} is the in-plane bending stiffness, γ is the mass per unit length, and a is the radius of the ring segment.

In 1934, Brown (Ref. 12) used a modified Rayleigh solution to obtain the natural frequency of the fundamental out-of-plane mode for a clamped circular ring segment. For a semi-circular ring segment, Brown's solution for the frequency ω in Hertz reduces to

$$\omega = \frac{.1084}{a^2}\left(\frac{C}{\gamma}\right)^{\frac{1}{2}} \tag{1.2}$$

assuming the ratio of in-plane bending stiffness to torsional stiffness is large ($k = EI_{yy}/C \geq 75$) where C is the torsional stiffness as defined by Timoshenko (Ref. 13), γ is the mass per unit length, and a is the radius of the ring segment.

The vibrational response of curved beams and rings attracted moderate attention during the 30's, 40's, and 50's as researchers sought to improve their predictions by incorporating refinements such as rotatory inertia and transverse shear deformation. In the interest of brevity, the body of literature from this period will not be addressed as it is of limited interest here. The interested reader may refer to two papers by Lang (Refs. 14 and 15) and the dissertation of Maddox (Ref. 16) for a complete review of this period.

In 1963, Hammoud and Archer (Ref. 17) published an interesting paper addressing the coupled vibrational response of complete rings and ring segments with asymmetric cross sections. They presented the coupled differential equations governing the in-plane and out-of-plane vibrations and used an approximate solution to the decoupled problem as their first guess in an iterative procedure to solve for the coupled natural frequencies.

Hammoud and Archer limited their scope to solid cross sections as their solution does not account for the effects of cross-sectional warping.

Maddox (Ref. 16) addressed the decoupled vibrations of a complete thin-walled ring with one plane of symmetry. His solution accounts for transverse shear deformation, rotatory inertia, cross-sectional warping, and shear center eccentricity. Maddox reduced a higher order shell theory to a ring theory by integrating around the contour of the cross section and making explicit assumptions on the shell displacements. Maddox showed that shear center eccentricity and warping have significant effects on the response of some thin-walled rings.

Endo (Ref. 18) solved for the vibrational response of a complete ring with an arbitrary cross section. Kirkhope, Bell, and Olmstead (Ref. 19) also solved for the coupled vibrational response of a complete ring with an arbitrary cross section and presented experimental data in order to test their solution. These solutions are restricted to solid cross sections since warping is not included. Williams (Ref. 20) developed the differential equations for complete thin-walled rings and applied them to several examples including ring segments with symmetric cross sections. Williams included the effects of transverse shear, rotatory inertia, and warping in his solution.

Rao (Ref. 21) solved for the out-of-plane vibrational response of complete rings and ring segments. Rao included transverse shear deformation and rotatory inertia in his solution. He found that he could model a variety of unusual boundary conditions. Culver (Ref. 22) used Vlasov's (Ref. 23) thin-walled beam theory in his solution for the decoupled out-of-plane response of a curved beam. Culver assumed the cross section of the beam was doubly symmetric and treated the inertia terms as a distributed load in Vlasov's static formulation. Culver does not consider the inertia terms associated with warping.

Gardner and Bert (Ref. 24) presented a new first approximation theory for the in-plane dynamic behavior of shear deformable structures. Several references are made about the application of this theory to composite structures, but it was not addressed explicitly. The paper does include some experimental data on thick full rings. Bhimaraddi (Ref. 25) specifically addresses the dynamic response of curved laminated beams, though his discussions are limited to rectangular cross sections. Bhimaraddi found that coupling of in-plane and out-of-plane modes can happen despite a geometrically symmetric cross section if the ring is an unsymmetric laminate. Bhimaraddi presents the coupled equations in terms of laminate properties and some experimental data from laminated rings with two lamina.

With the exception of Bhimaraddi (Ref. 25), the author knows of no research directed at the vibrational response of curved composite beams. Further, there seems to be a dramatic lack of experimental data for curved beams of any cross section or material system. This research will help to fill these voids.

Statics

The static portion of the literature review will be limited to those papers which specifically address thin-walled curved beams or have an important bearing on this research. Though much work preceded Timoshenko's series of papers (Ref. 13) on thin-walled beams, his work unified the existing engineering theories on the bending, torsion, and buckling of beams with thin-walled open cross sections. He presented new developments such as the concepts of warping, shear center, and torsion center. His papers address thin-walled beams in a very thorough manner, though he does not treat curved beams.

Vlasov (Ref. 23) derived a beam theory for thin-walled beams including the effects of curvature. This represents the first detailed discussion of curved thin-walled beams. Vlasov included the effects of warping and rotatory inertia. He restricted his attention to thin rings facilitating the neglect of transverse shear deformation and shear center eccentricities. He also assumed that the cross section is infinitely rigid in its own plane. Gjelsvik (Ref. 26) presents Vlasov's theory in more modern terminology though it does not include the material on curved beams.

Bauld and Tzeng (Ref. 27) extended Vlasov's theory to account for anisotropic material properties common in laminated composites. This theory uses modulus weighted section properties to account for stiffness variations through the thickness of the walls. This theory assumes that all the branches are midplane symmetric and the beams are straight. Though the theory was developed for straight beams, it could be extended to include curved beams. Lo (Ref. 28) used this theory in his analysis of flexural-torsional buckling of laminated composite columns.

Mabson (Ref. 29) discusses some of the differences between isotropic and composite curved thin-walled beams. Mabson shows that composite cross sections are more susceptible to flexural deformations than isotropic cross sections. This indicates that composite beams may be more likely to violate the assumption that the cross section is infinitely rigid within its own plane. Mabson suggests a way of calculating effective cross-sectional stiffnesses for composite laminated beams of various cross sections.

Tralli (Ref. 30) and Noor (Ref. 7) have both used hybrid finite elements to evaluate the static response of thin-walled structures. Tralli's approach addresses only straight beams, but will handle closed as well as open sections. While Tralli's program is limited to static analysis, Noor's finite element was also developed for the free-vibrational analysis of curved thin-walled beams. Noor's program is used extensively in this research and will be discussed more thoroughly in Chapter 5.

Summary

Having attempted to provide some of the background and motivation for this study, the remaining material will be devoted to describing the research. The test specimen's manufacture, material system, and dimensions are discussed in Chapter 2. The experimental apparatus and test procedures are presented in Chapter 3. The experimental results are presented in Chapter 4. The analytical effort is outlined in Chapter 5. Correlation of experimental and numerical results comprise Chapter 6. Concluding remarks and recommendations for future work are presented in Chapter 7.

Chapter 2

Test Specimens

Design and Fabrication

Conventional aircraft designs use thin-walled frames and beams to build the skeleton of a fuselage. The test specimens for this research are intended to represent fuselage frames. Two semi-circular frames were tested, a symmetric I-section and an asymmetric channel section. The cross-sectional shapes are shown in Fig. 5. Channel and I-sections are commonly used in conventional aircraft designs and provide the opportunity to investigate the effect of symmetry. In tests of composite fuselage subsections (Ref. 6), it was found that the skin substantially strengthened and stabilized the subsections. This motivated the addition of a thick layer of 'skin' to the outside of each frame. The layer of 'skin' is intended to simulate the out-of-plane stabilizing effect of the fuselage skin.

The test specimens were fabricated using AS4/5208, graphite/epoxy, preimpregnated, unidirectional, tape. The tape was manufactured by Narmco and the specimens were laid up by Bell Textron. The nominal material properties for AS4/5208

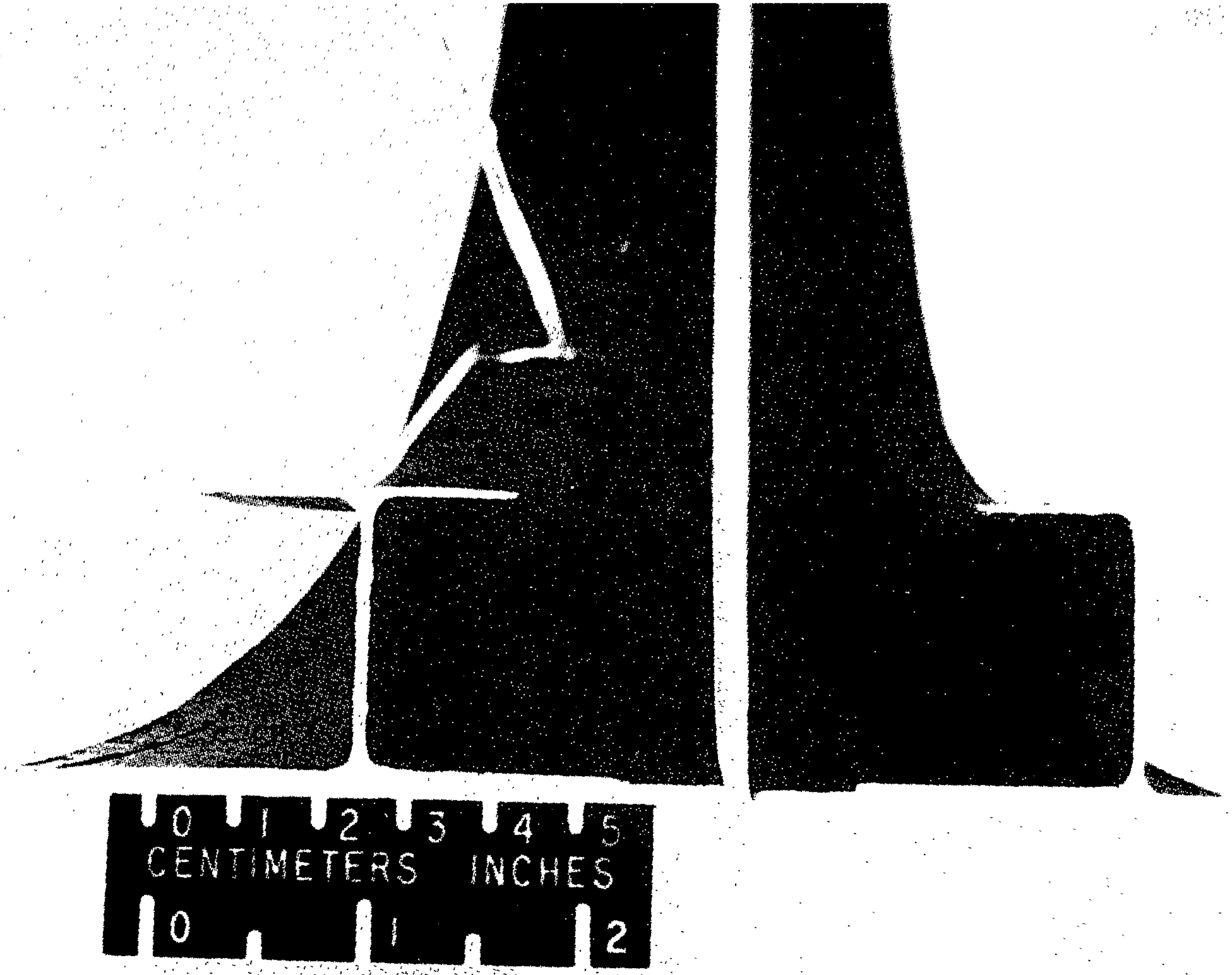

ORIGINAL PAGE
BLACK AND WHITE PHOTOGRAPH

Figure 5. Cross sections of the test specimens: The photograph shows the cross sections of the I-section and channel section specimens. A sixteen ply 'skin' is bonded to the outside flanges of each specimen. The cap flanges are the smaller flanges furthest from the skin.

are presented in Table 1. The specimens were laid up using a quasi-isotropic sequence following the schematic in Fig. 6. The specified angles are measured with respect to the circumferential axis of the specimen. The layup in the 8 ply cap flanges is $(\pm 45/0/90)_s$. The layup for the 16 ply skin is $(\pm 45/0/90)_{2s}$. In the region where the attachment flanges are bonded to the skin, the 24 ply layup is $(\pm 45/0/90/90/0/\mp 45/\pm 45/0/90/\pm 45/0/90/90/0/\mp 45/90/0/\mp 45)_T$. Although this layup is asymmetric, a classical analysis of this region shows that the coupling terms are negligible. The web of the channel specimen has the same layup as the cap flanges, but the web of the I-specimen has an anti-symmetric layup $(\pm 45/0/90/90/0/\pm 45)_T$, resulting in significant extension-bending coupling terms. It will be evident from the data in subsequent chapters, that the anti-symmetric layup in the web of the I-section specimen did not adversely effect its symmetric response.

Table 1. Nominal material properties for AS4/5208 from Narmco

Property		Value
Longitudinal Modulus	E_{11}	18.40×10^6 psi
Transverse Modulus	E_{22}	1.64×10^6 psi
Transverse Modulus	E_{33}	1.64×10^6 psi
In-plane Shear Modulus	G_{12}	0.87×10^6 psi
Transverse Shear Modulus	G_{13}	0.87×10^6 psi
Transverse Shear Modulus	G_{23}	0.49×10^6 psi
In-plane Poisson Ratio	ν_{12}	0.30
Transverse Poisson Ratio	ν_{13}	0.30
Transverse Poisson Ratio	ν_{23}	0.35
Lamina Thickness	t	0.0055 in
Material Mass Density	ρ	1.80×10^{-3} $(\text{lb-sec}^2)/(\text{ft-in}^3)$

The nominal dimensions of the test specimens are shown in Fig. 7. The diameter of the frames is 72 inches and the cross-sectional heights are about 1.5 inches. This geometry places the frames in the category of thin rings. The effects of rotatory inertia and transverse shear typically have little effect on the response of thin rings.

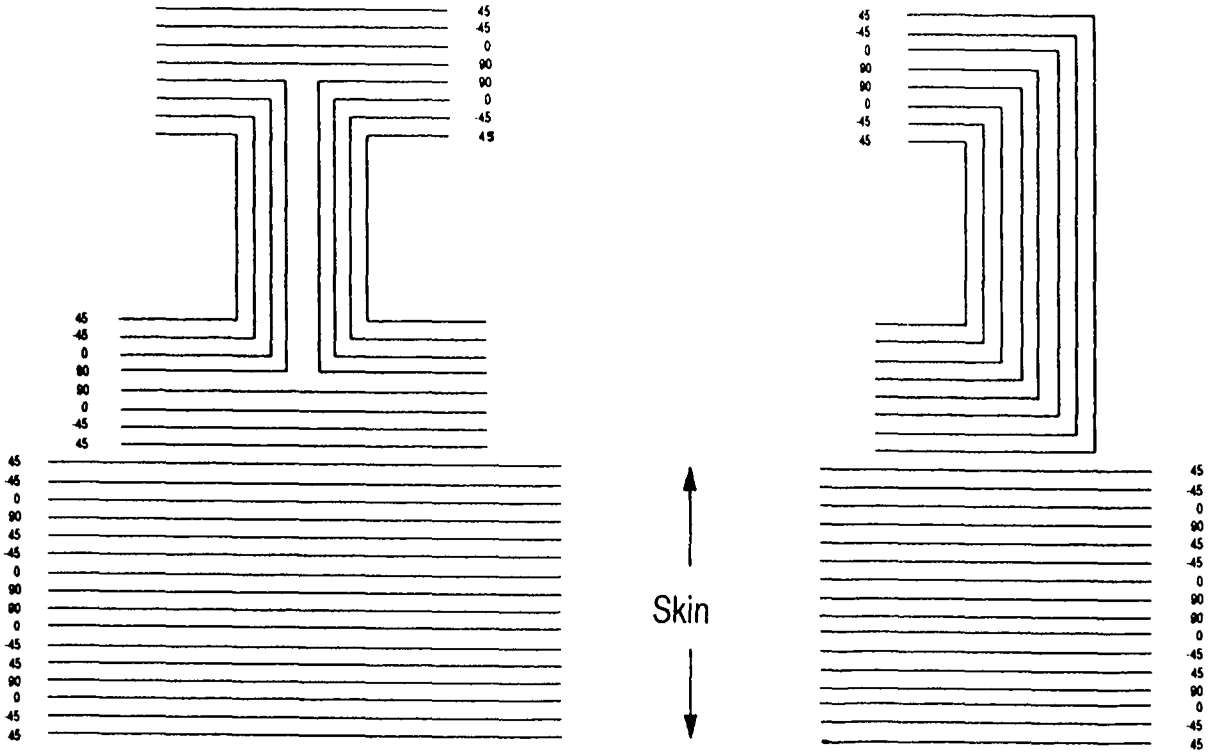
45
-45
0
90
90
0
-45
45
45
-45
0
90
90
0
-45
45
45
-45
0
90
45
-45
0
90
90
0
-45
45
90
0
-45
45
Skin
45
-45
0
90
90
0
-45
45
45
-45
0
90
45
-45
0
90
90
0
-45
45
90
0
-45
45

Figure 6. Specimen layup: The layup for the channel section and I-section specimens is shown schematically.

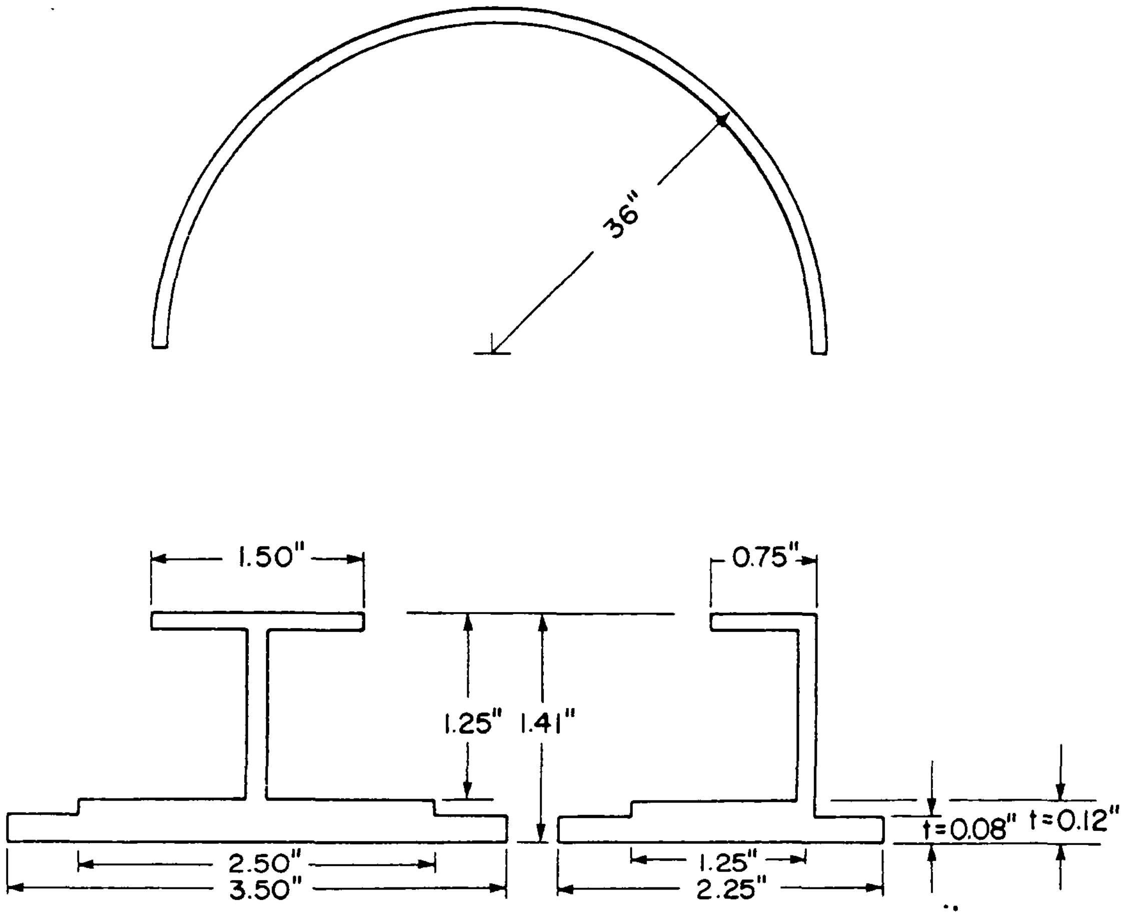
36"
1.50"
0.75"
1.25"
1.41"
t=0.08"
t=0.12"
2.50"
3.50"
1.25"
2.25"

Figure 7. Specimen dimensions: The radial and cross-sectional dimensions of the tests specimens are presented in two views.

Specimen Characterization

The results of an ultrasonic inspection of the web of the channel specimen is shown in Fig. 8. The white patches indicate regions which may be damaged or substandard, raising questions about the consistency of the stiffness properties with respect to circumference. Subsequent tests were designed to investigate this concern. After the static and dynamic tests were completed, the I-section specimen was instrumented for a crush test and the channel specimen was cut into five ring segments for further evaluation. Four of the segments were tested in three point bending to determine if the bending stiffness was constant with respect to circumference. These specimens had a uniform arc of about forty degrees. The fifth ring segment was cut into tensile and shear coupons for material characterization tests.

The three point bend test configuration is shown in Fig. 9. The ring segments were supported at their ends across a span of eighteen inches. The segments were loaded radially by hanging twenty pound calibration weights from the center of the segments. A load fixture was used to apply the load to the segments such that the segments did not twist. The displacements were measured using dial indicators. Each specimen was tested five times and the resulting data was averaged. The results of the tests are presented in Fig. 10. The load displacement curves for the four segments are very consistent. The slope of the lines fall within ±3 % of the average slope. These results negated much of the concern about circumferential stiffness nonuniformity suggested by the ultrasound scan.

The last segment was cut into two tensile and three shear coupons for material characterization tests. The coupon tests were intended to confirm the effective moduli

ORIGINAL PAGE
BLACK AND WHITE PHOTOGRAPH

ORIGINAL PAGE IS
OF POOR QUALITY

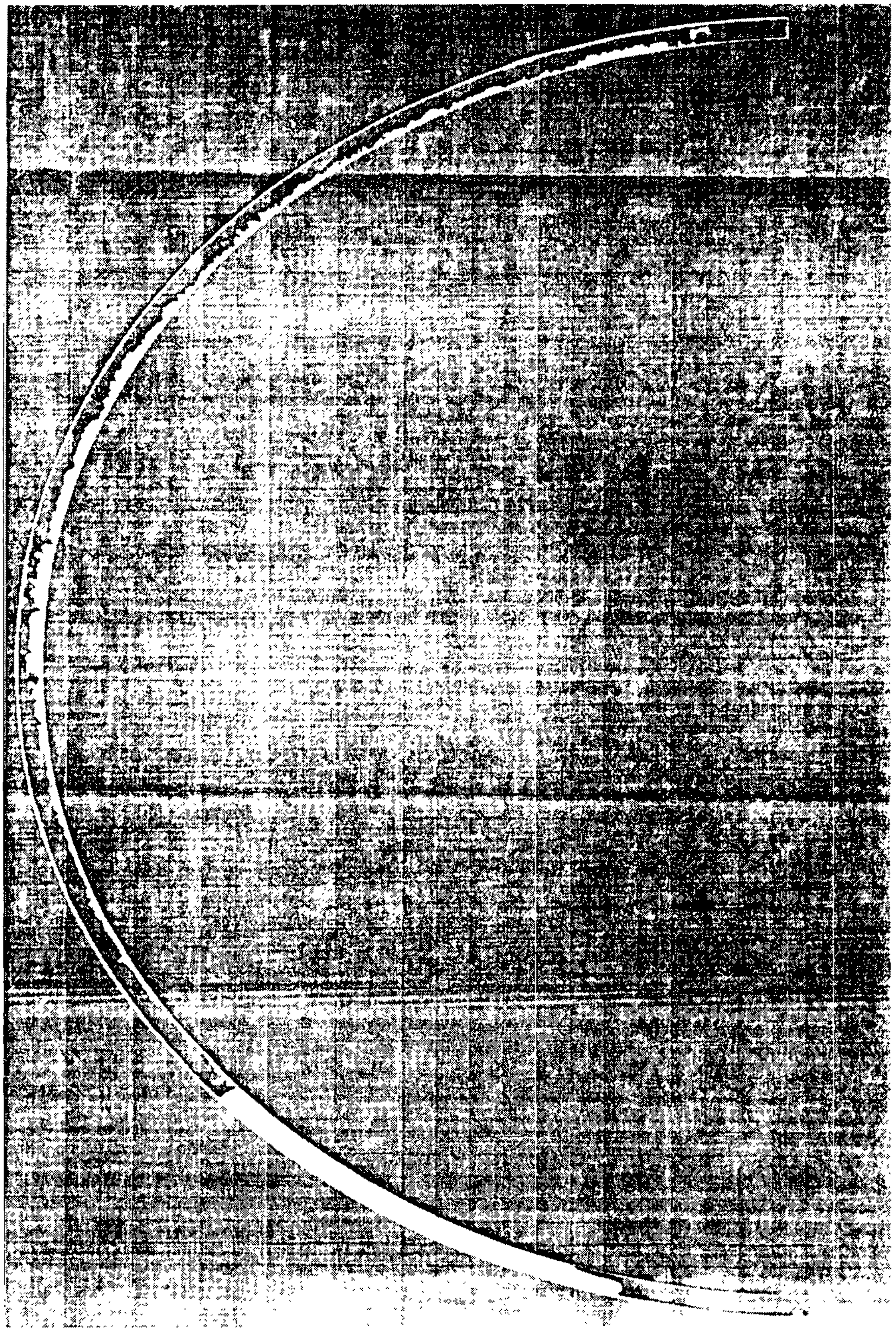

Figure 8. Ultrasound scan of the channel specimen: The figure shows the results of an ultrasound scan of the web of the channel section specimen. White patches indicate regions which may be damaged or substandard.

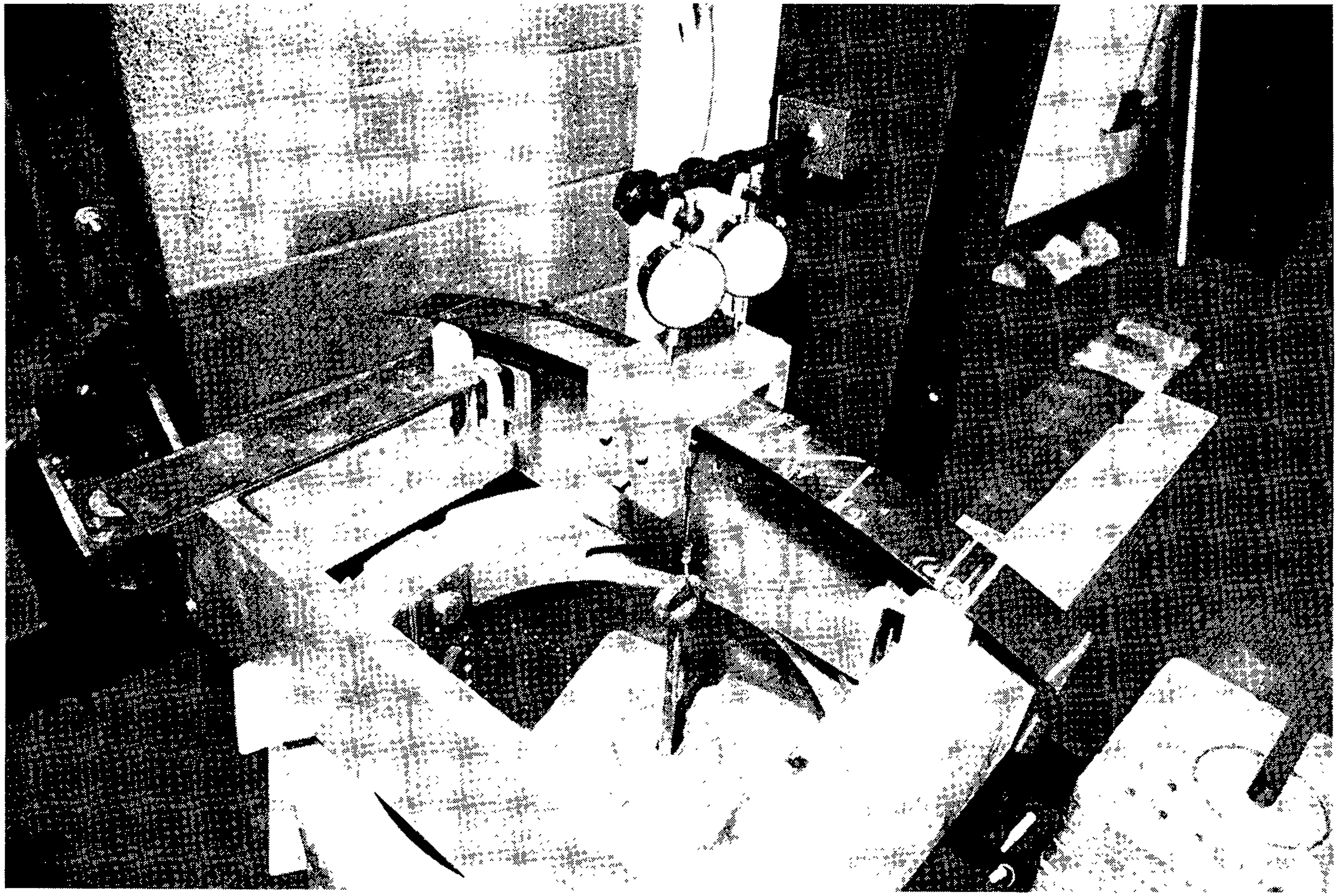

Figure 9. Three-point bend test configuration: The photograph shows the test apparatus for the three point bend tests. The ring segments were supported at the ends and loaded at the midspan. The deflections were measured using two dial indicators.

ORIGINAL PAGE
BLACK AND WHITE PHOTOGRAPH

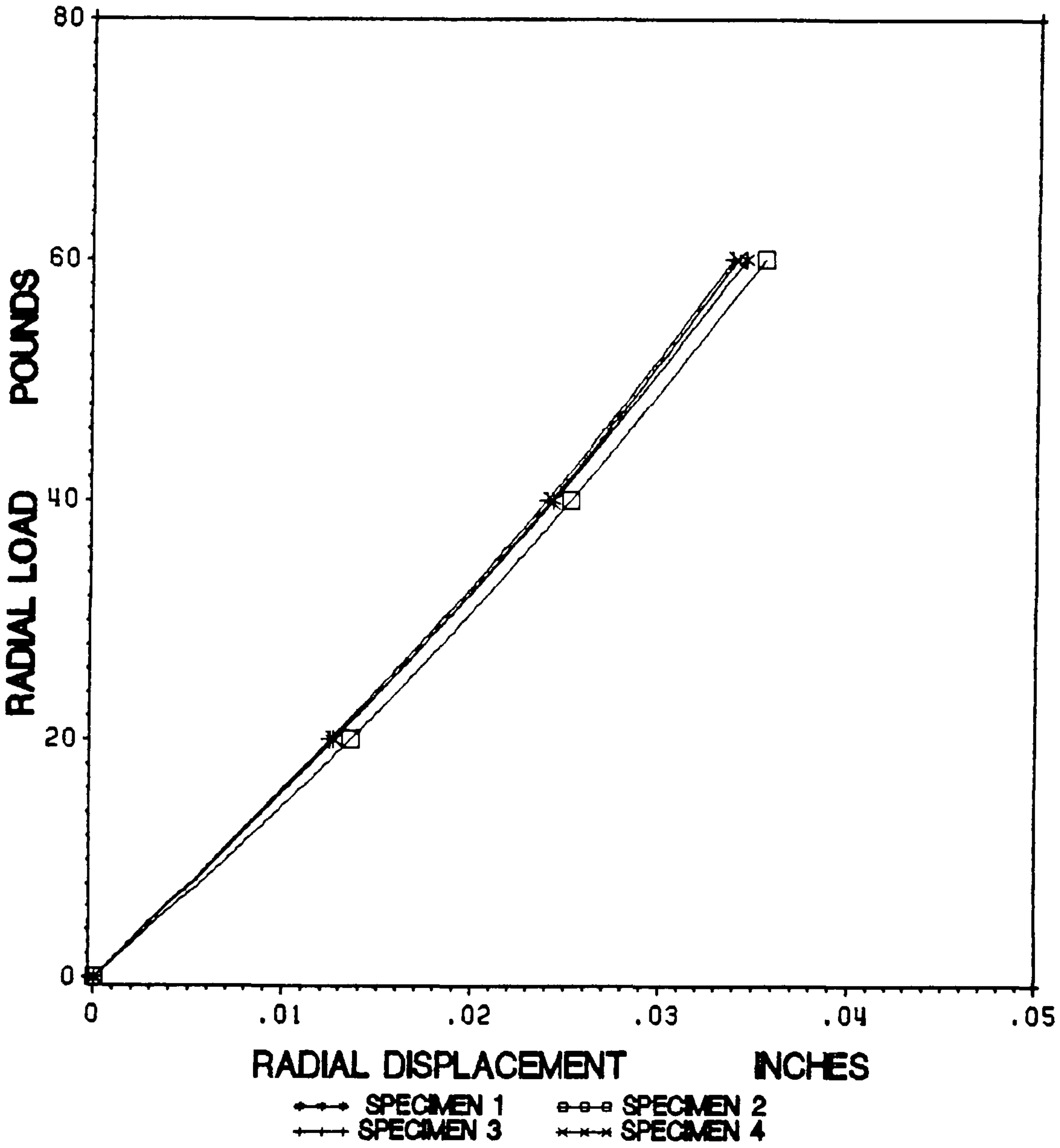

Figure 10. Load-displacement data from three-point bend tests: The plot shows the load versus displacement plot for the four segments cut from the channel specimen. The slopes of the lines are very consistent indicating consistent bending stiffnesses.

(E_{xx} and G_{xy}) calculated from classical lamination theory and nominal material properties.

The shear coupons were cut from the web of the section since those coupons had to be flat. The Iosipescu shear test was chosen because of the size limitations on the shear coupons. The shear coupons were cut according to the dimensions specified by Pindera, et al. (Ref. 31). The coupons were instrumented with a three arm rectangular rosette (electrical resistance foil gages) which had a gage length of two millimeters. The results of the shear tests are presented in Fig. 11. The tests gave consistent values for the shear modulus, but the coupons did not fail in shear because of the quasi-isotropic layup. The laminates failed by edge brooming in the 90° layers at the contact points.

Two tension coupons, six inches by 5/8 inches, were cut from the cap flange of the channel specimen. The initial geometry is curved, but the eight ply quasi-isotropic layup is sufficiently flexible that the initial curvature has little effect on the test. The coupons were instrumented with a three arm rectangular rosette on one side and a uniaxial gage on the other side for bending correction. The two tension tests gave nearly identical results for the extensional modulus E_{xx} and failure strain. The stress versus strain plots for the two tensile tests are shown in Fig. 12. The failure strain in the tension tests was about 1 % for both coupons.

The results of the material characterization tests are summarized in Table 2. The experimental values for E_{xx} and G_{xy} compared well with the analytical predictions from classical lamination theory. The discrepancy in the extensional modulus was less than 1 %. The discrepancy in the shear modulus was about 8 %. The experimentally determined stiffness properties were used in all of the analyses for both the channel section and the I-section specimens.

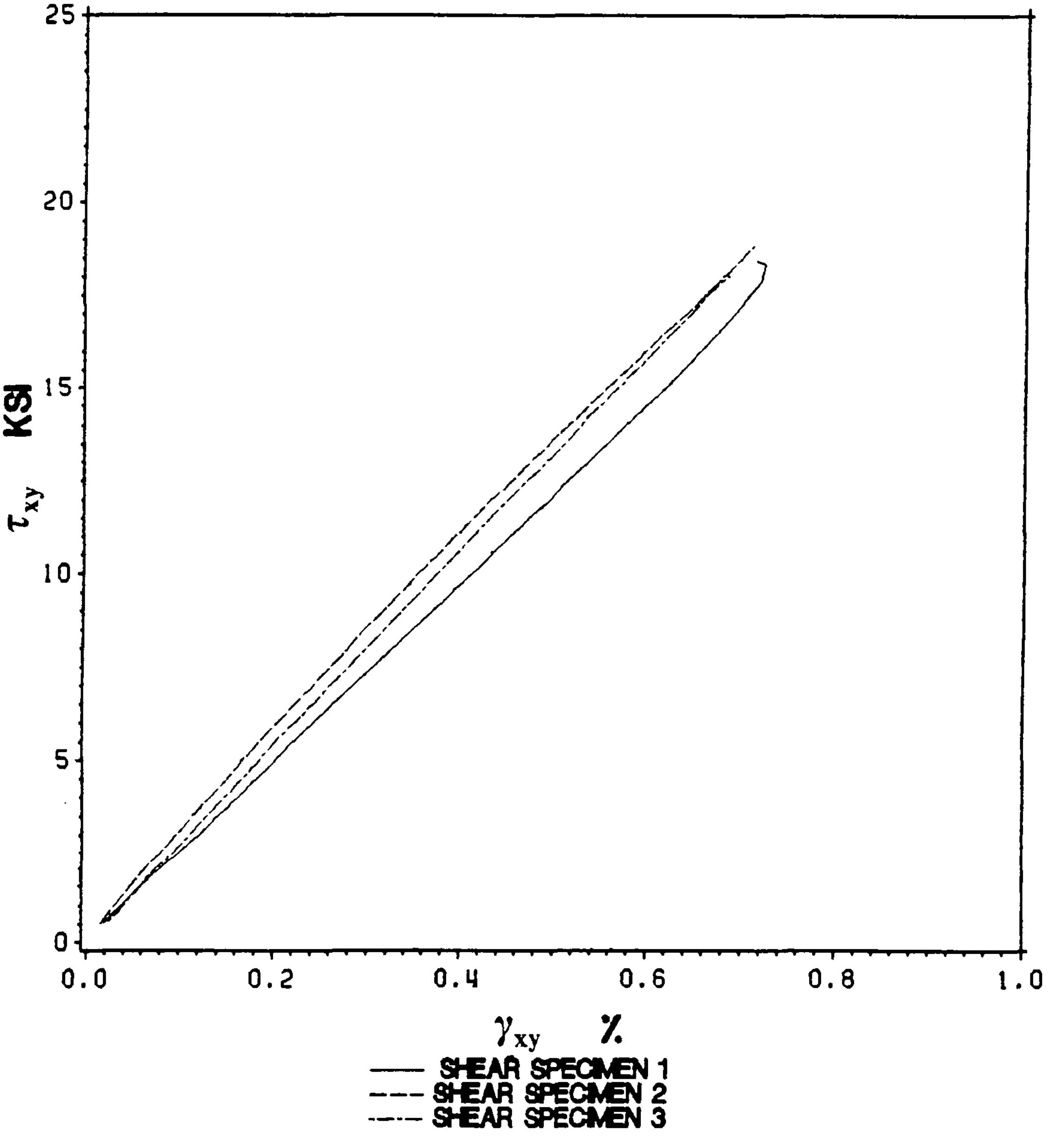

Figure 11. Iosipescu shear test results: The plot shows the shear stress versus shear strain results for the three iosipescu shear coupons cut from the web of the channel specimen.

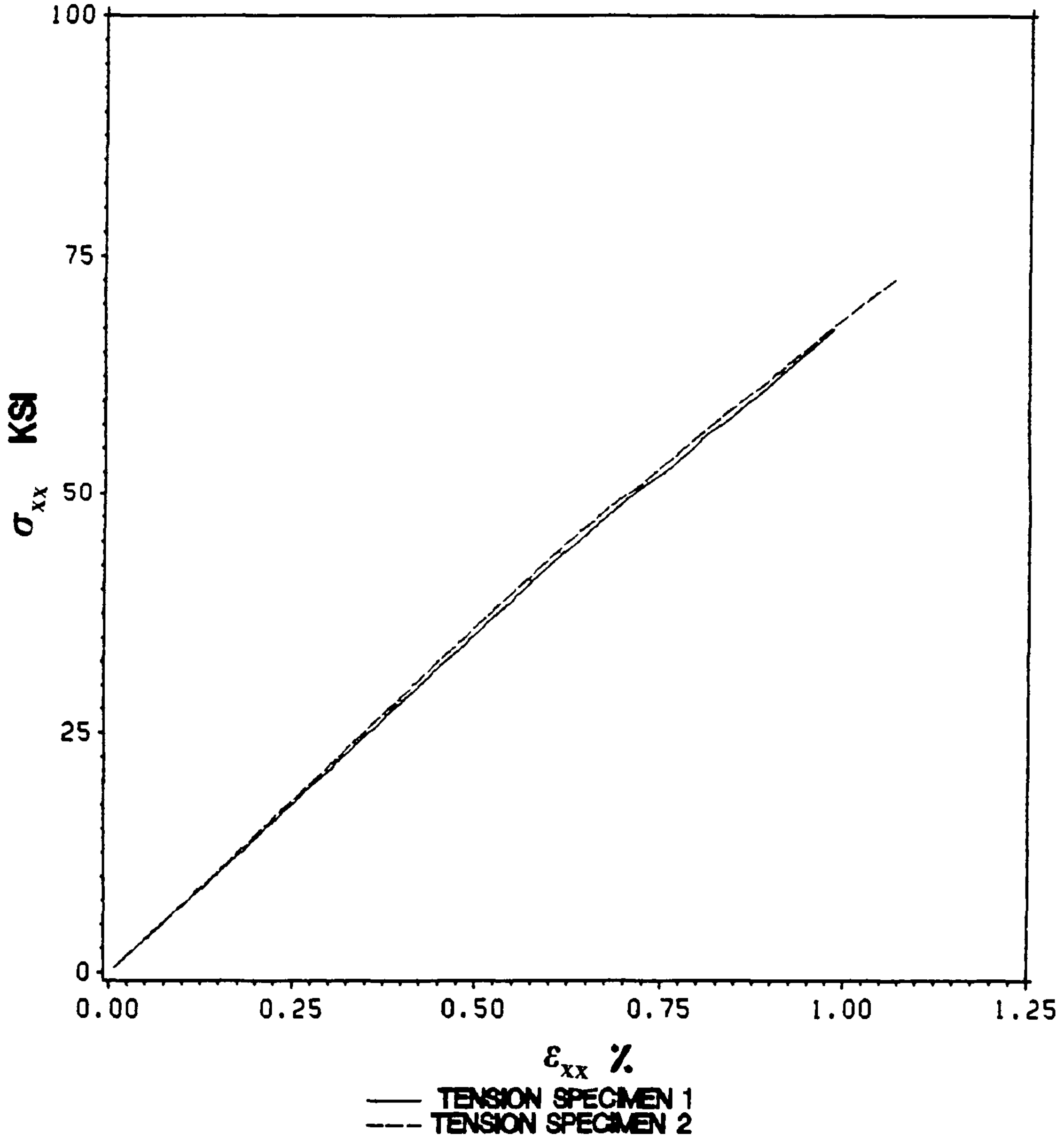

Figure 12. Tension test results: The plot shows the stress versus strain results for the two tensile coupons cut from the cap flange of the channel specimen.

Table 2. Engineering constants from quasi-isotropic coupon tests

Property		Experimental	Analytical	Error[a]
Extensional Modulus	E_{xx}	7.361 x 10^6 psi	7.423 x 10^6 psi	0.84 %
In-plane shear modulus	G_{xy}	2.655 x 10^6 psi	2.862 x 10^6 psi	7.79 %

[a] (Analysis - Exp)/Exp x 100

Chapter 3

Experimental Apparatus and Tests

The experimental scope of this research includes both dynamic and static tests. The dynamic portion of the experimental program employs several test methods to obtain the natural frequencies and the associated mode shapes. The static phase of the research program involves subjecting the specimens to combined loads at the midspan and measuring the resulting displacements at the midspan. After the dynamic and static tests were completed, the I-section specimen was instrumented with strain gages and prepared for a quasi-static crush test. The experimental apparatus and test procedure for each type of test will be discussed independently. The dynamic tests will be discussed first followed by the static tests and the crush test.

Dynamic Tests

This section presents the experimental apparatus and procedures involved in the dynamic tests. The first set of tests were run with free-free boundary conditions and used an air shaker to excite the specimens. After these tests, the ends of the specimens were secured in aluminum end fixtures using Hysol 934 potting compound. The remaining tests were run with clamped-clamped boundary conditions. Each set of tests involved exciting the specimens radially and laterally in order to excite both in-plane and out-of-plane modes. The tests are differentiated by the boundary conditions used. The free-free frame tests will be discussed first followed by the clamped-clamped frame tests.

Free-Free Frame Tests

The free-free frame tests were conducted using the facilities at the Landing and Impact Dynamics Branch at NASA Langley Research Center. The experimental setup for the free-free air shaker tests is shown in Fig. 13. The specimens were hung by elastic bands at two points to emulate free-free boundary conditions. These tests used an air shaker to excite the specimens with pulses of compressed air. The frequency and magnitude of the excitation were variable. The air shaker was a portable unit that required no physical attachment to the specimens. Thus, the air shaker could be oriented in different directions to excite both in-plane and out-of-plane modes.

The response of the specimens was monitored with a hand held velocity probe. The response signal from the probe was monitored visually on an oscilloscope. The probe detected in-plane motion when oriented radially and out-of-plane motion when oriented perpendicular to the plane of the frame. A natural frequency was isolated when the

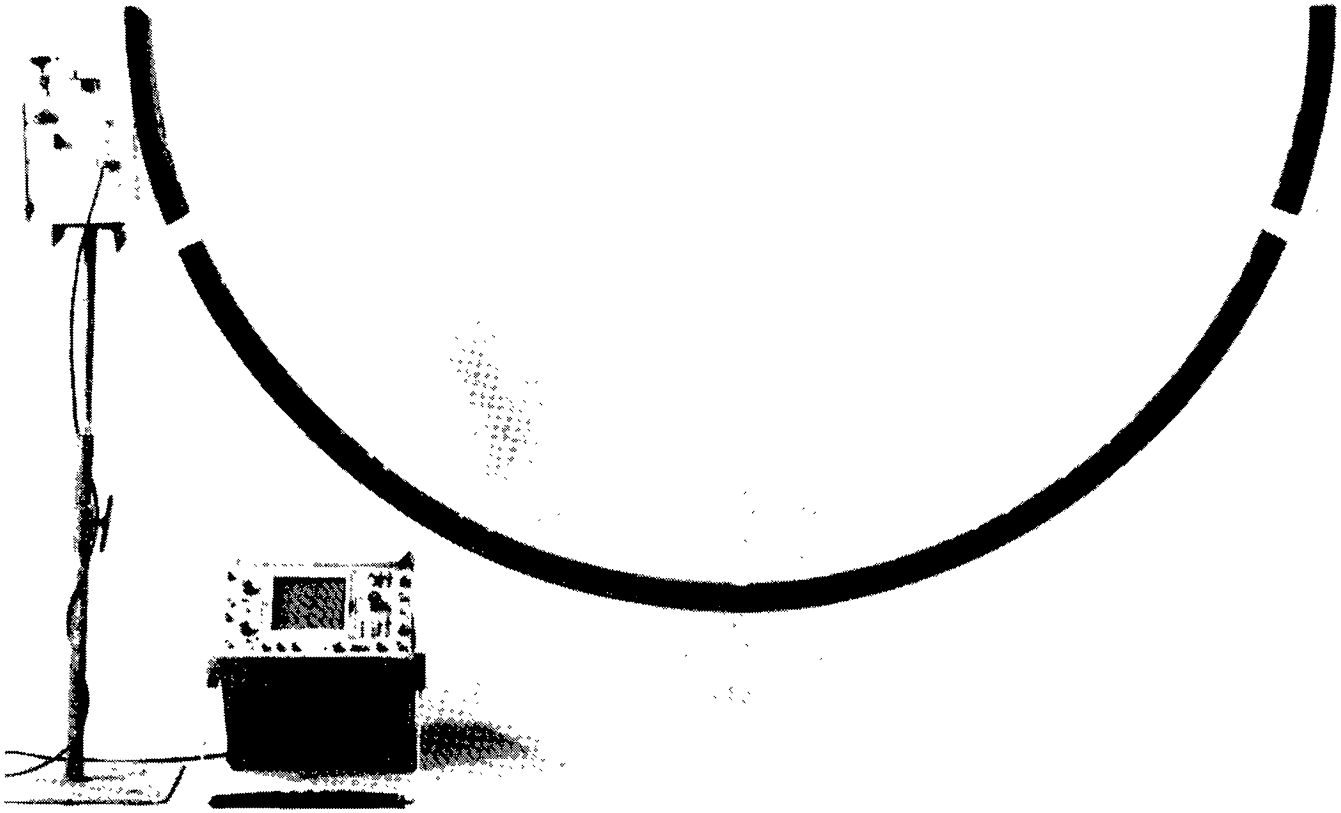

Figure 13. Free-free frame vibrational test setup: The specimens were hung by elastic bands at two points and excited at one end by an air shaker. The response of the frames was monitored using a velocity probe and an oscilloscope.

ORIGINAL PAGE
BLACK AND WHITE PHOTOGRAPH

oscilloscope displayed a strong, clean, constant sinusoidal signal. A natural frequency was tuned in much the same way that a radio station is tuned in. Once a natural frequency was isolated, a strobe light was used to to determine the frequency of excitation. The specimen was excited at that frequency while the mode shape was studied and the nodes located. The frequencies for the rigid body modes were much lower than the frequency of the first vibrational mode indicating that the boundary conditions were achieved satisfactorily. The rigid body modes include in-plane and out-of-plane pendulum and rotational modes.

Clamped-Clamped Frame Tests

The clamped-clamped frame tests were conducted using the facilities in the Department of Aerospace and Ocean Engineering at Virginia Polytechnic Institute and State University. The objectives of these tests were to determine the natural frequencies and node locations of the clamped-clamped resonant modes and to obtain information on the dynamic response of the frames over a range of frequencies in the form of frequency response plots. A structural analyzer was used to generate the frequency response plots. Based on the frequency response plots, a signal generator was used to excite the individual modes enabling the location of the nodal positions to be determined.

The clamped-clamped tests used a Synergistic Technology Incorporated (STI) model 11/23 structural analyzer to generate the excitation signal and process the response data. The structural analyzer employs two interacting software packages set up on a VAX minicomputer to control the excitation signal and to collect and process the data. A flowchart of the test procedure is presented in Fig. 14. The excitation signal is routed through an amplifier to an electromagnetic shaker. The electromagnetic shaker

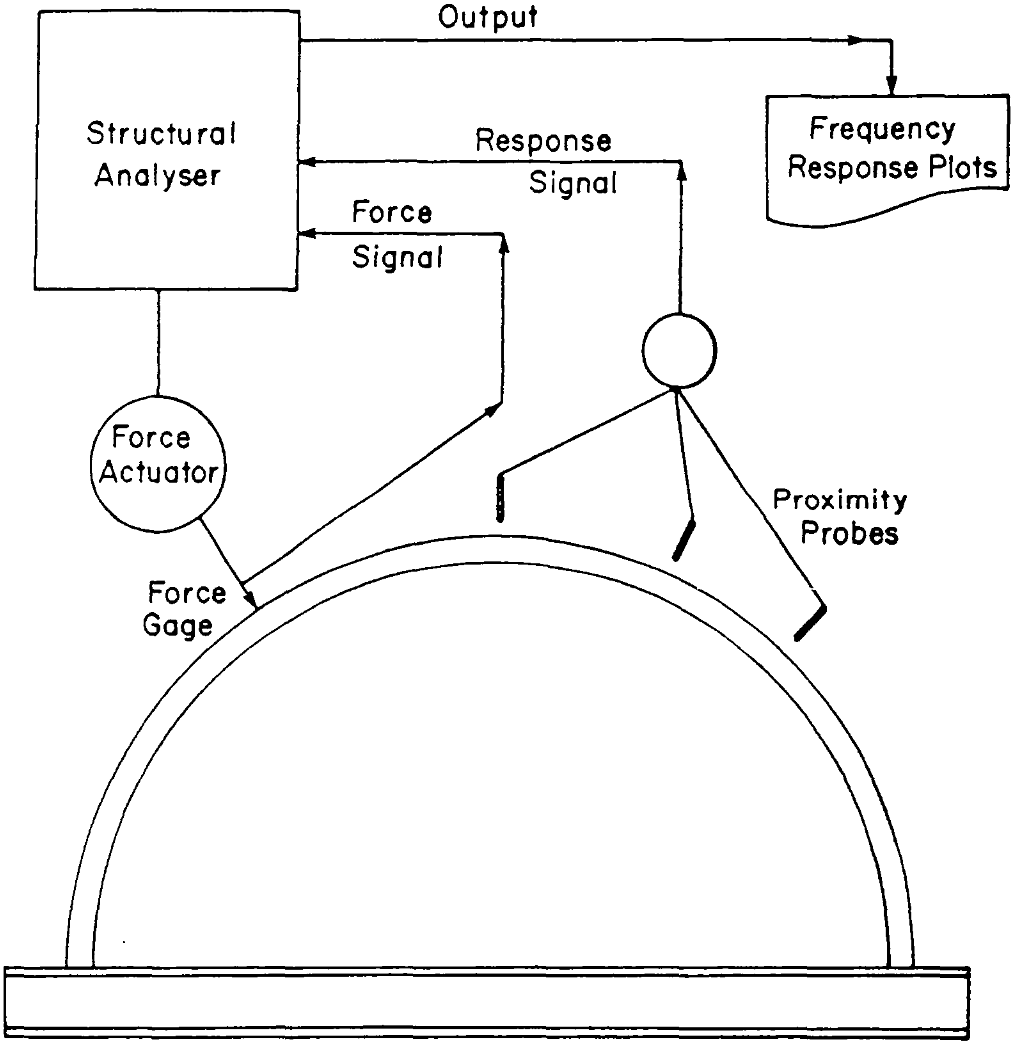
Output
Structural Analyser
Frequency Response Plots
Response Signal
Force Signal
Force Actuator
Force Gage
Proximity Probes

Figure 14. **Structural analyzer test flowchart:** The structural analyzer collected force and response data from the force gage and proximity probes. Fast Fourier Transforms of the force and response data were calculated. Output displacement was divided by input force and plotted on a log scale versus frequency in the form of frequency response plots.

is attached to the specimen via a sting and a piezoelectric force gage. The force gage monitors the amplitude and frequency of the input force and sends this information to the structural analyzer. The response of the frame is detected by Bently-Nevada non-contacting magnetic proximity probes which measure the displacement of small magnetic targets. A typical arrangement of the electromagnetic shaker, force gage, and a proximity probe is presented in Fig. 15.

The operator prescribes a frequency range and step size for a given test. The structural analyzer sweeps through the frequency range, exciting the specimen at each frequency for fifty cycles and samples data from the force gage and proximity probes. The structural analyzer calculates Fast Fourier Transforms (FFT's) of the collected force and displacement data, divides displacement FFT by the force FFT and plots this ratio on a log scale versus frequency in hertz.

The force actuator and proximity probes were oriented in different directions in order to excite and detect both in-plane and out-of-plane modes, respectively. The radial orientations for the force actuator and proximity probes are shown in Fig. 15. The out-of-plane orientations for the shaker and proximity probes are shown in Figs. 16 and 17. The specimens were clamped to a massive steel structure using C-clamps in an effort to obtain clamped-clamped boundary conditions. The steel structure was shimmed and leveled to provide a stable test platform. The shaker and the proximity probes were hung from separate steel structures isolating them from the test specimen.

The structural analyzer results are presented in the form of frequency response plots and phase angle diagrams. A plot was generated for each probe in each test. The plots for an in-plane test of the I-section specimen are shown in Fig. 18. Spikes in the frequency response plots, accompanied by shifts in the phase diagram, indicate resonant modes. The structural analyzer tests provided excellent values for the natural frequencies

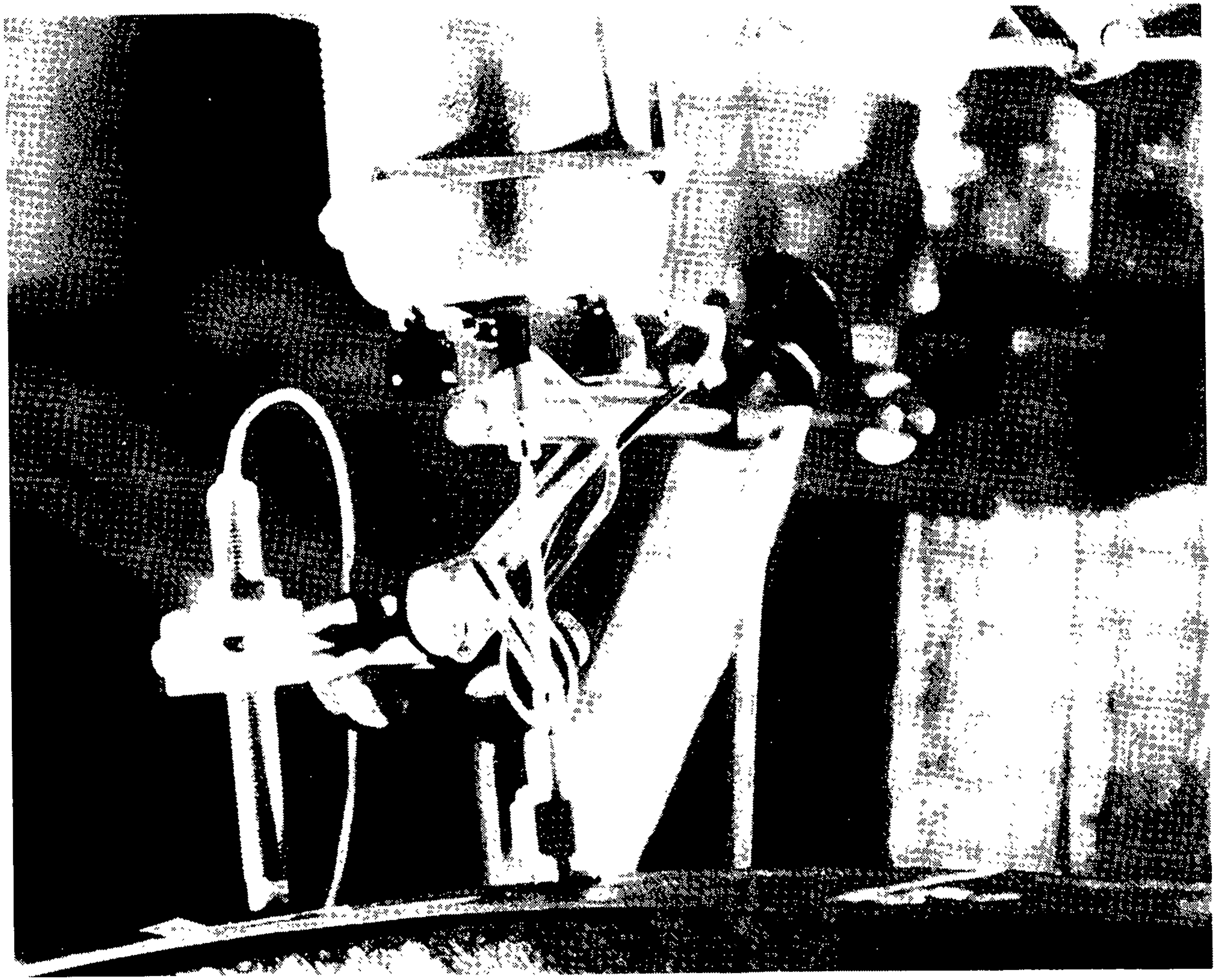

Figure 15. **Experimental apparatus for clamped-clamped dynamic tests:** The electromagnetic shaker inputs a radial excitation force through the force gage to the specimen. A proximity probe monitors the radial response of the test specimen.

ORIGINAL PAGE
BLACK AND WHITE PHOTOGRAPH

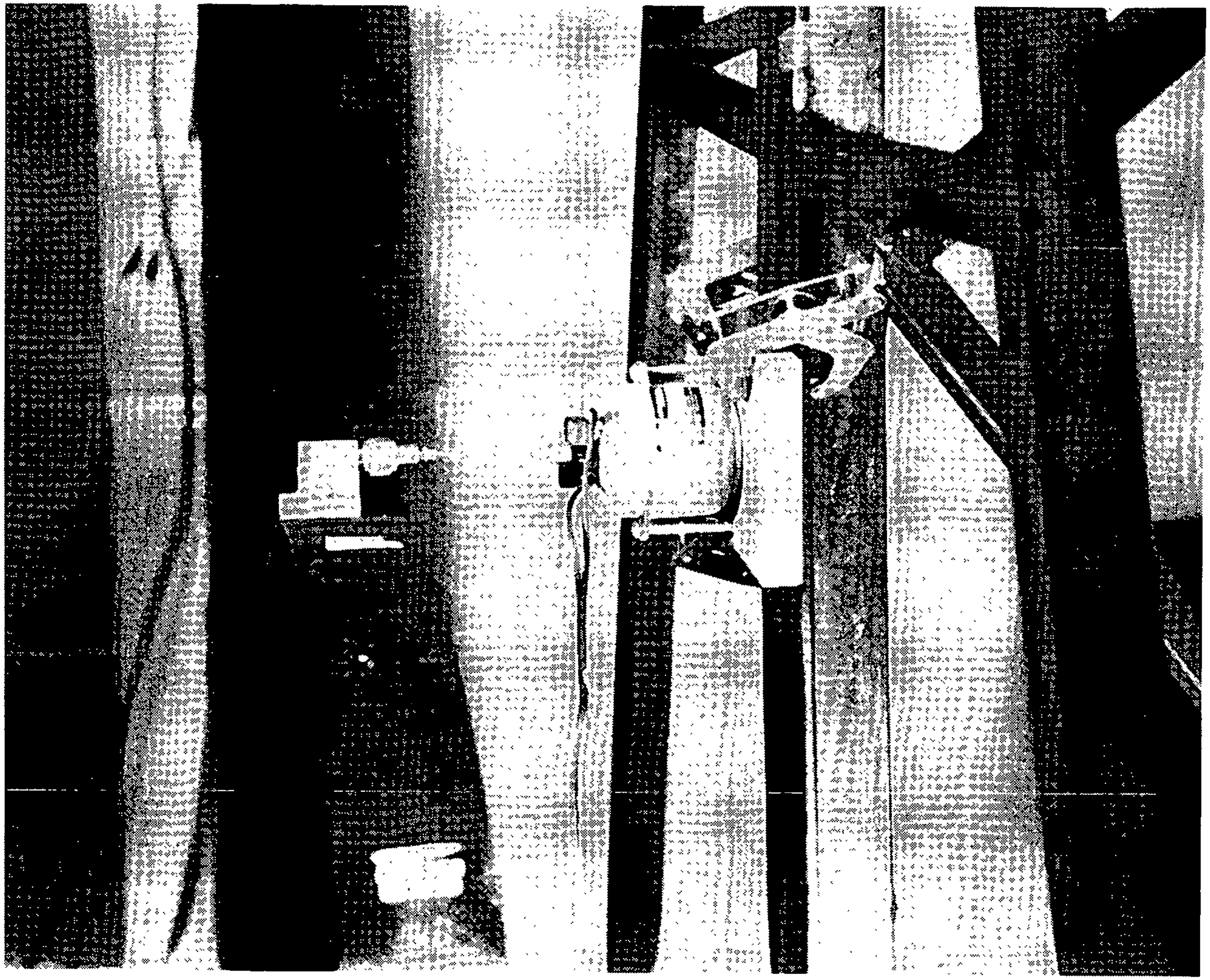

ORIGINAL PAGE
BLACK AND WHITE PHOTOGRAPH

Figure 16. Experimental apparatus for clamped-clamped dynamic tests: The electromagnetic shaker inputs a lateral excitation force through the force gage to the specimen.

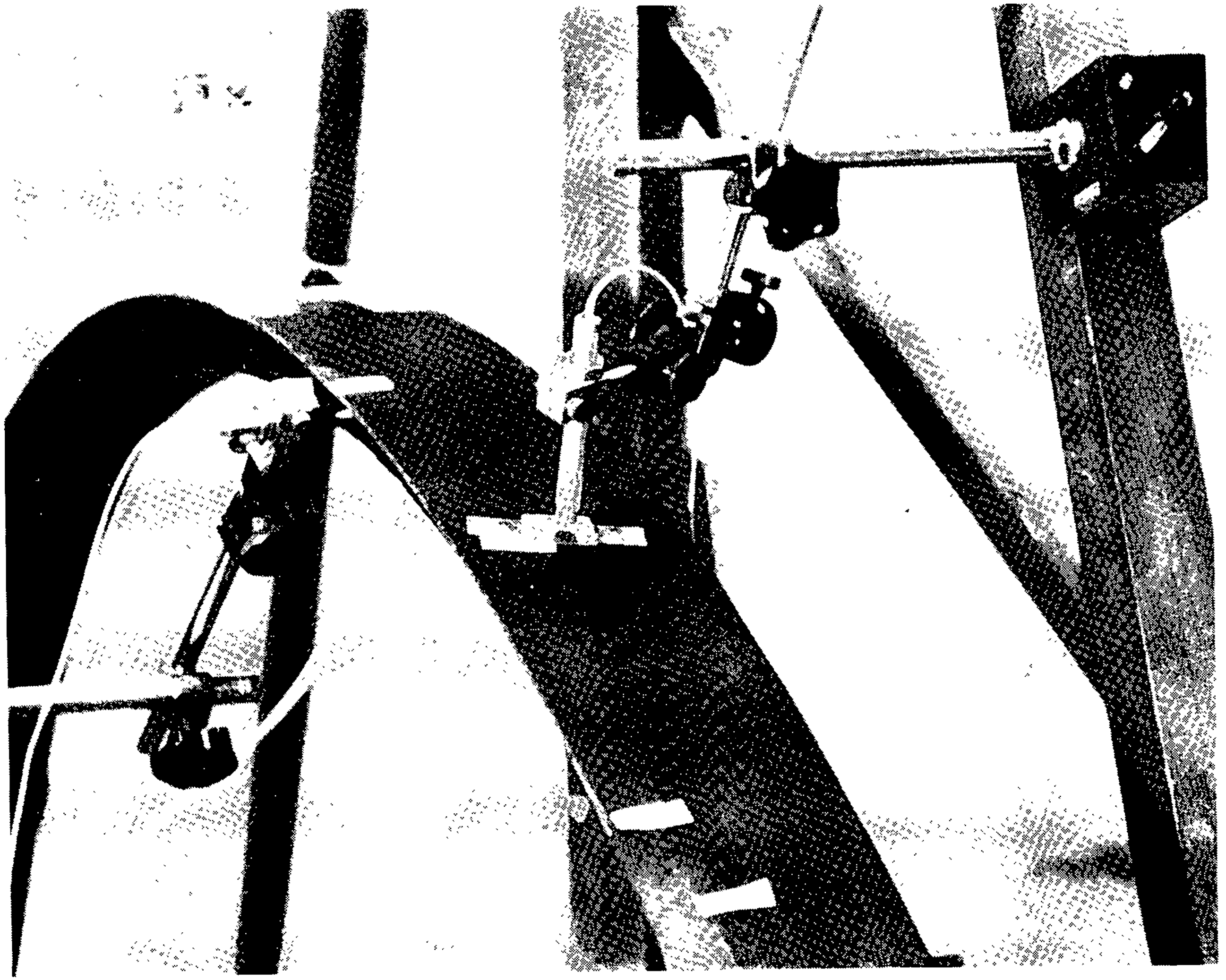

Figure 17. Experimental apparatus for clamped-clamped dynamic tests: Two proximity probes are used to detect radial and lateral motion.

ORIGINAL PAGE
BLACK AND WHITE PHOTOGRAPH

of the resonant modes, however, the test procedure made it impossible to study the mode shapes of the modes associated with the spikes. It is impossible to identify the type of mode or the nodal locations from the structural analyzer test data. A signal generator was used to identify the modes and locate nodal positions.

The signal generator was used to excite the specimens at the frequencies corresponding to the spikes in the frequency response plots. The signal generator sent the signal to the electromagnetic shaker which excited the specimen. The signal from the force gage was not monitored during these tests. The response signals from the proximity probes were monitored visually one at a time on an oscilloscope. The mode was tuned in by monitoring the response signals on the oscilloscope and adjusting the frequency of excitation similar to the air shaker tests. Once a mode was isolated it could be excited indefinitely enabling mode identification and the location of nodal positions.

Static Tests

This section discusses the test apparatus and procedures used in the static portion of the experimental program. The objective of these tests was to determine the flexibility matrices which relate radial, lateral, and twist displacements (W,V,ϕ) to the radial, lateral, and torsional loads (P,Q,T) at the midspan of the test specimens. The displacement-load relation is

$$\begin{Bmatrix} W \\ V \\ \phi \end{Bmatrix} = \begin{bmatrix} \alpha_{11} & \alpha_{12} & \alpha_{13} \\ \alpha_{21} & \alpha_{22} & \alpha_{23} \\ \alpha_{31} & \alpha_{32} & \alpha_{33} \end{bmatrix} \begin{Bmatrix} P \\ Q \\ T \end{Bmatrix} \tag{3.1}$$

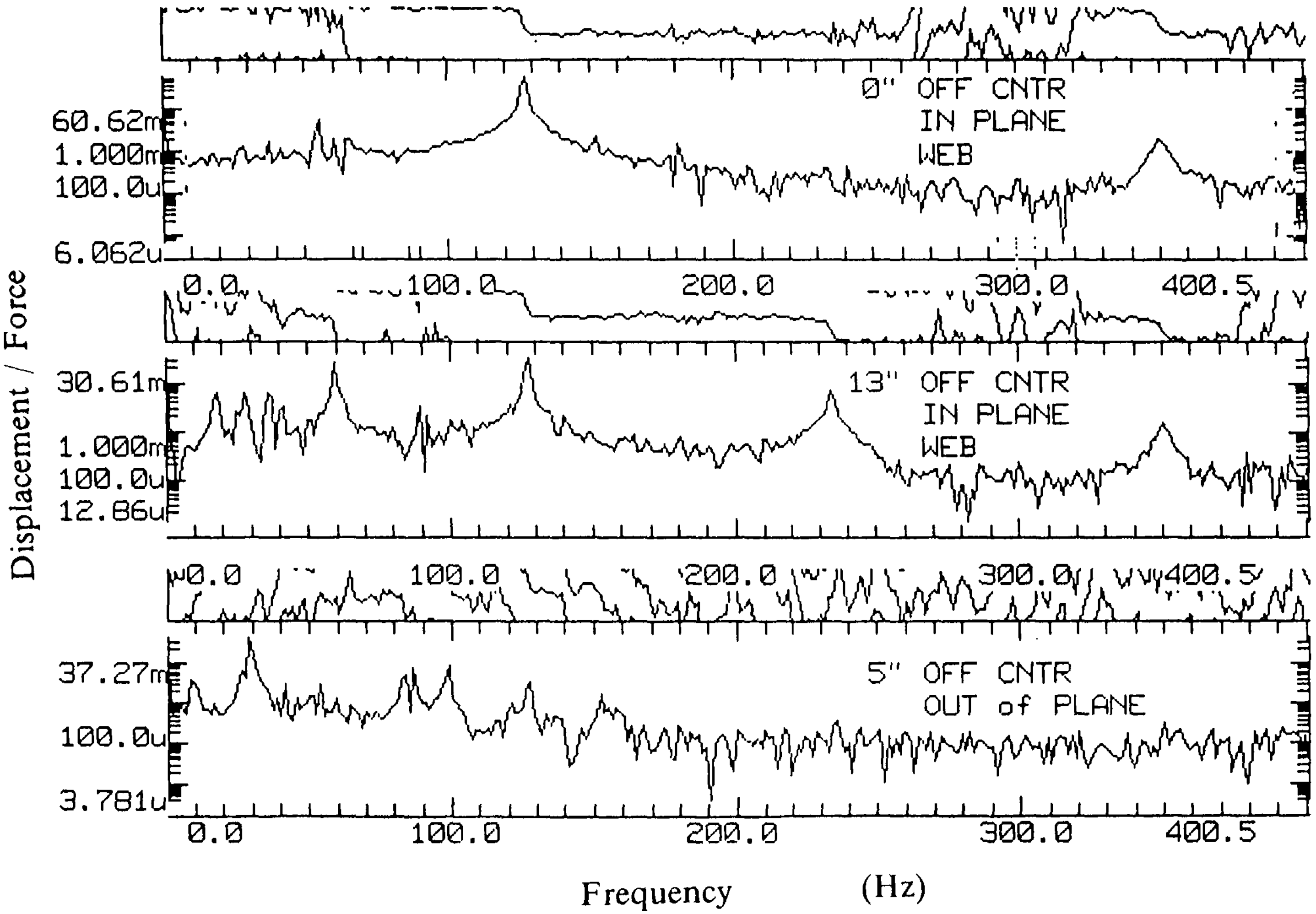

Figure 18. Frequency response plots for the I-section specimen: Frequency response plots for the I-section specimen under radial excitation. Spikes indicate natural frequencies.

where α_{ij} are the flexibility influence coefficients.

Two sets of static tests were necessary to generate all of the flexibility influence coefficients. The in-plane tests loaded the specimen with a radial force and a torque, thus facilitating calculation of the first and third columns of the flexibility matrix. The out-of-plane tests loaded the frames with a lateral load and a torque, enabling the calculation of the second and third columns. In both sets of tests, the frames were clamped to a massive steel structure which was shimmed and leveled to provide a consistent test platform. The in-plane static tests will be discussed first followed by the out-of-plane tests.

In-Plane Static Tests

The in-plane static tests generated a radial load by hanging twenty pound calibration weights from the specimens using a load fixture attached to the specimen. The load fixture and the coordinate system are shown schematically in Fig. 19. The weights were hung from a steel cable which was positioned between two nuts on a threaded rod. By moving the nuts along the threaded rod, the load could be traversed across the cross section, thus changing the torque applied to the cross section. The torque for each test is the product of the radial load (P) and the moment arm (D). The moment arm is the distance along the threaded rod from the load application point to some point of reference where the torque is taken to be zero. It is convenient to define this point of reference as the point where a radial load causes no twist and no lateral deformation. This point is analogous to the shear center of a straight beam.

Photographs of the load fixture and the in-plane static test apparatus are shown in Figs. 20 and 21, respectively. Displacement measurements were taken at the midspan

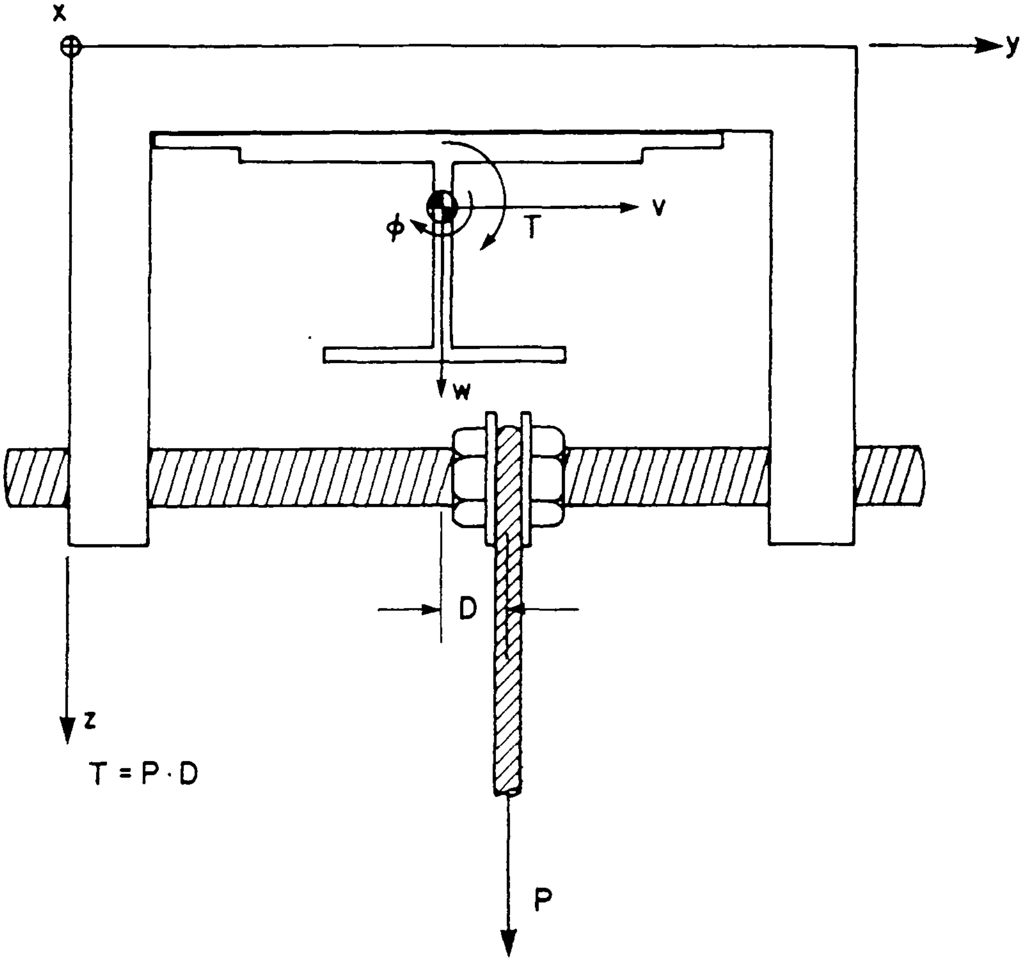

Figure 19. Load fixture and Coordinate system: The load fixture applied radial, and torsional loads to the specimen. The applied torque was the product of the radial load (P) and the moment arm (D). Radial (W), lateral (V), and twist (ϕ) deformations were measured with respect to the centroidal coordinate system shown.

using dial indicators which have a range of one inch and a resolution of .0005 inches. Two dial indicators were oriented radially on top of the load fixture and a third was oriented laterally on the side of the load fixture. Assuming that the cross section of the test specimen and the load fixture move as a rigid body, three measurements are sufficient to define the deformed position of a body moving in a plane. The data from the dial indicators were resolved into lateral and radial displacements of the centroid and the twist of the cross section. The data reduction scheme used to obtain the centroidal displacements and a sample of the reduced data are presented in Appendix B. The dial indicators were attached to separate steel frames isolating them from the specimens. Readings were taken each time a weight was loaded or unloaded and the values were averaged. The frames were loaded radially to 120 pounds.

For the in-plane static tests, the displacement-load relationship reduces to the following equation because the lateral load (Q) is assumed zero. Thus, the middle column, α_{12}, α_{22}, and α_{32} , cannot be calculated from the in-plane tests.

$$\begin{Bmatrix} W \\ V \\ \phi \end{Bmatrix} = \begin{bmatrix} \alpha_{11} & \alpha_{13} \\ \alpha_{21} & \alpha_{23} \\ \alpha_{31} & \alpha_{33} \end{bmatrix} \begin{Bmatrix} P \\ T \end{Bmatrix} \qquad (3.2)$$

The nonlinearities of this problem are most prevalent when the frames bend out of plane. In order to minimize the nonlinear response, the maximum loads were selected such that the maximum lateral displacement was limited to one half inch. This limitation effectively dictated the maximum allowable torque since the maximum radial load was already set. The torque is the product of the radial load and moment arm, thus the moment arm was adjusted to keep the lateral displacement within the allowed limit.

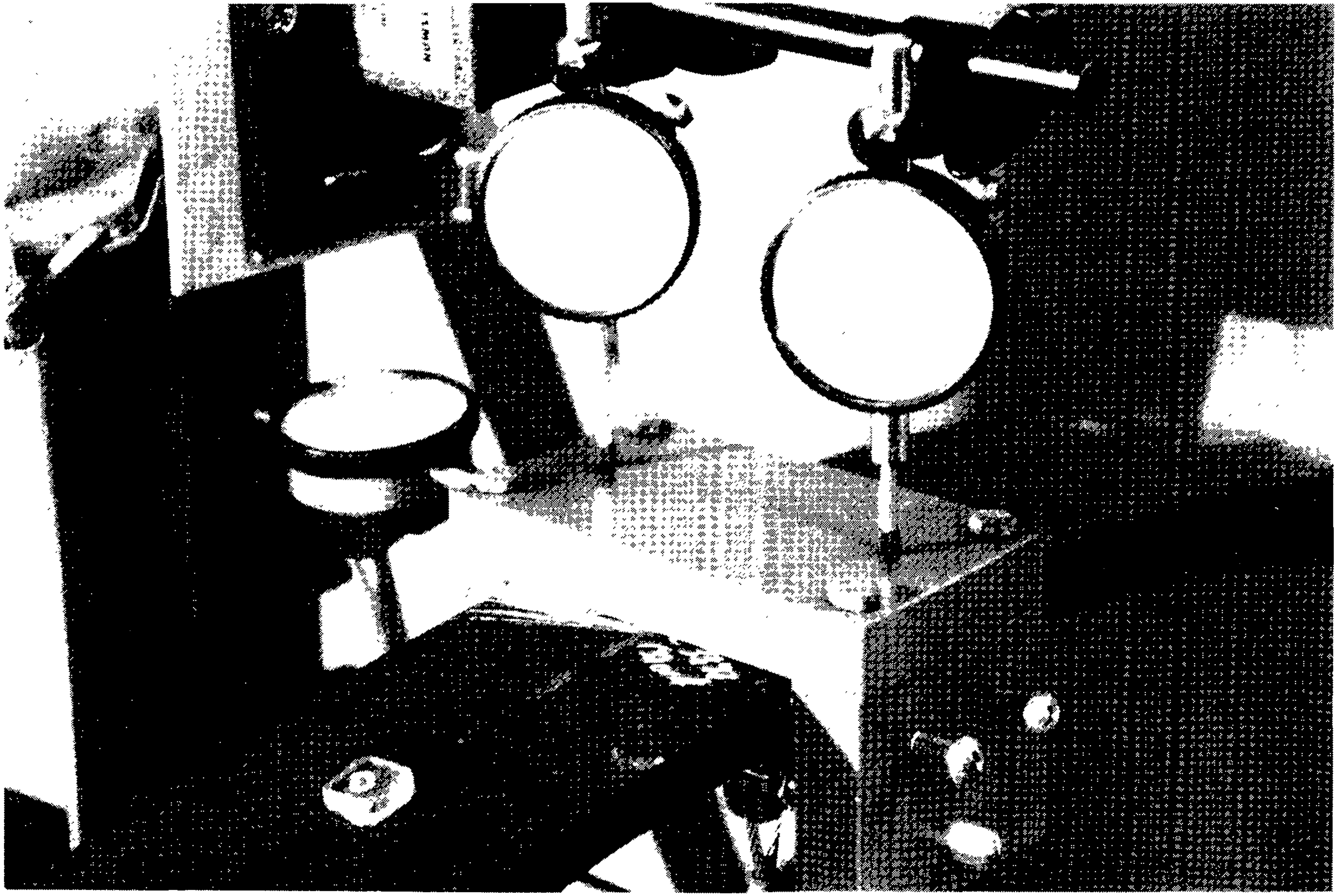

Figure 20. **Load fixture:** Dial indicators were used to measure the displacements of the midspan. A data reduction scheme was used to obtain the centroidal displacements.

ORIGINAL PAGE
BLACK AND WHITE PHOTOGRAPH

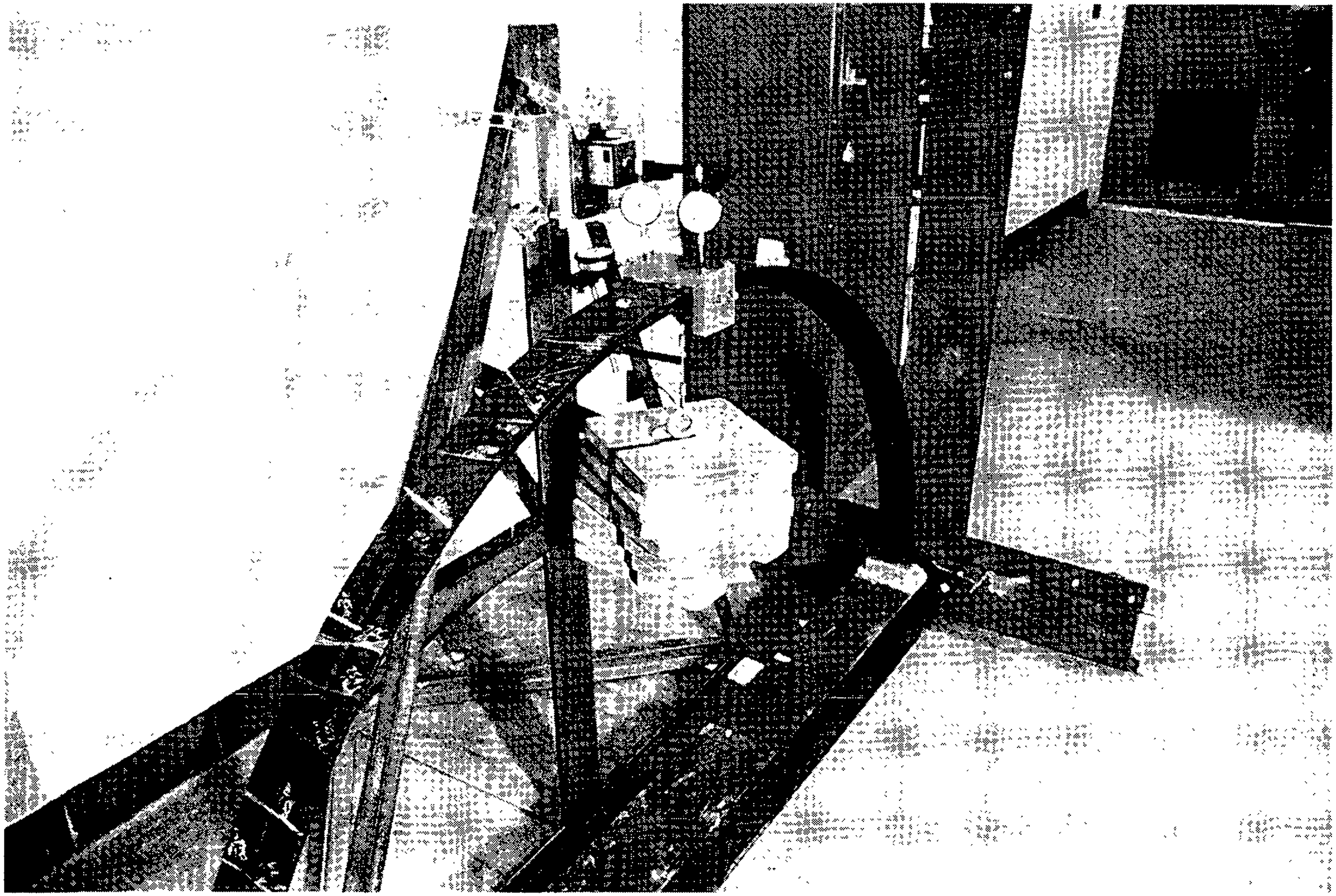

Figure 21. In-plane test apparatus: Twenty pound calibration weights were hung from the load fixture to generate the radial load. The torque was changed by moving the line of action of the radial load relative to the cross section.

ORIGINAL PAGE
BLACK AND WHITE PHOTOGRAPH

The point of zero twist marked the center of the test range for each specimen. Since the I-section specimen was stiffer then the channel specimen with respect to torsion, the maximum moment arm for the I-specimen was correspondingly larger resulting in a larger test range. Many tests were run with the load application point traversing through the test range subjecting the tests specimens to positive and negative torques. The results of the static tests were plotted as load versus displacement for various values of the moment arm. The flexibility influence coefficients were calculated from this data.

Out of Plane Static Tests

The out-of-plane tests required slight changes in the test apparatus and procedures. The out-of-plane tests involved loading the specimens with a lateral load and a torque. The load fixture was modified (Fig. 22) so that loads could be applied perpendicular to the plane of the frame. The load fixture had a tendency to pull away from the test specimen requiring the load fixture to be tied to the specimen, thus, forcing the load fixture and the test specimen to deform as a rigid body. The frames are very compliant laterally requiring smaller loads to reach the limiting lateral displacement. The moment arm reference points for the out-of-plane tests were chosen as the centroid of the cross sections.

Photographs of the modified load fixture and the test apparatus for the out-of-plane static tests are shown in Figs. 23 and 24, respectively. Calibration weights were hung from a piece of twine which was routed over a pulley and attached to the load fixture. The load application point was changed by traversing two nuts along a threaded rod similar to the in-plane tests. Changing the load application point effectively changed

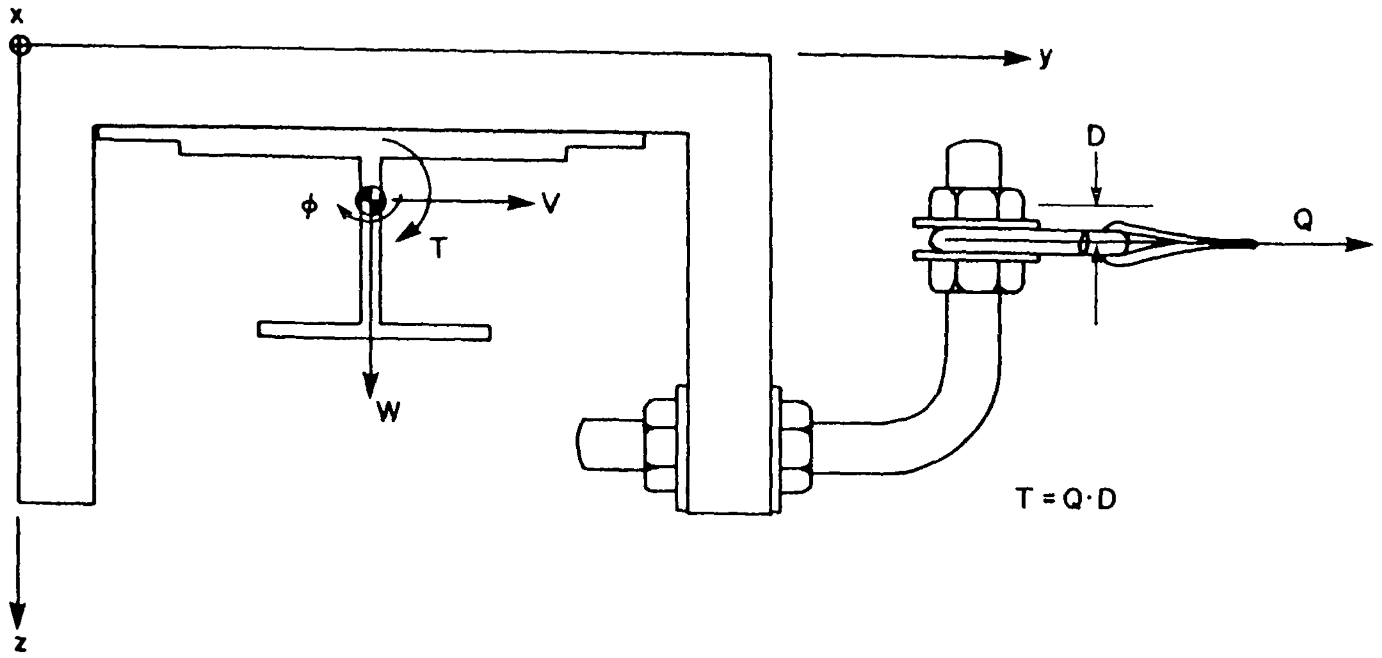

Figure 22. Schematic of modified load fixture: Load fixture was modified for the out-of-plane tests to accept lateral loads. The torque (T) was taken to be the product of the lateral load (Q) and the moment arm (D) where the moment arm was the perpendicular distance from the centroid to the line of action of the lateral load.

the relative torque applied to the specimen. The pulley was mounted on a traverse so that the twine could be kept level, thus, keeping the load perpendicular to the frame.

For the out-of-plane static tests, the displacement-load relationship reduces to the following equation because the radial load (P) is assumed zero.

$$\begin{Bmatrix} W \\ V \\ \phi \end{Bmatrix} = \begin{bmatrix} \alpha_{12} & \alpha_{13} \\ \alpha_{22} & \alpha_{23} \\ \alpha_{32} & \alpha_{33} \end{bmatrix} \begin{Bmatrix} Q \\ T \end{Bmatrix} \tag{3.3}$$

Thus, the first column, α_{11}, α_{21}, and α_{31} , cannot be calculated from the out-of-plane tests. The torque (T) is the product of the lateral load (Q) and the moment arm (D). Three dial indicators were used to measure the displacements of the specimen at the midspan. The dial indicators were arranged in the same manner as in the in-plane tests, thus, the same data reduction scheme was used.

Maximum lateral loads of 4.5 and 2.3 pounds were used for the I-section and channel section specimens, respectively. Readings were taken from the dial indicators each time a weight was loaded or unloaded. The resulting data was then averaged. After each test the moment arm was incremented by one-eighteenth of an inch (one turn on threaded rod) and the procedure was repeated. The test range for the out-of-plane tests was larger than the test range in the in-plane tests, but the loads were much smaller yielding smaller torques.

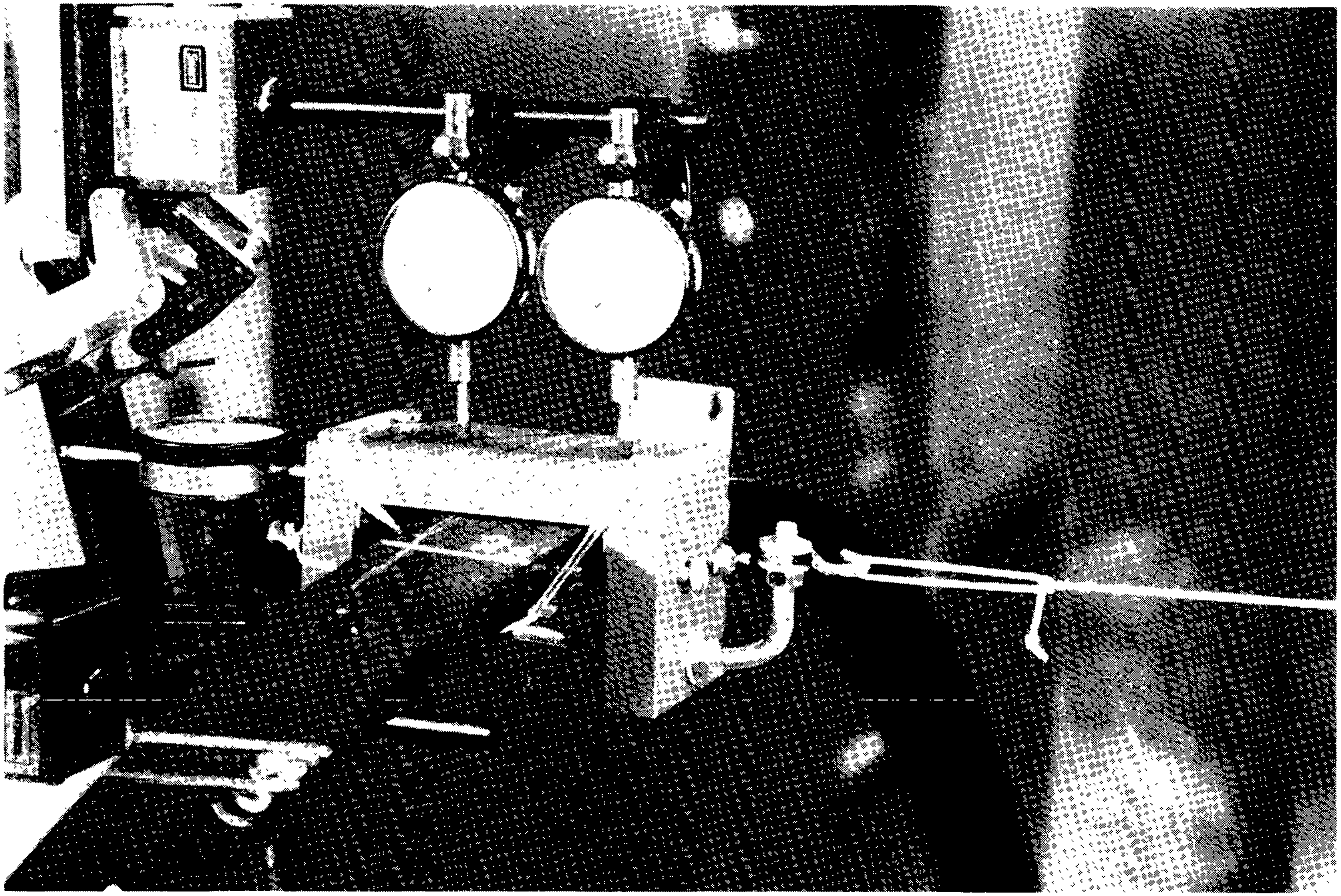

Figure 23. Photograph of modified load fixture and dial indicators: Dial indicators were used to measure the displacement of the load fixture at the midspan. The load fixture was tied to the specimen to force them to deform as a rigid body.

ORIGINAL PAGE
BLACK AND WHITE PHOTOGRAPH

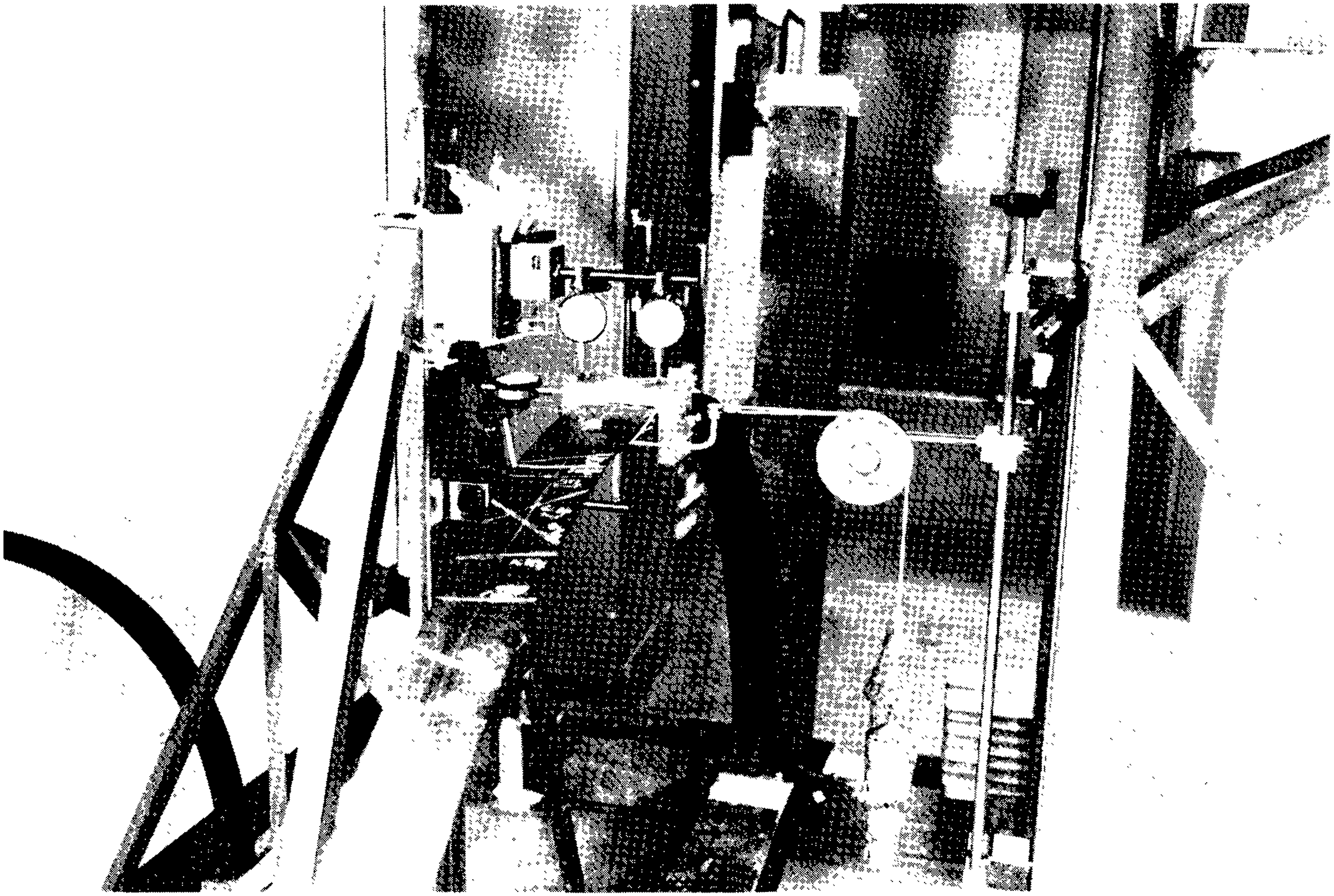

Figure 24. Out of plane test apparatus: Load path for the out-of-plane tests. The load was applied perpendicular to the frame by hanging weights from a line looped over a pulley.

ORIGINAL PAGE
BLACK AND WHITE PHOTOGRAPH

Crush Test

The crush test is part of the ensuing phase of this research and only has a tangential application to this study.[1] The objective of the crush test was to obtain experimental data on the large deflection, failure, and post failure responses of the frame. To obtain this data, the I-section specimen was loaded radially through successive failure events. The current research is only concerned with the linear small deflection response of the frame, however, since the crush test loading is similar to the in-plane static tests, the crush test provided a second opportunity to determine the flexibility coefficient α_{11}.

A photograph of the test apparatus is shown in Fig. 25. The frame was restrained from deforming laterally or twisting at the midspan and the potted ends were bolted to an I-beam to simulate clamped-clamped boundary conditions. The crush test was slightly different from the in-plane static tests where the midspan was unrestrained and the potted ends were clamped to the I-beam. The frame was instrumented with strain gages to measure the strain distribution. A string potentiometer was used to measure the radial displacement. A Tinius-Olsen test machine was used to apply the load. For the midspan restrained specimen, the displacement-load relation is

$$\begin{Bmatrix} W \\ 0 \\ 0 \end{Bmatrix} = \begin{bmatrix} \alpha_{11} & \alpha_{12} & \alpha_{13} \\ \alpha_{21} & \alpha_{22} & \alpha_{23} \\ \alpha_{31} & \alpha_{32} & \alpha_{33} \end{bmatrix} \begin{Bmatrix} P \\ Q \\ T \end{Bmatrix} \tag{3.4}$$

where V and ϕ have been restrained and Q and T are not necessarily zero. Thus, if α_{12} and α_{13} are sufficiently small the radial displacement is simply the product of the ra-

---

[1] The static crush test was conducted at Virginia Tech in cooperation with Mr. E. Moas, graduate research assistant, and Professor O. H. Griffin. This project is also supported by the Landing and Impact Dynamics Branch, NASA Langley Research Center.

ORIGINAL PAGE
BLACK AND WHITE PHOTOGRAPH

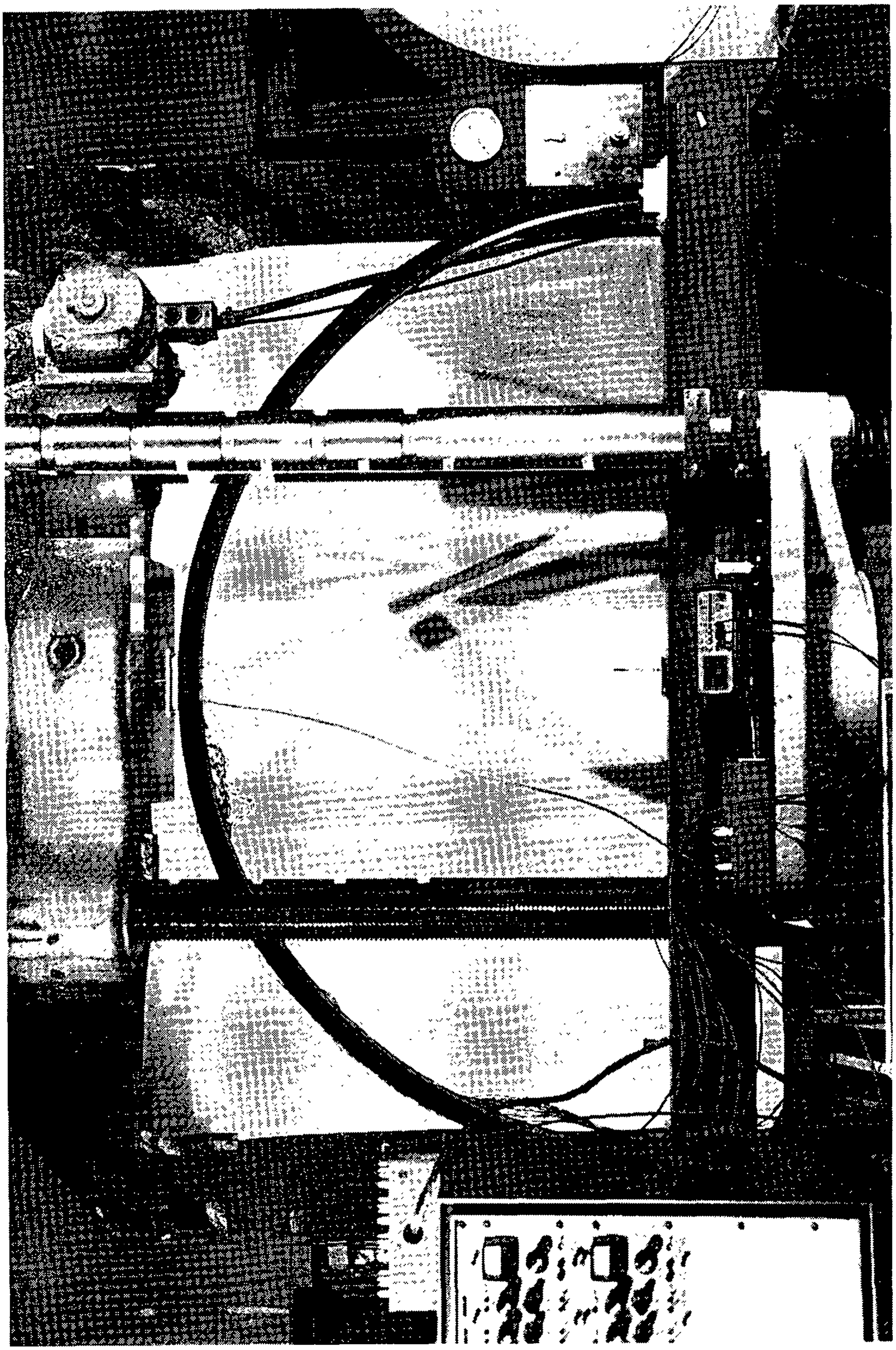

Figure 25. Crush test apparatus: The I-section specimen was clamped to a steel I-beam and crushed radially by a Tinius-Olsen load machine.

dial load and α_{11}. The flexibility coefficient α_{11} was obtained directly from the load-displacement plot.

Chapter 4

Experimental Results

Data from the dynamic testing is presented first followed by the static test data. The dynamic test data includes the natural frequencies and node locations of the specimens for free-free and clamped-clamped boundary conditions. The static test data is presented in plots of load versus displacement. The flexibility influence coefficients were calculated from this data.

Dynamic Test Data

In general, the vibrational response of the frames can be divided into in-plane and out-of-plane motion. The vibrational response of the I-specimen completely decouples into in-plane and out-of-plane modes. All the modes of the channel specimen exhibit coupling between in-plane and out-of-plane motions, but the modes were clearly dominated by one type of motion. The photograph in Fig. 26 is representative of the coupled response observed in the modes of the channel section specimen. The photograph shows the first free-free in-plane flexure mode of the channel specimen. Though the cross section experiences some lateral and twisting motion, the dominant motion is radial. The photograph in Fig. 27 shows a pure out-of-plane motion indicative of the uncoupled response displayed by the I-section specimen. The photographs in Figs. 26 and 27 were taken during the free-free vibrational tests using a strobe light which was tuned to twice the excitation frequency. Using this technique the cross section was illuminated at either extreme of the motion, thus, capturing the characteristic motion of that mode.

A mode was identified by two characteristics, the dominant motion and the number of nodes in the mode shape. The nodes of an in-plane mode are defined as those points where the radial motion is nearly zero. This does not mean that the out-of-plane displacement is zero there, though in general it is small too. Likewise, the nodes of an out-of-plane mode are defined as those points where the out-of-plane bending and twisting motions are nearly zero.

Three distinct types of modes were observed in the free-free vibrational tests, whereas only two types of modes were observed in the clamped-clamped tests. For the free-free tests, motions associated with in-plane bending, out-of-plane bending, and torsion were observed at different frequencies. For the clamped-clamped tests, motions associated with in-plane bending and coupled out-of-plane bending and torsion were observed at different frequencies. Clamped end conditions caused a stronger coupling between out-of-plane bending and torsion than is present in the free end case. For either end condition, the initial curvature of the specimens statically couples the out-of-plane bending moment and the torque. However, the magnitudes of these actions are likely to be much less for the free-free case than for the clamped-clamped case. This may be the reason for the relatively uncoupled motions associated with out-of-plane bending and

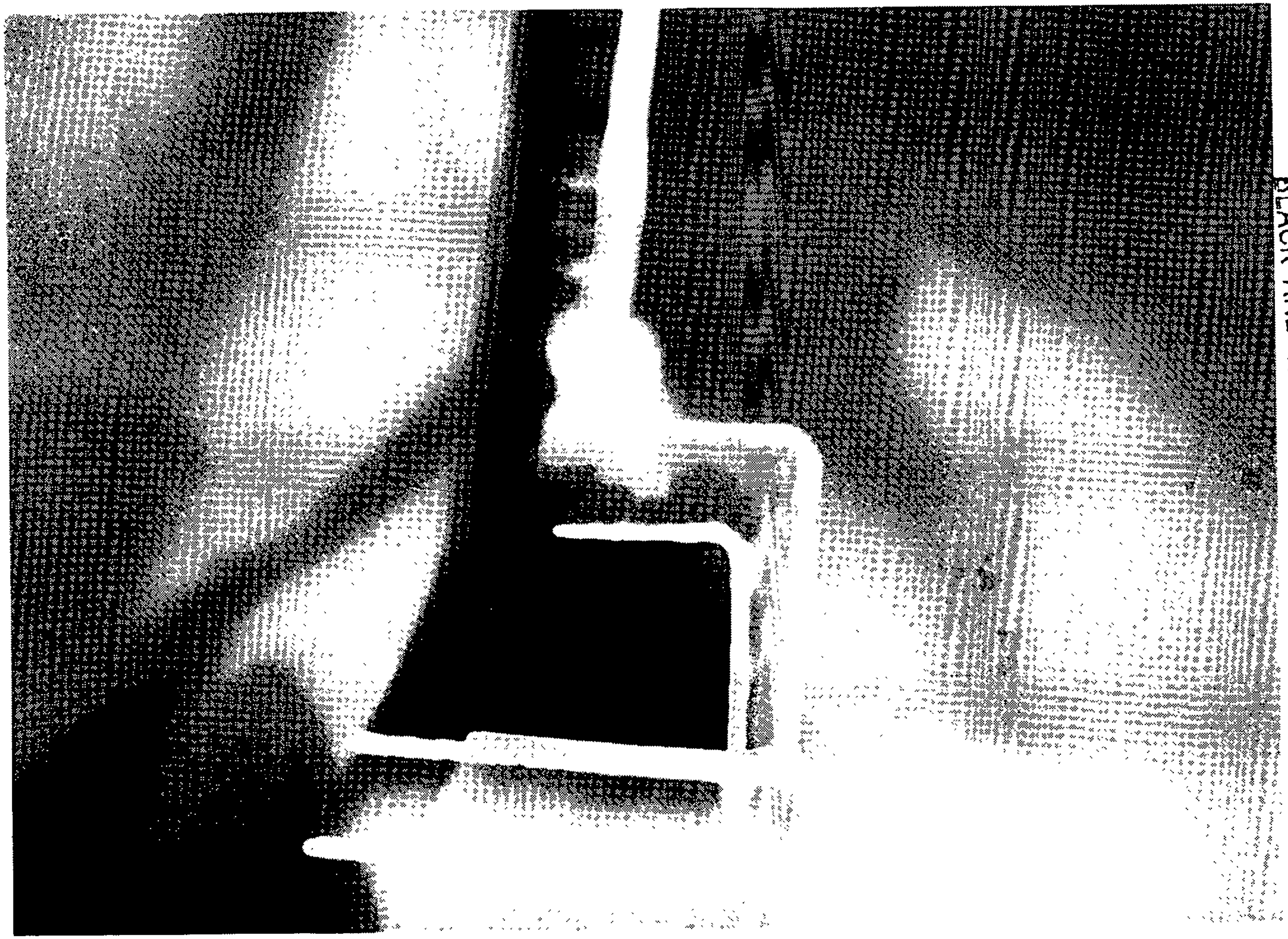

ORIGINAL PAGE
BLACK AND WHITE PHOTOGRAPH

Figure 26. First free-free in-plane mode of the channel specimen: The motion shown in the photograph is typical of the coupled response demonstrated by the channel section specimen.

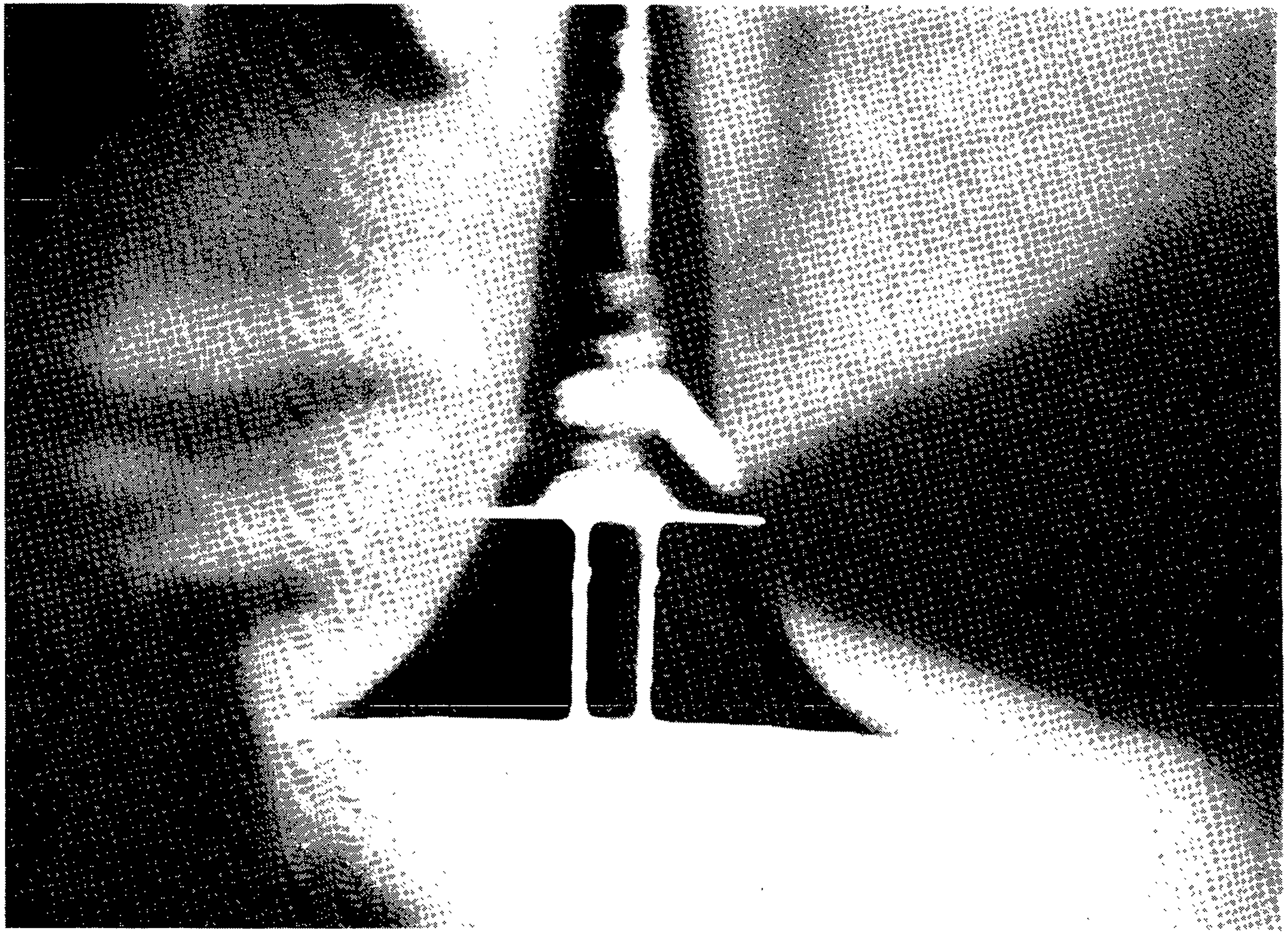

Figure 27. Second free-free out-of-plane mode of the I-specimen: The cross-sectional motion shown in the photograph is purely lateral. Thus, the I-section decouples in-plane and out-of-plane response.

ORIGINAL PAGE
BLACK AND WHITE PHOTOGRAPH

torsion observed in the free-free tests. For example, out-of-plane bending dominates the motion in the mode at 26.3 Hz for the free-free I-specimen shown in Fig. 27. The same I-specimen vibrating at 57.2 Hz, as shown in the photograph in Fig. 28, exhibits a torsionally dominant motion.

Natural frequencies and node locations for the free-free in-plane, out-of-plane, and torsional modes for both specimens are presented in Table 3. The natural frequencies are in hertz and the node locations are measured in radians from the midspan. The node locations are symmetrically located about the midspan. The plot in Fig. 29 compares the in-plane, out-of-plane, and torsional natural frequencies of the two specimens. The number of nodes is plotted on the horizontal axis and the natural frequency is in hertz on the vertical axis. The frequencies associated with the in-plane modes of the I-specimen are higher than the frequencies associated with the in-plane modes of the channel specimen. This indicates that the I-specimen is stiffer radially. The data for the two specimens show increasing frequencies with increasing number of nodes in the modes. The in-plane natural frequencies for the channel specimen are consistently 15-25 % lower than the corresponding I-specimen frequencies. The curves in Fig. 29 (B) correspond to the natural frequencies of the out-of-plane flexure and torsional modes of both test specimens. The torsional natural frequencies associated with the I-specimen are consistently higher than the corresponding channel modes indicating that the I-specimen is stiffer with respect to torsion. The natural frequencies for the out-of-plane flexural modes for the two specimens coincide.

The results of the clamped-clamped vibrational tests for the I-section and channel section specimens are presented in Table 4. The frequencies are in hertz and the node locations are in radians measured from the midspan. The clamped ends are counted as two nodes. Thus, two nodes is the minimum number in a mode for the clamped-clamped

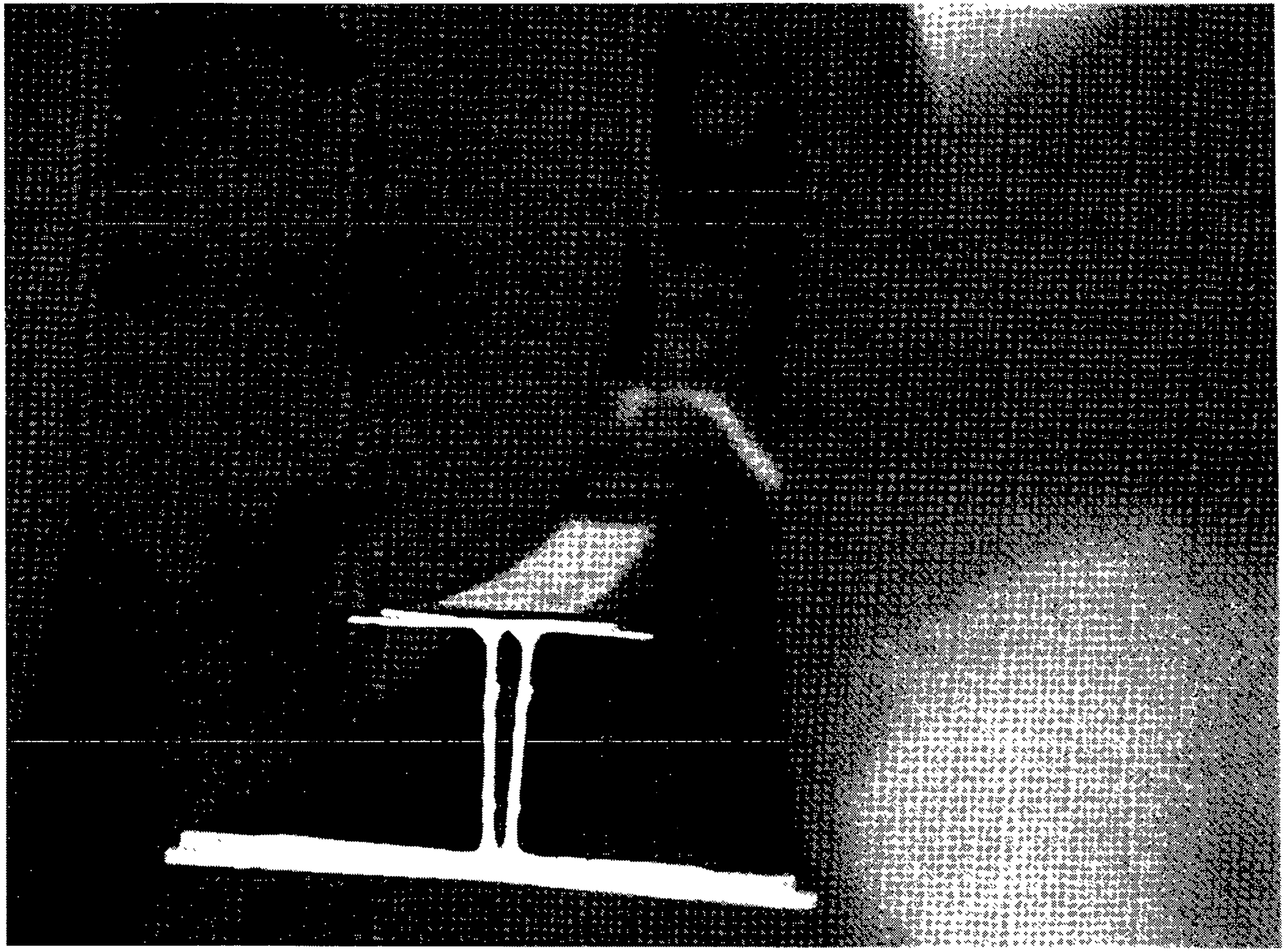

Figure 28. **First free-free torsional mode of the I-specimen:** The motion of the cross section is predominantly torsional with a small amount of lateral motion compared to the out-of-plane flexure mode in Fig. 27. The free-free boundary conditions reduce the effect of the geometric coupling between torsion and out-of-plane bending.

ORIGINAL PAGE
BLACK AND WHITE PHOTOGRAPH

Table 3. Natural frequencies and node locations of the free-free modes

	No. of Nodes	Freq Hz	Node Locations Radians from Midspan						
I-specimen									
In-plane	2	25.8			-0.61		0.63		
	3	78.3			-1.09	-0.02	1.05		
	4	151.0		-1.22	-0.43		0.43	1.23	
	5	259.0		-1.30	-0.70	-0.01	0.66	1.29	
	6	388.0							
Out-of-plane	3	8.1			-1.16	0.02	1.16		
	4	26.3		-1.30	-0.48		0.48	1.28	
Torsion	3	57.2			-0.75	0.02	0.72		
	4	97.5		-0.98	-0.30		0.30	0.95	
	5	146.0		-1.08	-0.51	0.01	0.53	1.08	
	6	200.0	-1.23	-0.92	-0.29		0.29	0.87	1.20
Channel specimen									
In-plane	2	18.4			-0.65		0.59		
	3	65.0			-1.10	-0.00	1.11		
	4	128.0		-1.22	-0.49		0.51	1.23	
	5	205.0		-1.31	-0.75	0.01	0.75	1.32	
	6	280.0							
Out-of-plane	3	7.4			-1.14	-0.01	1.15		
	4	26.1		-1.28	-0.45		0.46	1.30	
Torsion	3	47.3			-1.07	0.02	1.01		
	4	87.5		-1.19	-0.47		0.44	1.16	
	5	137.0		-1.20	-0.68	0.01	0.66	1.18	
	6	188.0	-1.23	-0.92	-0.29		0.29	0.87	1.20

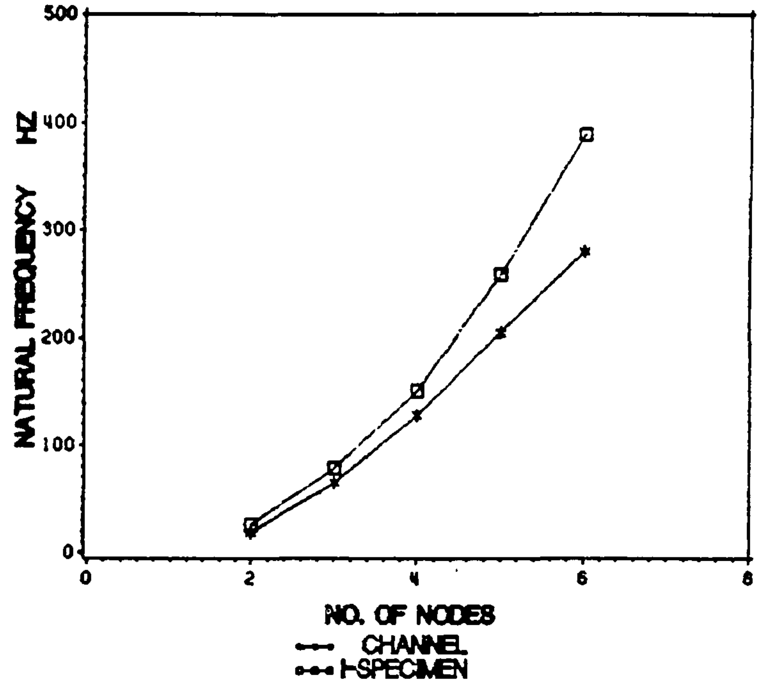

(A) IN-PLANE MODES

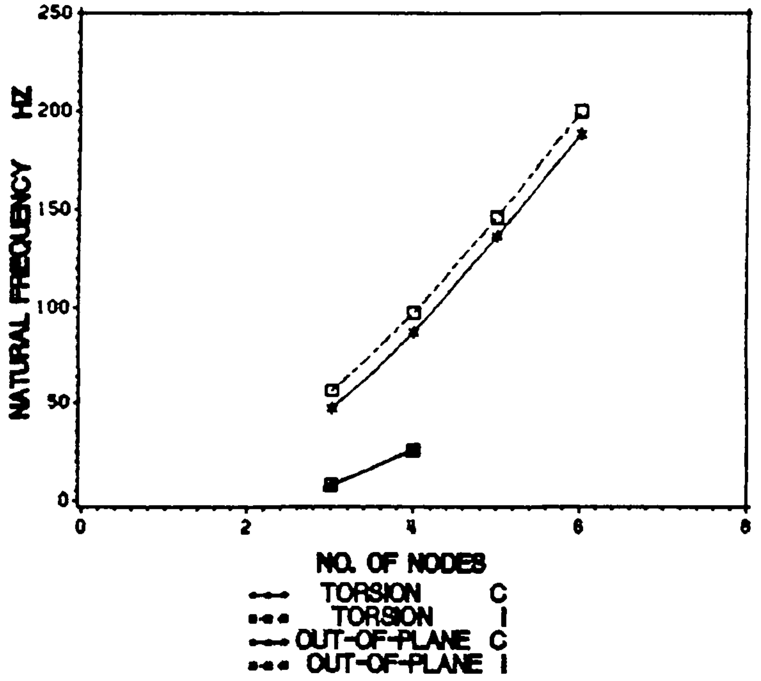

(B) TORSIONAL AND OUT-OF-PLANE MODES

Figure 29. Comparison of free-free natural frequencies: The in-plane and out-of-plane natural frequencies for both test specimens are shown in the two plots. The number of nodes in a mode is plotted on the horizontal axis and natural frequency in hertz on the vertical axis.

Table 4. Natural frequencies and node locations of the clamped-clamped modes

	No. of Nodes	Freq Hz	Node Locations Radians from Midspan								
I-specimen											
In-plane	3	57.8				-1.57	0.00	1.57			
	4	127.2			-1.57	-0.57		0.58	1.57		
	5	233.0			-1.57	-0.72	0.00	0.75	1.57		
	6	350.6		-1.57	-0.94	-0.26		0.28	0.94	1.57	
	7	490.2		-1.57	-1.01	-0.49	-0.01	0.48	1.01	1.57	
	8	617.3									
Out-of-plane	2	8.2				-1.57		1.57			
	3	29.8				-1.57	-0.04	1.57			
	4	64.3			-1.57	-0.34[a]		0.49	1.57		
	5	110.4			-1.57	-0.62	-0.01	0.58	1.57		
	6	157.8		-1.57	-0.85	-0.28		0.25	0.88	1.57	
	7	164.7		-1.57	-1.02	-0.42[a]	0.08	0.54	1.08	1.57	
	8	207.4	-1.57	-1.23	-0.74	-0.24		0.22	0.73	1.20	1.57
	9	254.7	-1.57	-1.28	-0.80	-0.37	0.07	0.43	0.85	1.31	1.57
	10	314.7									
Channel specimen											
In-plane	3	44.6				-1.57	-0.01	1.57			
	4	99.1			-1.57	-0.58		0.61	1.57		
	5	176.0			-1.57	-0.84	-0.14	0.82	1.57		
	6	276.7		-1.57	-0.98	-0.29		0.28	0.94	1.57	
	7	413.0									
Out-of-plane	2	7.4				-1.57		1.57			
	3	25.4				-1.57	0.09	1.57			
	4	55.4			-1.57	-0.40		0.35	1.57		
	5	91.1			-1.57	-0.60	-0.05	0.60	1.57		
	6	148.8		-1.57	-0.85	-0.28		0.27	0.83	1.57	
	7	155.2		-1.57	-1.00	-0.29	-0.01	0.35	0.90	1.57	
	8	187.7	-1.57	-1.26	-0.76	-0.26		0.25	0.76	1.26	1.57
	9	216.0	-1.57	-1.26	-0.84	-0.37	0.06	0.37	0.72	1.20	1.57
	10	265.0									

[a] Node near the force actuator

specimen tests. In general, the nodes are distributed symmetrically about the midspan except when a node falls close to the force actuator, which tends to distort the mode shape.

The in-plane and out-of-plane natural frequencies for both specimens are compared in Fig. 30. The response of the two specimens is qualitatively the same. The in-plane natural frequencies of the I-specimen are consistently higher. The first out-of-plane mode for the two specimens is nearly identical, which is similar to the coincident out-of-plane flexural modes observed for the two specimens in the free-free tests. The natural frequencies of the I-specimen for subsequent out-of-plane modes are higher than the corresponding channel specimen frequencies. The reduction of the increase in frequency with increasing number of nodes in Fig. 30 (B) at six nodes is explained by a softening of the end restraint conditions.

Static Test Data

The experimental data from the static tests is presented in plots of load versus displacement. The flexibility influence coefficients were calculated using a least squares routine which fitted the best plane to the data. The load-displacement plots will be discussed first followed by the data reduction scheme and the flexibility influence coefficients.

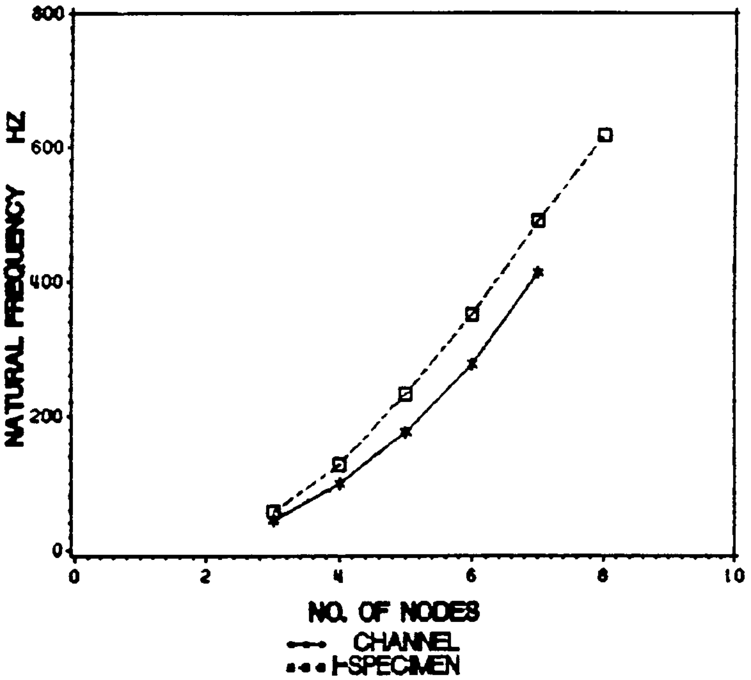

(A) IN-PLANE MODES

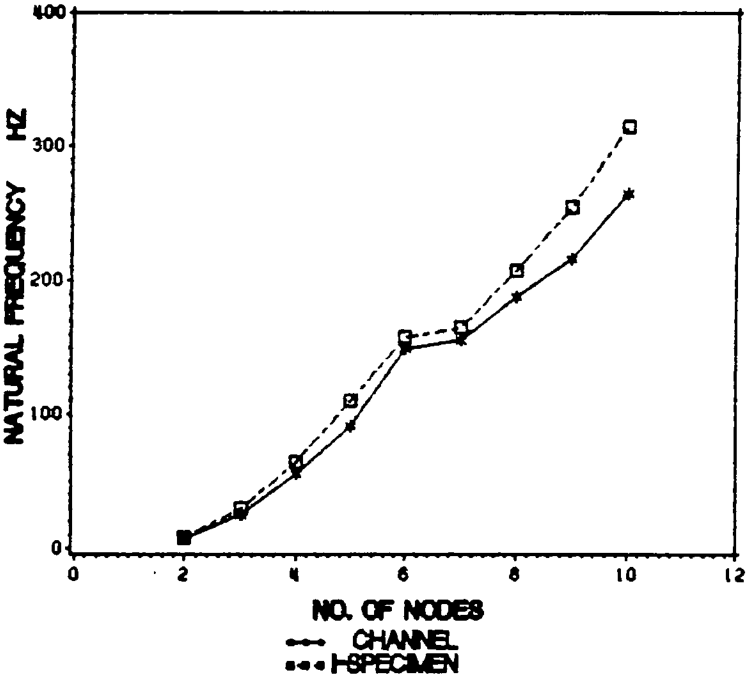

(B) OUT-OF-PLANE MODES

Figure 30. Comparison of clamped-clamped natural frequencies: The in-plane and out-of-plane natural frequencies for both specimens are compared in the two plots. The number of nodes in a mode is plotted on the horizontal axis and natural frequency in hertz on the vertical axis.

Load-Displacement Plots

In the ensuing presentation of the load-displacement plots, each figure will present the data for both specimens. The data associated with the I-specimen will be presented in the (A) part of each figure and the data for the channel specimen will be presented in the (B) part. The data from the in-plane static tests will be plotted as radial load versus radial, lateral, and twist displacements for various values of the moment arm. The out-of-plane static test data will be presented as lateral load versus radial, lateral, and twist displacements for various values of the moment arm. The applied torque in either test is the product of the applied force and the moment arm. The in-plane test data will be presented first followed by the out-of-plane test data.

The plots of radial load versus radial displacement are presented in Fig. 31. The I-specimen data is linear through the maximum radial load and shows no sensitivity to the applied torque. This indicates that the flexibility coefficient α_{13} is small. The channel specimen data is linear through a radial load of sixty pounds. The spread in the curves for the channel specimen indicates that the channel specimen's flexibility coefficient α_{13} is not zero.

The plots of radial load versus lateral displacement are shown in Fig. 32. The I-specimen data is symmetrically arranged about the zero torque line $(D=0)$. The fan shape indicates that the flexibility coefficient α_{23} is nonzero. Nonlinearities appear in some of the curves, but the data corresponding to smaller moment arms is linear through a radial load of sixty pounds. The channel specimen data is not symmetrically arranged about the zero torque line. This indicates that the channel specimen's value for flexibility coefficient α_{23} is dependent on the sign of the torque. The curvature in the data for the channel specimen is more pronounced than in the I-specimen data.

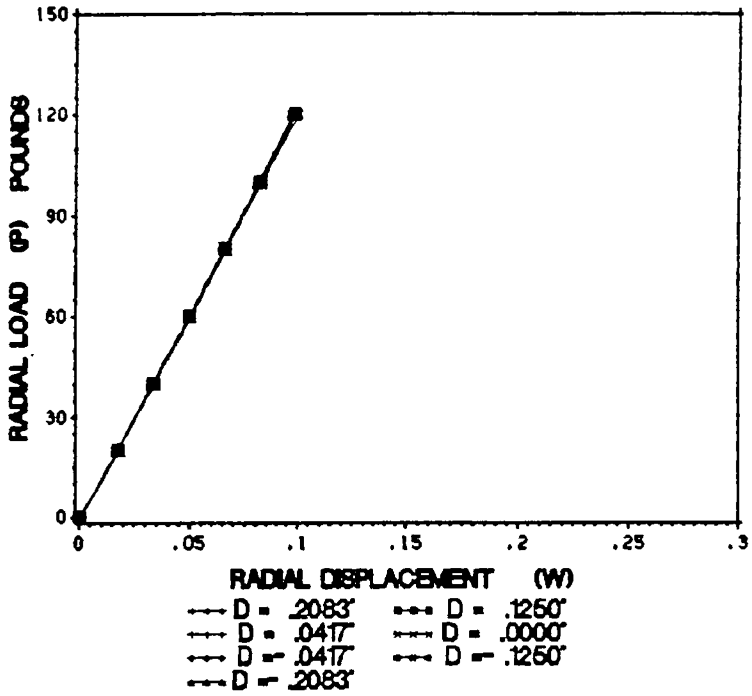

(A) I-SPECIMEN

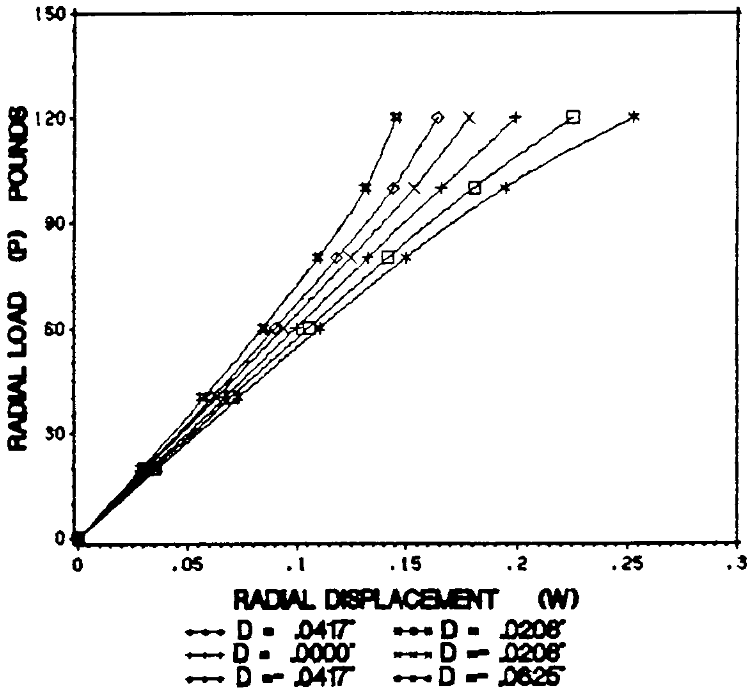

(B) CHANNEL SPECIMEN

Figure 31. Radial load versus radial displacement: Radial displacement in inches is plotted on the horizontal axis and radial load in pounds on the vertical. The I-section data is linear and insensitive to torque. The channel specimen exhibits nonlinear response and a sensitivity to torque.

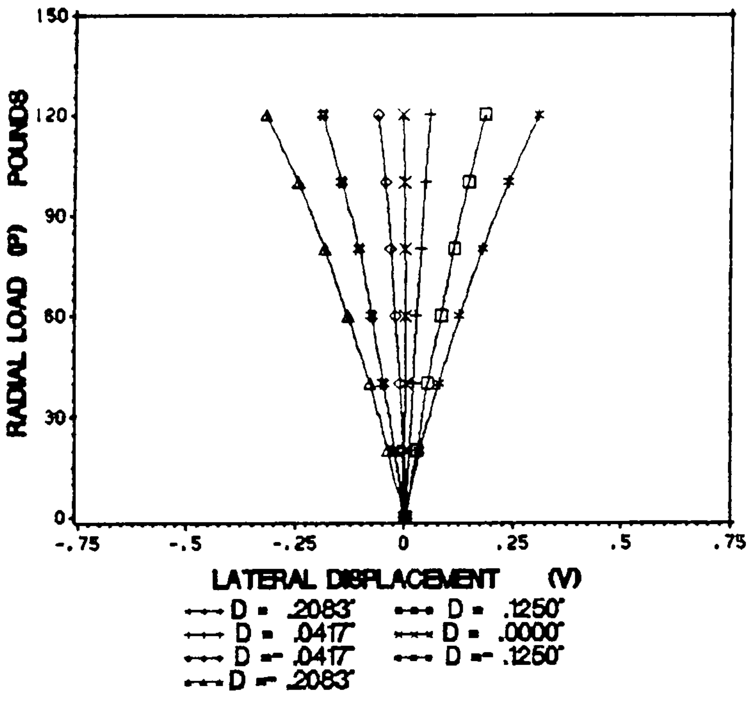

(A) I-SPECIMEN

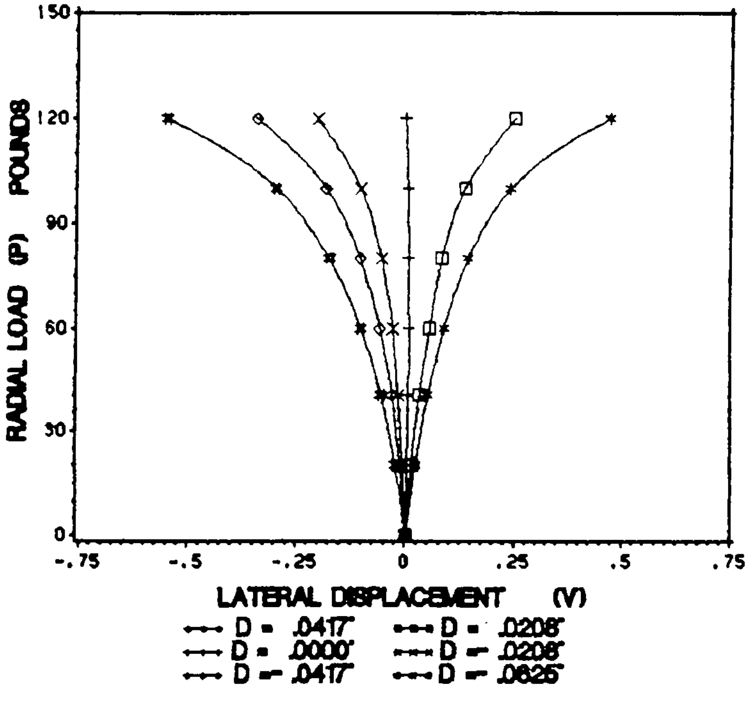

(B) CHANNEL SPECIMEN

Figure 32. Radial load versus lateral displacement: Lateral displacement in inches is plotted on the horizontal axis and radial load in pounds on the vertical. The I-section data is symmetrically arranged about the zero torque line. The channel data is not symmetrically arranged indicating α_{23} is dependent on the sign of the torque.

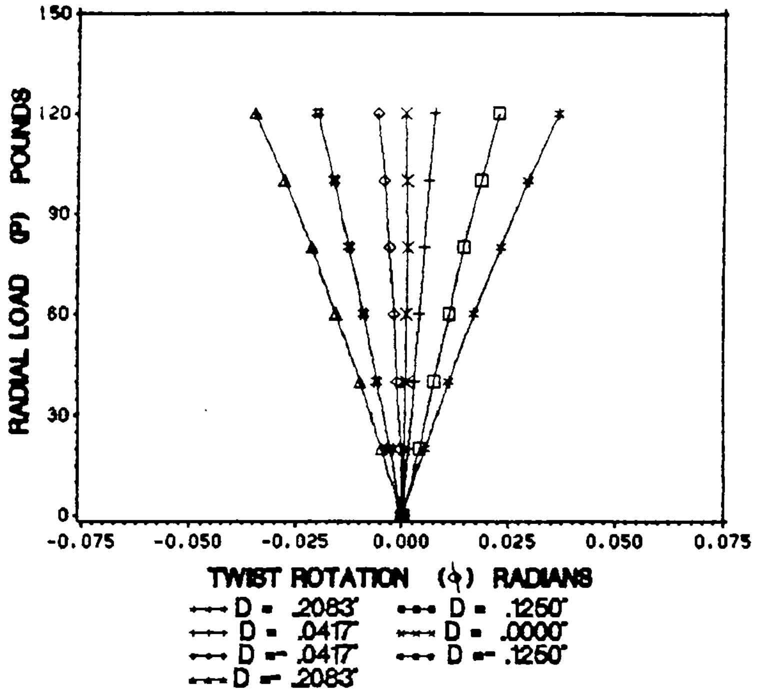

(A) I-SPECIMEN

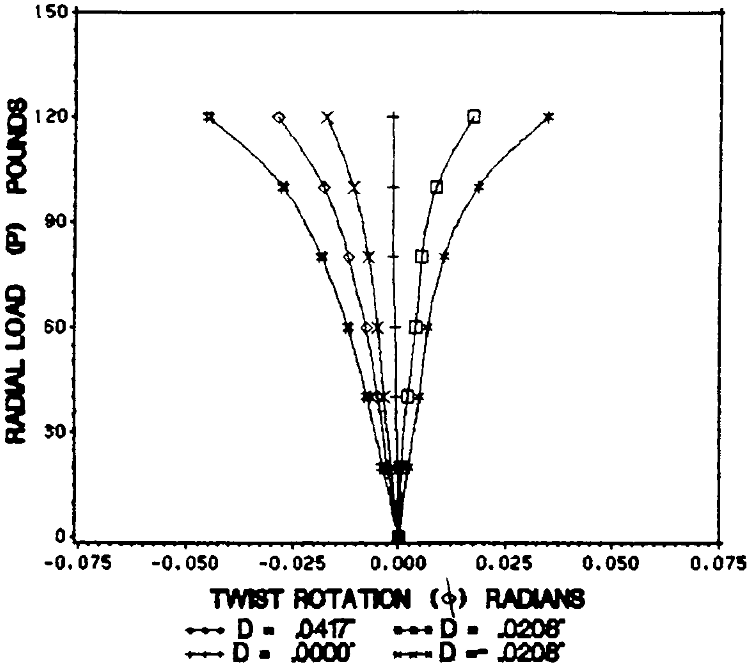

(B) CHANNEL SPECIMEN

Figure 33. Radial load versus twist displacement: Twist displacement in radians is plotted on the horizontal axis and radial load in pounds on the vertical. The I-section data is symmetrically arranged about the zero torque line. The channel data is not symmetrically arranged indicating α_{33} is dependent on the sign of the torque.

The plots of radial load versus twist are presented in Fig. 33. The I-specimen data is symmetrically arranged about the zero torque line indicating a consistent value for flexibility coefficient α_{33}. Generally, the data is linear through the highest radial load. The data for the channel specimen is not symmetrically arranged indicating that the channel's torsional stiffness α_{33} is dependent on the sign of the torque. The curves are linear through a radial load of sixty pounds.

The plots of lateral load versus radial displacement from the out-of-plane static tests are presented in Fig. 34. The I-specimen data shows significant radial displacements indicating that the flexibility coefficient α_{12} is nonzero. This is inconsistent with the vibrational experimental data since a nonzero value of α_{12} couples the in-plane and out-of-plane responses. This inconsistency of a nonzero α_{12} is thought to be due to a geometric nonlinear effect of the reference arc of the frame. For inextensional response, an out-of-plane displacement in either direction at midspan would cause a radially inward displacement. This is analogous to a cantilevered beam subject to a transverse load in which the axial displacement at the tip is directed inward no matter the sense of the applied load. The radial displacement for the channel specimen is also nonzero. It is difficult to say how much of the radial deformation is a function of the geometric nonlinearity and how much is due to the coupling caused by the asymmetric cross section.

Plots of lateral load versus lateral and twist displacements are presented in Figs. 35 and 36, respectively. The I-specimen data for the two figures is linear through the maximum lateral load. The data for the channel specimen exhibits very slight curvature.

The in-plane and out-of-plane static tests were necessary to generate all three columns of the flexibility matrix. The frames are stiffer in the radial direction enabling higher loads, hence larger torques. The smaller torques in the out-of-plane tests resulted

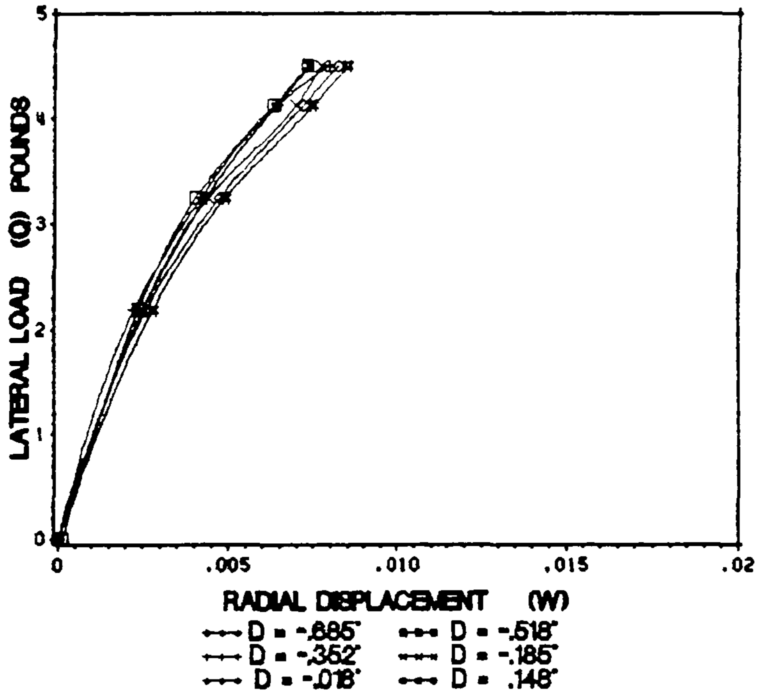

(A) I-SPECIMEN

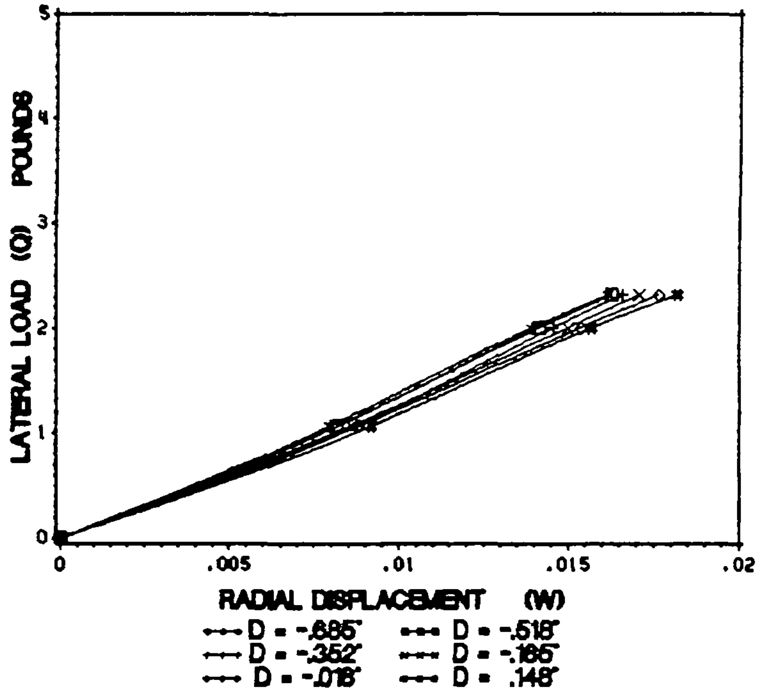

(B) CHANNEL SPECIMEN

Figure 34. Lateral load versus radial displacement: Radial displacement in inches is plotted on the horizontal axis and lateral load in pounds on the vertical. The I-section data is nonlinear and nonzero which is inconsistent with previous observations. Channel data is linear and shows substantial radial displacements.

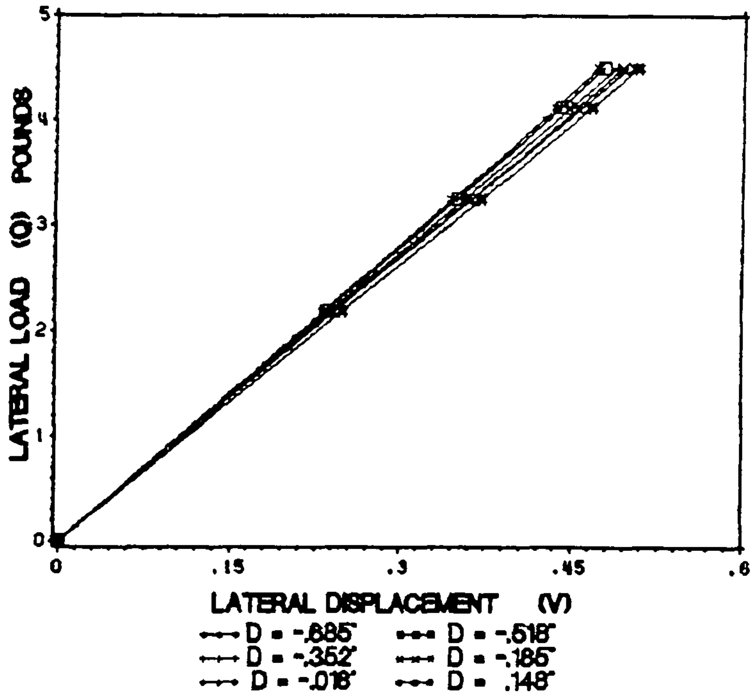

(A) I-SPECIMEN

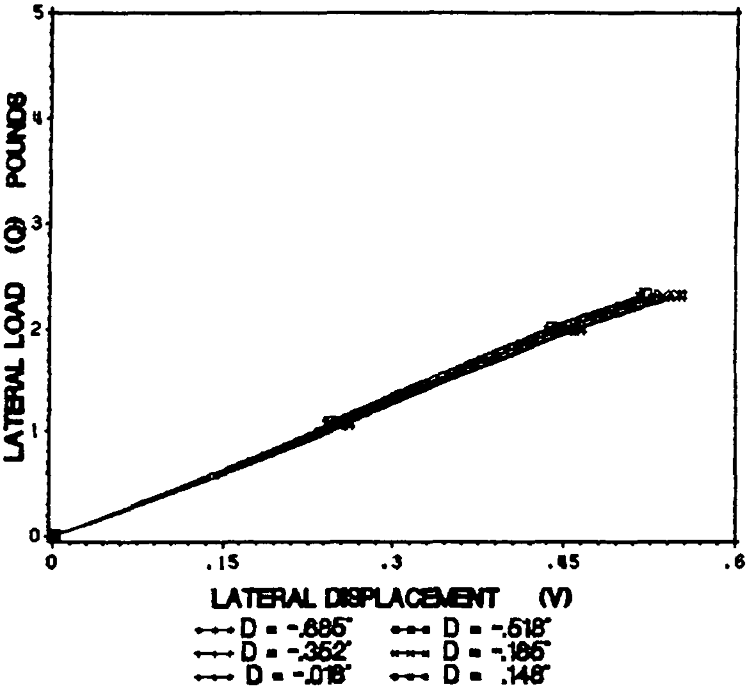

(B) CHANNEL SPECIMEN

Figure 35. Lateral load versus lateral displacement: Lateral displacement in inches is plotted on the horizontal axis and lateral load in pounds on the vertical. The I-section data is linear through the maximum lateral load. The channel data exhibits some curvature. The data points are closely spaced.

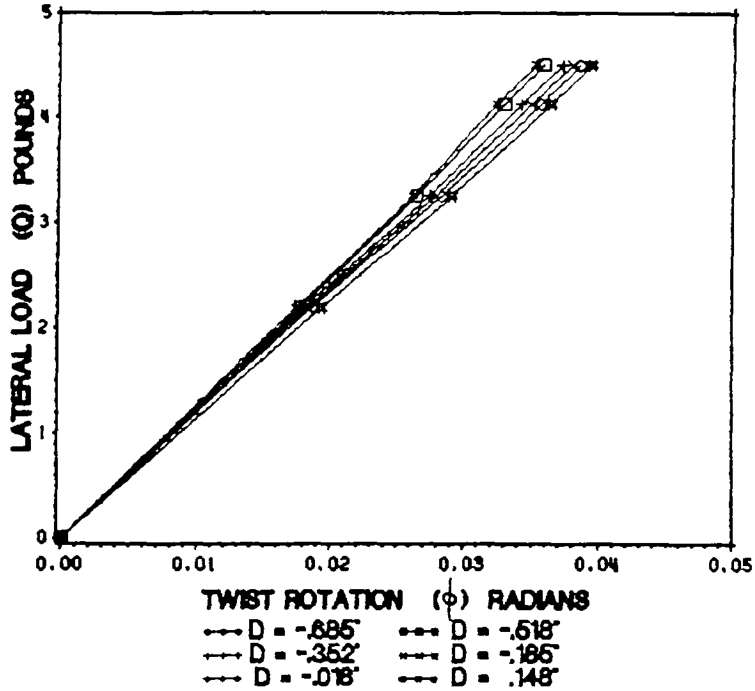

(A) I-SPECIMEN

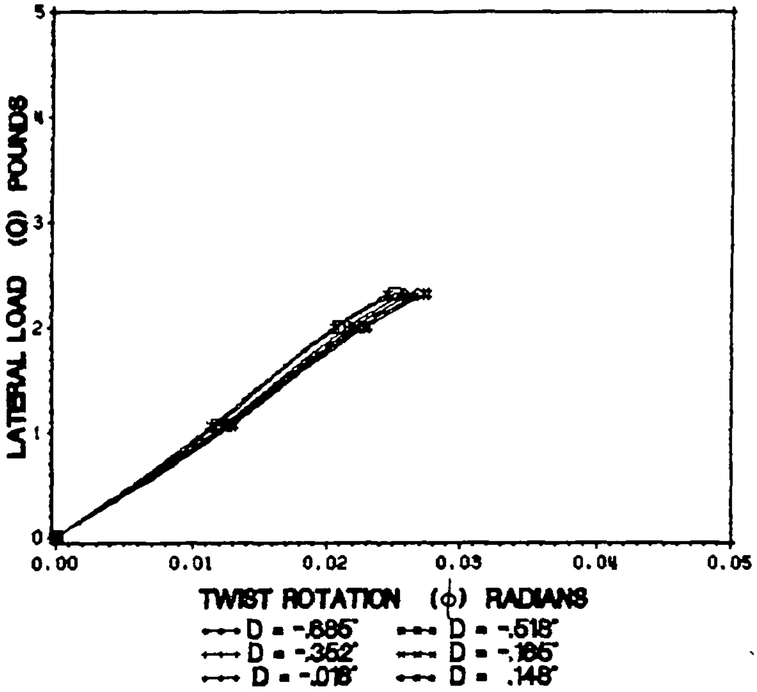

(B) CHANNEL SPECIMEN

Figure 36. Lateral load versus twist displacement: Twist displacement in radians is plotted on the horizontal axis and lateral load in pounds on the vertical. The I-section data is linear through a lateral load of three pounds. The channel data is slightly nonlinear.

in smaller effects which were difficult to measure reliably. Thus, the data from the in-plane tests is regarded as more reliable than the out-of-plane test data.

Data Reduction

For the in-plane tests, the load-displacement relations reduce to

$$\begin{Bmatrix} W \\ V \\ \phi \end{Bmatrix} = \begin{bmatrix} \alpha_{11} & \alpha_{13} \\ \alpha_{21} & \alpha_{23} \\ \alpha_{31} & \alpha_{33} \end{bmatrix} \begin{Bmatrix} P \\ T \end{Bmatrix} \tag{4.1}$$

Many tests for different values of the radial load and moment arm yield an algebraically overdetermined system. This situation occurs frequently in experimental research when more data are generated than would be required if absolute precision was possible. If such precision was possible, only two tests would be required to determine the flexibility coefficients.

The first of Eqs. (4.1) can be interpreted as a plane in the W, P, T space. Similar interpretations can be given to the second and third equations. The flexibility coefficients were calculated by fitting the best planes to the experimental data using a least squares routine. The experimental data were treated in groups in order to better understand the response of the frames under different loads. The experimental data was divided according to the value of the radial load and the algebraic sign of the torque. Thus, flexibility coefficients were calculated for positive and negative torques for each value of the radial load.

For the out-of-plane tests, the load-displacement relations reduce to

$$\begin{Bmatrix} W \\ V \\ \phi \end{Bmatrix} = \begin{bmatrix} \alpha_{12} & \alpha_{13} \\ \alpha_{22} & \alpha_{23} \\ \alpha_{32} & \alpha_{33} \end{bmatrix} \begin{Bmatrix} Q \\ T \end{Bmatrix} \tag{4.2}$$

Similar to the in-plane tests, repetitive tests yielded an algebraically overdetermined system. The relations in The first of Eqs. (4.2) can be interpreted as a plane in the W, Q, T space. Similar interpretations can be given to the second and third equations. The flexibility coefficients were calculated by fitting the best plane to the experimental data using a least squares routine. Flexibility coefficients were calculated for each value of the lateral load.

In general, the in-plane tests measured the flexibility coefficients more consistently than the out-of-plane tests, and the coefficients on the diagonal were measured more consistently then the off-diagonal terms. With the exception of α_{23} and α_{32} , the off-diagonal terms were small in magnitude and had a significant amount of scatter associated with them. The α_{23} terms are significant because of the coupling between out-of-plane bending and torsion due to the curved geometry.

No attempt was made to force the flexibility matrix to be symmetric. Enforcing symmetry in the flexibility matrix would substantially alter the values of the off-diagonal coefficients. The curved frames loaded at the midspan present geometric nonlinearities and the test data indicates this. Forcing the matrix to be symmetric would misrepresent the data and therefore the response of the frames.

Flexibility Influence Coefficients

Table 5. Flexibility influence coefficients for I-specimen from in-plane tests

Radial Load	T[a]	α_{11}	α_{33}	α_{23}	α_{13}	α_{31}	α_{21}
		x 10^{-3}	x 10^{-2}	x 10^{-1}	x 10^{-4}	x 10^{-4}	x 10^{4}
lbs	+/-	in/lb	1/in-lb	1/lb	1/lb	1/lb	in/lb
P = 20	-	0.875	0.136	0.092	1.750	0.415	0.086
P = 20	+	0.874	0.134	0.108	1.410	0.301	0.104
P = 40	-	0.843	0.134	0.101	0.930	0.265	0.741
P = 40	+	0.842	0.128	0.102	1.200	0.257	0.575
P = 60	-	0.831	0.137	0.105	0.415	0.228	0.422
P = 60	+	0.838	0.130	0.106	0.135	0.218	0.478
P = 80	-	0.823	0.136	0.110	0.200	0.175	0.178
P = 80	+	0.823	0.133	0.110	0.372	0.159	0.187
P = 100	-	0.814	0.138	0.116	-.056	0.081	-.188
P = 100	+	0.815	0.141	0.121	0.969	0.096	-.284

[a] Algebraic sign of applied torque

The flexibility influence coefficients for the I-specimen from the in-plane tests are presented in Table 5. Flexibility coefficients are presented for radial loads from 20 to 100 pounds for both positive and negative torques. The second column indicates the algebraic sign of the applied torque. In general, the flexibility coefficients for the I-specimen were unaffected by the sign of the torque.

The values for the flexibility coefficient α_{11} get gradually smaller with increasing value of the radial load indicating a stiffening in the response of the frame. The values for flexibility coefficient α_{33} obtained for negative torques are slightly larger than the values obtained for positive torques, however, the difference in magnitudes is small. The values for flexibility coefficient α_{23} become gradually larger with increasing radial load indicating a slight softening in the measured response. The values for flexibility coefficients α_{13}, α_{31}, and α_{21} are small and are inconsistently measured. Significant scatter in the data associated with these coefficients make a reliable determination of their magnitudes difficult. This indicates that their affect on the response of the frame is small. This is consistent with the uncoupled vibrational response observed in the dynamic tests since these coefficients couple the in-plane and out-of-plane static responses.

The flexibility influence coefficients for the channel specimen from the in-plane tests are presented in Table 6. Flexibility coefficients are presented for radial loads from 20 to 100 pounds for both positive and negative torques. The values for flexibility coefficient α_{11} are consistent with respect to the algebraic sign of the applied torque and with respect to the magnitude of the radial load. The values for α_{11} for the channel specimen are roughly twice the magnitude of corresponding values for the I-specimen. The channel specimen does not exhibit the stiffening response observed in the I-specimen. The values for flexibility coefficients α_{33} and α_{23} become steadily larger with increasing radial load indicating a softening in the torsional resistance. Further, the values for α_{33} and α_{23} obtained for negative torques are consistently smaller than values obtained for positive

Table 6. Flexibility influence coefficients for channel specimen from in-plane tests

Radial Load	T*	α_{11}	α_{33}	α_{23}	α_{13}	α_{31}	α_{21}
lbs	+/-	x 10^{-3} in/lb	x 10^{-2} 1/in-lb	x 10^{-1} 1/lb	x 10^{-2} 1/lb	x 10^{-4} 1/lb	x 10^{-3} in/lb
P = 20	-	1.64	0.250	0.196	0.313	-0.332	0.049
P = 20	+	1.66	0.290	0.219	0.301	-0.232	0.164
P = 40	-	1.66	0.258	0.224	0.361	-0.248	0.079
P = 40	+	1.66	0.295	0.264	0.377	-0.154	0.157
P = 60	-	1.65	0.284	0.271	0.391	-0.463	0.065
P = 60	+	1.66	0.285	0.308	0.411	-0.200	0.150
P = 80	-	1.65	0.323	0.341	0.442	-0.209	0.028
P = 80	+	1.66	0.332	0.394	0.492	-0.067	0.139
P = 100	-	1.65	0.394	0.457	0.526	-0.219	0.025
P = 100	+	1.66	0.454	0.548	0.655	-0.071	0.132

* Algebraic sign of applied torque

torques. This indicates that the torsional stiffness of the channel specimen is a function of the algebraic sign of the torque. The values for flexibility coefficients α_{13} and α_{31} differ by two orders of magnitude and have opposite signs. The magnitudes of the values for α_{31} depend on the sign of the torque. The scatter associated with these values makes reliable determination difficult. The values for flexibility coefficient α_{21} are a function of the sign of the applied torque and tend to get smaller with increasing value of the radial load.

The flexibility coefficients for the I-specimen from the out-of-plane tests are presented in Table 7. Coefficients are presented for four values of the lateral load. The values for flexibility coefficient α_{22} are measured consistently for each value of the lateral load. The values for flexibility coefficient α_{33} are also measured consistently, however, the values are about 20 % smaller than corresponding values obtained from the in-plane tests. The values for flexibility coefficients α_{23} and α_{32} are roughly the same magnitude, however, their magnitudes are consistently 15-20 % smaller than the values for α_{23} obtained from the in-plane tests. The values for flexibility coefficient α_{13} are inconsistently measured and the scatter associated with this coefficient is significant. The values for flexibility coefficient α_{12} become steadily larger with increasing lateral load and are about 100 times larger than the values for α_{21} obtained from the in-plane tests. As was discussed previously, this is thought to be due to a geometrically nonlinear response similar to the end shortening of a cantilevered straight beam.

The flexibility influence coefficients for the channel specimen from the out-of-plane tests are presented in Table 8. Flexibility coefficients are presented for three values of the lateral load. The values for flexibility coefficient α_{22} are measured fairly consistently. The magnitude of the values are roughly twice the magnitude of the corresponding values for the I-specimen indicating that the channel specimen is twice as compliant laterally. The values for flexibility coefficient α_{33} become smaller with increasing value of the lateral

Table 7. Flexibility influence coefficients for I-specimen from out-of-plane tests

Lateral Load	α_{22}	α_{33}	α_{23}	α_{32}	α_{13}	α_{12}
		x 10^{-2}	x 10^{-2}	x 10^{-2}	x 10^{-3}	x 10^{-2}
lbs	in/lb	1/in-lb	1/lb	1/lb	1/lb	in/lb
Q = 2.187	0.112	0.100	0.802	0.864	0.232	0.118
Q = 3.250	0.113	0.111	0.874	0.877	0.368	0.148
Q = 4.125	0.112	0.114	0.860	0.864	0.400	0.173
Q = 4.500	0.110	0.105	0.595	0.857	0.324	0.181

load. This trend is opposite to the trend observed in the values for the α_{33} from the in-plane tests. The values for α_{33} from the out-of-plane tests are much smaller than the values obtained from the in-plane tests. The values for flexibility coefficient α_{23} are relatively consistent and compare more favorably with corresponding values from the in-plane tests. The values for α_{32} are about 60 % of the values for α_{23}. The values for flexibility coefficient α_{12} are measured consistently and are much larger than the values for α_{21} from the in-plane tests. It is believed that the larger values for α_{12} is indicative of a geometrically nonlinear response.

The values for α_{23} and α_{33} which were obtained from the out-of-plane tests are generally smaller than the corresponding values obtained from the in-plane tests. The fact that the flexibility coefficients calculated from the two tests are not consistent is disturbing. The out-of-plane tests used very small lateral loads and smaller torques. The resulting displacements due to the torques were correspondingly smaller making them more difficult to measure experimentally. Thus, the values for α_{23} and α_{33} obtained from the in-plane static tests are considered more reliable.

Crush Test

The load displacement curve from the quasi-static crush test is presented in Fig. 37. The slope of the curve is roughly linear through a radial load of 400 pounds. The inverse of the slope in this region corresponds to α_{11}. The value for α_{11} from the crush test is 0.64×10^{-3} inches per pound. This value is significantly smaller than the α_{11} value obtained from the in-plane static tests. Thus, the crush test exhibits a stiffer radial response. This discrepancy is likely due to the different boundary conditions. The experimental boundary conditions for the crush test involved bolting the potted ends to

Table 8. Flexibility influence coefficients for channel specimen from out-of-plane tests

Lateral Load	α_{22}	α_{33}	α_{23}	α_{32}	α_{13}	α_{12}
		x 10^{-2}	x 10^{-1}	x 10^{1}	x 10^{2}	x 10^{2}
lbs	in/lb	1/in-lb	1/lb	1/lb	1/lb	in/lb
Q = 1.063	0.242	0.169	0.214	0.120	0.139	0.842
Q = 2.000	0.229	0.156	0.177	0.113	0.115	0.768
Q = 2.313	0.235	0.146	0.194	0.116	0.096	0.757

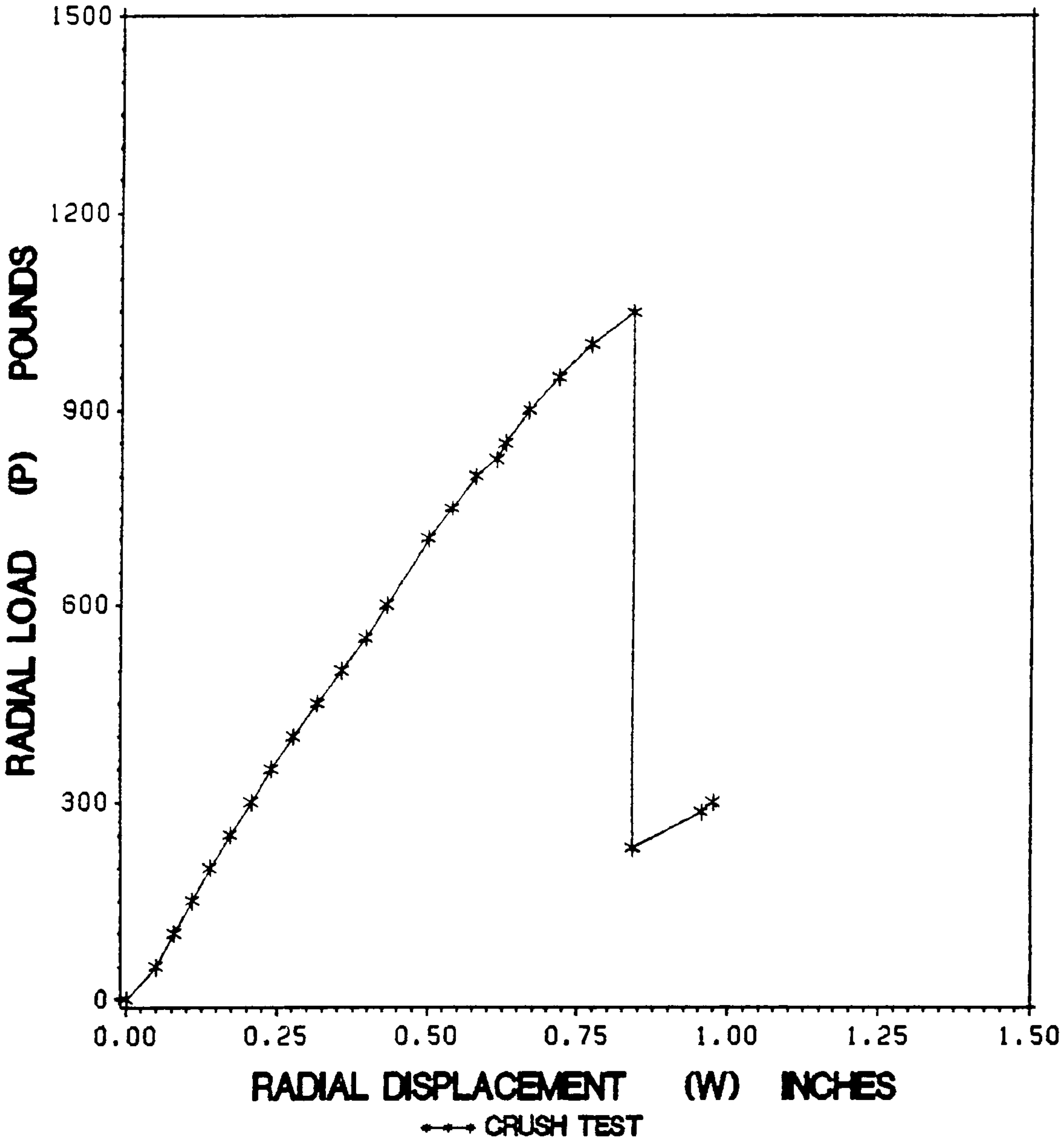

Figure 37. Crush test load displacement plot: Load versus radial displacement for the crush test of the I-section specimen.

the I-beam where the static tests used clamps. It will be shown in the Chapter 6 that the in-plane response is very sensitive to small changes in the boundary conditions.

The crush test was conducted as part of a related research effort by Mr. E. Moas, Graduate Research Assistant, and Professor O. H. Griffin that is sponsored by the landing and Impact Dynamics Branch, NASA Langley Research Center. The failure and post failure response of the frame will be addressed in detail by these researchers. The failure of the frame will be presented here in an effort to be complete without benefit of detailed analysis.

The initial failure event involved two simultaneous buckles in the web of the specimen. One buckle occurred at midspan and the other was located about eight inches to one side. The buckles are shown in Fig. 38. The initial failure occurred at a radial load of 1048 pounds. The strain in the region of the buckles at failure was significantly lower than the anticipated material failure strain suggesting a local instability possibly exacerbated by the unsymmetric layup in the web.

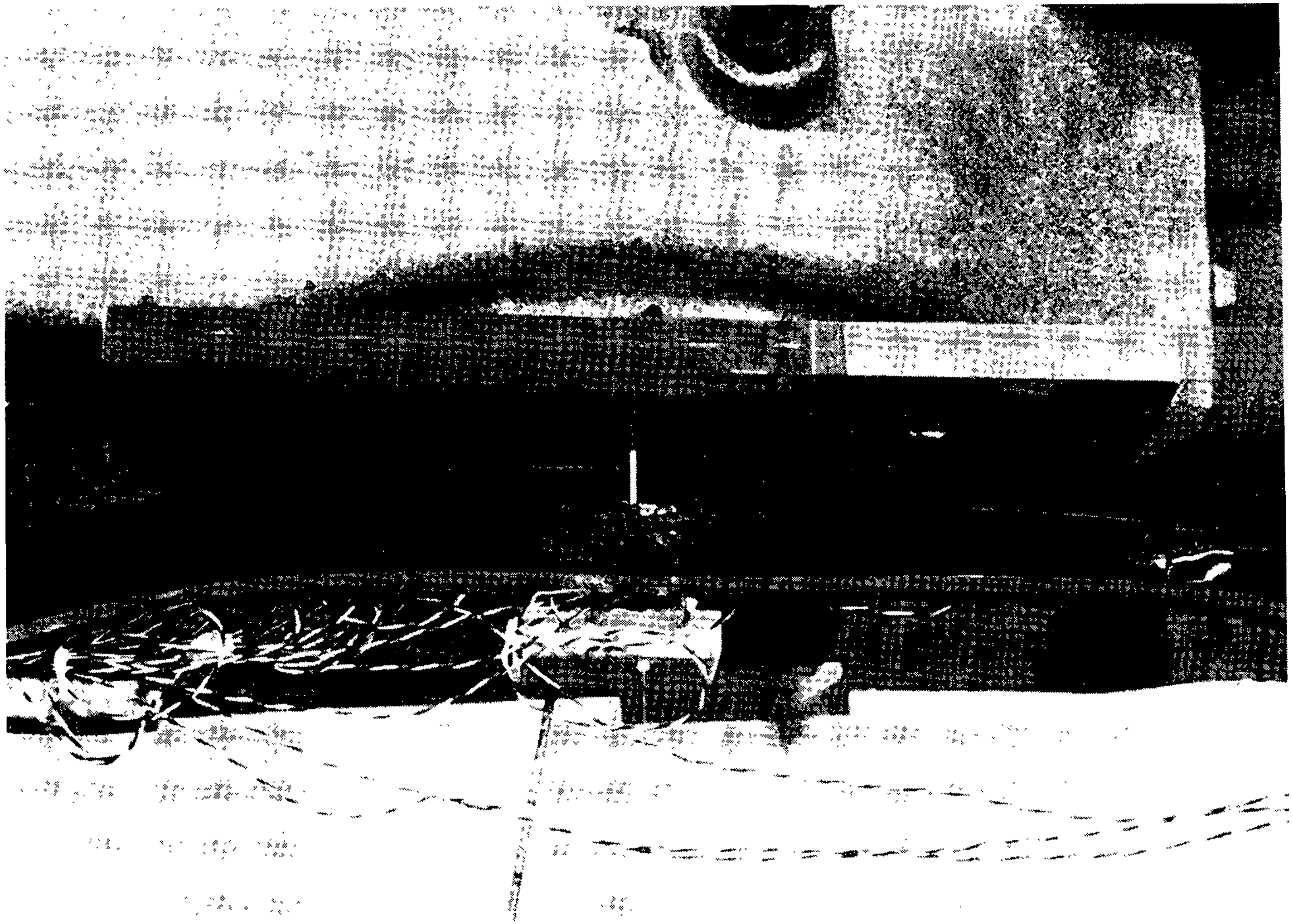

Figure 38. **Initial failures for crush test:** Local buckling in the web at the midspan and 10 degrees to one side were the first failures in the I-section crush test.

ORIGINAL PAGE
BLACK AND WHITE PHOTOGRAPH

Chapter 5

Analysis

Several structural analyses used to predict the linear static and vibrational response of the curved composite test specimens are discussed in this chapter. The first section traces the development of Vlasov's thin-walled, curved beam theory. One-dimensional continuum solutions for the decoupled in-plane and out-of-plane vibrational, and the in-plane static responses, are presented. Finally, the finite element computer program developed by Noor et al. (Ref. 7) is discussed. The finite element is based on a Vlasov-type thin-walled curved beam theory and includes the additional effects of transverse shear deformation and rotatory inertia. The finite element was developed specifically for the analysis of curved thin-walled beams with open sections.

Thin-Walled Curved Beam Theory

The thin-walled curved beam theory presented here was originally developed by Vlasov (Ref. 23). Culver (Ref. 22) used Vlasov's theory in his solution for the decoupled out-of-plane vibrational response for a curved thin-walled beam with a doubly symmetric cross section. Culver included the inertia terms by treating them as a periodic distributed static load. In this development, the strain energy relations are formed similar to Vlasov and then the kinetic energy is derived in a manner consistent with the kinematic assumptions and includes the inertial effects due to warping displacements. Hamilton's principle is used to obtain the differential equations of motion for a curved beam with a single plane of symmetry coinciding with the plane of curvature. The theory is extended by incorporating the constitutive relations of laminated composites into the Hooke's law expression.

Strain Energy

A ring segment is defined with respect to cylindrical coordinates (r,θ,y) as shown in Fig. 39. The radius measured from the origin O is written as $r = a\text{-}z$, where a is the radius of the circle through the centroids of each cross section normal to the circumferential direction, and z is a cross-sectional coordinate directed radially inward toward origin O. Coordinate x is defined to be the arc length on the centroidal circle ($x = a\theta$). At a generic cross section, the orthogonal coordinates x, y, and z are defined by the right-hand-screw rule. The cross section is assumed to be uniform along the circumference and to be symmetric about the $r\text{-}\theta$ (or z-x) plane. Thus, the cross-sectional axes y and z are principal centroidal axes of the cross section.

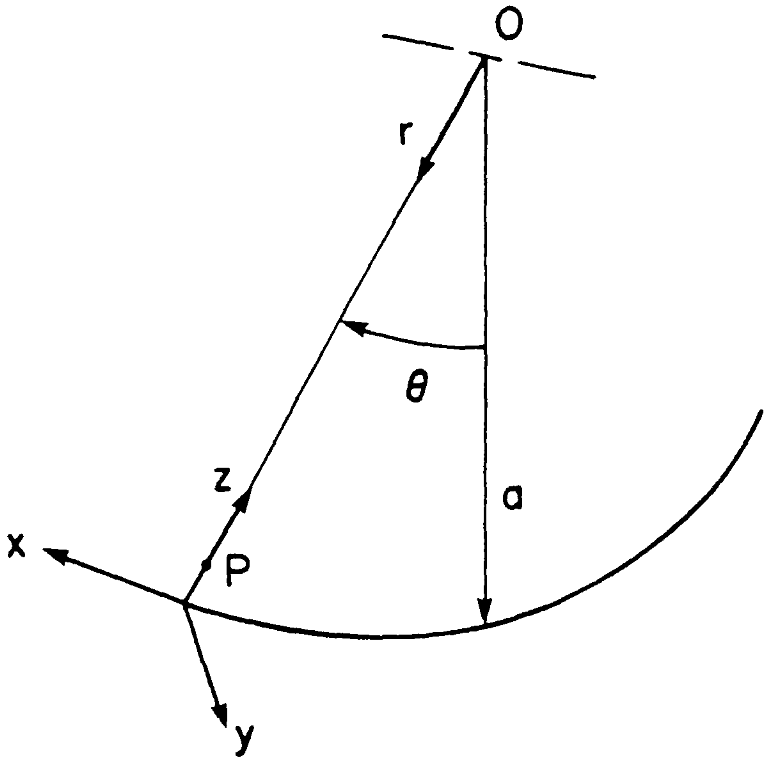

Figure 39. **Cylindrical and cross-sectional coordinates:** The sketch shows a cylindrical coordinate system for a curved beam with the origin O at the center of the beam and a cross-sectional coordinate system (x,y,z) at some generic point on the arc.

Relative to the cross-sectional coordinate axes y and z, shell coordinates s and ζ are defined to describe a thin-walled element of the curved beam. A contour line C is defined that is at the middle of the wall thickness, and s is the arc length coordinate along this contour. The contour is a continuous arc with a piecewise continuous tangent. The tangent to the contour can jump at junctions between flanges and webs, for example. The shell thickness coordinate ζ is measured normal to the tangent of the contour at s; $\zeta = 0$ on the contour, and $|\zeta| \leq h/2$, where h is the wall thickness. In general, h can be a function of s. The positive directions of coordinates s and ζ are fixed by defining (ζ, s, θ) as a right-handed orthogonal set of directions at a generic point in the shell space as shown in Fig. 40. A material point in the wall of an element in the cross section located at s and ζ is also described by coordinates y and z according to the relation

$$y(s,\zeta) = \bar{y}(s) + \zeta \sin\alpha(s) \tag{5.1}$$

$$z(s,\zeta) = \bar{z}(s) - \zeta \cos\alpha(s) \tag{5.2}$$

in which $\bar{y}(s)$ and $\bar{z}(s)$ are the coordinates of the contour C, and α is the angle between the positive y-axis and the positive tangent direction on the contour at s. Angle α is positive if measured counterclockwise when viewed down the positive θ-axis. On the contour, the differential coordinates satisfy

$$\frac{d\bar{y}}{ds} = \cos\alpha \qquad \frac{d\bar{z}}{ds} = \sin\alpha \tag{5.3}$$

From Eqs. (5.1-5.3) the following derivatives are obtained for later use

$$\frac{\partial y}{\partial s} = (1 + \zeta/R_s)\cos\alpha \ , \qquad \frac{\partial z}{\partial s} = (1 + \zeta/R_s)\sin\alpha \tag{5.4}$$

C2

$$\frac{\partial y}{\partial \zeta} = \sin\alpha\ , \qquad \frac{\partial z}{\partial \zeta} = -\cos\alpha \tag{5.5}$$

in which $1/R_s = d\alpha/ds$, and R_s is the radius of curvature of the contour in the y-z plane.

The shear center for the section lies along the z-axis at $z = z_p$, because of the assumed symmetry. In thin-walled beam theory, the coordinates of a point on the contour relative to the shear center are r(s), which is measured along the normal to the contour at s, and q(s) which is measured along the tangent to the contour at s. Coordinates r and q are called contour coordinates. Coordinate r(s) is not to be confused with the cylindrical coordinate r introduced earlier. In general, the cylindrical coordinate r is replaced with a-z. Thus, a material point in the wall located at s and ζ can be defined in terms of r, q, y, and z as follows

$$r(s) + \zeta = y\sin\alpha - (z - z_p)\cos\alpha \tag{5.6}$$

$$q(s) = y\ \cos\alpha + (z - z_p)\ \sin\alpha \tag{5.7}$$

The displacement components in the θ-, y-, and z- directions are designated u, v, and w, respectively. In Vlasov's curved beam theory, these are given by

$$u(\theta,y,z) = U(\theta) - y\phi_z(\theta) + z\phi_y(\theta) - \omega(s,\zeta)\tau(\theta) \tag{5.8}$$

$$v(\theta,y,z) = V(\theta) - (z - z_p)\,\phi_x(\theta) \tag{5.9}$$

$$w(\theta,y,z) = W(\theta) + y\phi_x(\theta) \tag{5.10}$$

in which $U(\theta)$ is the circumferential displacement of the centroid, $V(\theta)$ and $W(\theta)$ are the y- and z- direction displacements, respectively, of the shear center, $\phi_x(\theta)$ is the rotation of the cross section about the shear center and is positive counterclockwise when

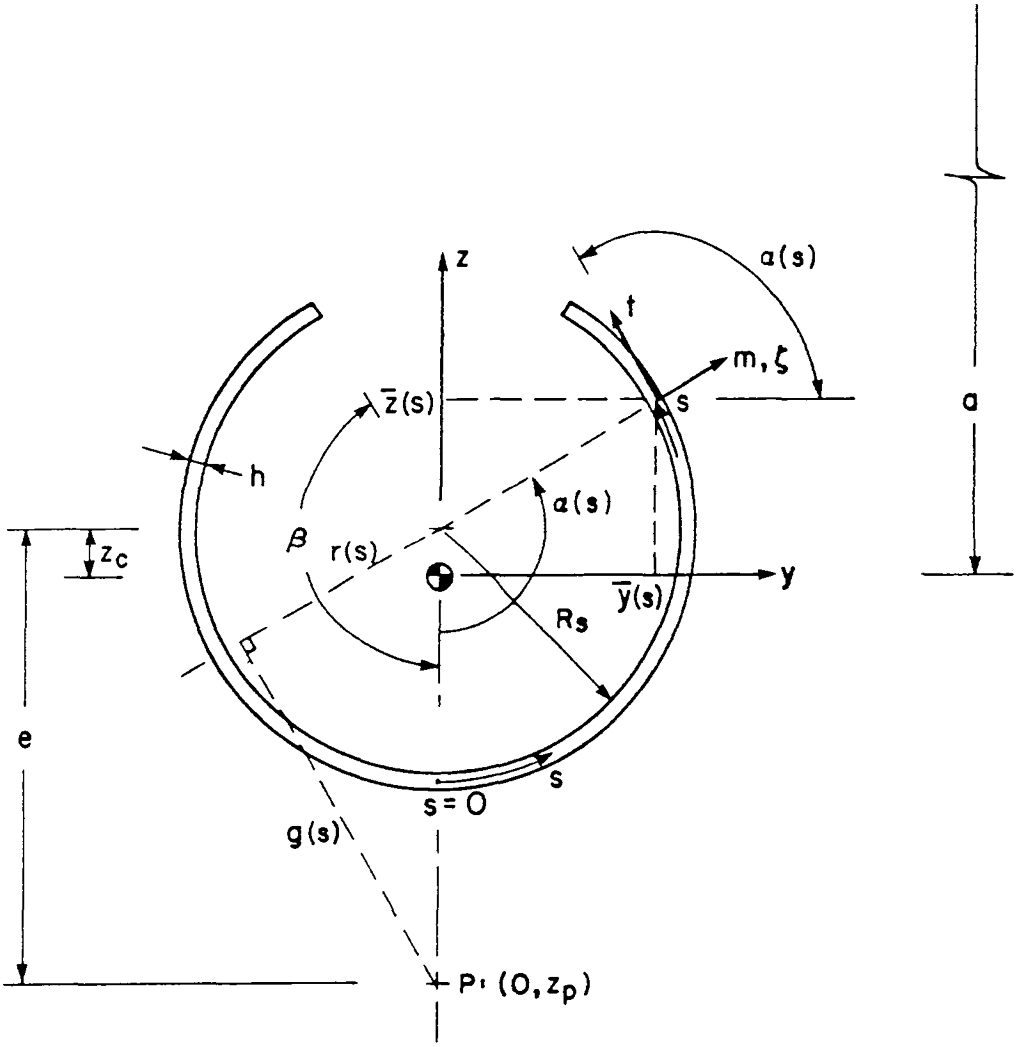
z
α(s)
t
m, ζ
z̄(s)
s
a
h
α(s)
β
r(s)
z_c
y
ȳ(s)
R_s
e
s
s = 0
g(s)
P: (0, z_p)

Figure 40. General symmetric cross section: The sketch illustrates the cross-sectional coordinates for an open, thin-walled circular section. Contour coordinates: r(s) and q(s). Shell wall coordinates: s, ζ. Cartesian coordinates of contour: ȳ(s), z̄(s).

viewed down the positive x-axis, $\phi_y(\theta)$ and $\phi_z(\theta)$ are rotations about the y- and z- axes, respectively, which are positive counterclockwise when viewed down their positive axes. Except for the term $\omega\tau$ in the expression for u, the displacements in Eqs. (5.8-5.10) represent a deformation for which plane sections remain plane. The term $\omega\tau$ represents warping of the cross section.

In cylindrical coordinates the linear strain-displacement equations are

$$\begin{aligned} \varepsilon_{\theta\theta} &= (u_{,\theta} - w)/(a - z) \\ \varepsilon_{yy} &= v_{,y} \\ \varepsilon_{zz} &= w_{,z} \\ \gamma_{\theta y} &= u_{,y} + v_{,\theta}/(a - z) \\ \gamma_{\theta z} &= u_{,z} + (w_{,\theta} + u)/(a - z) \\ \gamma_{yz} &= v_{,z} + w_{,y} \end{aligned} \tag{5.11}$$

in which partial differentiation with respect to a coordinate is denoted by a comma with the coordinate following as a subscript. Substituting the displacements of Eqs. (5.8-5.10) into the strains in Eqs. (5.11) results in

$$(a - z)\,\varepsilon_{\theta\theta} = U' - W - y(\phi'_z + \phi_x) + z\phi'_y - \omega\tau' \tag{5.12}$$

$$\varepsilon_{yy} = \varepsilon_{zz} = 0 \tag{5.13}$$

$$(a - z)\,\gamma_{\theta y} = -(a - z_p)\phi_z + V' - (z - z_p)(\phi'_x - \phi_z) - (a - z)\omega_{,y}\tau \tag{5.14}$$

$$(a - z)\,\gamma_{\theta z} = W' + U + a\phi_y + y(\phi'_x - \phi_z) - [(a - z)\omega_{,z} + \omega]\tau \tag{5.15}$$

$$\gamma_{yz} = 0 \tag{5.16}$$

in which a prime represents an ordinary derivative with respect to θ . Vanishing of the strains in Eqs. (5.13) and (5.16) indicates there is no distortion within the cross section. The rotation-displacement relations are taken as

$$\phi_y = -(W' + U)/a \tag{5.17}$$

$$\phi_z = V'/(a - z_p) \tag{5.18}$$

and the unit twist-rotation relation is taken as

$$\tau = (\phi'_x - \phi_z)/(a - z_p) \tag{5.19}$$

As a consequence of Eqs. (5.17-5.19), the transverse shearing strains $\gamma_{\theta y}$ and $\gamma_{\theta z}$ in Eqs. (5.14) and (5.15) are rewritten as

$$(a - z)\gamma_{\theta y} = -[(a - z_p)(z - z_p) + (a - z)\omega,_y]\tau \tag{5.20}$$

$$(a - z)\gamma_{\theta z} = [(a - z_p)y - (a - z)\omega,_z - \omega]\tau \tag{5.21}$$

The transverse shear strain components in the shell coordinates (ζ, s, θ) are $\gamma_{\theta s}$ and $\gamma_{\theta\zeta}$. They are given by the transformation equations

$$\gamma_{\theta s} = \gamma_{\theta y} \cos\alpha + \gamma_{\theta z} \sin\alpha \tag{5.22}$$

$$\gamma_{\theta\zeta} = \gamma_{\theta y} \sin\alpha - \gamma_{\theta z} \cos\alpha \tag{5.23}$$

After substitution of Eqs. (5.20) and (5.21) into (5.22) and (5.23) , the transverse shear strains in shell coordinates are

$$\begin{aligned}(a - z)\gamma_{\theta s} = {} & [(a - z_P)(y \sin\alpha - (z - z_P)\cos\alpha) \\ & - (a - z)(\omega,_y \cos\alpha + \omega,_z \sin\alpha) - \omega \sin\alpha]\tau\end{aligned} \tag{5.24}$$

$$\begin{aligned}(a - z)\gamma_{\theta\zeta} = {} & [-(a - z_p)(y \cos\alpha + (z - z_p)\sin\alpha) \\ & - (a - z)(\omega,_y \sin\alpha - \omega,_z \cos\alpha) + \omega \cos\alpha]\tau\end{aligned} \tag{5.25}$$

From the chain rule and Eqs. (5.4) and (5.5), partial derivatives of the warping function in shell coordinates are

$$\omega,_s = (1 + \zeta/R_s)(\omega,_y \cos\alpha + \omega,_z \sin\alpha) \tag{5.26}$$

$$\omega,_\zeta = \omega,_y \sin\alpha - \omega,_z \cos\alpha \tag{5.27}$$

As a consequence of Eqs. (5.6) and (5.7) for the contour coordinates, and Eqs. (5.26) and (5.27), the transverse shear strains are

$$(a - z)\gamma_{\theta s} = [(a - z_p)(r(s) + \zeta) - (a - z)(1 + \zeta/R_s)^{-1}\omega,_s - \omega \sin\alpha]\tau \tag{5.28}$$

$$(a - z)\gamma_{\theta\zeta} = [-(a - z_p)q(s) - (a - z)\omega,_\zeta + \omega \cos\alpha]\tau \tag{5.29}$$

Using Eqs. (5.4) and (5.5) it can be shown that

$$\frac{(a - z)^2}{(1 + \zeta/R_s)}\frac{\partial}{\partial s}\left(\frac{\omega}{a - z}\right) = (a - z)(1 + \zeta/R_s)^{-1}\omega,_s + \omega \sin\alpha \tag{5.30}$$

$$(a - z)^2 \frac{\partial}{\partial\zeta}\left(\frac{\omega}{a - z}\right) = (a - z)\omega,_\zeta - \omega \cos\alpha \tag{5.31}$$

and with these identities Eqs. (5.28) and (5.29) are rewritten as

$$(a - z)\gamma_{\theta s} = \left\{(a - z_p)(r(s) + \zeta) - \frac{(a - z)^2}{(1 + \zeta/R_s)}\frac{\partial}{\partial s}\left(\frac{\omega}{a - z}\right)\right\}\tau \tag{5.32}$$

$$(a - z)\gamma_{\theta\zeta} = \left\{-(a - z_p)q(s) - (a - z)^2\frac{\partial}{\partial\zeta}\left(\frac{\omega}{a - z}\right)\right\}\tau \tag{5.33}$$

The Vlasov assumption is that the transverse shear strain vanishes on the contour; that is, $\gamma_{\theta s}(s, \zeta = 0) = 0$. Let $\omega(s, \zeta = 0) = \overline{\omega}(s)$, and the Vlasov assumption implies from Eqn. (5.32) that

$$(a - z_p)r(s) - (a - \overline{z})^2\frac{d}{ds}\left(\frac{\overline{\omega}}{a - \overline{z}}\right) = 0 \tag{5.34}$$

Integrating Eqn. (5.34) with respect to s from s = 0 to s, we write

$$\overline{\omega}(s) = (a - z_p)(a - \overline{z}(s))\int_0^s \frac{r(s)}{(a - \overline{z}(s))^2}ds \tag{5.35}$$

in which the origin of s is selected such that the integral in Eqn. (5.35) vanishes if the integration limits are over the entire contour C. For thin rings, the largest cross-sectional dimension is less than one-tenth the radius a. Thus, $a-\overline{z} \simeq a$, and Eqn. (5.35) is approximated by

$$\overline{\omega}(s) = \int_0^s r(s)ds \tag{5.36}$$

which is the same expression as used in straight beam theory. The geometric interpretation of $\overline{\omega}$ in Eqn. (5.36) is twice the area swept-out by a ray whose one end is fixed at the shear center and the other end moves on the contour from s = 0 to s. For this reason, the contour warping function of Eqn. (5.36) is called the sectorial area.

The Kirchhoff-Love assumption is appropriate for the thin-walled shell elements of the curved beam. This implies the transverse shear strain component $\gamma_{\theta\zeta}$ vanishes. Setting the coefficient of τ in Eqn. (5.33) to zero, and then integrating with respect to ζ, we obtain

$$\omega(s,\zeta) = [(a - z_p)q(s) + (a - \bar{z})\tilde{\omega}(s)]/\cos\alpha + \zeta\tilde{\omega}(s) \tag{5.37}$$

in which $\tilde{\omega}(s)$ is the thickness warping function. The first term on the right-hand-side of Eqn. (5.37) is independent of ζ and is identified as the contour warping function $\bar{\omega}(s)$. As a result of this identification, the expression for the thickness warping function is

$$\tilde{\omega}(s) = -\frac{(a - z_p)}{(a - \bar{z})}q + \frac{\bar{\omega}}{R_\theta} \tag{5.38}$$

where

$$1/R_\theta = \cos\alpha/(a - \bar{z}) \tag{5.39}$$

The quantity $1/R_\theta$ is the normal curvature of the θ-curve in the shell element reference surface. Thus, the warping function for the cross section is

$$\omega(s,\zeta) = \bar{\omega}(s) + \zeta\tilde{\omega}(s) \tag{5.40}$$

with the contour warping function $\bar{\omega}(s)$ given in Eqn. (5.35) and the thickness warping by Eqn. (5.38).

The distribution of the shear strain component $\gamma_{\theta s}$ through the thickness of the shell wall is approximated as a linear function of ζ. A series expansion in ζ of the coefficient of the unit twist τ in Eqn. (5.32), subject to the Vlasov assumption (5.34), Eqs. (5.2), (5.4-5.7), and (5.38-5.40), results in

$$(a - z)\gamma_{\theta s} = \left\{ \frac{2(a - z_p)^2}{(a - \bar{z})} \zeta + O(\zeta^2) \right\} \tau \tag{5.41}$$

The terms of order ζ^2 and higher are neglected in Eqn. (5.41).

The nonzero strains are $\varepsilon_{\theta\theta}$, Eqn. (5.12), and $\gamma_{\theta s}$ in Eqn. (5.41). These can be rewritten in the form

$$(1 - \bar{z}/a)(1 + \zeta/R_\theta)\varepsilon_{\theta\theta} = e - y\kappa_z + z\kappa_y - \omega(\tau'/a) \tag{5.42}$$

$$(1 - \bar{z}/a)(1 + \zeta/R_\theta)\gamma_{\theta s} = \frac{2(a - z_p)^2}{a(a - \bar{z})} \zeta\tau \tag{5.43}$$

where

$$(a - z) = a(1 - \bar{z}/a)(1 + \zeta/R_\theta) \tag{5.44}$$

$$e = (U' - W)/a \tag{5.45}$$

$$\kappa_z = (\phi'_z + \phi_x)/a \tag{5.46}$$

$$\kappa_y = \phi'_y/a \tag{5.47}$$

Eqn. (5.44) follows from Eqn. (5.2) and from the definition of $1/R_\theta$ Eqn. (5.39). The quantity e Eqn. (5.45) represents the circumferential stretching strain of the centroidal line, κ_z is the change in curvature out of the plane of the curved beam, and κ_y is the change in curvature in the plane of the curved beam. Substituting Eqn. (5.1) for y, Eqn. (5.2) for z, and Eqn. (5.40) for ω, into Eqn. (5.42) gives the circumferential strain as an explicit function of ζ. The result is

$$\begin{aligned}(1 - \bar{z}/a)(1 + \zeta/R_\theta)\varepsilon_{\theta\theta} &= e - \bar{y}\kappa_z + \bar{z}\kappa_y - \bar{\omega}(\tau'/a) \\ &\quad - \zeta[\sin\alpha\,\kappa_z + \cos\alpha\,\kappa_y + \tilde{\omega}(\tau'/a)]\end{aligned} \tag{5.48}$$

The strain energy increment for the curved beam is

$$\delta\bar{U} = \int_{Vol} (\sigma_{\theta\theta}\delta\varepsilon_{\theta\theta} + \sigma_{\theta s}\delta\gamma_{\theta s})dVol \tag{5.49}$$

in which $\sigma_{\theta\theta}$ is the circumferential normal stress and $\sigma_{\theta s}$ is the shear stress. The differential volume element is

$$dVol = (a - z)d\theta dA = (1 + \zeta/R_s)(1 + \zeta/R_\theta)d\zeta\,(1 - \bar{z}/a)ds\,ad\theta \tag{5.50}$$

in which the area element within the θ-cross section is expressed in terms of shell coordinates s and ζ. The strain increments $\delta\varepsilon_{\theta\theta}$ and $\delta\gamma_{\theta s}$ in Eqn. (5.49) are obtained in terms of the increments of the bar strains δe, $\delta\kappa_z$, $\delta\kappa_y$, and $\delta\tau$ from Eqs. (5.43) and (5.48). These strain increments are substituted into the strain energy increment (5.49) using the volume element in Eqn. (5.50). Integrations over the cross section are performed, and the resulting strain energy increment for the curved beam is written as

$$\delta\bar{U} = \int_{\theta_1}^{\theta_2} [N\delta e + M_y\delta\kappa_y + M_z\delta\kappa_z + M_\omega(\delta\tau'/a) + T_s\delta\tau]ad\theta \tag{5.51}$$

in which $\theta \in (\theta_1, \theta_2)$, $\theta_2 > \theta_1$, and the curved beam resultants are defined by the contour integrals

$$N = \int_C N_\theta ds \tag{5.52}$$

$$M_y = \int_C (N_\theta \bar{z} - M_\theta \cos\alpha) ds \tag{5.53}$$

$$M_z = -\int_C (N_\theta \bar{y} + M_\theta \sin\alpha) ds \tag{5.54}$$

$$M_\omega = -\int_C (N_\theta \bar{\omega} + M_\theta \tilde{\omega}) ds \tag{5.55}$$

$$T_s = 2(1 - z_p/a)^2 \int_C \frac{M_{\theta s}}{(1 - \bar{z}/a)} ds \tag{5.56}$$

The shell resultants appearing in the contour integrals of Eqs. (5.52-5.56) are defined by the following integrals through the thickness of the shell elements:

$$(N_\theta, M_\theta) = \int_h (1, \zeta) \sigma_{\theta\theta} (1 + \zeta/R_s) d\zeta \tag{5.57}$$

$$M_{\theta s} = \int_h \zeta \sigma_{\theta s} (1 + \zeta/R_s) d\zeta \tag{5.58}$$

The curved beam resultant N acts in the circumferential direction at the centroid of the cross section. The bending resultants M_y and M_z are vectorally directed along the positive y- and z-axes, respectively, by the right-hand screw rule. The bimoment M_ω is taken to act in the circumferential direction at the shear center. The bimoment is statically equivalent to zero force and zero moment. The Saint Venant torque T_s is directed circumferentially and also acts at the shear center.

Kinetic Energy

The kinetic energy is

$$\overline{T} = \frac{1}{2}\int_{Vol} (\dot{u}^2 + \dot{v}^2 + \dot{w}^2)\rho dVol \tag{5.59}$$

where ρ denotes the mass density, and the overdot denotes a partial derivative with respect to time. Time derivatives of the displacements are determined from Eqs. (5.8-5.10). Using Eqs. (5.1), (5.2), and (5.40), these time derivatives can be written explicitly in terms of contour coordinates $\overline{y}(s)$, $\overline{z}(s)$, $\overline{\omega}(s)$, and $\tilde{\omega}(s)$, and the thickness coordinate ζ. The results are

$$\begin{aligned}\dot{u}(s, \theta, \zeta, t) = \dot{U}(\theta,t) - \overline{y}(s)\dot{\phi}_z(\theta,t) + \overline{z}\dot{\phi}_y(\theta,t) - \overline{\omega}\dot{\tau}(\theta,t) \\ - \zeta[\dot{\phi}_z(\theta,t)\sin\alpha(s) + \dot{\phi}_y(\theta,t)\cos\alpha(s) + \tilde{\omega}(s)\dot{\tau}(\theta,t)]\end{aligned} \tag{5.60}$$

$$\dot{v}(s, \theta, \zeta, t) = \dot{V}(\theta,t) - (\overline{z}(s) - z_p)\dot{\phi}_x(\theta,t) + \zeta\dot{\phi}_x(\theta,t)\cos\alpha(s) \tag{5.61}$$

$$\dot{w}(s, \theta, \zeta, t) = \dot{W}(\theta,t) + \overline{y}(s)\dot{\phi}_x(\theta, t) + \zeta\dot{\phi}_x(\theta,t)\sin\alpha(s) \tag{5.62}$$

These relations for the velocity components are substituted into the kinetic energy (5.59) along with the volume element (5.50). Integration over the cross section is performed and the result is

$$\overline{T} = \frac{1}{2} \int_{\theta_1}^{\theta_2} \dot{\underset{\sim}{u}}^T \, \underline{m} \, \dot{\underset{\sim}{u}} \, a d\theta \tag{5.63}$$

in which the 7x1 velocity vector $\dot{\underset{\sim}{u}}$ is

$$\dot{\underset{\sim}{u}}(\theta,t) = [\dot{U},\ \dot{V},\ \dot{W},\ \dot{\phi}_x,\ \dot{\phi}_y,\ \dot{\phi}_z,\ \dot{\tau}]^T \tag{5.64}$$

and the 7x7 symmetric mass matrix $\underline{m}$ is

$$\begin{array}{c} \begin{array}{ccccccc} \dot{U} & \dot{V} & \dot{W} & \dot{\phi}_x & \dot{\phi}_y & \dot{\phi}_z & \dot{\tau} \end{array} \\ \begin{bmatrix} m_{11} & 0 & 0 & 0 & m_{15} & m_{16} & m_{17} \\ & m_{22} & 0 & m_{24} & 0 & 0 & 0 \\ & & m_{33} & m_{34} & 0 & 0 & 0 \\ & & & m_{44} & 0 & 0 & 0 \\ & & & & m_{55} & m_{56} & m_{57} \\ & & & & & m_{66} & m_{67} \\ \text{Symm} & & & & & & m_{77} \end{bmatrix} \end{array} \tag{5.65}$$

The nonzero elements of the mass matrix are the contour integrals

$$
\begin{aligned}
m_{11} = m_{22} = m_{33} &= \int_C m(1 - \bar{z}/a)\, ds \\
m_{15} &= \int_C (m\bar{z} - I_\zeta \cos\alpha)(1 - \bar{z}/a)\, ds \\
m_{16} = -m_{34} &= -\int_C (m\bar{y} + I_\zeta \sin\alpha)(1 - \bar{z}/a)\, ds \\
m_{17} &= -\int_C (m\overline{\omega} + I_\zeta\tilde{\omega})(1 - \bar{z}/a)\, ds \\
m_{24} &= \int_C (-m(\bar{z} - z_p) + I_\zeta \cos\alpha)(1 - \bar{z}/a)\, ds \\
m_{44} &= \int_C (m(r^2 + q^2) + 2I_\zeta r + I_{\zeta\zeta})(1 - \bar{z}/a)\, ds \\
m_{55} &= \int_C [m\bar{z}^2 - 2I_\zeta\bar{z}\cos\alpha + I_{\zeta\zeta}\cos^2\alpha](1 - \bar{z}/a)\, ds \qquad (5.66) \\
m_{56} &= \int_C [-m\overline{yz} + I_\zeta(\bar{y}\cos\alpha - \bar{z}\sin\alpha) + I_{\zeta\zeta}\sin\alpha\cos\alpha](1 - \bar{z}/a)\, ds \\
m_{57} &= \int_C [-m\overline{z\omega} + I_\zeta(-\bar{z}\tilde{\omega} + \cos\alpha\,\overline{\omega}) + I_{\zeta\zeta}\cos\alpha\tilde{\omega}](1 - \bar{z}/a)\, ds \\
m_{66} &= \int_C [m\bar{y}^2 + 2I_\zeta\bar{y}\sin\alpha + I_{\zeta\zeta}\sin^2\alpha](1 - \bar{z}/a)\, ds \\
m_{67} &= \int_C [m\overline{y\omega} + I_\zeta(\bar{y}\tilde{\omega} + \overline{\omega}\sin\alpha) + I_{\zeta\zeta}\sin\alpha\tilde{\omega}](1 - \bar{z}/a)\, ds \\
m_{77} &= \int_C [m\overline{\omega}^2 + 2I_\zeta\overline{\omega}\tilde{\omega} + I_{\zeta\zeta}\tilde{\omega}^2](1 - \bar{z}/a)\, ds
\end{aligned}
$$

in which the mass properties of the shell wall are

$$(m,\ I_\zeta,\ I_{\zeta\zeta}) = \int_h (1,\ \zeta,\ \zeta^2)\,\rho(1 + \zeta/R_s)(1 + \zeta/R_\theta)\,d\zeta \qquad (5.67)$$

Hamilton's Principle

The variational statement of dynamic equilibrium is Hamilton's principle. For no external loads acting on the curved beam, Hamilton's principle is

$$\int_{t_1}^{t_2} (\delta\overline{T} - \delta\overline{U})dt = 0 \qquad (5.68)$$

where the time limits satisfy $t_2 > t_1$. The four independent functional degrees of freedom are U, V, W, and ϕ_x. Rotations ϕ_y and ϕ_z, and the unit twist τ, depend on on U, V, W, and ϕ_x as shown by Eqs. (5.17-5.19). Lagrange multipliers are introduced to keep the seven functional degrees of freedom U, V, W, ϕ_x, ϕ_y, ϕ_z, and τ in the functional independent. The shear force Q_z is the Lagrange multiplier associated with rotation ϕ_y, shear force Q_y is the Lagrange multiplier associated with rotation ϕ_z, and the torque T is the Lagrange multiplier associated with unit twist τ. The augmented functional is

$$\int_{t_1}^{t_2} (\delta\overline{T} - \delta\overline{U}^*)dt = 0 \qquad (5.69)$$

where

$$\delta\overline{U}^{*} = \delta\overline{U} + \int_{\theta_1}^{\theta_2}\{Q_y[\delta V'/(a - z_p) - \delta\phi_z] + Q_z[(\delta W' + \delta U)/a + \delta\phi_y] \\ + T[(\delta\phi'_x - \delta\phi_z)/(a - z_p) - \delta\tau]\}\, a d\theta \tag{5.70}$$

The variation of the kinetic energy obtained from Eqn. (5.63) and the variation of the augmented strain energy in Eqn. (5.70) are substituted into the variational principle Eqn. (5.69). In addition Eqs. (5.45-5.47) and (5.51) are substituted in the appropriate manner into the variational principle. After these substitutions, the inertia terms are integrated by parts with respect to time, and the variations in the degrees of freedom δU, δV, δW, $\delta\phi_x$, $\delta\phi_y$, $\delta\phi_z$, and $\delta\tau$ at times t_1 and t_2 vanish according to Hamilton's principle. Integrating by parts with respect to θ yields the Euler-Lagrange equations associated with each functional degree of freedom.

$$\delta U: \qquad -m_{11}\ddot{U} - m_{15}\ddot{\phi}_y - m_{16}\ddot{\phi}_z - m_{17}\ddot{\tau} + N'/a - Q_z/a = 0 \tag{5.71}$$

$$\delta V: \qquad -m_{22}\ddot{V} - m_{24}\ddot{\phi}_x + Q'_y/(a - z_p) = 0 \tag{5.72}$$

$$\delta W: \qquad -m_{33}\ddot{W} - m_{34}\ddot{\phi}_x + N/a + Q'_z/a = 0 \tag{5.73}$$

$$\delta\phi_x: \qquad -m_{24}\ddot{V} - m_{34}\ddot{W} - m_{44}\ddot{\phi}_x - M_z/a + T'/(a - z_p) = 0 \tag{5.74}$$

$$\delta\phi_y: \qquad -m_{15}\ddot{U} - m_{55}\ddot{\phi}_y - m_{56}\ddot{\phi}_z - m_{57}\ddot{\tau} + M'_y/a - Q_z = 0 \tag{5.75}$$

$$\delta\phi_z: \qquad -m_{16}\ddot{U} - m_{56}\ddot{\phi}_y - m_{66}\ddot{\phi}_z - m_{67}\ddot{\tau} + M'_z/a \\ + Q_y + T/(a - z_p) = 0 \tag{5.76}$$

$$\delta\tau: \qquad -m_{17}\ddot{U} - m_{57}\ddot{\phi}_y - m_{67}\ddot{\phi}_z - m_{77}\ddot{\tau} + M'_{\omega}/a - T_s + T = 0 \tag{5.77}$$

The seven boundary conditions at $\theta = \theta_1$ and $\theta = \theta_2$ are

$$\begin{array}{cc}
\text{Essential} & \text{Natural} \\
U & N \\
V & (1 - z_p/a)^{-1} Q_y \\
W & Q_z \\
\phi_x & (1 - z_p/a)^{-1} T \\
\phi_y & M_y \\
\phi_z & M_z \\
\tau & M_\omega
\end{array} \tag{5.78}$$

Hooke's Law

It is assumed that the shell elements comprising the thin-walled curved beam are laminated from materials having monoclinic symmetry with respect to a ζ-surface (a surface on which ζ is constant). Monoclinic symmetry is exhibited by an off-axis lamina reinforced with continuous and aligned fibers. This is the case for the graphite-epoxy specimens in this study. The fiber direction, commonly labeled the 1-axis, is established by a counterclockwise rotation through an angle $\bar{\theta}$ from the positive s-axis to the 1-axis, looking down the positive ζ -axis. In beam theories, the lateral stresses are assumed to vanish in Hooke's law. This assumption implies that stress components σ_{ss}, $\sigma_{\zeta\zeta}$, and $\sigma_{s\zeta}$ are zero in the generalized strain-stress relations. Thus, for an off-axis lamina the strain-stress relations are

$$\begin{aligned} \varepsilon_{\theta\theta} &= S'_{22}\sigma_{\theta\theta} + S'_{26}\sigma_{\theta s} \\ \gamma_{\theta\zeta} &= S'_{44}\sigma_{\theta\zeta} \\ \gamma_{s\theta} &= S'_{62}\sigma_{\theta\theta} + S'_{66}\sigma_{\theta s} \end{aligned} \tag{5.79}$$

in which the off-axis compliances are

$$\begin{aligned} S'_{22} &= S_{11}n^4 + (2S_{12} + S_{66})m^2n^2 + S_{22}m^4 \\ S'_{26} = S'_{62} &= (2S_{11} - 2S_{12} - S_{66})mn^3 - (2S_{22} - 2S_{12} - S_{66})m^3n \\ S'_{44} &= S_{44}m^2 + S_{55}n^2 \\ S'_{66} &= 2(2S_{11} + 2S_{22} - 4S_{12} - S_{66})m^2n^2 + S_{66}(m^4 + n^4) \end{aligned} \tag{5.80}$$

with $m = \cos\bar{\theta}$ and $n = \sin\bar{\theta}$. The on-axis compliances in terms of engineering constants are

$$\begin{aligned} S_{11} &= 1/E_1\ ,\ S_{21} = -\nu_{12}/E_1\ ,\ S_{22} = 1/E_2 \\ S_{44} &= 1/G_{23}\ ,\ S_{55} = 1/G_{13}\ ,\ S_{66} = 1/G_{12} \end{aligned} \tag{5.81}$$

The transverse shear strain $\gamma_{\theta\zeta}$ was assumed to vanish by the Kirchhoff-Love assumption. As a consequence, the second of Eqs. (5.79) is neglected. Writing the inverse of the two remaining equations in Hooke's law from Eqs. (5.79) we have

$$\begin{aligned} \sigma_{\theta\theta} &= R_{22}\varepsilon_{\theta\theta} + R_{26}\gamma_{\theta s} \\ \sigma_{\theta s} &= R_{26}\varepsilon_{\theta\theta} + R_{66}\gamma_{\theta s} \end{aligned} \tag{5.82}$$

in which the reduced transformed stiffnesses are

$$(R_{22}, R_{26}, R_{66}) = (S'_{66}, -S'_{26}, S'_{22})/[S'_{22}S'_{66} - (S'_{26})^2] \tag{5.83}$$

For an isotropic material, $R_{22} = E$, $R_{26} = 0$, $R_{66} = G$, where E and G are the modulus of elasticity and the shear modulus, respectively.

The Hooke's law for the curved beam is obtained as follows. The strain relation for $\varepsilon_{\theta\theta}$ in Eqn. (5.48) and the relation for $\gamma_{\theta s}$ in Eqn. (5.43) are substituted into Eqs. (5.82) to get the stresses in terms of beam strains e, κ_y, κ_z, τ'/a, and τ. These stress-beam strain equations are in turn substituted into the definitions of the shell resultants N_θ, M_θ, and $M_{\theta s}$ in Eqs. (5.57) and (5.58). Finally, these shell resultant-beam strain relations are substituted into the definitions of the beam resultants in Eqs. (5.52-5.56). The result of these manipulations is

$$\begin{bmatrix} N \\ M_y \\ M_z \\ M_\omega \\ T_s \end{bmatrix} = \begin{bmatrix} EA & ES_y & -ES_z & -ES_\omega & EH \\ & EI_{yy} & -EI_{zy} & -EI_{\omega y} & EH_c \\ & & EI_{zz} & EI_{\omega z} & -EH_s \\ & & & EI_{\omega\omega} & -EH_q \\ \text{Symm} & & & & GJ \end{bmatrix} \begin{bmatrix} e \\ \kappa_y \\ \kappa_z \\ \tau'/a \\ \tau \end{bmatrix} \tag{5.84}$$

in which

$$EA = \int_C a_{22}(1 - \bar{z}/a)^{-1} ds \tag{5.85}$$

$$ES_y = \int_C (a_{22}\bar{z} - b_{22}\cos\alpha)(1 - \bar{z}/a)^{-1} ds \tag{5.86}$$

$$ES_z = \int_C (a_{22}\bar{y} + b_{22}\sin\alpha)(1 - \bar{z}/a)^{-1}ds \qquad (5.87)$$

$$ES_\omega = \int_C (a_{22}\overline{\omega} + b_{22}\tilde{\omega})(1 - \bar{z}/a)^{-1}ds \qquad (5.88)$$

$$EH = 2(1 - z_p/a)^2 \int_C b_{26}(1 - \bar{z}/a)^{-2}ds \qquad (5.89)$$

$$EI_{yy} = \int_C (a_{22}\bar{z}^2 - 2b_{22}\bar{z}\cos\alpha + d_{22}\cos^2\alpha)(1 - \bar{z}/a)^{-1}ds \qquad (5.90)$$

$$EI_{zy} = \int_C (a_{22}\overline{zy} + b_{22}(\bar{z}\sin\alpha - \bar{y}\cos\alpha) - d_{22}\sin\alpha\cos\alpha)(1 - \bar{z}/a)^{-1}ds \quad (5.91)$$

$$EI_{\omega y} = \int_C (a_{22}\overline{z\overline{\omega}} + b_{22}(\bar{z}\tilde{\omega} - \overline{\omega}\cos\alpha) - d_{22}\tilde{\omega}\cos\alpha)(1 - \bar{z}/a)^{-1}ds \qquad (5.91)$$

$$EH_c = 2(1 - z_p/a)^2 \int_C (b_{26}\overline{z} - d_{26}\cos\alpha)(1 - \overline{z}/a)^{-2} ds \tag{5.93}$$

$$EI_{zz} = \int_C (a_{22}\overline{y}^2 + 2b_{22}\overline{y}\sin\alpha + d_{22}\sin^2\alpha)(1 - \overline{z}/a)^{-1} ds \tag{5.94}$$

$$EI_{\omega z} = \int_C (a_{22}\overline{y\omega} + b_{22}(\overline{y}\tilde{\omega} + \overline{\omega}\sin\alpha) + d_{22}\tilde{\omega}\sin\alpha)(1 - \overline{z}/a)^{-1} ds \tag{5.95}$$

$$EH_s = 2(1 - z_p/a)^2 \int_C (b_{26}\overline{y} + d_{26}\sin\alpha)(1 - \overline{z}/a)^{-2} ds \tag{5.96}$$

$$EI_{\omega\omega} = \int_C (a_{22}\overline{\omega}^2 + 2b_{22}\overline{\omega}\tilde{\omega} + d_{22}\tilde{\omega}^2)(1 - \overline{z}/a)^{-1} ds \tag{5.97}$$

$$EH_q = 2(1 - z_p/a)^2 \int_C (b_{26}\overline{\omega} + d_{26}\tilde{\omega})(1 - \overline{z}/a)^{-2} ds \tag{5.98}$$

$$GJ = 4(1 - z_p/a)^4 \int_C d_{66}(1 - \bar{z}/a)^{-3} ds \qquad (5.99)$$

In the contour integrals of Eqs. (5.85-5.99), which define the curved beam stiffnesses, coefficients in the integrals appear that are based on integrated stiffness properties through the shell wall thickness. The formulas for these integrated stiffness properties are

$$(a_{22}, b_{22}, d_{22}) = \int_h (1, \zeta, \zeta^2) R_{22}(1 + \zeta/R_s)(1 + \zeta/R_\theta)^{-1} d\zeta \qquad (5.100)$$

$$(a_{26}, b_{26}, d_{26}) = \int_h (1, \zeta, \zeta^2) R_{26}(1 + \zeta/R_s)(1 + \zeta/R_\theta)^{-1} d\zeta \qquad (5.101)$$

$$d_{66} = \int_h R_{66}\zeta^2(1 + \zeta/R_s)(1 + \zeta/R_\theta)^{-1} d\zeta \qquad (5.102)$$

Within the cross section, the positions of the modulus-weighted centroid, shear center, and contour origin (position where $s=0$), are determined by requiring selected stiffness terms in Eqs. (5.84) to vanish. Requiring the modulus weighted first moments ES_y and ES_z to vanish locates the z and y positions, respectively, of the centroid. The y and z positions of the shear center are determined by setting the modulus-weighted first sectorial moments $EI_{\omega y}$ and $EI_{\omega z}$, respectively, to zero. The condition that the modulus-weighted sectorial area ES_{ω} vanishes determines the position of the contour origin. Finally, the direction of the principal axes is determined from the condition that the modulus weighted product moment EI_{zy} equals zero. Thus, Hooke's law for a curved beam using principal coordinates of the cross section simplifies to

$$\begin{bmatrix} EA & 0 & 0 & 0 & EH \\ & EI_{yy} & 0 & 0 & -EH_c \\ & & EI_{zz} & 0 & -EH_s \\ & & & EI_{\omega\omega} & -EH_q \\ \text{Symm} & & & & GJ \end{bmatrix} \tag{5.103}$$

The stiffness matrix in Eqn. (5.103) is not diagonal because of the presence of the "EH" terms. If the laminated wall construction is specially orthotropic, then the terms $EH = EH_c = EH_s = EH_q = 0$, and the stiffness matrix is diagonal. For a specially orthotropic laminate, the lamina fiber angles $(\bar{\theta})$ are either zero or ninety degrees so $S'_{26} = 0$ in the second of Eqs. (5.80), and $R_{26} = 0$ in Eqs. (5.83). For $R_{26} = 0$, Eqn. (5.101) shows that shell stiffnesses $a_{26} = b_{26} = d_{26} = 0$, and consequently EH, EH_c, EH_s, and EH_q all vanish.

For a symmetric laminated wall construction, shell stiffness b_{22} in Eqn. (5.100) and b_{26} in Eqn. (5.101) are zero. This simplifies the computation of the beam stiffnesses in Eqs. (5.85-5.99). The term EH in Eqn. (5.89) is zero if b_{26} is zero, but terms EH_c, EH_s, and EH_q are not zero because d_{26} is not zero. The shell stiffness term d_{26} reflects bend-twist coupling of symmetric laminates containing off-axis plies. For straight beams with symmetric laminated walls, Bauld and Tzeng (Ref. 27) have derived similar terms to the EH terms presented here. These authors point out that Vlasov's assumption that $\gamma_{\theta s} = 0$ on the reference surface is only applicable to symmetric laminated wall construction. For thin curved beams, the largest cross-sectional dimension is less than one-tenth the radius a. It is permissible, then, to neglect $\bar{z}(s)/a$ and z_p/a with respect to unity in all the formulas presented for the curved beam. For thin walls h/R_s and h/R_θ are also small with respect to unity, and are neglected in the shell wall stiffness formulas of Eqs. (5.100-5.102). Consequently, for thin curved beams with thin wall cross sections, the formulas for the beam stiffnesses, Eqn. (5.85-5.99), reduce to those of a straight beam theory.

If the thin-walled curved beam is made of an isotropic and homogeneous material, then the reduced stiffnesses are $R_{22} = E$, $R_{26} = 0$, and $R_{66} = G$. Using principal coordinates in the cross section, and assuming a thin curved beam with thin walls made from an isotropic and homogeneous material, Hooke's law is

$$\begin{aligned} N &= EAe \\ M_y &= EI_{yy}\kappa_y \\ M_z &= EI_{zz}\kappa_z \\ M_\omega &= EI_{\omega\omega}\tau'/a \\ T_s &= GJ\tau \end{aligned} \tag{5.104}$$

In Eqs. (5.104), E is Young's modulus, G is the shear modulus, A is the area of the cross section, I_{yy} is the second area moment about the y-axis, I_{zz} is the second area moment about the z-axis, $I_{\omega\omega}$ is the second sectorial moment (or the warping coefficient), and J is the effective polar moment for Saint Venant's torque T_s . These geometric properties of the cross section are given by the formulas

$$
\begin{aligned}
A &= \int_C h\,ds \\
I_{yy} &= \int_C [h\bar{z}^2 + (h^3/12)\cos^2\alpha]ds \\
I_{zz} &= \int_C [h\bar{y}^2 + (h^3/12)\sin^2\alpha]ds \\
I_{\omega\omega} &= \int_C [h\bar{\omega}^2 + (h^3/12)\tilde{\omega}^2]ds \\
J &= \frac{1}{3}\int_C h^3 ds
\end{aligned}
\qquad (5.105)
$$

In some thin wall beam theories the terms with h^3 in Eqs. (5.105) are neglected except in the equation for J.

Continuum Solutions

This section describes the development of continuum solutions for the in-plane static and vibrational response for a thin curved beam with homogeneous, isotropic, thin-walled, construction. For the special case of a symmetric cross section, the equations decouple allowing individual solutions for the in-plane and out-of-plane responses. An out-of-plane vibration solution is also presented.

In-Plane Vibration Solution

The equations of motion as stated in Eqs. (5.71)-(5.77) are extensively coupled by the inertia terms. A continuum solution for the coupled equations would be very difficult. For our special case, the differential equations of motion which govern the the in-plane response (5.71, 5.73, and 5.75) reduce to

$$\delta U: \qquad -m_{11}\ddot{U} + N'/a - Q_z/a = 0 \tag{5.106}$$

$$\delta W: \qquad -m_{33}\ddot{W} + N/a + Q'_z/a = 0 \tag{5.107}$$

$$\delta \phi_y: \qquad -m_{55}\ddot{\phi}_y + M'_y/a - Q_z = 0 \tag{5.108}$$

in which $m_{11} = m_{33} = \rho A = \overline{m}$, and $m_{55} = \rho I_{yy}$. Solving Eqn. (5.108) for Q_z and substituting into Eqs. (5.106) and (5.107) yields

$$-\overline{m}\ddot{U} + N'/a = -\rho I_{yy}\ddot{\phi}_y/a + M'_y/a^2 \tag{5.109}$$

$$-\overline{m}\ddot{W} + N/a = \rho I_{yy}\ddot{\phi}_y/a^2 - M''_y/a^2 \tag{5.110}$$

Using the expressions for ϕ_y in Eqn. (5.17), M_y and N in Eqs. (5.104), e in Eqn. (5.45), κ_y in Eqn. (5.47) and substituting into Eqs. (5.109) and (5.110) yields

$$\frac{EA}{a^2}(U'' - W') + \frac{EI_{yy}}{a^4}(W''' + U'') = \overline{m}\ddot{U} + \frac{\rho I_{yy}}{a^2}(\ddot{W}' + \ddot{U}) \tag{5.111}$$

$$\frac{EA}{a^2}(U' - W) - \frac{EI_{yy}}{a^4}(W'''' + U''') = \overline{m}\ddot{W} - \frac{\rho I_{yy}}{a^2}(\ddot{W}'' + \ddot{U}') \tag{5.112}$$

A separable solution is assumed of the form

$$\begin{Bmatrix} U(\theta,t) \\ W(\theta,t) \end{Bmatrix} = \begin{Bmatrix} A \\ B \end{Bmatrix} e^{\eta\theta} e^{i\lambda t} \qquad (5.113)$$

in which $i = \sqrt{-1}$, λ is the frequency in radians per second, and η is an unknown parameter. To determine η, first substitute Eqn. (5.113) into Eqs. (5.111) and (5.112) to get

$$\begin{bmatrix} \overline{C}_1 & \overline{C}_2 \\ \overline{C}_2 & \overline{C}_4 \end{bmatrix} \begin{Bmatrix} A \\ B \end{Bmatrix} = \begin{Bmatrix} 0 \\ 0 \end{Bmatrix} \qquad (5.114)$$

where

$$\begin{aligned} \overline{C}_1 &= \eta^2\Big[\frac{EA}{a^2} + \frac{EI_{zz}}{a^4}\Big] + \lambda^2\Big[\overline{m} + \frac{m_{55}}{a^2}\Big] \\ \overline{C}_2 &= \eta\Big[\eta^2\frac{EI_{zz}}{a^4} - \frac{EA}{a^2} + \lambda^2\frac{m_{55}}{a^2}\Big] \\ \overline{C}_4 &= \eta^4\frac{EI_{zz}}{a^4} + \frac{EA}{a^2} - \lambda^2\Big[\overline{m} - \eta^2\frac{m_{55}}{a^2}\Big] \end{aligned} \qquad (5.115)$$

Second, a nontrivial solution for A and B in Eqs. (5.114) requires that the determinant of the coefficient matrix vanishes, and this leads to a cubic equation (characteristic equation) in η^2. The six roots of η are denoted η_j ,j = 1,2, ... 6, and may occur as complex conjugate pairs. For each root η_j , Eqs. (5.114) also yield the eigenvector components

$$P_j = (B/A)_j \qquad , \ \eta = \eta_j \qquad (5.116)$$

Thus, the general solution to Eqs. (5.111) and (5.112) is

$$\begin{Bmatrix} U(\theta,t) \\ W(\theta,t) \end{Bmatrix} = e^{i\lambda t} \sum_{j=1}^{6} C_j \begin{Bmatrix} 1 \\ P_j \end{Bmatrix} e^{\eta_j \theta} \tag{5.117}$$

where C_j are the unknown constants. The constants C_j are determined from the boundary conditions. For example, clamped end conditions, see Eqs. (5.78), require U, W, and ϕ_y to vanish at $\theta = \theta_1$ and $\theta = \theta_2$. This leads to the six homogeneous equations

$$\begin{aligned} U(\theta_1) &= \sum_{j=1}^{6} C_j \; e^{\eta_j \theta_1} = 0 \\ U(\theta_2) &= \sum_{j=1}^{6} C_j \; e^{\eta_j \theta_2} = 0 \\ W(\theta_1) &= \sum_{j=1}^{6} C_j \; P_j \; e^{\eta_j \theta_1} = 0 \\ W(\theta_2) &= \sum_{j=1}^{6} C_j \; P_j \; e^{\eta_j \theta_2} = 0 \\ W'(\theta_1) &= \sum_{j=1}^{6} C_j \; P_j \eta_j \; e^{\eta_j \theta_1} = 0 \\ W'(\theta_2) &= \sum_{j=1}^{6} C_j \; P_j \eta_j \; e^{\eta_j \theta_2} = 0 \end{aligned} \tag{5.118}$$

These are written in matrix form as

$$\underline{A}\, \underset{\sim}{C} = 0 \tag{5.119}$$

in which $\underline{A}$ is a 6 x 6 matrix and $\underset{\sim}{C}^T = [C_j]$. Nontrivial solutions to Eqn. (5.119) require the determinant of $\underline{A}$ to vanish. Since the six roots of η are functions of λ , and η appears as an exponent in the coefficients of matrix A, this is a nonlinear eigenproblem for the eigenfrequency λ . The solution proceeds by a determinant plotting method, in which λ is assumed, the six roots of η_j are computed along with the six values of P_j , and the determinant of $\underline{A}$ in Eqn. (5.119) is calculated. Increasing values of λ are selected until a sign change in the determinant occurs, and Newton's method is used to converge on the frequency. For a given frequency, the eigenvectors $\underset{\sim}{C}$ of Eqn. (5.119) are obtained to give the mode shape. Although the determinant plotting technique is a not very good numerical method for large matrices, it works well enough for the matrices encountered in this problem.

The boundary conditions for the free-free case are

$$\begin{aligned} N(\theta_1) &= N(\theta_2) = 0 \\ M_y(\theta_1) &= M_y(\theta_2) = 0 \\ Q_z(\theta_1) &= Q_z(\theta_2) = 0 \end{aligned} \tag{5.120}$$

The equations for pinned boundary conditions are

$$\begin{aligned} U(\theta_1) &= U(\theta_2) = 0 \\ W(\theta_1) &= W(\theta_2) = 0 \\ M_y(\theta_1) &= M_y(\theta_2) = 0 \end{aligned} \tag{5.121}$$

The equations for pinned boundary conditions with torsional springs are

$$\begin{aligned} U(\theta_1) &= U(\theta_2) = 0 \\ W(\theta_1) &= W(\theta_2) = 0 \\ M_y(\theta_1) &= \alpha_T W'(\theta_1) \\ M_y(\theta_2) &= \alpha_T W'(\theta_1) \end{aligned} \tag{5.122}$$

Where α_T is the torsional spring constant.

In-Plane Static Solution

For a thin curved beam with isotropic, homogeneous, thin-walled construction and a monosymmetric cross section, the equilibrium equations describing the in-plane static response can be obtained from the equations of motion (5.106-5.108) by discarding the inertia terms. The resulting equations are

$$\delta U: \qquad N'/a - Q_z/a = 0 \tag{5.123}$$

$$\delta W: \qquad N/a + Q'_z/a = 0 \tag{5.124}$$

$$\delta \phi_y: \qquad M'_y/a - Q_z = 0 \tag{5.125}$$

Eliminating Q_z in Eqs. (5.123) and (5.124) using (5.125) yields

$$N'/a - M'_y/a^2 = 0 \tag{5.126}$$

$$N/a + M''_y/a^2 = 0 \tag{5.127}$$

Substituting the relations for N and M_y from Hooke's law in Eqn. (5.104), Eqs. (5.126) and (5.127) become

$$\frac{EA}{a^2}(U'' - W') + \frac{EI_{yy}}{a^4}(W''' + U'') = 0 \tag{5.128}$$

$$\frac{EA}{a^2}(U' - W) - \frac{EI_{yy}}{a^4}(W'''' + U''') = 0 \tag{5.129}$$

where A and I_{yy} are defined in Eqn. (5.105). Dividing Eqs. (5.128) and (5.129) by EA/a^2 results in

$$U'' - W' + \hat{r}^2(W''' + U'') = 0 \tag{5.130}$$

$$U' - W - \hat{r}^2(W'''' + U''') = 0 \tag{5.131}$$

in which $\hat{r}^2 = I_{yy}/(Aa^2)$ is the square of the slenderness ratio.

Assume the in-plane displacements can be represented by

$$\begin{Bmatrix} U \\ W \end{Bmatrix} = \begin{Bmatrix} A \\ B \end{Bmatrix} e^{\eta\theta} \tag{5.132}$$

Substituting Eqs. (5.132) into the differential Eqs. (5.130) and (5.131) leads to the following characteristic equation for η

$$\hat{r}^2\eta^2(\eta^2 + 1)^2 = 0 \tag{5.133}$$

The roots of this characteristic equation are 0, 0 , +i, +i, -i, -i, in which $i = \sqrt{-1}$. Thus, there are three repeated roots for η, and the procedure presented by Kaplan (Ref. 32) was used to construct six linearly independent solutions to Eqs. (5.130) and (5.131). The solution is

$$\begin{aligned} \begin{Bmatrix} U \\ W \end{Bmatrix} &= C_1\begin{Bmatrix} 1 \\ 0 \end{Bmatrix} + C_2\begin{Bmatrix} \theta \\ 1 \end{Bmatrix} + C_3\begin{Bmatrix} \cos\theta \\ -\sin\theta \end{Bmatrix} + C_4\begin{Bmatrix} \sin\theta \\ \cos\theta \end{Bmatrix} \\ &\quad + C_5\begin{Bmatrix} \theta\cos\theta \\ -\theta\sin\theta + \tilde{r}\cos\theta \end{Bmatrix} + C_6\begin{Bmatrix} \theta\sin\theta \\ \theta\cos\theta - \tilde{r}\sin\theta \end{Bmatrix} \end{aligned} \tag{5.137}$$

where $\tilde{r}$ is defined as $[1 - \hat{r}^2]/[1 + \hat{r}^2]$.

The solution in Eqn. (5.137) satisfies the differential equilibrium equations exactly and can be used to model the static response of a thin curved beam subjected to combined in-plane loading. A curved beam subjected to a radial load f_r, a tangential load f_θ, and an in-plane couple whose moment is $\underset{\sim}{m}_y$ at a location defined by $\theta = \theta^*$ is shown in Fig. 41. The curved beam is supported at $\theta = (\theta_1, \theta_2)$ and $\theta_1 < \theta^* < \theta_2$.

This loading requires that two solutions be implemented over the beam, one for the left portion $(\theta_1 < \theta < \theta^*)$ of the curved beam and one for the right portion $(\theta^* < \theta < \theta_2)$. Thus, the solution for the left-hand-side is

$$\begin{Bmatrix} U_L \\ W_L \end{Bmatrix} = \sum_{j=1}^{6} C_j \underset{\sim}{\delta}_j(\theta) \qquad \theta_1 < \theta < \theta^* \tag{5.138}$$

and for the right-hand-side

$$\begin{Bmatrix} U_R \\ W_R \end{Bmatrix} = \sum_{j=1}^{6} C_{j+6} \underset{\sim}{\delta}_j(\theta) \qquad \theta^* < \theta < \theta_2 \tag{5.139}$$

where $\underset{\sim}{\delta}_j(\theta)$ are the six linearly independent solutions from Eqn. (5.137).

The problem requires twelve equations to solve for the twelve unknown constants C_j. Six of the equations can be obtained from transition conditions at θ^*. Continuity of the beam at θ^* requires that the displacements and rotation at θ^* are continuous requiring

$$\begin{aligned} U(\theta^*_-) &= U(\theta^*_+) \\ W(\theta^*_-) &= W(\theta^*_+) \\ W'(\theta^*_-) &= W'(\theta^*_+) \end{aligned} \tag{5.140}$$

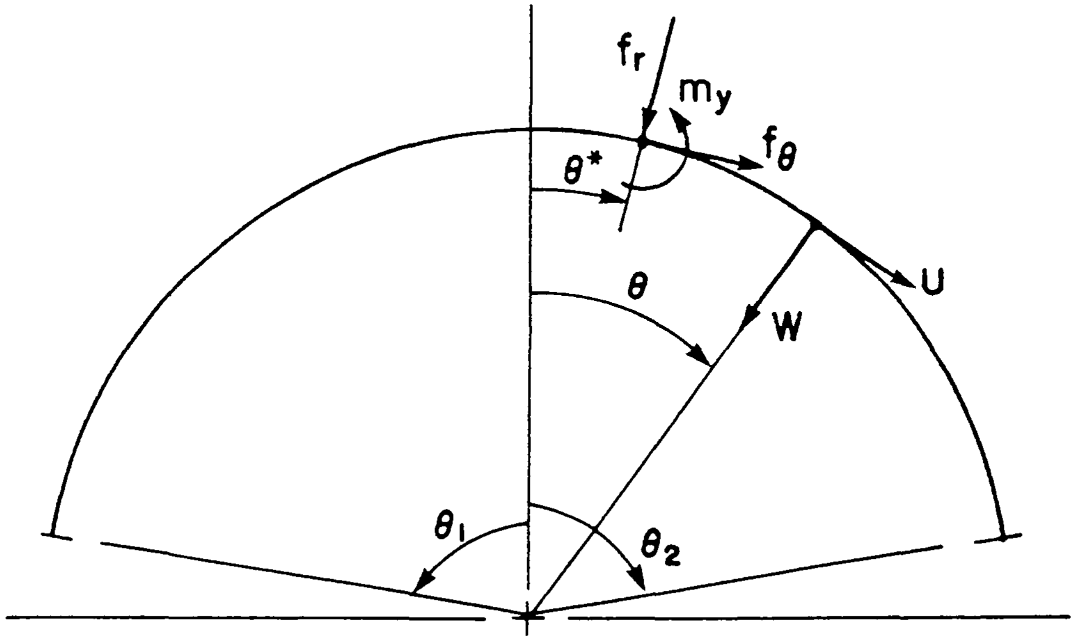
f_r
m_y
f_θ
θ^*
θ
U
W
θ_1
θ_2

Figure 41. Loading for in-plane static solution: A curved beam is subjected to radial, tangential, and bending loads at $\theta = \theta^*$. The curved beam is supported at the ends ($\theta = \theta_1$ and $\theta = \theta_2$).

in which a quantity with a "+" superscript is evaluated from the right interval and a "-" superscript implies the quantity is evaluated from the left interval.

Equilibrium of a infinitesimal element at $\theta = \theta^*$ provides three jump conditions in the actions given by

$$\begin{aligned} N(\theta^*_+) - N(\theta^*_-) &= -f_\theta \\ M(\theta^*_+) - M(\theta^*_-) &= -m_y \\ Q_{z\theta^*_+} - Q_z(\theta^*_-) &= f_r \end{aligned} \tag{5.141}$$

The remaining six equations can be obtained from the boundary conditions at $\theta = \theta_1$ and $\theta = \theta_2$. The boundary conditions for clamped, pinned, free, and pinned with a torsional spring are provided in Eqs. (5.118) and (5.120-5.122), respectively. Thus, using three boundary conditions at $\theta = \theta_1$, three continuity conditions of Eqs. (5.140), the three jump conditions of Eqs. (5.141), and three boundary conditions at $\theta = \theta_2$, a set of linear equations can be written in the form

$$\underset{\sim}{A}\,\underset{\sim}{C} = \underset{\sim}{F} \tag{5.142}$$

where $\underset{\sim}{A}$ is a 12 x 12 matrix of coefficients, $\underset{\sim}{C}$ is a 12 x 1 vector containing the unknown constants, and $\underset{\sim}{F}$ is a 12 x 1 load vector. The solution vector $\underset{\sim}{C}$ was determined by Gaussian elimination.

Having found the solution vector, the displacements of the beam are given by Eqs. (5.137-5.139). Differentiating and substituting into Eqs. (5.45) and (5.47) gives the extensional strain and the change in curvature, respectively. Substituting the strains into Eqn. (5.104) provides the beam actions N and M_y.

Out-of-Plane Vibration Solution

The differential equations of motion which govern the out-of-plane vibrational response of a thin curved beam with thin, isotropic, homogeneous, walls can be obtained from Eqs. (5.72), (5.74), and (5.76) and (5.77). For the special case of a symmetric cross section using principal centroidal axes, these equations reduce to

$$\delta V: \qquad -m_{22}\ddot{V} - m_{24}\ddot{\phi}_x + Q'_y/a = 0 \tag{5.143}$$

$$\delta \phi_x: \qquad -m_{24}\ddot{V} - m_{44}\ddot{\phi}_x - M_z/a + T'/a = 0 \tag{5.144}$$

$$\delta \phi_z: \qquad -m_{66}\ddot{\phi}_z + M'_z/a + Q_y + T/a = 0 \tag{5.145}$$

$$\delta \tau: \qquad -m_{77}\ddot{\tau} + M'_{\omega}/a - T_s + T = 0 \tag{5.146}$$

Having assumed the cross-sectional coordinates are the principal centroidal axes, $m_{24} = m_{11}z_p = \overline{m}z_p$, $m_{44} = \rho[(I_{yy} + I_{zz}) + Az_p^2]$, $m_{66} = \rho I_{zz}$, and $m_{77} = \rho I_{\omega\omega}$ where A, I_{yy}, I_{zz}, $I_{\omega\omega}$ are defined in Eqs. (5.105). If the cross section is doubly symmetric, the centroid coincides with the shear center and z_p is zero. Solving Eqs. (5.145) and (5.146) for the shear force Q_y and the torque T, respectively, and substituting into Eqs. (5.143) and (5.144) yields

$$-\frac{T'_s}{a^2} + \frac{M''_{\omega\omega}}{a^3} - \frac{M''_z}{a^2} = \frac{\rho I_{\omega\omega}}{a^2}\ddot{\tau}' - \frac{\rho I_{zz}}{a}\ddot{\phi}'_z + \overline{m}\ddot{V} + \overline{m}z_p\ddot{\phi}_x \tag{5.147}$$

$$\frac{T'_s}{a} - \frac{M''_{\omega\omega}}{a^2} - \frac{M_z}{a} = \frac{-\rho I_{\omega\omega}}{a}\ddot{\tau}' + m_{44}\ddot{\phi}_x + \overline{m}z_p\ddot{V} \tag{5.148}$$

Using Hooke's law Eqn. (5.104) and substituting for ϕ_z, τ, and κ_z using Eqs. (5.18), (5.19), and (5.46), respectively, Eqs. (5.147) and (5.148) become

$$\begin{aligned}\bar{m}\ddot{V} + \bar{m}z_p\ddot{\phi}_x - \frac{\rho I_{zz}}{a^2}\ddot{V}'' + \frac{\rho I_{\omega\omega}}{a^3}(\ddot{\phi}_x'' - \frac{\ddot{V}''}{a}) + \frac{GJ}{a^3}(\phi_x'' - \frac{V''}{a})& \\ + \frac{EI_{zz}}{a^3}(\phi_x'' + \frac{V''''}{a}) - \frac{EI_{\omega\omega}}{a^5}(\phi_x'''' - \frac{V''''}{a}) = 0&\end{aligned} \tag{5.149}$$

$$\begin{aligned}\bar{m}z_p\ddot{V} + m_{44}\ddot{\phi}_x - \frac{\rho I_{\omega\omega}}{a^2}(\ddot{\phi}_x'' - \frac{\ddot{V}''}{a}) - \frac{GJ}{a^2}(\phi_x'' - \frac{V''}{a})& \\ + \frac{EI_{zz}}{a^2}(\phi_x + \frac{V''}{a}) + \frac{EI_{\omega\omega}}{a^4}(\phi_x'''' - \frac{V''''}{a}) = 0&\end{aligned} \tag{5.150}$$

A separable solution is assumed of the form

$$\begin{Bmatrix} V(\theta, t) \\ \phi_x(\theta, t) \end{Bmatrix} = \begin{Bmatrix} A \\ B \end{Bmatrix} e^{\eta\theta}\, e^{i\lambda t} \tag{5.151}$$

in which $i = \sqrt{-1}$, λ is the natural frequency in radians per second, and η is an unknown parameter. To determine η, first substitute Eqs. (5.151) into Eqs. (5.149) and (5.150) to get

$$\begin{bmatrix} \bar{C}_1 & \bar{C}_2 \\ \bar{C}_2 & \bar{C}_4 \end{bmatrix} \begin{Bmatrix} A \\ B \end{Bmatrix} = \begin{Bmatrix} 0 \\ 0 \end{Bmatrix} \tag{5.152}$$

where

$$\bar{C}_1 = \eta^4[\frac{EI_{zz}}{a^4} + \frac{EI_{\omega\omega}}{a^6}] - \eta^2\frac{GJ}{a^4} + \lambda^2[-\bar{m} + \eta^2(\frac{\rho I_{zz}}{a^2} + \frac{\rho I_{\omega\omega}}{a^4})]$$

$$\bar{C}_2 = -\eta^4\frac{EI_{\omega\omega}}{a^5} + \eta^2[\frac{GJ}{a^3} + \frac{EI_{zz}}{a^3}] + \lambda^2[-\bar{m}z_p - \frac{\rho I_{\omega\omega}}{a^3}\eta^2] \tag{5.153}$$

$$\overline{C}_4 = \eta^4 \frac{EI_{\omega\omega}}{a^4} - \eta^2 \frac{GJ}{a^2} + \frac{EI_{zz}}{a^2} + \lambda^2[-m_{44} + \frac{\rho I_{\omega\omega}}{a^2}\eta^2]$$

A nontrivial solution for A and B in Eqs. (5.152) requires that the determinant of the coefficient matrix vanishes, and this leads to a quartic equation (characteristic equation) in η^2. The eight roots of η are denoted η_j , $j = 1,2, \ldots 8$, and may occur in complex conjugate pairs. For each root η_j, Eqs (5.152) also yield the eigenvector components

$$P_j = (B/A)_j \qquad , \eta = \eta_j \tag{5.154}$$

Thus, the general solution to Eqs. (5.149) and (5.150) is

$$\begin{Bmatrix} V(\theta, t) \\ \phi_x(\theta, t) \end{Bmatrix} = e^{i\lambda t} \sum_{j=1}^{8} C_j \begin{Bmatrix} 1 \\ P_j \end{Bmatrix} e^{\eta_j \theta} \tag{5.155}$$

where C_j, $j = 1,2, \ldots 8$, are unknown constants. The constants C_j are determined from the boundary conditions. For example, clamped end conditions, see Eqs. (5.78), require V, ϕ_x, V', and ϕ'_x to vanish at $\theta = \theta_1$ and $\theta = \theta_2$. This leads to the eight homogeneous equations

$$
\begin{aligned}
V(\theta_1) &= \sum_{j=1}^{8} C_j \, e^{\eta_j \theta_1} = 0 \\
V(\theta_2) &= \sum_{j=1}^{8} C_j \, e^{\eta_j \theta_2} = 0 \\
\phi_x(\theta_1) &= \sum_{j=1}^{8} C_j \, P_j \, e^{\eta_j \theta_1} = 0 \\
\phi_x(\theta_2) &= \sum_{j=1}^{8} C_j \, P_j \, e^{\eta_j \theta_2} = 0 \\
V'(\theta_1) &= \sum_{j=1}^{8} C_j \, \eta_j \, e^{\eta_j \theta_1} = 0 \\
V'(\theta_2) &= \sum_{j=1}^{8} C_j \, \eta_j \, e^{\eta_j \theta_2} = 0 \\
\phi'_x(\theta_1) &= \sum_{j=1}^{8} C_j \, P_j \eta_j \, e^{\eta_j \theta_1} = 0 \\
\phi'_x(\theta_2) &= \sum_{j=1}^{8} C_j \, P_j \eta_j \, e^{\eta_j \theta_2} = 0
\end{aligned}
\tag{5.156}
$$

These are written in matrix form as

$$\underline{A}\underset{\sim}{C} = 0 \tag{5.157}$$

in which $\underline{A}$ is an 8x8 matrix and $\underset{\sim}{C}^T = [C_j]$. Nontrivial solutions to Eqs. (5.152) require the determinant of $\underline{A}$ to vanish. Since the roots of η are functions of λ , and η appears as an exponent in the coefficients of matrix A, this is a nonlinear eigenproblem for the eigenfrequency λ. The solution proceeds by a determinant plotting method, in which λ is assumed, the eight roots η_j are computed along with the eight values of P_j, and the determinant of $\underline{A}$ in Eqn. (5.152) is calculated. Increasing values of λ are selected until a sign change in the determinant occurs, and Newton's method is used to converge on the frequency. For a given frequency, the eigenvectors $\underset{\sim}{C}$ of Eqn. (5.155) are obtained to give the mode shape.

The boundary conditions for the free-free case are

$$\begin{aligned} Q_y(\theta_1) &= Q_y(\theta_2) = 0 \\ T(\theta_1) &= T(\theta_2) = 0 \\ M_z(\theta_1) &= M_z(\theta_2) = 0 \end{aligned} \tag{5.158}$$

The equations for pinned boundary conditions are

$$\begin{aligned} V(\theta_1) &= V(\theta_2) = 0 \\ \phi_x(\theta_1) &= \phi_x(\theta_2) = 0 \\ M_z(\theta_1) &= M_z(\theta_2) = 0 \\ M_\omega(\theta_1) &= M_\omega(\theta_2) = 0 \end{aligned} \tag{5.159}$$

Finite Element Computer Program

The finite element computer program used extensively in this study was developed by Noor et al., (Ref. 7) specifically for the free-vibrational analysis of curved thin-walled beams with open sections. The analytical formulation is based on a Vlasov-type, thin-walled, curved beam theory similar to the theory discussed in this chapter. This section briefly discusses the analytical development of the finite element relying heavily on the equations presented previously to point out some interesting differences. Some practical aspects of using the program will also be related.

$$
\begin{aligned}
V(\theta_1) &= \sum_{j=1}^{8} C_j \; e^{\eta_j \theta_1} = 0 \\
V(\theta_2) &= \sum_{j=1}^{8} C_j \; e^{\eta_j \theta_2} = 0 \\
\phi_x(\theta_1) &= \sum_{j=1}^{8} C_j \; P_j \; e^{\eta_j \theta_1} = 0 \\
\phi_x(\theta_2) &= \sum_{j=1}^{8} C_j \; P_j \; e^{\eta_j \theta_2} = 0 \\
V'(\theta_1) &= \sum_{j=1}^{8} C_j \; \eta_j \; e^{\eta_j \theta_1} = 0 \\
V'(\theta_2) &= \sum_{j=1}^{8} C_j \; \eta_j \; e^{\eta_j \theta_2} = 0 \\
\phi'_x(\theta_1) &= \sum_{j=1}^{8} C_j \; P_j \eta_j \; e^{\eta_j \theta_1} = 0 \\
\phi'_x(\theta_2) &= \sum_{j=1}^{8} C_j \; P_j \eta_j \; e^{\eta_j \theta_2} = 0
\end{aligned}
\tag{5.156}
$$

These are written in matrix form as

$$\underline{A}\underset{\sim}{C} = 0 \tag{5.157}$$

in which $\underline{A}$ is an 8x8 matrix and $\underset{\sim}{C}^T = [C_j]$. Nontrivial solutions to Eqs. (5.152) require the determinant of $\underline{A}$ to vanish. Since the roots of η are functions of λ , and η appears as an exponent in the coefficients of matrix A, this is a nonlinear eigenproblem for the eigenfrequency λ. The solution proceeds by a determinant plotting method, in which λ is assumed, the eight roots η_i are computed along with the eight values of P_j, and the determinant of $\underline{A}$ in Eqn. (5.152) is calculated. Increasing values of λ are selected until a sign change in the determinant occurs, and Newton's method is used to converge on the frequency. For a given frequency, the eigenvectors $\underset{\sim}{C}$ of Eqn. (5.155) are obtained to give the mode shape.

The boundary conditions for the free-free case are

$$
\begin{aligned}
Q_y(\theta_1) &= Q_y(\theta_2) = 0 \\
T(\theta_1) &= T(\theta_2) = 0 \\
M_z(\theta_1) &= M_z(\theta_2) = 0
\end{aligned}
\tag{5.158}
$$

The equations for pinned boundary conditions are

$$
\begin{aligned}
V(\theta_1) &= V(\theta_2) = 0 \\
\phi_x(\theta_1) &= \phi_x(\theta_2) = 0 \\
M_z(\theta_1) &= M_z(\theta_2) = 0 \\
M_\omega(\theta_1) &= M_\omega(\theta_2) = 0
\end{aligned}
\tag{5.159}
$$

Finite Element Computer Program

The finite element computer program used extensively in this study was developed by Noor et al., (Ref. 7) specifically for the free-vibrational analysis of curved thin-walled beams with open sections. The analytical formulation is based on a Vlasov-type, thin-walled, curved beam theory similar to the theory discussed in this chapter. This section briefly discusses the analytical development of the finite element relying heavily on the equations presented previously to point out some interesting differences. Some practical aspects of using the program will also be related.

Element Formulation

The finite element developed by Noor et al., includes the effects of transverse shear deformation which were not included by Vlasov nor in the development presented in this chapter. A modified form of the Hellinger-Reissner mixed variational principle was used to develop the element. Including transverse shear deformation adds an additional two degrees of freedom, and reduces the continuity requirements from C^1 to C^0 for the transverse displacements V and W.

The Hooke's law relation used in the element development is

$$\begin{bmatrix} N_x \\ M_z \\ M_y \\ M_\omega \\ Q_y \\ Q_z \\ T_s \end{bmatrix} = \begin{bmatrix} EA & 0 & 0 & -ES_\omega & 0 & 0 & 0 \\ & EI_{zz} & -EI_{zy} & EI_{\omega z} & 0 & 0 & 0 \\ & & EI_{yy} & -EI_{\omega y} & 0 & 0 & 0 \\ & & & EI_{\omega\omega} & 0 & 0 & 0 \\ & & & & GA_y & 0 & 0 \\ & & & & & GA_z & 0 \\ \text{SYMM} & & & & & & GJ \end{bmatrix} \begin{bmatrix} e \\ \kappa_z \\ \kappa_y \\ \Psi \\ \gamma^0_{\theta y} \\ \gamma^0_{\theta z} \\ \tau \end{bmatrix} \qquad (5.160)$$

in which the additional curved beam strain measures relative to those presented earlier are

$$\begin{aligned} \Psi' &= \phi''_x/a^2 \\ \gamma^0_{\theta y} &= V'/a - \phi_z \\ \gamma^0_{\theta z} &= (W' + U)/a + \phi_y \end{aligned} \qquad (5.161)$$

The notation used by Noor has been transliterated into the notation used in this study. The finite element code was developed for isotropic homogeneous materials, thus, the

"EH" stiffness terms characteristic of composite materials do not appear. A consequence of this is that the finite element model cannot model the bend-twist coupling of laminated specimens.

The coordinate system used in calculating the section properties places the origin and the pole at the centroid; thus, only the first moments of area S_y and S_z are zero. A diagonal stiffness matrix offers few advantages in a numerical solution. The section area properties A_y and A_z provide the opportunity to model the shear stiffness employing shear correction factors to the shear stiffness GA.

The torsional strain component τ in Eqn. (5.160) is consistent with the torsional strain used in the Hooke's law relation in Eqn. (5.104). However, the warping strain component Ψ' in the first of Eqs. (5.161) is not the same as the strain measure τ'/a used for the bimoment in the Hooke's law of Eqs. (5.104).

To achieve C^0 continuity for the rotation ϕ_x a new kinematic variable θ^0 is introduced that is defined to be the derivative of rotation ϕ_x. This kinematic relation is enforced via a Lagrange multiplier $\overline{\Lambda}$. Thus, both θ^0 and ϕ_x are represented by C^0 interpolation functions in the element.

The functional used in the element development is

$$\Pi = \Pi_{HR} + \int_C \overline{\Lambda}(\phi'_x - \theta^0)a\,d\theta - \frac{1}{2\varepsilon_p}\int_C (\overline{\Lambda})^2 a\,d\theta \qquad (5.162)$$

where Π_{HR} is the Hellinger-Reissner functional, $\overline{\Lambda}$ is the Lagrange multiplier associated with the constraint condition, and ε_p is the penalty parameter in the regularization term.

The finite element equations for each element can be cast in the following compact form

$$\begin{bmatrix} -F & 0 & S \\ 0 & \frac{P}{\varepsilon_p} & Q^t \\ S^t & Q & 0 \end{bmatrix} \begin{Bmatrix} H \\ \lambda \\ X \end{Bmatrix} = \Omega^2 \begin{bmatrix} 0 & 0 & 0 \\ 0 & 0 & 0 \\ 0 & 0 & M \end{bmatrix} \begin{Bmatrix} H \\ \lambda \\ X \end{Bmatrix} \tag{5.163}$$

where $\{H\}$, $\{\lambda\}$, and $\{X\}$ are the internal force parameters, Lagrange multiplier parameters, and nodal displacements, respectively; $[F]$ is the flexibility matrix, $[S]$ is the strain-displacement matrix. Finally, $[P]$ and $[Q]$ are matrices associated with the constraint condition and the regularization term in the augmented functional.

The regularization term in Eqn. (5.162) results in replacing one of the zero diagonal submatrices in the discrete equations (Eqn. 5.163) of the Lagrange multiplier approach with a nonzero diagonal matrix, $[P]/\varepsilon_p$. Mathematically, the submatrix cannot be zero but physically it should be. The penalty parameter is used to keep the regularization term small. Thus, an important consideration in this formulation is the proper selection of the penalty parameter. The accuracy of the solution increases with increasing values of ε_p . However, for very large values, the equations become ill-conditioned, thereby increasing the round-off errors.

Application to Test Specimens

Noor's finite element program was developed for vibrational analysis, but it can be used to predict the static response as well, thus, it was used to model both the static and the vibrational tests. In the static mode, loads are applied to the model at the nodes and the program predicts the deformations and strains caused by the applied loads. When the program is run in the dynamic mode, it calculates the ten lowest natural frequencies (eigenvalues) and their associated mode shapes (eigenvectors). In addition, the program calculates the strain energy distribution in each mode. The strain energies due to axial strain, shear strain, in-plane bending, out-of-plane bending, torsion, and warping are calculated for each mode.

The strain energy distributions for the modes of the I-section and channel section specimens are presented in Fig. 42. The extensional, shear, and warping energies are uniformly small in all modes. The strain energies in the I-specimen modes are either pure in-plane bending or a combination of torsional and out-of-plane bending energies. Thus, the modes of the I-specimen were easily identified as in-plane or out-of-plane modes on the basis of strain energy distribution.

The strain energy distributions associated with the modes of the channel specimen always exhibit some degree of coupling between the in-plane and out-of-plane responses. The channel specimen's even numbered modes are dominated by in-plane bending energy and the remaining modes are dominated by torsional and out-of-plane bending energies. In general, if the energy in a mode consists of more than 85 % in-plane bending, than that mode is considered an in-plane mode. If out-of-plane bending and torsional energies comprise more than 85 % of the total energy, than that mode is considered an out-of-plane mode. All of the modes of the channel specimen fit one definition or the other, thus, the modes are easily classified based on their energy distribution.

With any finite element code, it is necessary to determine the number of elements required for convergence. Convergence studies for static and dynamic cases were conducted for both test specimens. The results of the dynamic convergence study are presented in Fig. 43. The natural frequencies converged for a sixteen element model. The sixteen element model was selected for both the static and dynamic analysis of both specimens from this convergence study. The elements have three nodes each providing thirty-three nodes and 231 degrees of freedom (7 degrees of freedom per node).

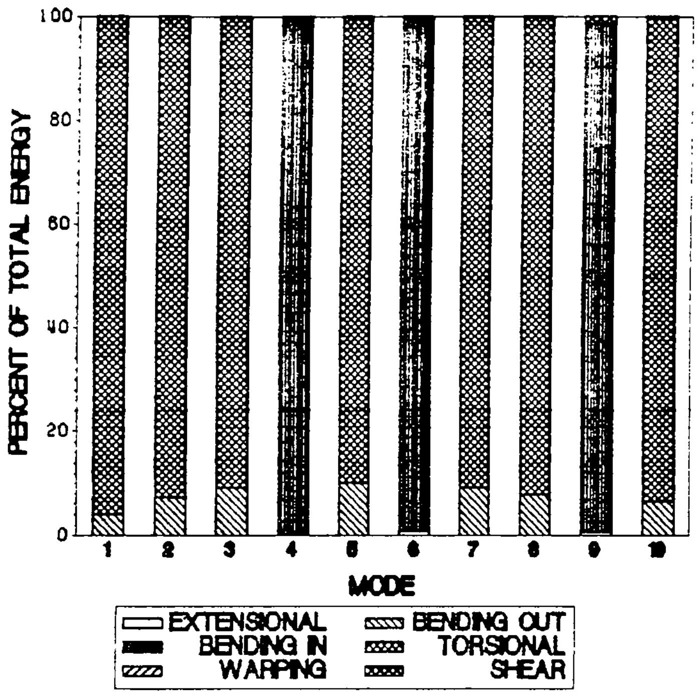

(A) I-SPECIMEN

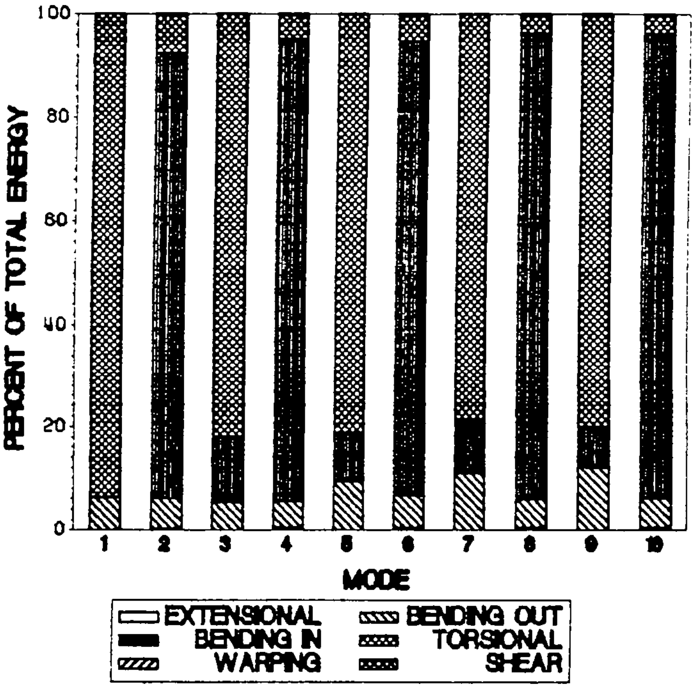

(B) CHANNEL SPECIMEN

Figure 42. Strain energy distributions in vibrational modes for both specimens: The strain energy distributions in the vibrational modes of both specimens are presented. Modes are arranged in order of increasing frequency.

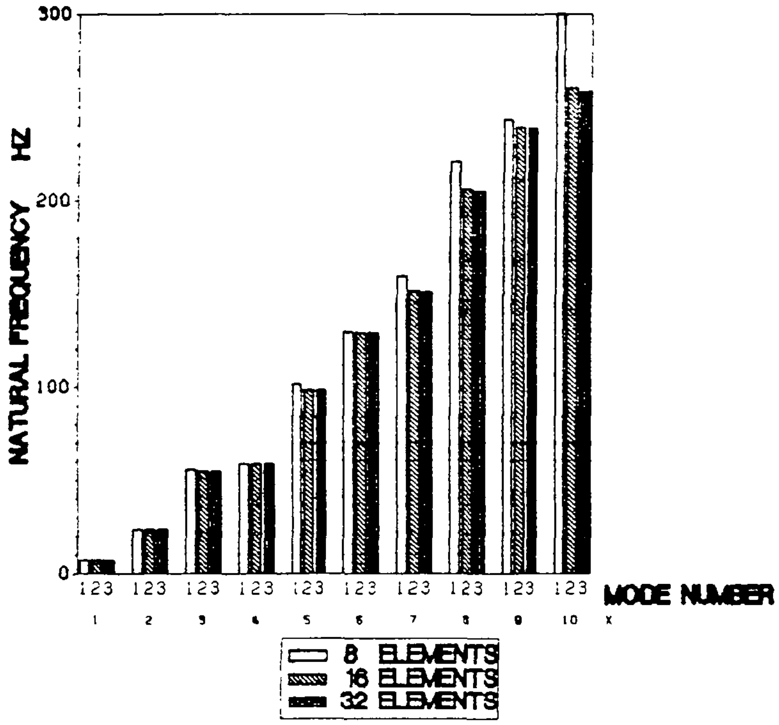

(A) I-SPECIMEN

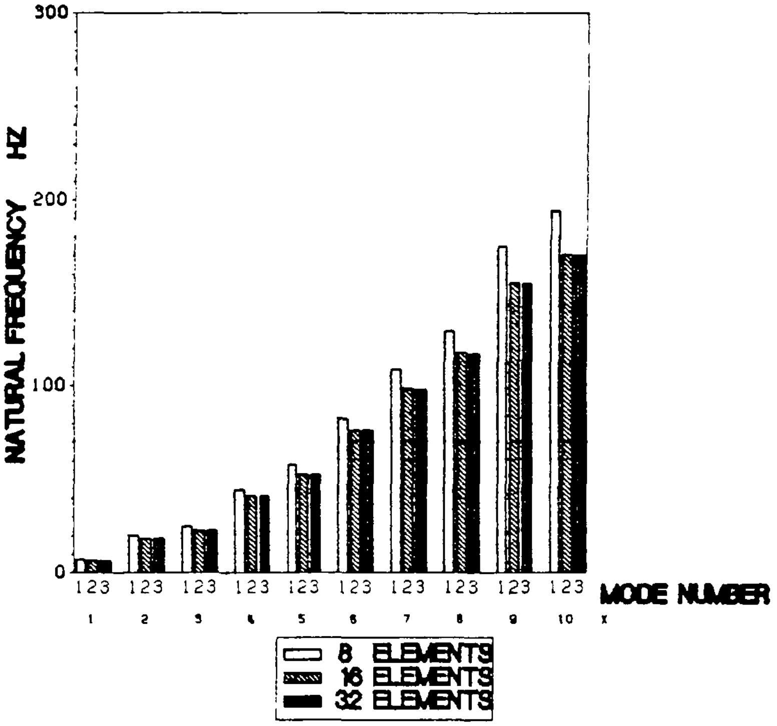

(B) CHANNEL SPECIMEN

Figure 43. **Number of elements convergence study:** The figure shows the convergence of the natural frequencies of both specimens for the 8, 16, and 32 element models. Modes are in order of increasing frequency. Natural frequencies are in hertz.

An important consideration in using the finite element program is the proper selection of the penalty parameter. The penalty parameter was chosen based on a convergence study conducted for static and dynamic cases for both specimens. The penalty parameter convergence studies were run for the sixteen element models. The convergence studies for the dynamic case for both specimens are presented in Fig. 44. The plots show that above a certain value of the penalty parameter the natural frequencies are constant. The smallest value of the penalty parameter for which all the predictions changed by less than 1 % was the value used in the subsequent analyses.

The plots show the affect of the penalty parameter on the natural frequencies of the second, third, and fourth out-of-plane mode and the first in-plane mode for both specimens. The I-specimen plot is smooth and continuous while the plot for the channel specimen is discontinuous. This is because the penalty parameter had no affect on the energy distributions in the I-specimen modes. Thus, the character of the mode was constant and only the natural frequency varied. Further, the penalty parameter only affected the out-of-plane modes of the I-specimen. Neither of these statements are true for the channel specimen.

The energy distributions in the channel modes varied extensively with the penalty parameter. A mode which was initially dominated by in-plane energy might eventually evolve into an out-of-plane mode, and an out-of-plane mode might gain in-plane energy until it had to be considered an in-plane mode. Thus, the penalty parameter affected both in-plane and out-of-plane modes. For penalty parameters in excess of 1×10^9, both the natural frequencies and energy distributions of both specimens had converged. The static and dynamic response of both specimens converged at the same value of the penalty parameter, thus, 1×10^9 was used as the value for the penalty parameter in subsequent analyses.

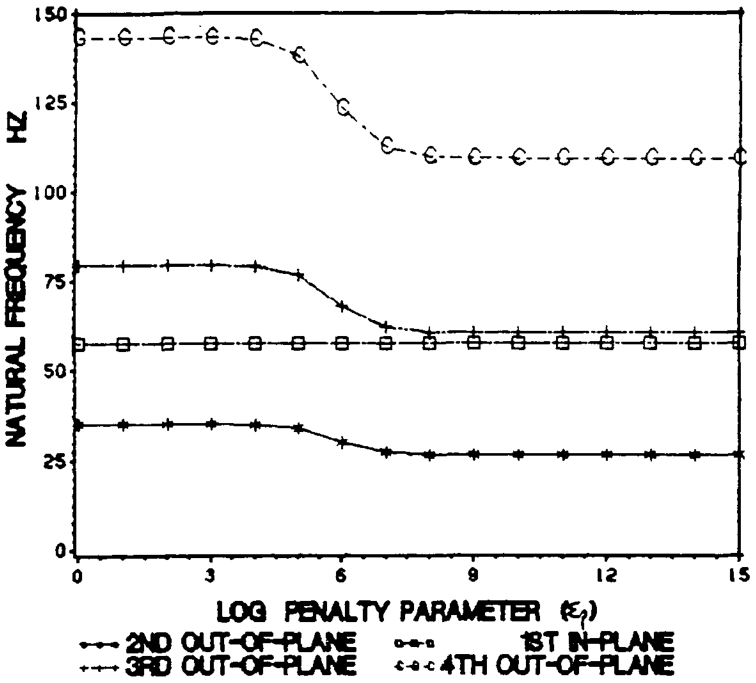

(A) I-SPECIMEN

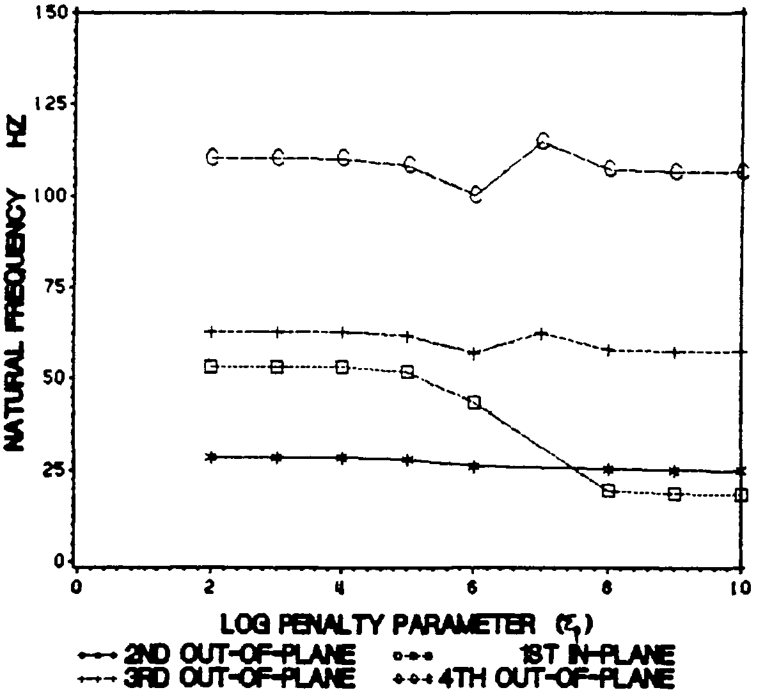

(B) CHANNEL SPECIMEN

Figure 44. Penalty parameter convergence study: The plots show the effects of the penalty parameter on the natural frequencies of the second, third, and fourth out-of-plane modes and the first in-plane mode for both specimens. The log of the penalty parameter is plotted on the horizontal axis.

The section properties used in Hooke's law in Eqn. (5.160) were also used in the mass matrix. These section properties were evaluated using a computer program presented by Coyette (Ref. 33). This program calculates the section properties for a thin-walled open cross section assuming the branches of the cross section are straight and are made of an isotropic homogeneous material. This program was subsequently modified to evaluate the modulus-weighted section properties in Eqs. (5.85-5.99) assuming the layup in the branches is symmetric. The modulus-weighted section properties were used in the static analysis. Since the finite element program uses the input section properties in both the stiffness and the mass matrices, the modulus-weighted section properties could not be used in the vibrational analysis. A listing of the section properties of both specimens is presented in Appendix C.

Chapter 6

Correlation of Numerical and Experimental Results

The numerical results from the finite element solution and the continuum solutions are presented with the corresponding experimental data for the I-specimen and channel specimen. In the first section, natural frequencies and mode shapes from the analyses are compared with the experimental data from the free-free and the clamped-clamped frame tests. In the second section, the predicted flexibility influence coefficients are compared with coefficients calculated from the static test data. The comparisons of primary interest involve the predictions from the finite element solution and the experimental data.

Correlation of Dynamic Data

The finite element program was used to predict the three-dimensional vibrational response of both specimens for clamped and pinned boundary conditions. The in-plane continuum vibrational solution was used to model the free-free frame tests of the I-specimen. The finite element program could not model the free-free frame tests because of the presence of the rigid body modes. The continuum solution also provided the versatility to model the end conditions as torsional springs providing valuable insight into the physical problem. The correlation of the free-free vibrational data is presented first followed by the correlation of the clamped-clamped vibrational data.

Free-Free Data

The numerical and experimental results for the in-plane, free-free natural frequencies of the I-specimen are presented in Table 9. The maximum error occurs in the first two modes where the errors are -3.5 and -8.2 % respectively. The discrepancies of the analysis with respect to the experiment in the first two modes are attributed to the stiffening influence of the elastic bands used to suspend the specimen. The elastic bands act like compliant springs and in the lower modes the energy in the elastic bands represents a sizable portion of the total energy in the mode. The higher modes have larger frequencies and consequently higher energies, thus, the amount of energy in the elastic bands relative to the specimen is less significant. The analytical predictions and experimental results for the four, five, and six node modes correlate quite well.

Table 9. Correlation of the free-free in-plane natural frequencies of the I-specimen

No. of Nodes	Experiment Hz	Analysis [a] Hz	Error[b] %
2	25.8	24.9	-3.5
3	78.3	71.9	-8.2
4	151.0	150.4	-0.4
5	259.0	257.1	-0.7
6	388.0	390.9	0.7

[a] Continuum solution
[b] (Analysis-Exp)/Exp x 100

The predicted four and five noded mode shapes of the I-specimen are shown in Fig. 45. The four and five node modes are presented because they provide an interesting test of the analytical solution. The experimentally located nodes are indicated by dots in the figure, the undeformed frame is represented by the solid line, and the analytical mode shape by the dashed line. The mode shapes were normalized to make the largest displacement 10 % of the radius. Thus, the mode shapes are exaggerated to make them more visible. The analytical mode shapes correlate quite well with the experimental data. The mode shapes for the two and three node modes are presented in Appendix A.

Clamped-Clamped Tests

The finite element program was used to model the clamped-clamped vibrational tests for both specimens. The continuum solution confirmed the predictions of the finite element solution for the in-plane response of the I-specimen. Initially, the analyses were run with clamped-clamped end conditions resulting in predictions which were consistently too high. Modeling the end conditions as hinges with respect to in-plane and out-of-plane rotations resulted in predictions which were generally too low. Thus, predictions using clamped-end and pinned-end conditions bracketed the experimental results indi-

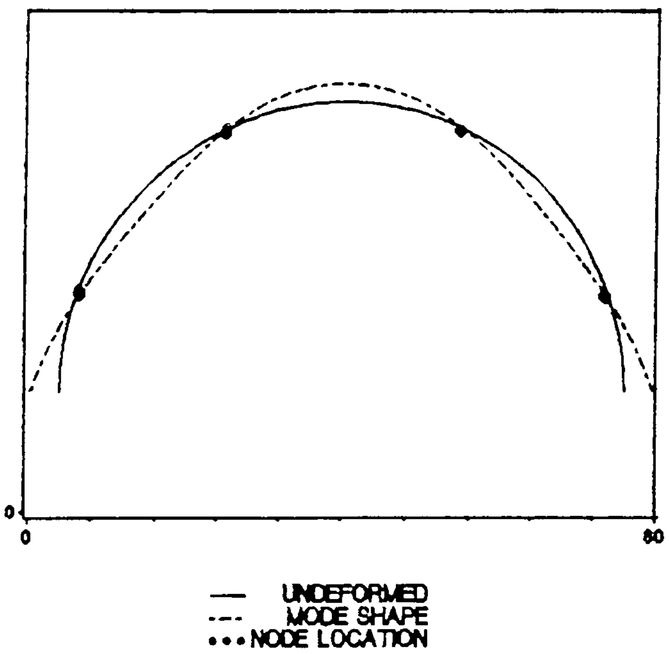

(A) FOUR NODE MODE

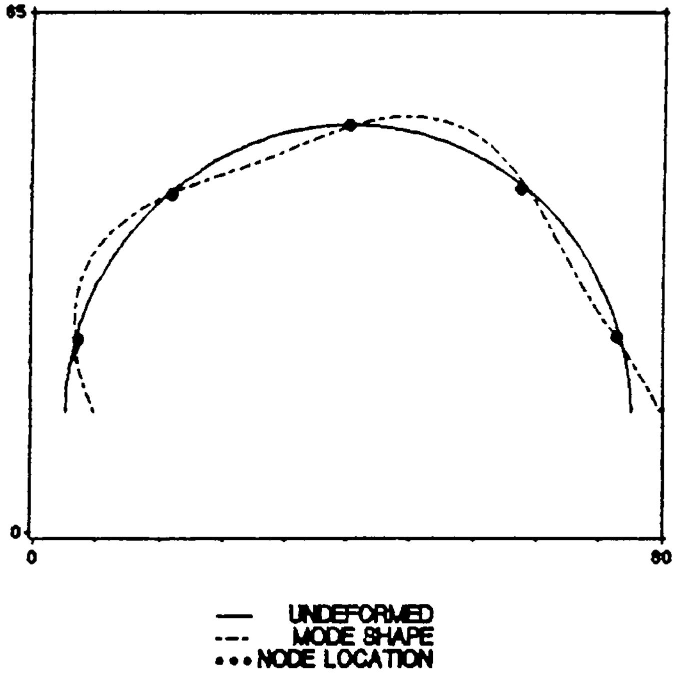

(B) FIVE NODE MODE

Figure 45. Free-free in-plane mode shapes for the I-specimen: The predicted mode shapes for the four and five node modes for the I-specimen are presented with the experimentally located nodes which are indicated by dots. The undeformed frames are represented by the solid lines and the analytically predicted mode shape by the dashed lines.

cating that the experimental boundary conditions acted like torsional springs. In the lower modes, the experimental results correlated well with the clamped-clamped predictions. In the higher modes, the experimental values correlated well with the pinned-pinned predictions. This indicates that as the frequency and energy of the modes increased, the clamping effectiveness of the boundary conditions decreased. In general, the numerical results from the finite element computer program correlated well with the experimental results with the exception of the in-plane modes of the channel specimen. The comparison of the in-plane results will be presented first followed by the out-of-plane results.

The predictions for the in-plane natural frequencies for the I-specimen from the finite element program are presented in Fig. 46. The dashed lines correspond to the analytical predictions obtained using clamped-end and pinned-end conditions. The first two experimental values correlate very well with the clamped-clamped predictions, but the experimental response begins to shift towards the pinned-pinned predictions in subsequent modes. The last in-plane mode (8 nodes) correlates well with the corresponding pinned-pinned prediction. In the higher modes, the relative difference between the frequencies for the pinned-end and clamped-end conditions decreases. For the eight noded in-plane mode, the difference between the frequencies for the clamped-end and pinned-end conditions is just slightly more than 6 %.

The experimental results and analytical predictions from the finite element program and continuum solutions are presented in Table 10. The predictions from the continuum solution essentially duplicate the predictions from the finite element code. The classical solutions from Den Hartog (Ref. 11) for the first in-plane natural frequencies for clamped and pinned boundary conditions are 59.4 and 29.9 hertz, respectively. These values correlate very well with the numerical predictions. The correlation between the

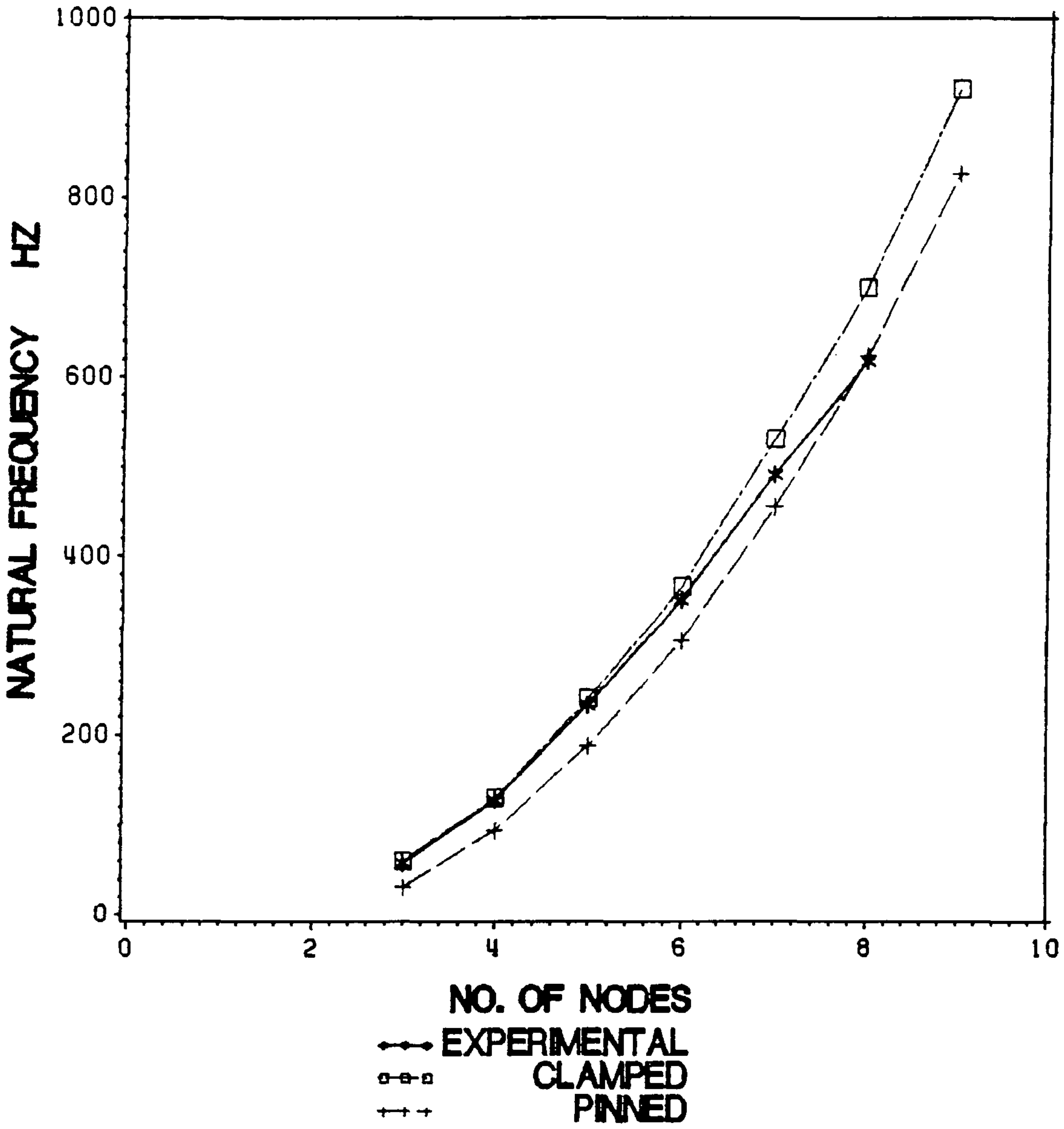

Figure 46. Clamped-clamped in-plane natural frequencies for the I-specimen: The analytical predictions for the clamped-end and pinned-end conditions are represented by the dashed lines and the experimental values are the solid line. The modes are ordered by the number of nodes circumferentially and the frequencies are in hertz.

analytical predictions for clamped-end conditions and the experimental values is good initially, but degrades in the higher modes.

Table 10. Correlation of clamped-clamped in-plane natural frequencies for the I-specimen

No. of	Experiment	Analyses			
		Clamped		Pinned	
		FEM[a]	Cntnm[b]	FEM[a]	Cntnm[b]
Nodes	Hz	Hz	Hz	Hz	Hz
3	57.7	59.0	58.6	30.6	30.3
4	127.2	129.3	128.7	93.2	92.5
5	233.0	239.9	238.9	187.8	186.6
6	350.6	365.8	364.6	305.6	303.7
7	490.0	529.5	527.7	454.0	451.2
8	617.0	699.2	696.8	622.6	618.3

[a] Finite element model from Ref. 7
[b] Continuum solution

The continuum analysis was easily adapted to model the end conditions as torsional springs. Modeling the end conditions as torsional springs provided the opportunity to match the experimental frequency for each mode. The results of this effort are presented in Table 11. The last column is the effective torsional spring stiffness necessary to obtain the analytical natural frequency which essentially matches the experimental value. The results show that the effective stiffness of the end conditions decreases with increasing frequency producing the transition from clamped to pinned boundary conditions.

Table 11. Effects of boundary spring stiffness on the in-plane vibrational response of the I-specimen

	Experiment	Continuum	Error[a]	Boundary Spring Stiffness
No. of Nodes	Hz	Hz	%	α_t in-lb/rad
3	57.5	57.48	-.035	9×10^5
4	127.2	127.32	0.094	9×10^5
5	233.0	233.60	0.258	6×10^5
6	350.6	348.58	-.576	3×10^5
7	490.0	485.38	-.951	1×10^5
8	617.0	618.20	0.200	1×10^3

[a] (Analysis-Exp)/Exp x 100

The curve in Fig. 47 shows the effect of the torsional spring constant on the prediction of the first in-plane natural frequency. The two horizontal lines represent the predictions for clamped-end and pinned-end conditions from the finite element program. The logarithm to the base ten of the spring stiffness is plotted on the horizontal axis. For very compliant and very stiff springs, the predicted natural frequency approaches the predictions for pinned-end and clamped-end conditions, respectively. The plus sign in the figure indicates the experimental value. The in-plane natural frequencies are sensitive to small changes in the torsional spring stiffness.

The experimental and numerical results for the in-plane natural frequencies for the channel specimen are presented in Table 12 and in Fig. 48. The correlation between the finite element predictions and the experimental results is poor. The predictions for the natural frequencies using both clamped-end and pinned-end conditions are much lower than the experimental results. A sensitivity analysis showed that the in-plane natural frequencies are very sensitive to the value of the first sectorial moment $I_{\omega y}$. This term

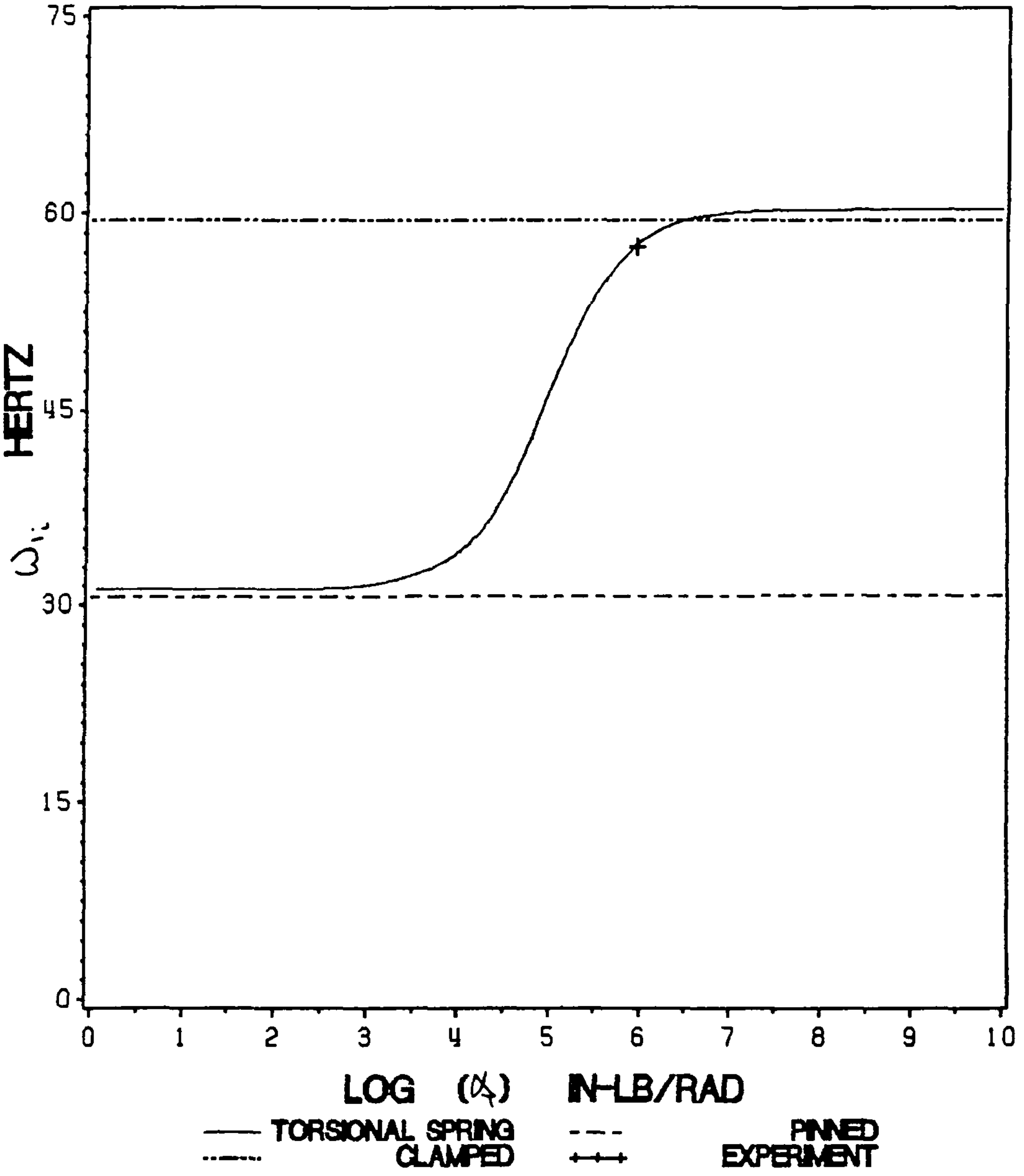

Figure 47. Effects of torsional spring end conditions: The solid line indicates the effect of the torsional spring stiffness on the frequency of the first in-plane mode of the I-specimen. The horizontal lines are the predictions obtained using clamped and pinned boundary conditions. The log of the torsional spring stiffness is plotted on the horizontal axis.

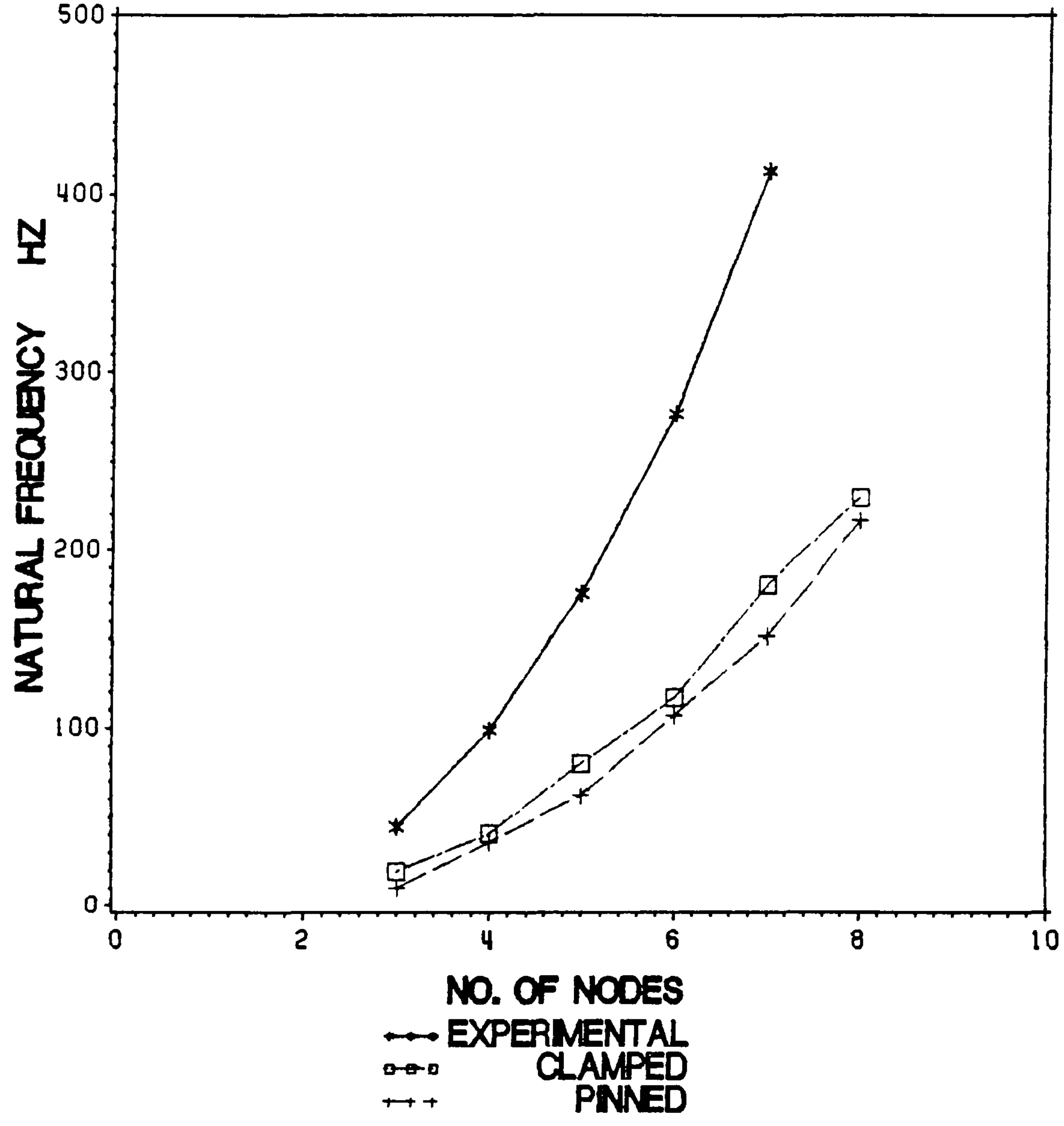

Figure 48. **Clamped-clamped, in-plane natural frequencies for the channel specimen:** The analytical predictions for the clamped-end and pinned-end conditions are represented by the dashed lines and the experimental values are the solid line. The modes are ordered by the number of nodes circumferentially and the frequencies are in hertz.

couples warping and in-plane bending. Other section properties characteristic of an asymmetric cross section did not have a significant effect on the in-plane response.

Table 12. Correlation of clamped-clamped, in-plane natural frequencies for the channel specimen

		FEM[a]	
	Experiment	Clamped	Pinned
No. of Nodes	Hz	Hz	Hz
3	44.6	18.8	10.0
4	99.1	41.5	35.6
5	176.0	76.7	61.9
6	276.7	118.3	107.2
7	413.0	171.3	151.8

[a] Finite element model from Ref. 7

The mode shapes for the five and six noded in-plane modes for both specimens are presented schematically in Figs. 49 and 50. The five and six node modes are used for the comparison because they provide an interesting test of the analysis. The mode shapes are shown in top and front views. In the top view, the reference axis of the undeformed frame is a straight line. The I-specimen mode shapes show pure radial motion while the mode shapes of the channel specimen exhibit both radial and lateral motions. The mode shapes for the I-specimen correlate very well with the experimental results. The mode shapes for the channel specimen agree fairly well despite the poor predictions for the natural frequencies.

The predictions from the finite element computer program for the out-of-plane natural frequencies for the I-specimen are presented with the corresponding experimental results in Fig. 51. The softening response exhibited by the experimental data seems to be attributable to the boundary conditions. The experimental data follows the clamped-

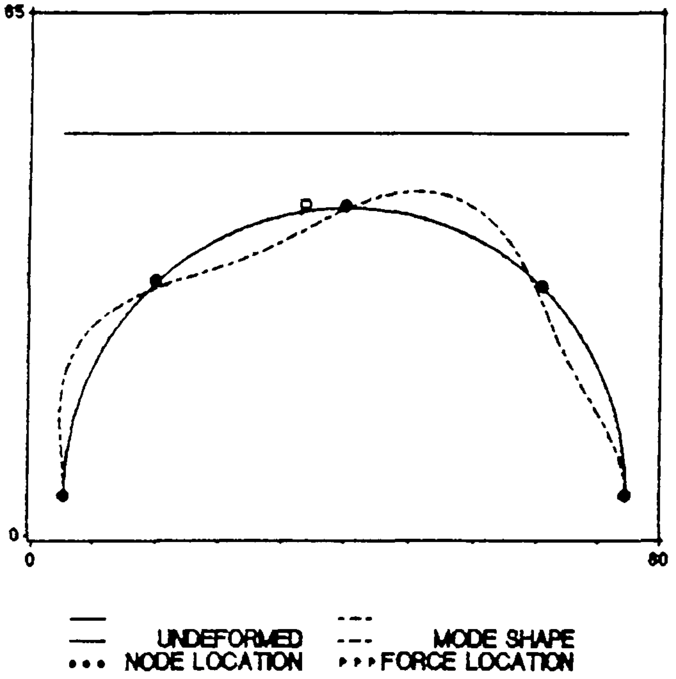

(A) I-SPECIMEN

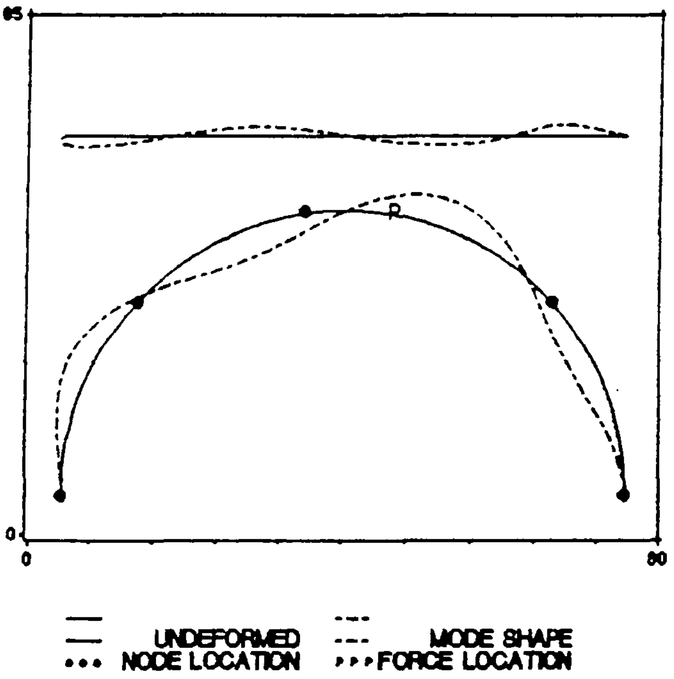

(B) CHANNEL SPECIMEN

Figure 49. Five noded, in-plane, clamped-clamped mode shape for both specimens: The five noded in-plane mode shapes for both sections are shown schematically. The experimentally located nodes are indicated by dots, the undeformed frames are represented by the solid lines and the analytically predicted mode shape by the dashed lines.

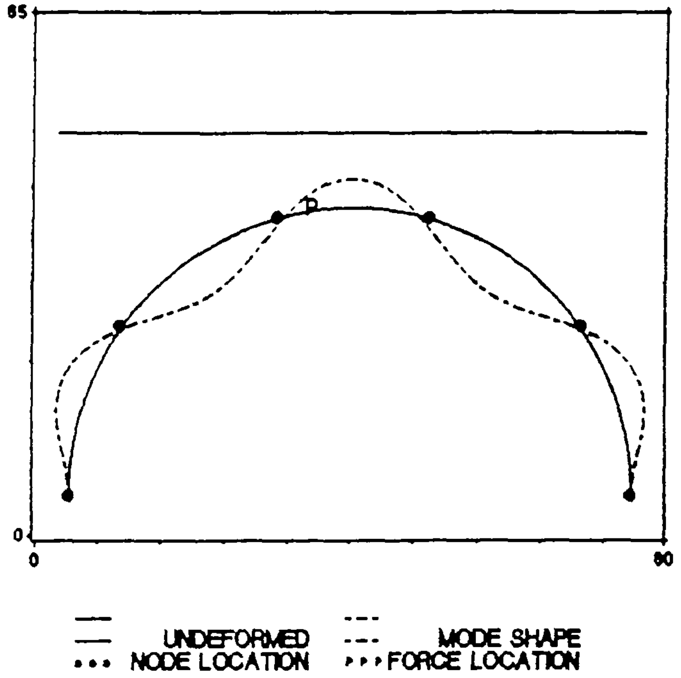

(A) I-SPECIMEN

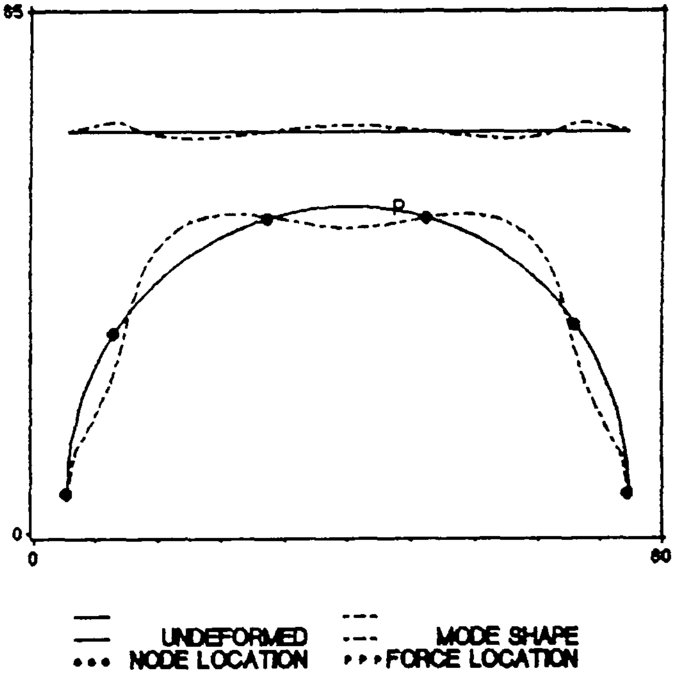

(B) CHANNEL SPECIMEN

Figure 50. Six noded, in-plane, clamped-clamped mode shape for both specimens: The six noded in-plane mode shapes for both specimens are shown schematically. The experimentally located nodes are indicated by dots, the undeformed frames are represented by the solid lines and the analytically predicted mode shape by the dashed lines.

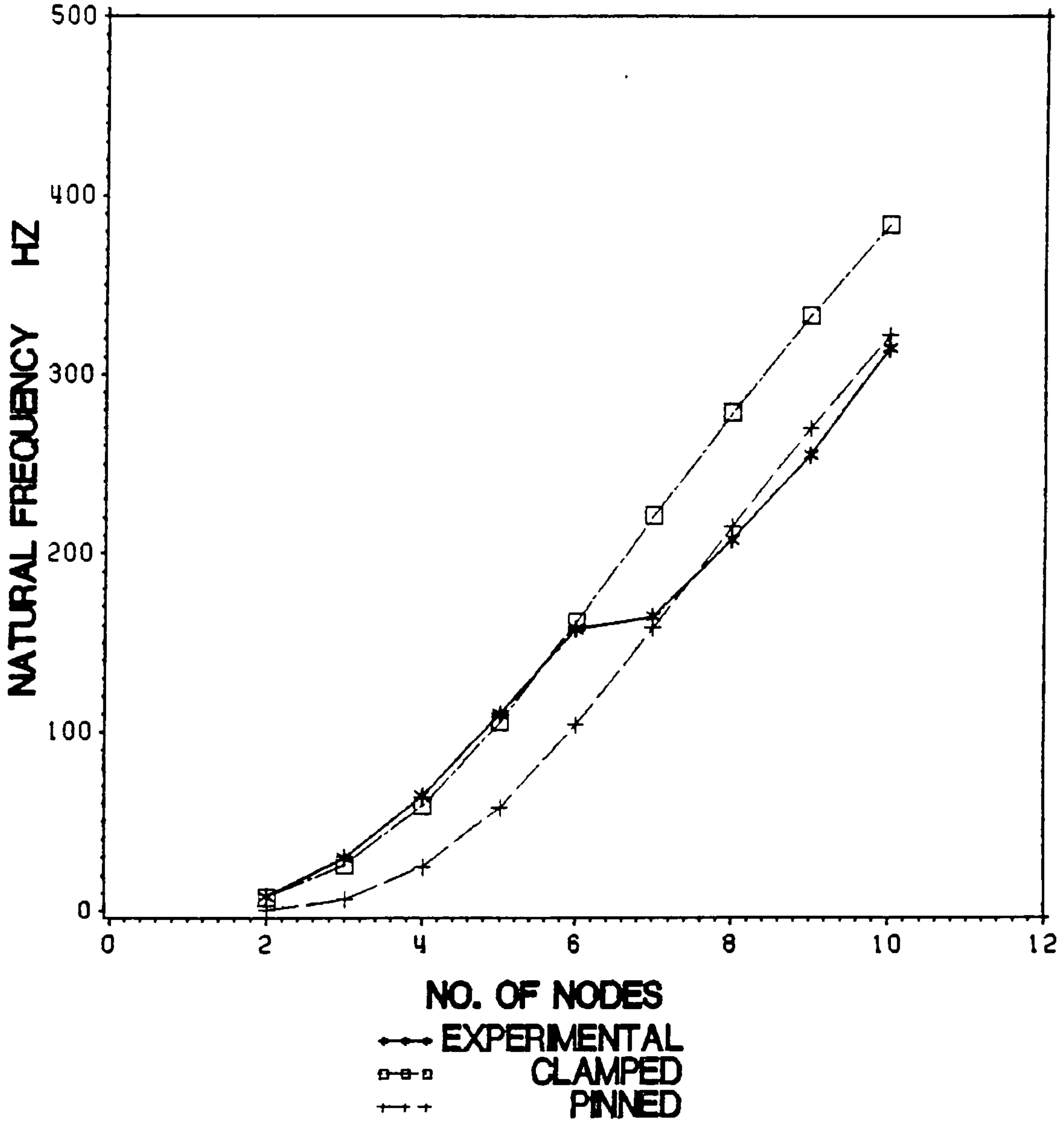

Figure 51. Clamped-clamped out-of-plane natural frequencies for the I-specimen: The analytical predictions for the clamped-end and pinned-end conditions are represented by the dashed lines and the experimental values are the solid line. The modes are ordered by the number of nodes circumferentially and the frequencies are in hertz.

end predictions through the first five modes, then shifts from clamped-end to pinned-end conditions between the fifth and sixth modes. This transition is very abrupt compared to the shift observed in the in-plane response. After the shift, the experimental data follows the pinned-end predictions closely.

A plot of the analytical predictions and the experimental results for the out-of-plane natural frequencies of the channel specimen is presented in Fig. 52. Due to the asymmetric cross section of the channel specimen, predictions for only the first six out-of-plane natural frequencies were obtained. The transition from clamped-end to pinned-end conditions was also observed in the out-of-plane response of the channel specimen. The finite element predictions agree well with the experimental data through the first three modes. The transition from effective clamped-end to effective pinned-end conditions begins in the fourth and fifth modes and is completed between the fifth and sixth modes. It appears that the pinned-end predictions would correlate with the higher experimental natural frequencies if those predictions were available.

The numerical and experimental results for the out-of-plane natural frequencies for both specimens are summarized in Table 13. Though the plots show good correlation in the first few modes, the discrepancy of the predicted frequency with respect to the experimental value for the fundamental mode is actually 8.5 % and 6.7 % for the I-specimen and channel specimen, respectively. The classical solution from Brown (Ref. 12) predicts a frequency of 7.5 Hz for the fundamental frequency of the I-specimen confirming the prediction from the finite element code. The prediction of 15.4 Hz obtained from the out-of-plane continuum solution is almost 100 % too high. The fact that none of the analyses can predict the fundamental frequency is disturbing. Generally, experimental frequencies are lower than those from the analysis. In this case, the exper-

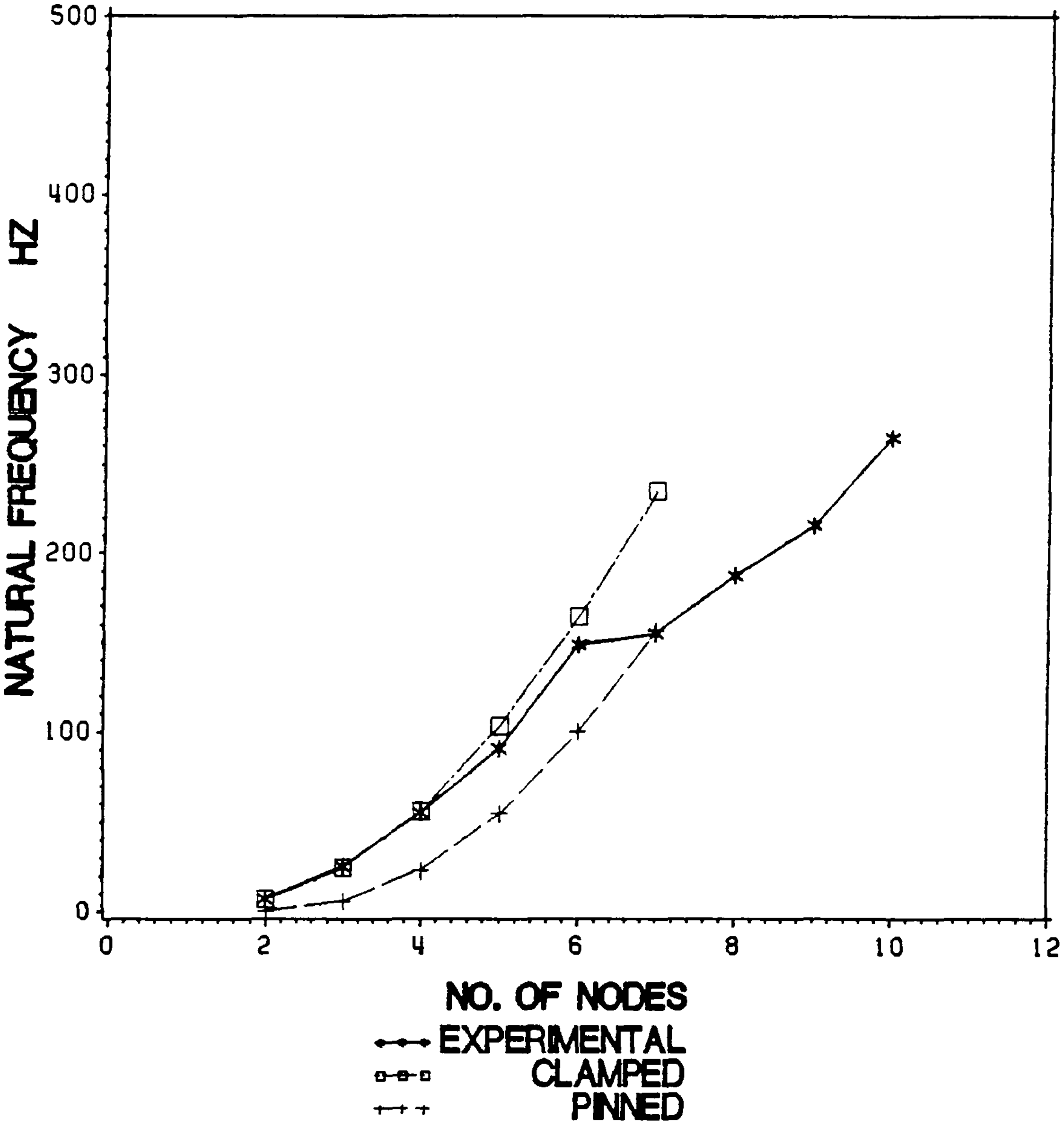

Figure 52. Clamped-clamped out-of-plane natural frequencies for the channel specimen: The analytical predictions for the clamped-end and pinned-end conditions are represented by the dashed lines and the experimental values are the solid line. The modes are ordered by the number of nodes circumferentially and the frequencies are in hertz.

Table 13. Correlation of clamped-clamped, out-of-plane natural frequencies for both specimens

		Experiment	FEM[a] Clamped	FEM[a] Pinned
Specimen	No. of Nodes	Hz	Hz	Hz
I-specimen	2	8.2	7.5	-
	3	29.8	25.4	6.3
	4	64.3	58.4	24.6
	5	110.4	105.4	57.7
	6	157.8	161.7	104.1
	7	164.7	220.7	158.5
	8	207.4	278.2	214.9
	9	254.7	332.0	269.8
	10	314.7	383.8	322.0
Channel	2	7.4	6.9	-
	3	25.4	24.2	5.9
	4	55.4	55.8	23.1
	5	91.1	103.7	54.7
	6	148.8	164.4	100.4
	7	155.2	234.8	156.6
	8	187.0		
	9	214.0		

[a] Finite element model from Ref. 7

imental results are higher than the analysis, which is not usually the case when correlating analysis and experiment. This discrepancy remains unresolved.

The mode shapes for the five and six node out-of-plane modes for both specimens are presented in Figs. 53 and 54, respectively. The mode shapes are shown in both top and front views. The mode shapes for the channel specimen modes show radial displacements as well as out-of-plane displacements. This is typical of the coupled response of the channel specimen. The mode shapes for the I-specimen show pure out-of-plane motion characteristic of an uncoupled response. Good correlation is observed between the predicted mode shapes and the experimentally located nodes for the mode shapes of both specimens. The correlation for the lower modes was generally as good or better. The mode shapes for the other modes are presented in Appendix A.

Correlation of Static Data

To correlate the experimental flexibility coefficients with the analytical values it is necessary to choose the experimental results which are most representative of the small deflection response of the frames. The in-plane test results are considered more reliable than the out-of-plane test results, therefore, the values for flexibility coefficients α_{13}, α_{23}, and α_{33} are taken from the in-plane tests. Specifically, the experimental values associated with the forty pound radial load are used in the correlation of the data for both specimens. The coefficients from the forty pound radial load were chosen because it was the lowest load with the least amount of scatter in the data associated with it. In the cases where the values for positive and negative torques are close, the values are averaged. When the magnitudes are significantly different, the value associated with the

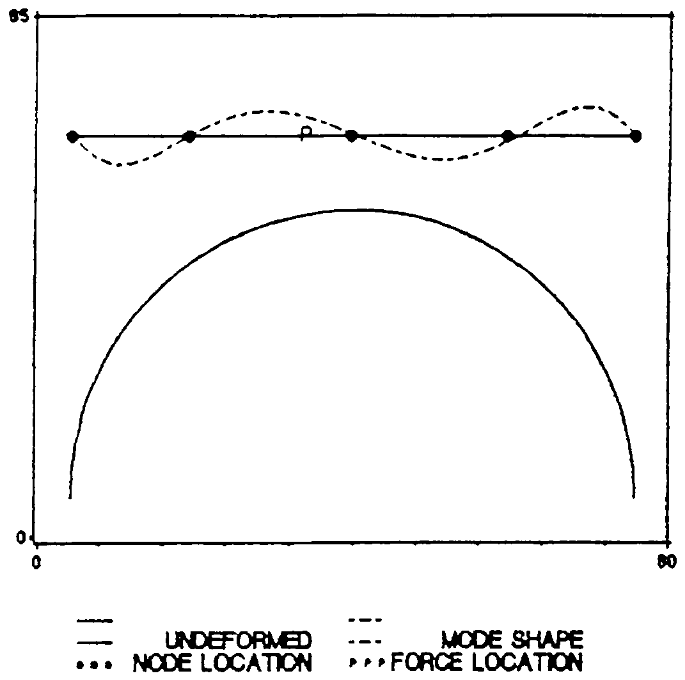
65
0
0
80
P
UNDEFORMED
MODE SHAPE
NODE LOCATION
FORCE LOCATION

(A) I-SPECIMEN

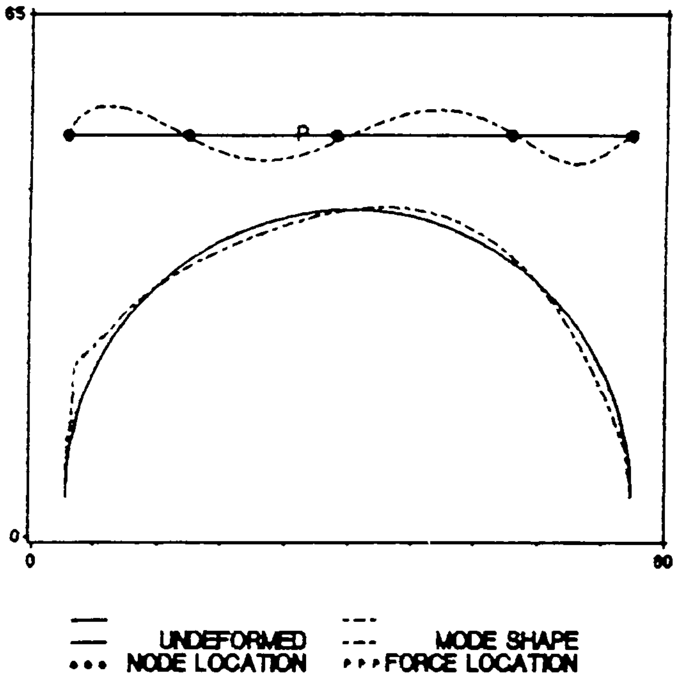
65
0
0
80
P
UNDEFORMED
MODE SHAPE
NODE LOCATION
FORCE LOCATION

(B) CHANNEL SPECIMEN

Figure 53. **Five noded, out-of-plane, clamped-clamped mode shape for both specimens:** The five noded out-of-plane mode shapes of both specimens are presented schematically. The experimentally located nodes are indicated by dots, the undeformed frames are represented by the solid lines and the analytically predicted mode shape by the dashed lines.

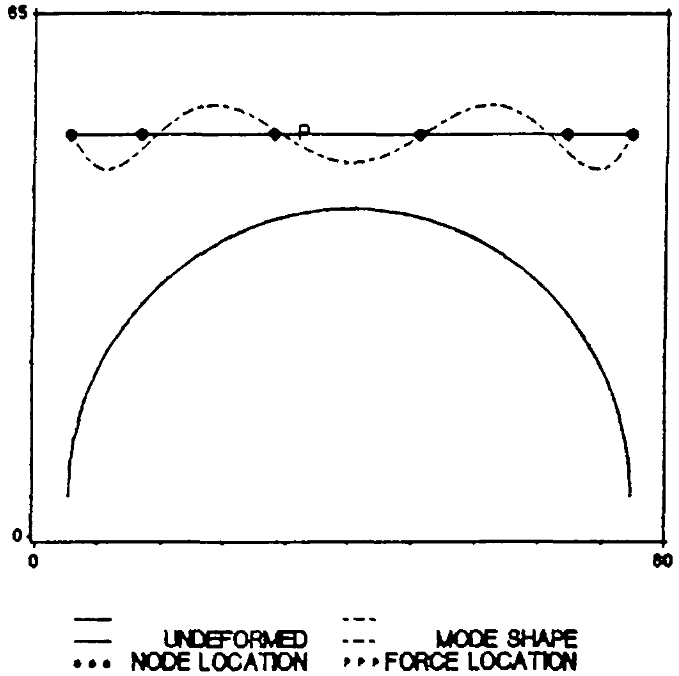

(A) I-SPECIMEN

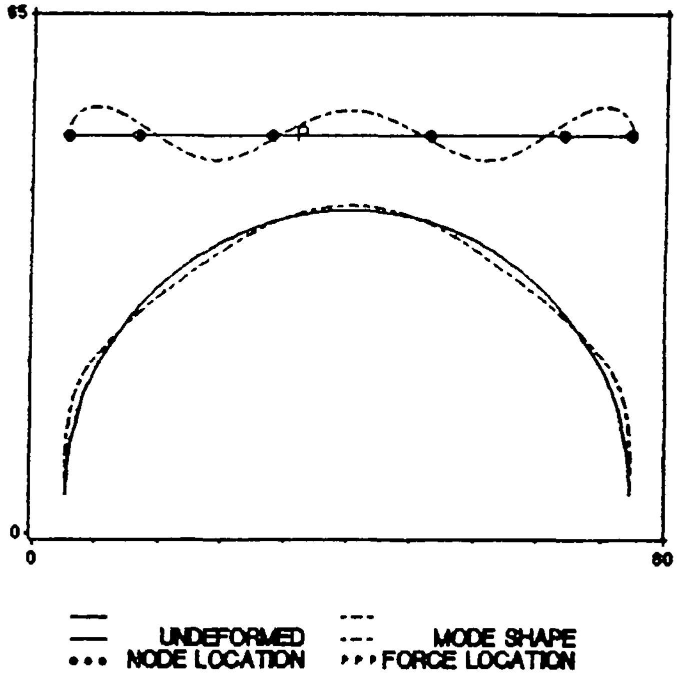

(B) CHANNEL SPECIMEN

Figure 54. **Six noded, out-of-plane, clamped-clamped mode shape for both specimens:** The six noded out-of-plane mode shapes of both specimens are shown schematically. The experimentally located nodes are indicated by dots, the undeformed frames are represented by the solid lines and the analytically predicted mode shape by the dashed lines.

negative torque is used in the correlation. The values for flexibility coefficients α_{12}, α_{22}, and α_{32} are only obtained from the out-of-plane tests. The values for these coefficients associated with lateral loads of 3.25 and 1.063 pounds are used for the I-specimen and channel specimen, respectively.

The experimental values for the flexibility coefficients are correlated primarily with predictions from the finite element solution. The predicted values were obtained using clamped boundary conditions and two types of section properties. The finite element program was developed for isotropic, homogeneous, materials. Purely geometric section properties are generally used as input to describe the cross section of the specimen. To try to account for the composite material system the modulus-weighted section properties discussed in Chapter 5 are also used. Thus, predictions obtained using modulus-weighted and geometric section properties are presented. The modulus-weighted section properties and the geometric section properties for both specimens are presented in Appendix C.

The finite element computer program uses linear elastic structural theory, thus, the predicted flexibility matrix is symmetric. The experimental tests measured the total response of the frames which is a combination of linear and nonlinear responses. As a result, the experimental flexibility matrices are generally not symmetric. The flexibility influence coefficients of primary interest are the diagonal terms; α_{11}, α_{22}, and α_{33}. These terms play the largest role in describing the load carrying behavior of the frames. With the exception of the α_{23} term, the off-diagonal terms play a small role in the static response of the frames. The significance of α_{23} is a result of the coupling between out-of-plane bending and torsion due to the curved geometry. The correlation of the static results for the I-specimen will be discussed first followed by the results of the channel specimen.

I-Specimen Results

The flexibility coefficient α_{11} for the I-specimen is a special case in that values for α_{11} were obtained from two independent tests and from two independent analyses. The analytical predictions and experimental results for the flexibility coefficient α_{11} are presented in Table 14. The finite element predictions using clamped and pinned boundary conditions bracket the experimental value from the in-plane static test, and also the crush test. The crush test result for α_{11} is closer to the prediction obtained for clamped-end conditions reflecting the difference in the experimental boundary conditions between the tests. The continuum static solution was used to model the end conditions as torsional springs. The torsional spring stiffness required to match the in-plane static test value for α_{11} is smaller than the torsional spring stiffnesses required to match the in-plane natural frequencies in Table 11. The lower torsional spring stiffness required in the static tests with respect to the vibrational test is probably due to the difference in the static mode shape and the vibrational mode shape.

Table 14. Correlation of flexibility coefficient α_{11} for the I-specimen

Source	α_{11} in/lb
Experiment	
Crush Test	0.640×10^{-3}
Static Test	0.843×10^{-3}
FEM[a]	
Pinned	0.926×10^{-3}
Clamped	0.578×10^{-3}
Continuum	
Spring[b]	0.8559×10^{-3}

[a] Finite element solution from Ref. 7

[b] Continuum solution with torsional spring stiffness $\alpha_t = 2 \times 10^4$ in-lb/rad .

The effect of the torsional spring constant on the value of flexibility coefficient α_{11} is demonstrated in Fig. 55. The logarithm to the base ten of the spring stiffness is plotted along the horizontal axis and α_{11} is plotted on the vertical axis. The two horizontal lines represent the predictions from the finite element program for clamped-end and pinned-end conditions. For very compliant springs and very stiff springs, the continuum analysis matches the predictions of the finite element code for pinned-end and clamped-end conditions, respectively. The plus sign in the figure indicates the experimental result, and it is closer to the pinned-end prediction than to the clamped-end prediction. Comparing the plots in Figs. 47 and 55 shows that the torsional spring stiffness required to achieve effectively clamped-end conditions are different for static and dynamic conditions. The effective stiffness of the experimental boundary conditions is higher for the dynamic tests than for the static tests.

The flexibility coefficients for the I-specimen from the finite element program using both modulus-weighted and geometric section properties are presented with the corresponding experimental values in Table 15. In general, the correlation between the experimental results and the predictions obtained using the modulus-weighted section properties is better than with the predictions obtained using the geometric section properties. The modulus-weighted values predict a stiffer response than the geometric section properties.

The discrepancy in the flexibility coefficient α_{11} is attributed to the flexibility in the experimental boundary conditions. The numerical predictions for flexibility coefficient α_{22} are significantly higher than the experimental result. The modulus-weighted value correlates the best, but it is 20 % higher (more compliant) than the experimental value. Torsional springs cannot explain this discrepancy since additional flexibility would make the predictions more compliant. This result is consistent with the discrepancy in the

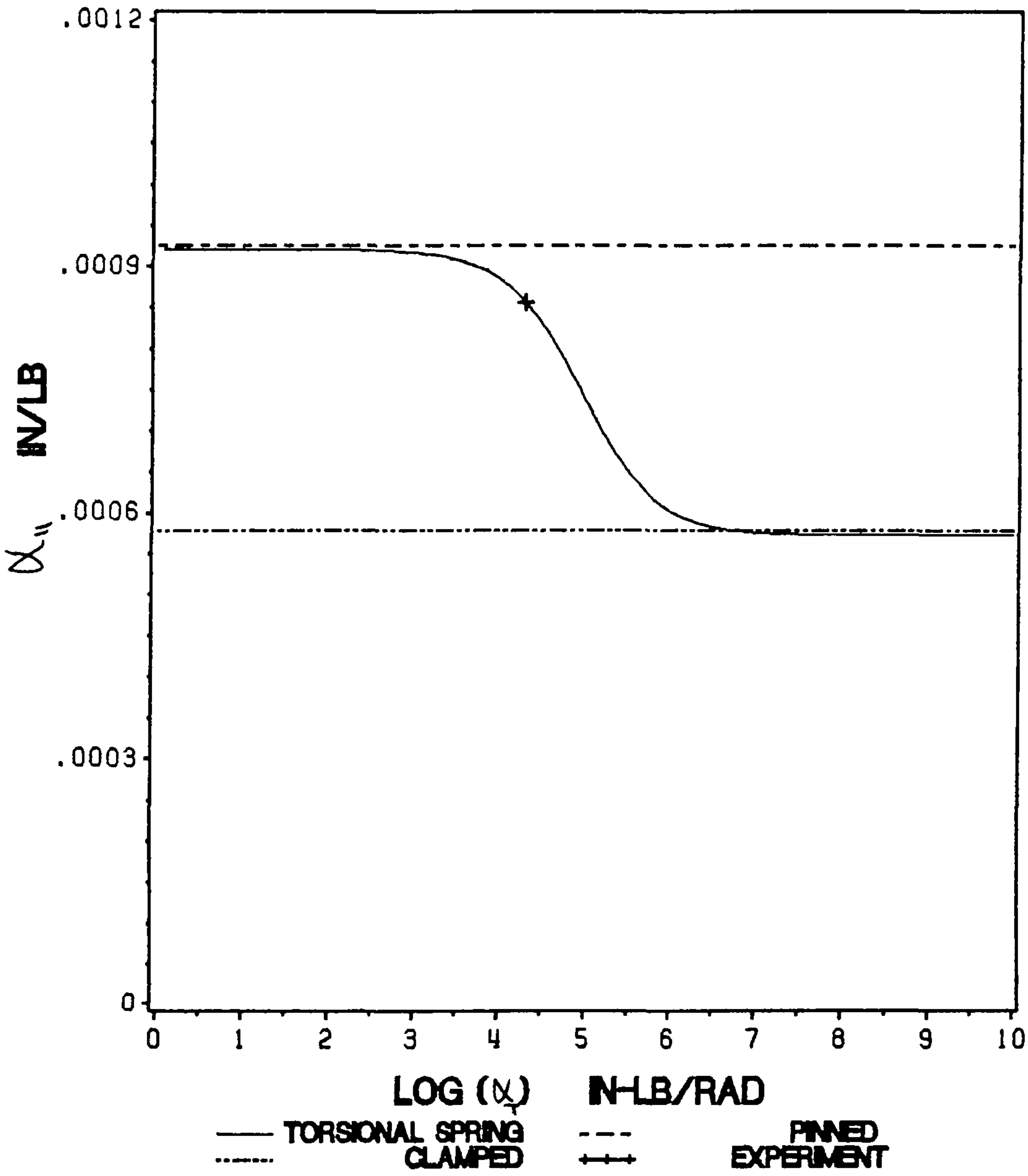

Figure 55. Influence of torsional spring stiffness on α_{11}: The plot shows that the value of α_{11} is very sensitive to small changes in the flexibility of the end conditions. The log of the torsional spring stiffness is plotted on the horizontal axis. The horizontal lines are the predictions for clamped-end and pinned-end conditions.

fundamental out-of-plane natural frequency of the I-specimen. The predicted values for flexibility coefficients α_{33} and α_{23} using modulus-weighted section properties correlate well with the experimental values. The predictions obtained using geometric section properties do not correlate as well. The correlation with the experimental result for α_{32} from the out-of-plane tests is not as good. The discrepancy is on the order of 20 % similar to the discrepancy in α_{22} .

Table 15. Correlation of the flexibility coefficients for the I-specimen

Flexibility Coefficient		Experiment	Analysis[a]	
			M-W[b]	Geometric[c]
α_{11}	in/lb	0.843×10^{-3}	0.5778×10^{-3}	0.6709×10^{-3}
α_{22}	in/lb	0.113	0.1406	0.2006
α_{33}	rad/in-lb	0.131×10^{-2}	0.1396×10^{-2}	0.1892×10^{-2}
α_{23}	1/lb	0.101×10^{-1}	0.1109×10^{-1}	0.1503×10^{-1}
α_{32}	1/lb	0.0877×10^{-1}	0.1109×10^{-1}	0.1503×10^{-1}
α_{12}	in/lb	0.148×10^{-2}	0.715×10^{-5}	0.834×10^{-5}
α_{21}	in/lb	0.658×10^{-4}	0.715×10^{-5}	0.834×10^{-5}
α_{13}	1/lb	0.107×10^{-3}	0.197×10^{-6}	0.497×10^{-6}
α_{31}	1/lb	0.261×10^{-4}	0.197×10^{-6}	0.497×10^{-6}

[a] Finite element solution from Ref. 7

[b] Modulus weighted section properties

[c] Geometric section properties

The predicted values for flexibility coefficients α_{12} and α_{13} are very small and can be interpreted as zero. The experimental value for flexibility coefficient α_{12} does not correlate well. This discrepancy is believed to be due to a geometric nonlinearity which cannot be modeled using linear structural theory. The experimental values for α_{21}, α_{13}, and α_{31} are small and were inconsistently measured. The scatter in the data associated with these coefficients indicates that the effects of these coefficients are too small to measure reliably. Thus, the discrepancies in these coefficients is not significant.

Channel Specimen Results

The flexibility coefficients for the channel specimen from the finite element program using both modulus-weighted and geometric section properties are presented with the corresponding experimental values in Table 16. In general, the correlation between the experimental results and the predictions obtained using the modulus-weighted section properties is better than with the predictions obtained using the geometric section properties. The predicted values for flexibility coefficient α_{11} are a minimum of five times larger than the experimental result. This discrepancy is too large to be explained by experimental anomalies. The discrepancy is consistent with the correlation observed in the in-plane natural frequencies of the channel specimen. A sensitivity analysis revealed that α_{11} is very sensitive to the first sectorial moment $I_{\omega y}$. Other section properties characteristic of an asymmetric section did not significantly effect the prediction of α_{11}.

The discrepancy in the values for flexibility coefficient α_{22} is consistent with the discrepancy in the fundamental out-of-plane natural frequency of the channel specimen. The discrepancy is smaller than the corresponding discrepancy in the I-specimen results. The experimental values for flexibility coefficients α_{33} and α_{23} corresponding to the negative torque data correlate well with the modulus-weighted predictions. The experimental value for α_{32} obtained from the out-of-plane tests does not correlate well with either of the predicted values.

Table 16. Correlation of the flexibility coefficients for the channel specimen

Flexibility Coefficient		Experiment	Analysis[a]	
			M-W[b]	Geometric[c]
α_{11}	in/lb	1.66 x 10^{-3}	8.013 x 10^{-3}	9.758 x 10^{-3}
α_{22}	in/lb	0.242	0.2678	0.3653
α_{33}	rad/in-lb	0.258 x 10^{-2}	0.2475 x 10^{-2}	0.3401 x 10^{-2}
α_{23}	1/lb	0.224 x 10^{-1}	0.197 x 10^{-1}	0.271 x 10^{-1}
α_{32}	1/lb	0.120 x 10^{-1}	0.197 x 10^{-1}	0.271 x 10^{-1}
α_{12}	in/lb	0.842 x 10^{-2}	1.456 x 10^{-2}	1.777 x 10^{-2}
α_{21}	in/lb	0.790 x 10^{-4}	1.456 x 10^{-2}	1.777 x 10^{-2}
α_{13}	1/lb	0.369 x 10^{-2}	0.407 x 10^{-4}	0.497 x 10^{-4}
α_{31}	1/lb	−.201 x 10^{-4}	0.407 x 10^{-4}	0.497 x 10^{-4}

[a] Finite element solution from Ref. 7
[b] Modulus weighted section properties
[c] Geometric section properties

The correlation of flexibility coefficients α_{12} and α_{31} is not bad. The values are at least on the same order of magnitude. However, the good correlation is considered a coincidence since the experimental value for α_{12} is likely measuring a geometrically non-linear response and the scatter in the data associated with α_{31} is very high. Even the predicted values for α_{12} and α_{31} should be considered carefully since they are linked to the poorly predicted in-plane response of the channel specimen. The experimental values for flexibility coefficients α_{21} and α_{13} do not correlate well with the predicted values. The experimental values are actually smaller than the corresponding values for the I-specimen. This is unusual since these coefficients couple the in-plane and out-of-plane responses and the coupling for the channel specimen is expected to be more pronounced than for the I-specimen. This indicates that the experimental values for these coefficients cannot be relied upon. Certainly the correlation in these coefficients cannot be treated seriously.

Chapter 7

Concluding Remarks

The primary purpose in this study was to evaluate a new finite element program which was developed by Noor et al., (Ref. 7) specifically for the free-vibrational analysis of curved, thin-walled beams with open sections. An experimental program was undertaken to generate data which was characteristic of the static and free-vibrational response of two test specimens. The test specimens were semi-circular, graphite-epoxy frames which were intended to represent aircraft fuselage frames. One test specimen had a symmetric I cross section and the other had an asymmetric channel cross section.

The experimental program consisted of both static and dynamic tests. A series of static tests generated the flexibility matrix which relates radial, lateral, and torsional loads at the midspan to radial, lateral, and twist displacements at the midspan. The dynamic tests provided the frequencies and node locations of the in-plane and out-of-plane free-vibrational modes for clamped-clamped end conditions.

The finite element program is based on a Vlasov-type, thin-walled, curved beam theory and accounts for the additional effects of transverse shear deformation and rotatory inertia. However, for the specimens in this study, transverse shearing deformations did not significantly contribute to the response. The analytical predictions from the finite element program were confirmed in part by independent continuum solutions for the in-plane static and dynamic response of a monosymmetric curved beam.

The analytical predictions correlated well with the experimental data from the symmetric I-specimen. It was found that the experimental boundary conditions acted like torsional springs instead of clamps. The analytical predictions for the natural frequencies using clamped-end and pinned-end conditions bracketed the experimental data. The analytically predicted mode shapes correlated quite well with the experimentally located node positions. The largest discrepancy occurred in the prediction of the first out-of-plane natural frequency, which was 8.5 % lower than the experimental value (see Table 13).

The analytical predictions for the static response of the I-specimen also correlated well with experimental data. A substantial discrepancy in flexibility coefficient α_{11} (radial displacement/radial load) was shown to be a function of the flexibility in the experimental boundary conditions. Further investigation showed that the static tests required a softer support to model the boundary conditions than was required in the dynamic tests (compare Tables 11 and 14). The analytical prediction for flexibility coefficient α_{22} (lateral displacement/lateral load) was larger than the experimental value. This is consistent with the discrepancy in the first out-of-plane natural frequency, since in both cases the analysis predicts a more compliant response than is seen in the experiments.

The correlation between analysis and experiment is less satisfactory for the channel specimen than for the I-specimen. In general, the predicted out-of-plane static and vibrational responses correlated well with the experimental data. The predictions for the out-of-plane natural frequencies using clamped-end and pinned-end conditions bracketed the experimental results (see Fig. 53). The predictions for flexibility coefficients

α_{33} and α_{23} correlated well with the experimental data(see Table 16). The analytical predictions for the first out-of-plane natural frequency (Table 13) and flexibility coefficient α_{22} (Table 16) were again predicted to be more compliant than the experimental results consistent with the I-specimen results. These discrepancies are worth noting since it is unusual when correlating analysis with experimental data to find the analysis more compliant than the experimental response.

Large discrepancies were observed between the analytical predictions for the in-plane static and vibrational responses of the channel specimen and the experimental data. The experimental natural frequencies are two to three times higher than the predicted values (see Table 12). Thus, the analysis is significantly more compliant than the experiment. Consistent with this, the analytical prediction for flexibility coefficient α_{11} (Table 16) is five times higher than the experimental values. Discrepancies of this magnitude are difficult to explain, however, further investigation did show that the in-plane response of the asymmetric channel specimen is extremely sensitive to the cross-sectional property $I_{\omega y}$ which couples in-plane bending and warping.

The finite element program was developed for isotropic homogeneous materials. The composite nature of the test specimens was accounted for in part by using modulus-weighted section properties in place of section properties calculated based purely on the geometry of the cross section. The flexibility influence coefficients obtained using the modulus-weighted section properties correlated better with the experimental data than did coefficients obtained using purely geometric section properties (see Tables 15 and 16).

The magnitudes of some of the experimentally measured flexibility coefficients were found to be a function of the algebraic sign of the applied torque (see Table 6 for example). The experimental values for flexibility coefficients α_{12} and α_{21} differed by two orders of magnitude (Table 5-8). The values for flexibility coefficients α_{13} and α_{31} were different magnitudes and in the case of the channel specimen were consistently of different signs. Linear structural theory predicts the flexibility matrix to be symmetric, and consequently cannot account for the asymmetry of the flexibility matrixes measured in the experiments. A detailed analysis of the static out-of-plane response of curved frames requires a solution capable of modeling geometric nonlinearities. This is particularly true for frames with asymmetric cross sections. The necessity for a nonlinear solution is less apparent in the vibrational response of the curved frames.

Future Work

The data from the experimental tests could be improved upon in a number of ways. Simply securing the ends in potting compound and clamping the ends to a steel beam was not sufficient to model clamped end conditions. More elaborate steps could be taken to obtain clamped conditions. As a minimum, the potted ends should be bolted to the steel beam. The resolution in the out-of-plane static tests might be increased if the specimens were loaded with less force and more torque. This requires using larger moment arms. Doing this without adding excessive weight to the specimens might not be a trivial exercise.

With respect to the analysis, this study has raised some serious doubt about the accuracy of the predictions from the finite element program for the in-plane response of a curved beam with an asymmetric cross section. Comparisons with similar experimental data for other asymmetric sections seems to be in order. Certainly, some effort should be made toward resolving this issue since this element is expected to be implemented in a larger finite element code.

The discrepancies in the in-plane response of the channel specimen are of a magnitude that makes it difficult to attribute them to the composite material system; however, extending the Hooke's law relation in the finite element program to account for the constitutive relations for laminated composites might help. Doing this may help explain the discrepancies in the fundamental out-of-plane natural frequencies, since they are of a much smaller magnitude.

Thin-walled curved beam theories are complicated and application to composite structures should be undertaken with some caution. The assumption in Vlasov's theory that the shear strain in the midplane of the wall vanishes is a result of isotropic elasticity. This assumption should be re-examined using anisotropic elasticity to determine if it is a valid assumption with respect to laminated composites.

Finally, a logical extension of this experimental work would be to load the frames to failure. Such tests would provide information on the large displacement response of the composite frames as well as first failure and post failure response. Research of this nature is certainly more germane to the issue of crashworthiness. This research is currently being conducted by Mr. E. Moas, Graduate Research Assistant, and Professor O. H. Griffin in cooperation with the Landing and Impact Dynamics Branch at NASA Langley Research Center through the NASA-Virginia Tech Composites Program.

REFERENCES

1. Farley, G. L., "Energy Absorption of Composite Materials," ***Journal of Composite Materials,*** Vol. 17, 1983.

2. Williams, M. S. and Hayduk, R. J., "Vertical Drop Test of a Transport Fuselage Section Located Forward of the Wing," ***NASA Technical Memorandum 85679,*** August, 1983.

3. Williams, M. S. and Hayduk, R. J., "Vertical Drop Test of a Transport Fuselage Center Section Including the Wheel Wells," ***NASA Technical Memorandum 85706,*** October, 1983.

4. Fasanella, E. L. and Alfaro-Bou, E., "Vertical Drop Test of a Transport Fuselage Section Located Aft of the Wing," ***NASA Technical Memorandum 89025,*** September, 1986.

5. Boitnott, R. L. and Carden, H. D., "Drop Testing and Analysis of Six-Foot Diameter Graphite-Epoxy Frames," ***in the Proceedings of the AHS National Specialists Meeting on Crashworthy Design of Rotorcraft,*** April, 1986.

6. Boitnott, R. L. and Fasanella, E. L., "Impact Evaluation of Composite Floor Sections," ***SAE Technical Paper Series 891018,*** April, 1989.

7. Noor, A. K., Peters, J. M., and Min, Byung-Jin, "Mixed Finite-Element Models for Free Vibrations of Thin-Walled Beams," ***NASA Technical Paper 2868***, February 1989.

8. Hoppe, R., "The Bending Vibration of a Circular Ring," ***Crelle Journal of Mathematics,*** Vol. 73, 1871, pp. 158.

9. Lamb, "On the Flexure and the Vibration of a Curved Bar," ***Proceedings of the London Mathematical Society,*** Vol. 19, 1888, pp. 365-376.

10. Love, A., **A Treatise on the Mathematical Theory of Elasticity,** Fourth Edition, Dover Publications, New York, 1944, pp. 451-454.

11. Den Hartog, J. P., "The Lowest Natural Frequency of Circular Arcs," ***Philosophical Magazine,*** Ser. 7, Vol. 5, 1928, pp. 400-408.

12. Brown, F. H., "Lateral Vibration of Ring-Shaped Frames," ***Journal of the Franklin Institute,*** Vol. 218, July 1934, pp. 41-48.

13. Timoshenko, S., "Theory of Bending, Torsion, and Buckling of Thin-Walled Members of Open Cross Section," ***Journal of the Franklin Institute,*** Vol. 236, No. 3, pp 201-219; No. 4, pp. 249-268; No.5, pp. 343-361, 1945.

14. Lang, T. E., "Vibrations of Thin Circular Rings, Part I. Solutions for Modal Characteristics and Forced Excitation," ***Technical Report No. 32-261,*** (contract no. NAS7-100) Jet Propulsion Laboratory, California Institute of Technology, July 1962.

15. Lang, T. E., "Vibrations of Thin Circular Rings, Part II, Modal Functions and Eigenvalues of Constrained Semi-Circular Rings," ***Technical Report No. 32-261,*** (contract no. NAS7-100) Jet Propulsion Laboratory, California Institute of Technology, March 1963.

16. Maddox, N. R., "Free Oscillations of Thin-Walled Open Section Circular Rings," ***Doctorate of Philosophy Dissertation, Georgia Institute of Technology,*** Atlanta, Georgia, October 1969.

17. Hammoud, A. S. and Archer, R. R., "On the Free Vibrations of Complete and Incomplete Rings," ***Developments in Mechanics,*** Vol. 2, Part 2, April 1963, pp. 489-524.

18. Endo, M., "Flexural Vibrations of a Ring with Arbitrary Cross Section," ***Bulletin of the Japan Society of Mechanical Engineers,*** Vol. 15, 1972, pp. 445-454.

19. Kirkhope, J., Bell, R. and Olmstead, J. L. D., "The Vibration of Rings of Unsymmetrical Cross Section," ***Journal of Sound and Vibration,*** Vol. 96, 1984, pp. 496-504.

20. Williams, H. E., "On the Equations of Motion of Thin Rings," ***Journal of Sound and Vibration,*** Vol. 26, No.4,1973, pp. 465-488.

21. Rao, S. S., "Effects of Transverse Shear and Rotatory Inertia on the Coupled Twist-Bending Vibrations of Circular Rings," ***Journal of Sound and Vibration,*** Vol. 16, No. 3, June 1971, pp.551-566.

22. Culver, G. C., "Natural Frequencies of Horizontally Curved Beams," ***Journal of the Structural Division, ASCE,*** April 1967, pp. 189-203.

23. Vlasov, V. Z., **Thin-Walled Elastic Beams,** Second Edition, Moscow, 1959; translated from Russian and published for the National Science Foundation, Washington, D.C., 1961.

24. Gardner, T. G. and Bert, C. W., "Vibration of Shear Deformable Rings: Theory and Experiment," ***Journal of Sound and Vibration,*** Vol. 103, 1985, pp. 549-565.

25. Bhimaraddi, A., "Generalized Analysis of Shear Deformable Rings and Curved Beams," ***International Journal of Solids Structures,*** Vol. 24, No. 4, 1988, pp. 363-373.

26. Gjelsvik, A., **The Theory of Thin-Walled Beams,** Wiley, New York, 1981.

27. Bauld, N. R. and Tzeng, L-S., "A Vlasov Theory for Fiber-Reinforced Beams with Thin-Walled Open Cross Sections," ***International Journal of Solids Structures,*** Vol. 20, No. 3, 1984 pp. 277-297.

28. Lo, P. K., "Comparison of Theory and Experiment for Flexural-Torsional Buckling of Laminated Composite Columns," ***Master of Science Thesis, Virginia Polytechnic Institute and State University,*** Blacksburg, Virginia, 24061, December 1985.

29. Mabson, G. E., "Effect of Curvature on Composite Material Beams," ***in the proceedings of the AIAA/ASME/ASCE/AHS/ASC 30th Structures, Structural Dynamics and Materials Conference, Part 4,***1989, Mobile, Alabama, pp. 1779-1787.

30. Tralli, A., "A Simple Hybrid Model for Torsion and Flexure of Thin-Walled Beams," ***Computers & Structures,*** Vol. 22, No. 4, 1986, pp. 649-658.

31. Pindera, M-J., Choksi, G., Hidde, J. S., Herakovich, C. T., "A Methodology for Accurate Shear Characterization of Unidirectional Composites," ***Journal of Composite Materials,*** Vol. 21, 1987, pp. 1164-1184.

32. Kaplan, W., **Ordinary Differential Equations,** Addison-Wesley Publishing Co. Inc., London, 1958, pp. 231-237.

33. Coyette, J. P., "An Improved Subroutine for the Estimation of Torsional Properties of Thin Walled Open Cross Sections," ***Engineering Computations,*** Vol. 4, September 1987, pp. 240-242.

Appendix A
Vibrational Test Data

This appendix contains some of the data from the vibrational tests that was not presented in the text. The first section contains the frequency response plots from the clamped-clamped tests. The second section contains the comparison of the analytical mode shapes and the experimental node locations.

Frequency Response Data from Dynamic Tests

The frequency response plots from the structural analyzer dynamic tests are presented here for the interested reader. Two sets of tests were run for each specimen, one series with radial excitation and one series with lateral excitation. The specimens were excited over a frequency range of 0-400 hertz. Noise began to dominate the response signal at about 375 hertz. In order to obtain sufficient resolution, it was necessary to test the specimens over smaller sub ranges, thus, the plots are presented in stages which overlap.

Three displacement probes were monitored in each test, thus, there are three plots in each figure. Each plot consists of a response curve and a phase angle curve. A natural frequency is marked by a spike in the response curve accompanied by a shift in the phase angle curve.

The probes were mounted in different orientations to detect both radial and lateral motion. The probe location and orientation is labeled in each plot. The three different orientations are defined in Fig. 56. The locations of the probes are measured in inches from the midspan of the specimen. The horizontal axis is the frequency of excitation in hertz and the vertical axis for the response curves has units of inches per pound on a log scale.

The I-specimen plots are presented first followed by the channel specimen plots. Ideally a mode is indicated by a sharp isolated spike, however, frequently the spikes are small and closely spaced making interpretation difficult. This is particularly true for the channel specimen plots where both in-plane and out-of-plane modes were excited with either radial or lateral excitation. The magnitude of the spikes is generally a poor indicator of the relative strengths of the modes. The spike magnitude is a strong function of probe location and the location of the electro-magnetic shaker. If the shaker or the probe are located near a node, the mode will be difficult to excite or detect, respectively. The plots are presented without further comment.

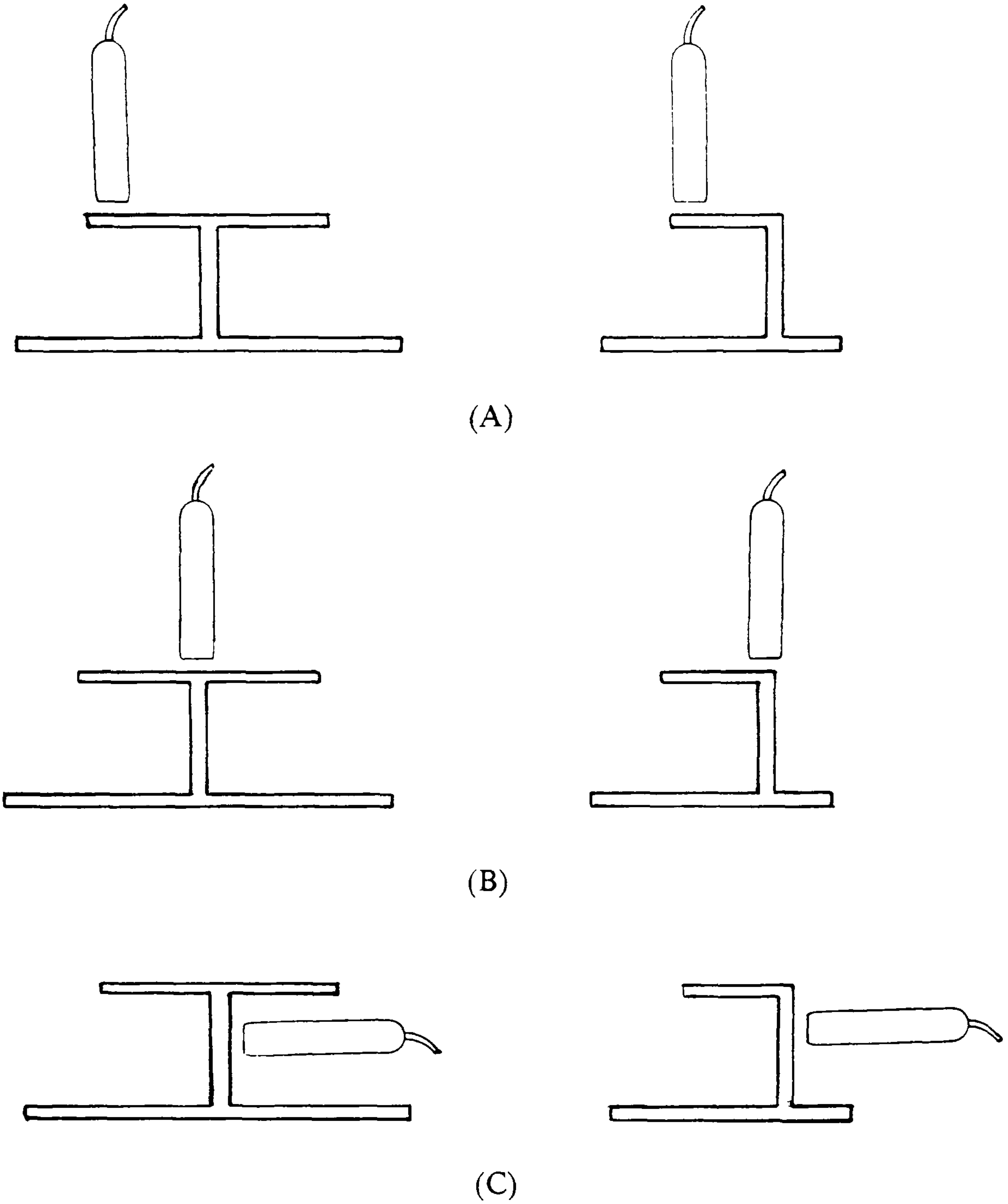

Figure 56. Proximity probe orientations for clamped-clamped vibrational tests: The probe orientations relative to both cross sections are presented in (A)-(C). (A) In-plane edge. (B) In-plane Web. (C) Out-of-plane.

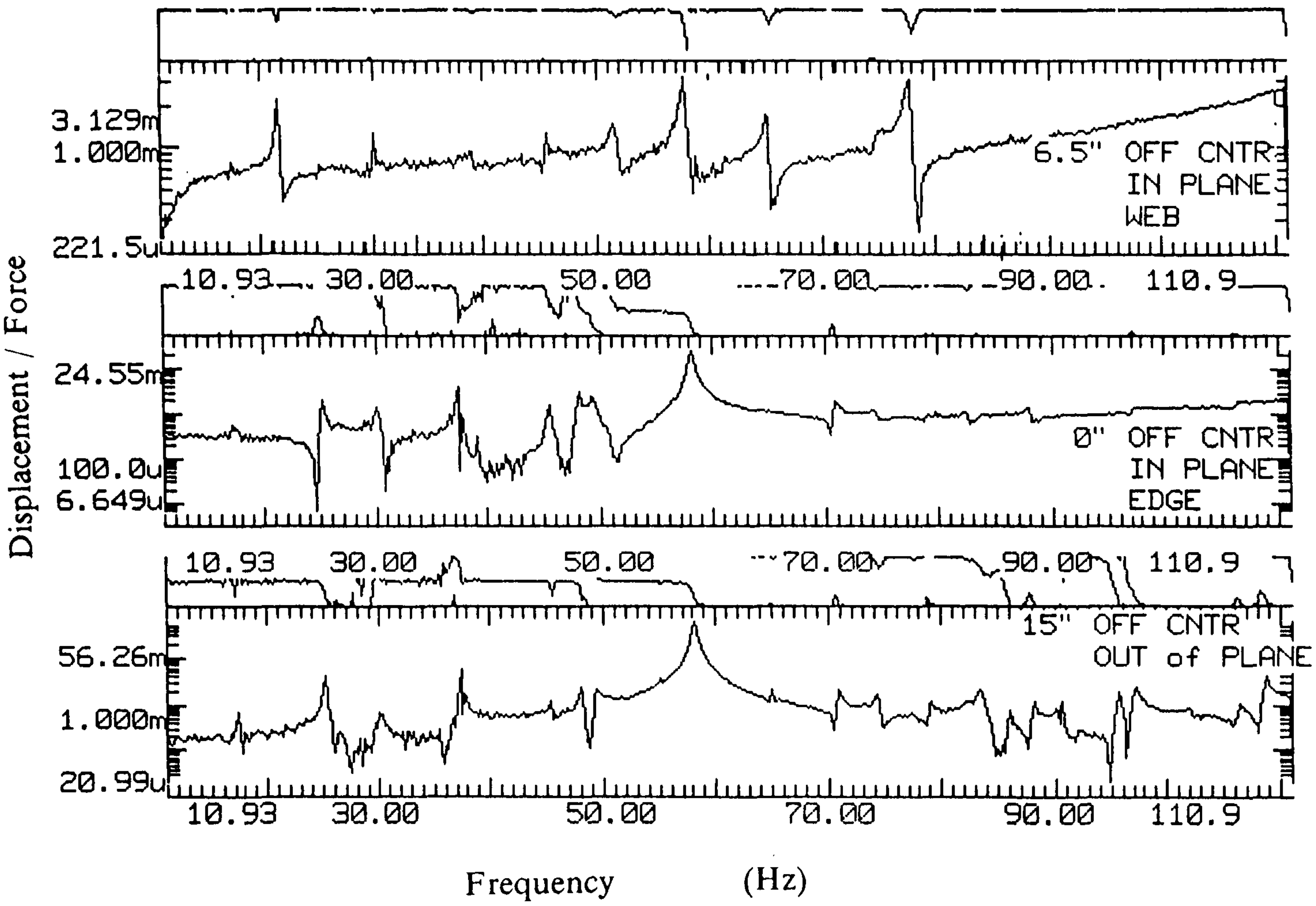

Figure 57. I-specimen frequency response plot for radial excitation; 11-111 Hz

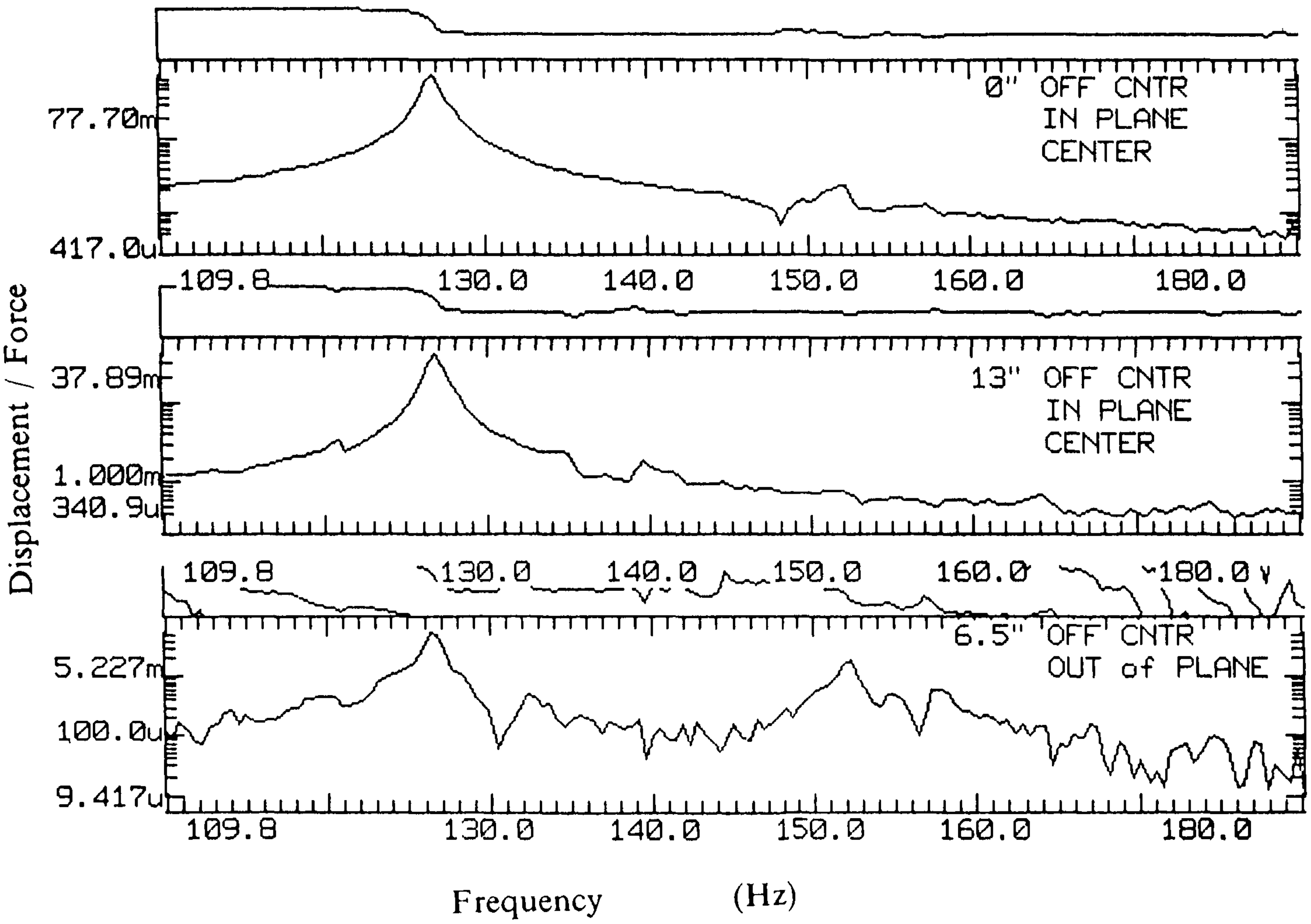

Figure 58. I-specimen frequency response plot for radial excitation; 110-180 Hz

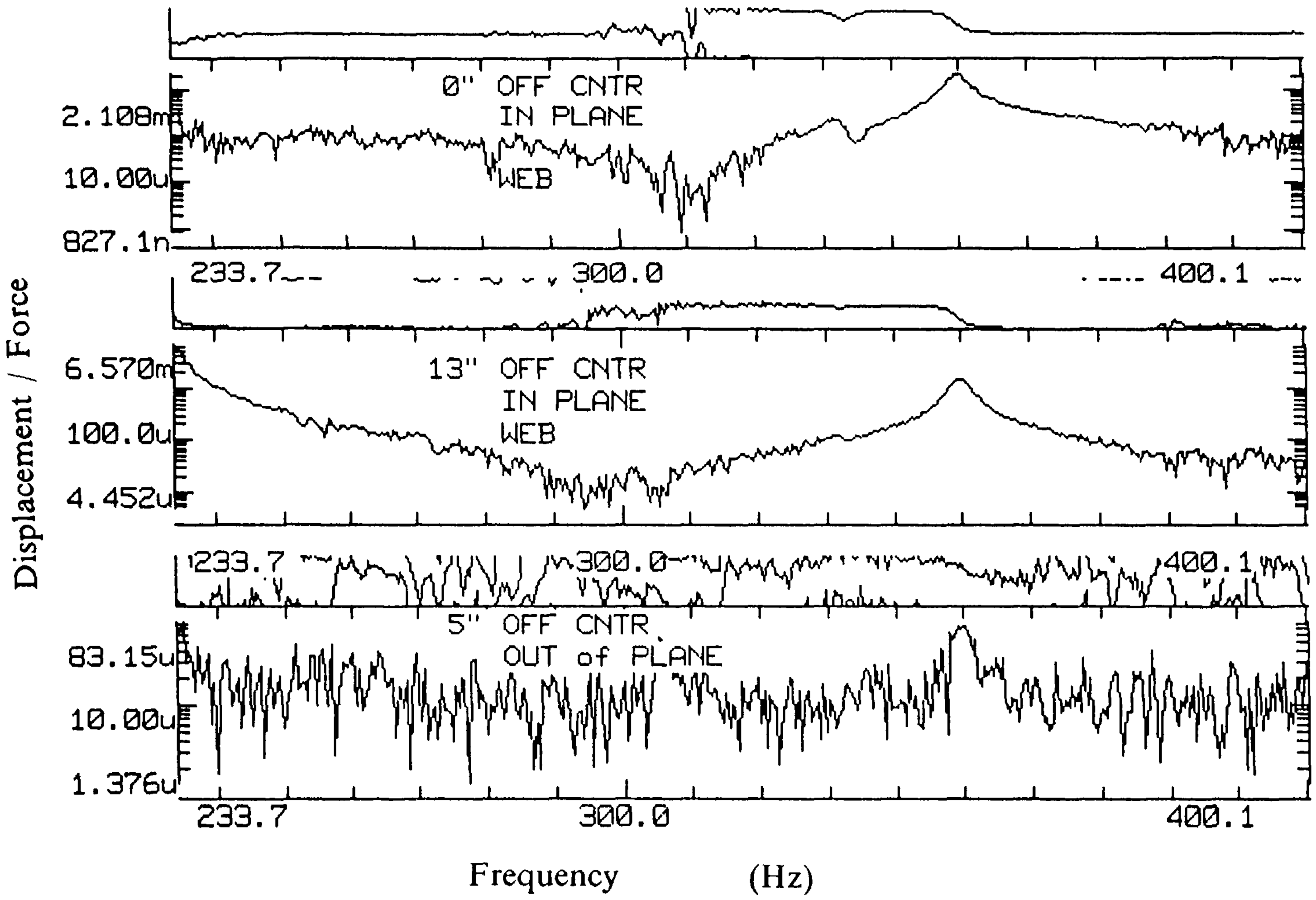

Figure 59. I-specimen frequency response plot for radial excitation; 233-400 Hz

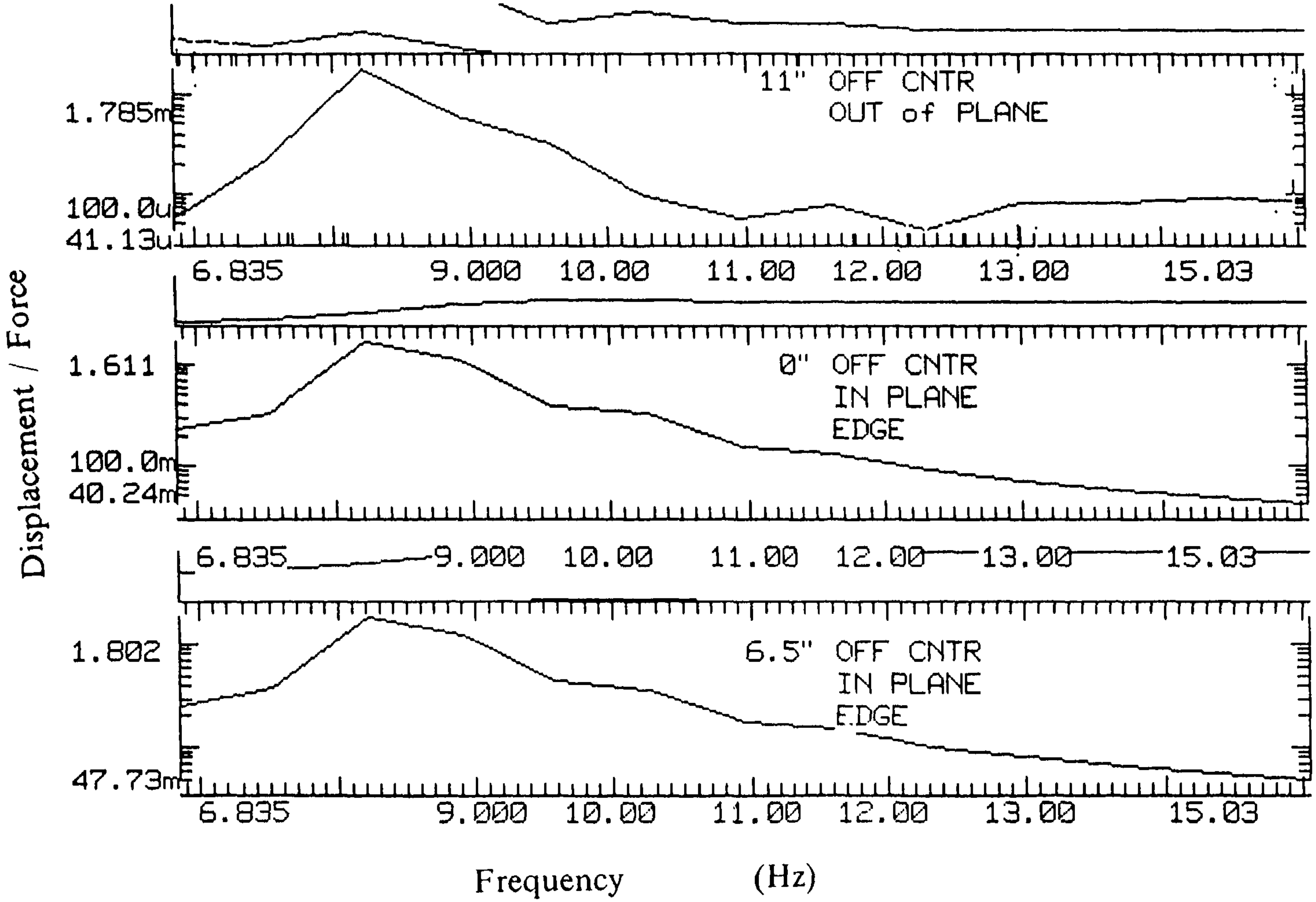

Figure 60. I-specimen frequency response plot for lateral excitation; 6.8-15 Hz

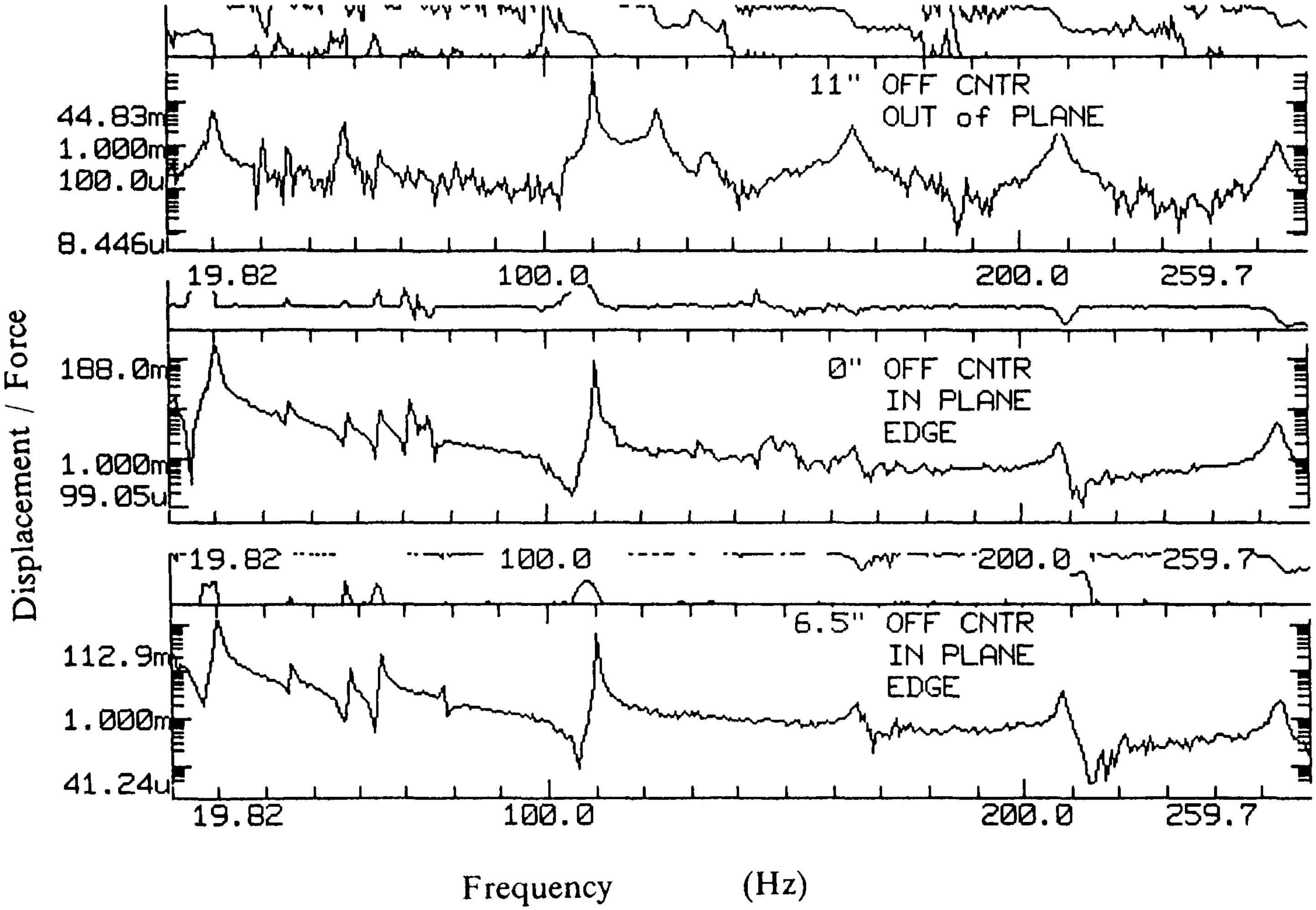

Figure 61. I-specimen frequency response plot for lateral excitation; 20-260 Hz

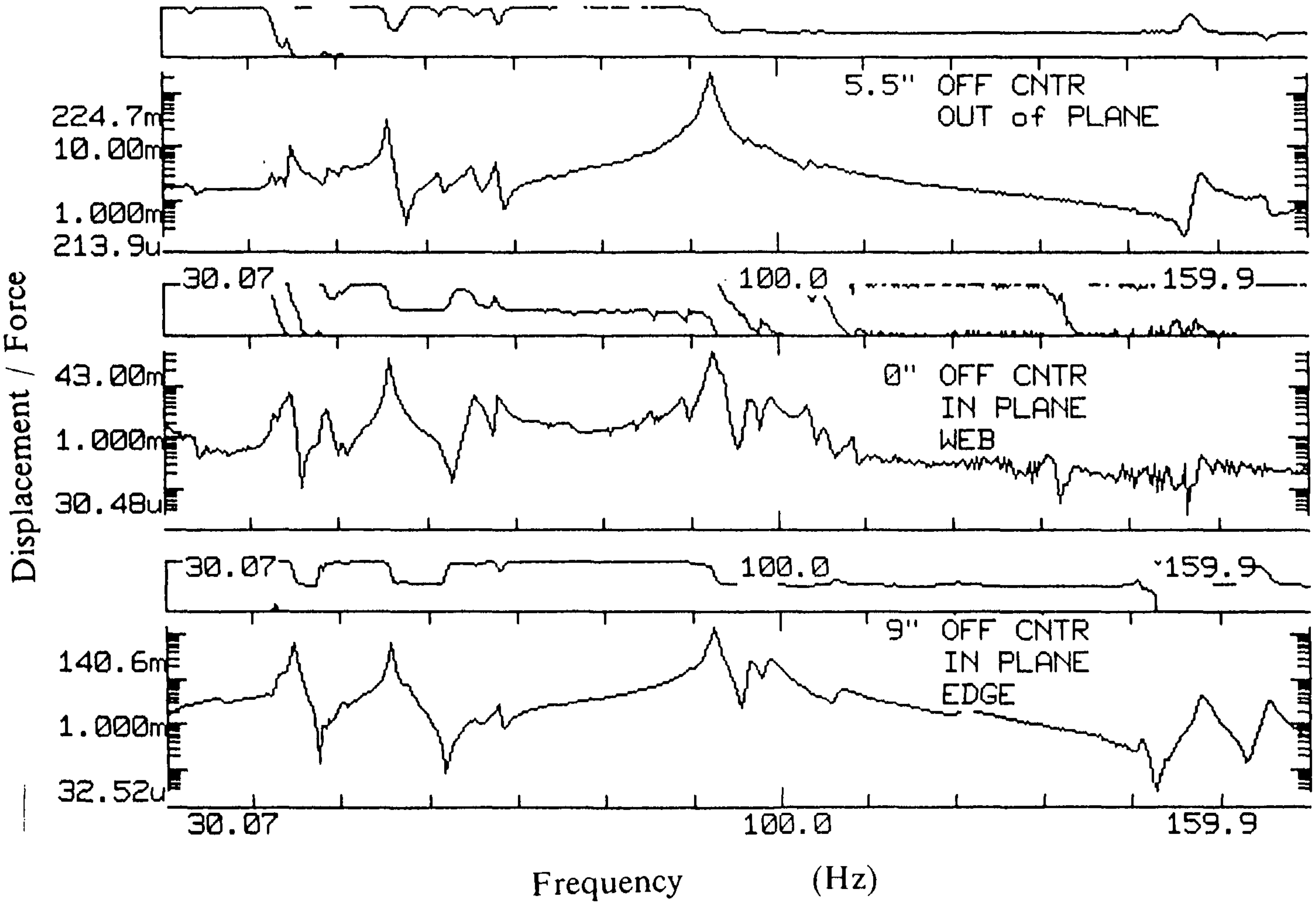

Figure 62. Channel specimen frequency response plot for radial excitation; 30-160 Hz

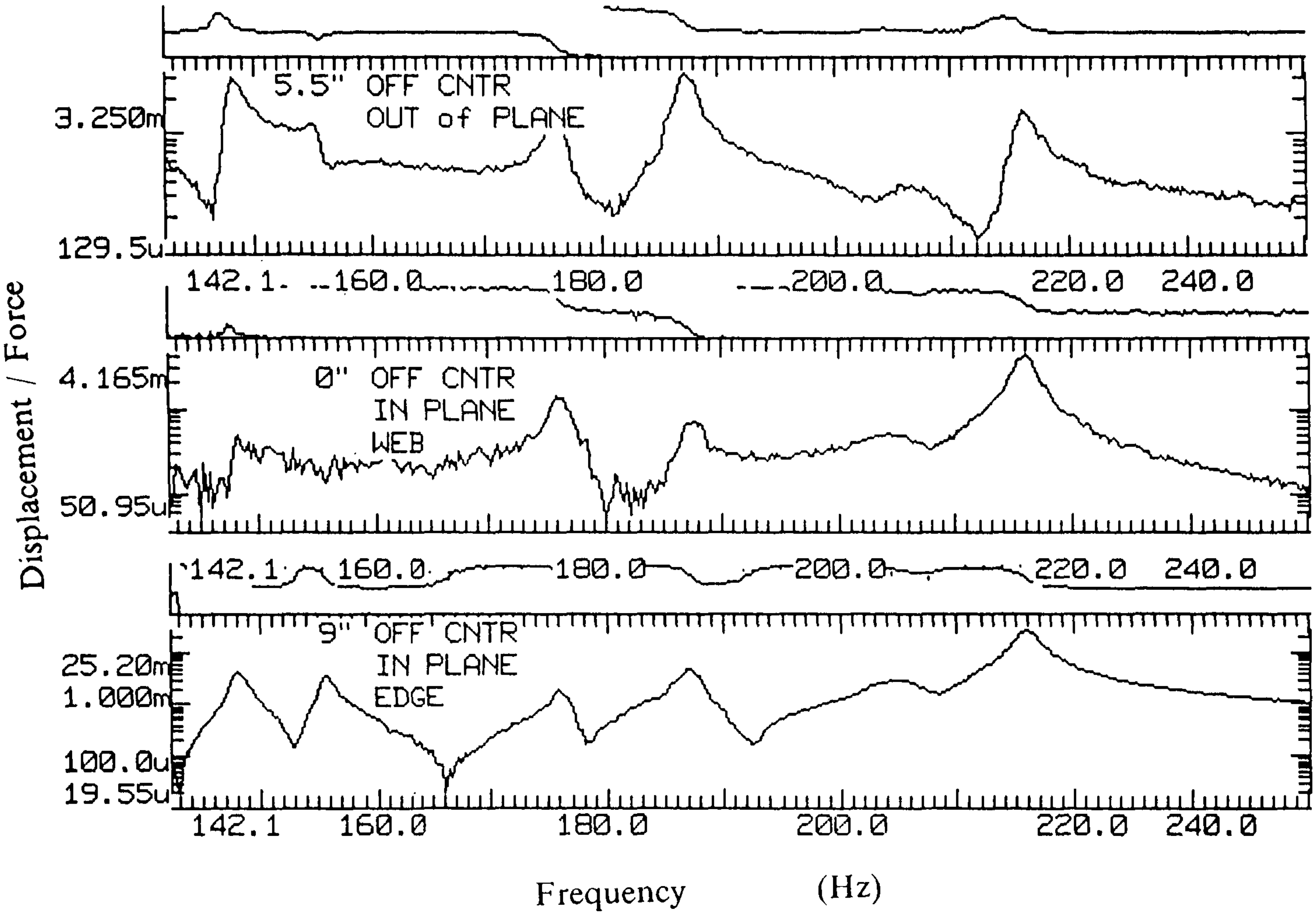

Figure 63. Channel specimen frequency response plot for radial excitation; 142-240 Hz

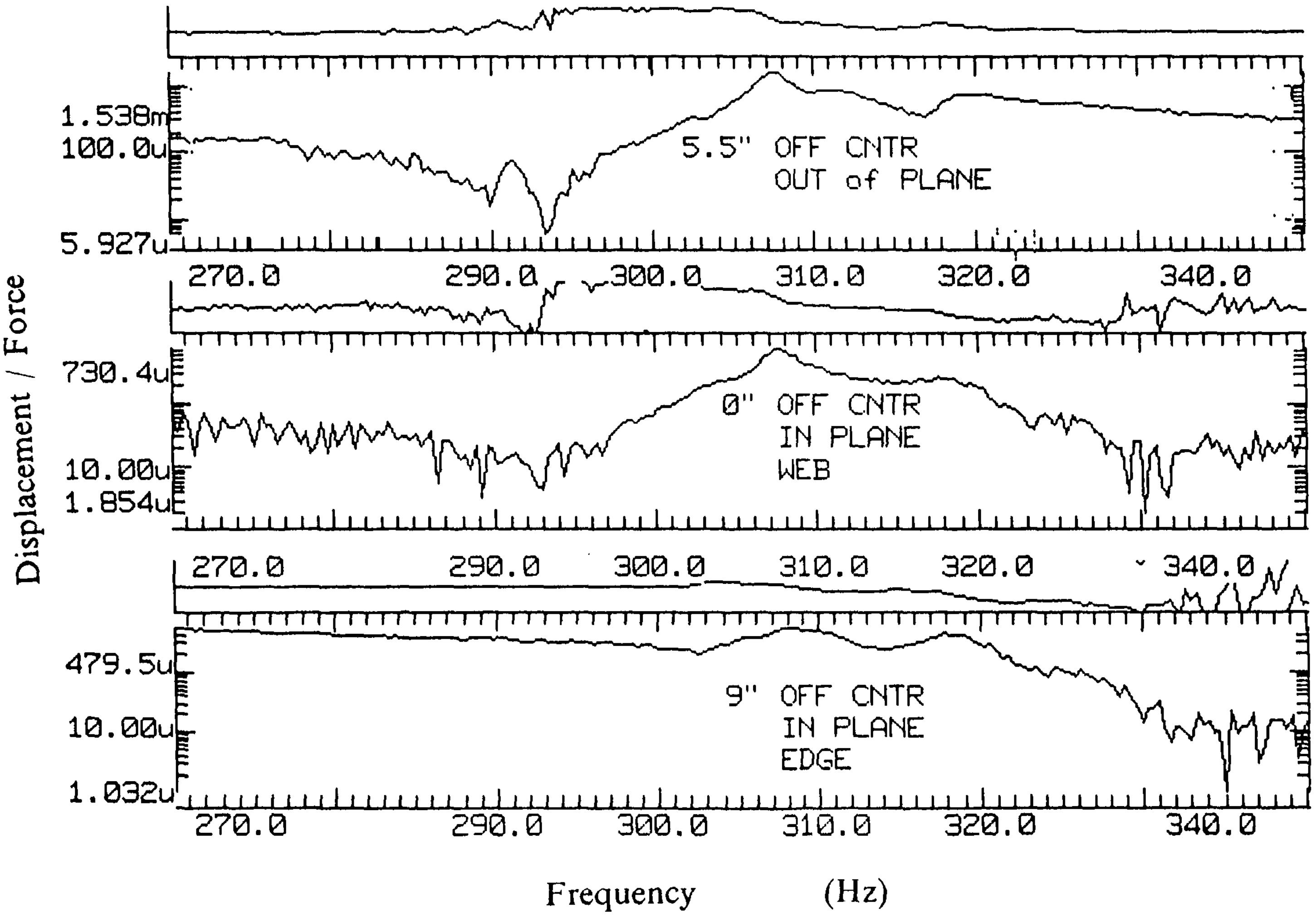

Figure 64. Channel specimen frequency response plot for radial excitation; 270-340 Hz

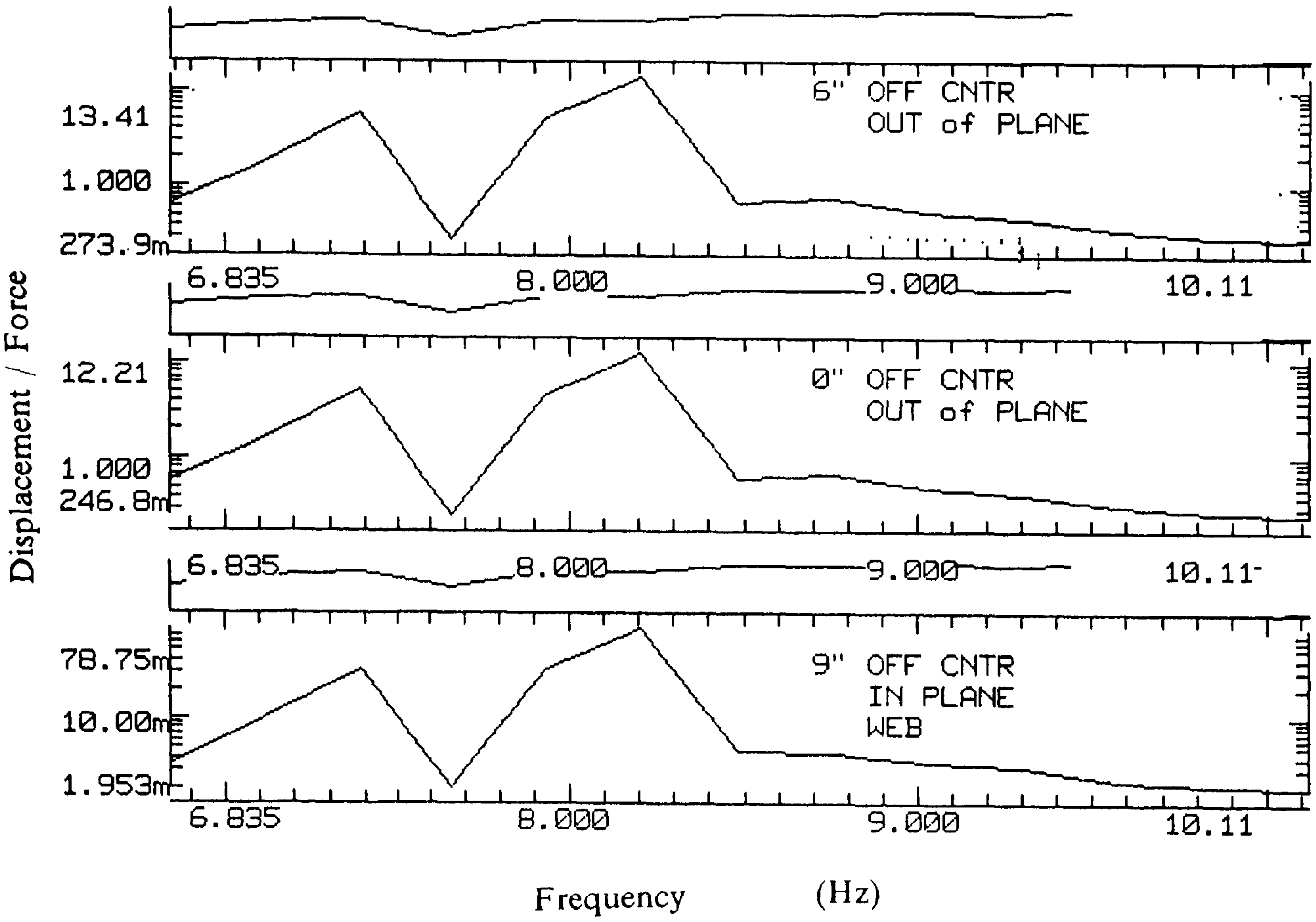

Figure 65. Channel specimen frequency response plot for lateral excitation; 6.8-10 Hz

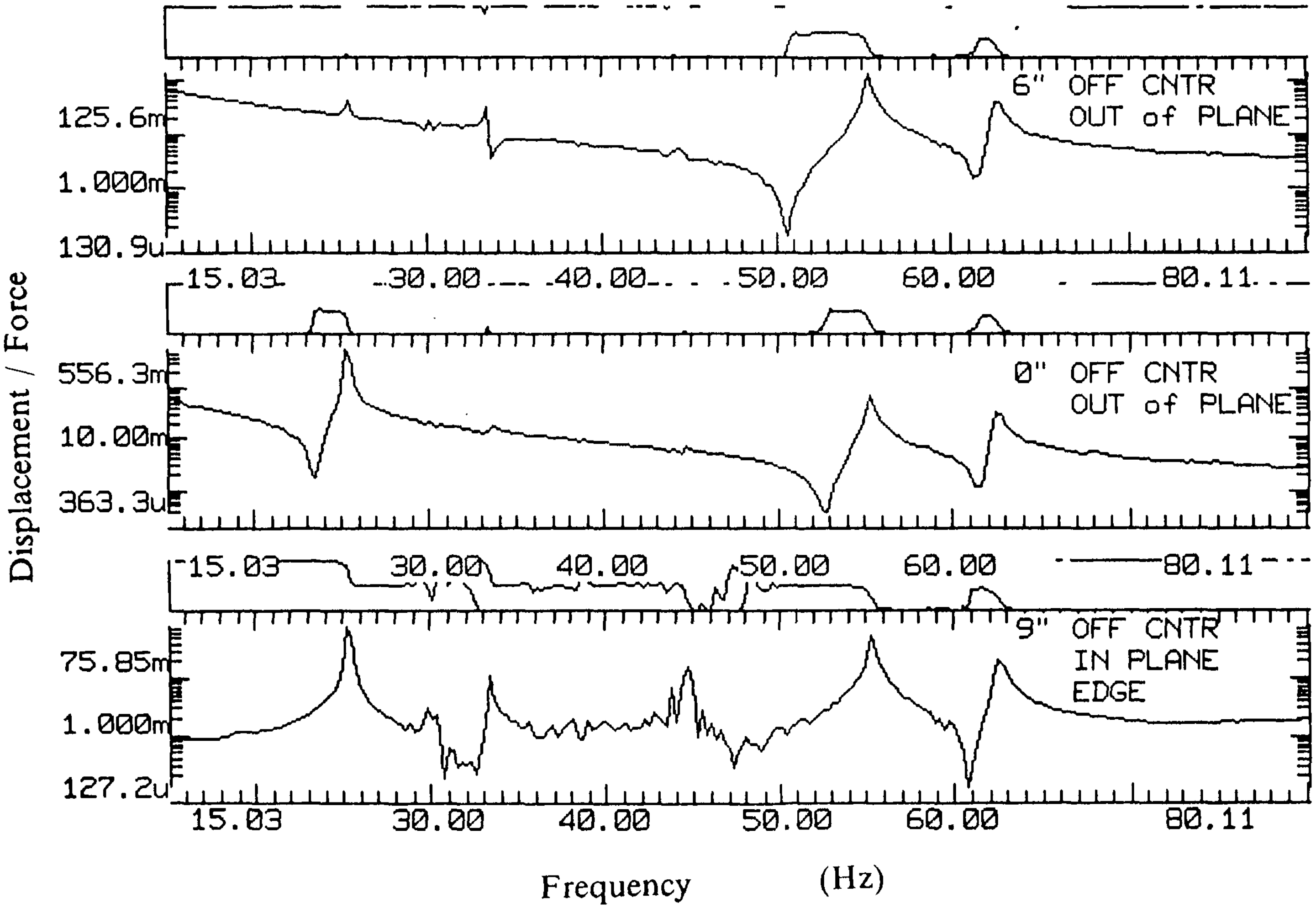

Figure 66. Channel specimen frequency response plot for lateral excitation; 15-80 Hz

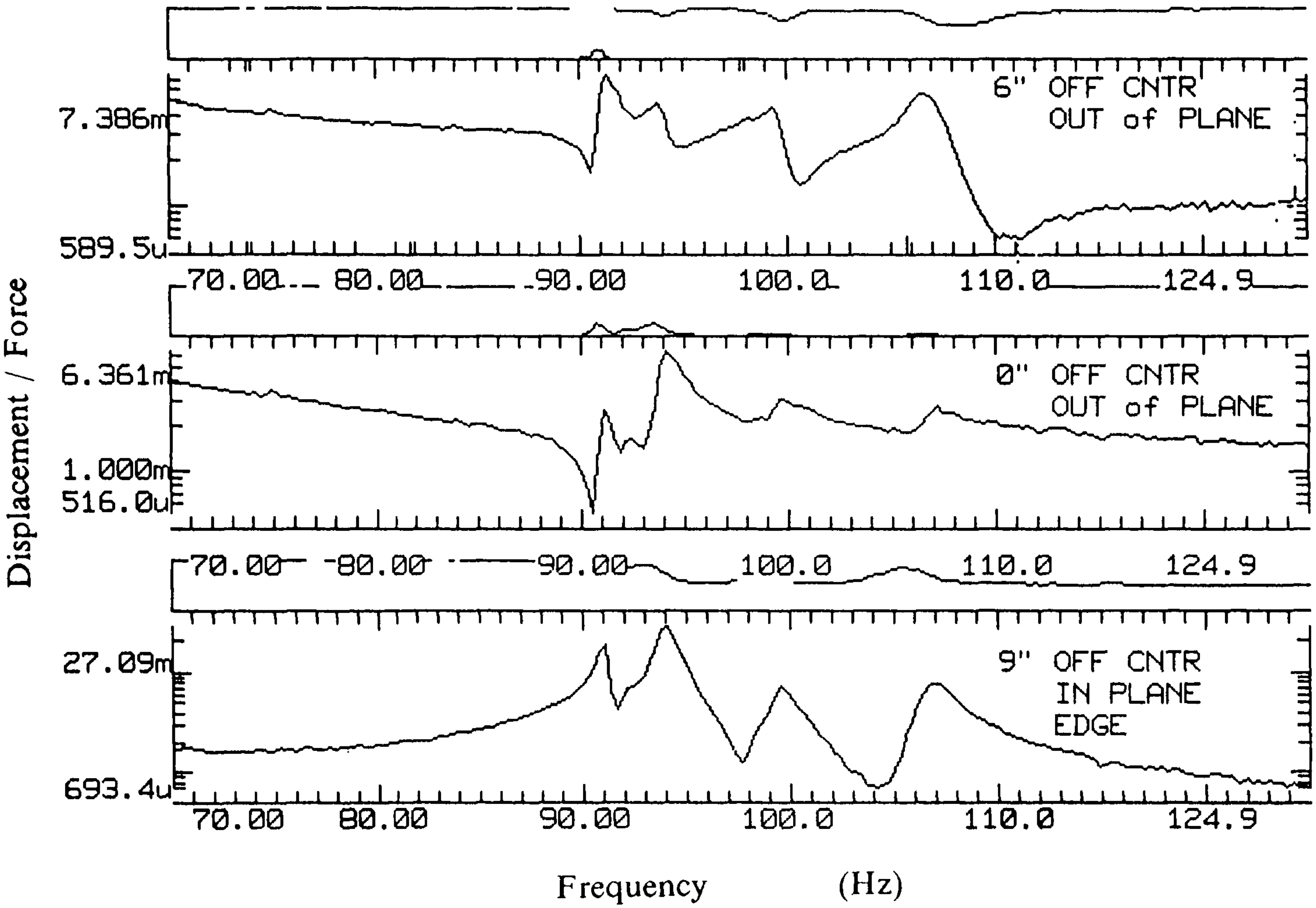

Figure 67. Channel specimen frequency response plot for lateral excitation; 70-125 Hz

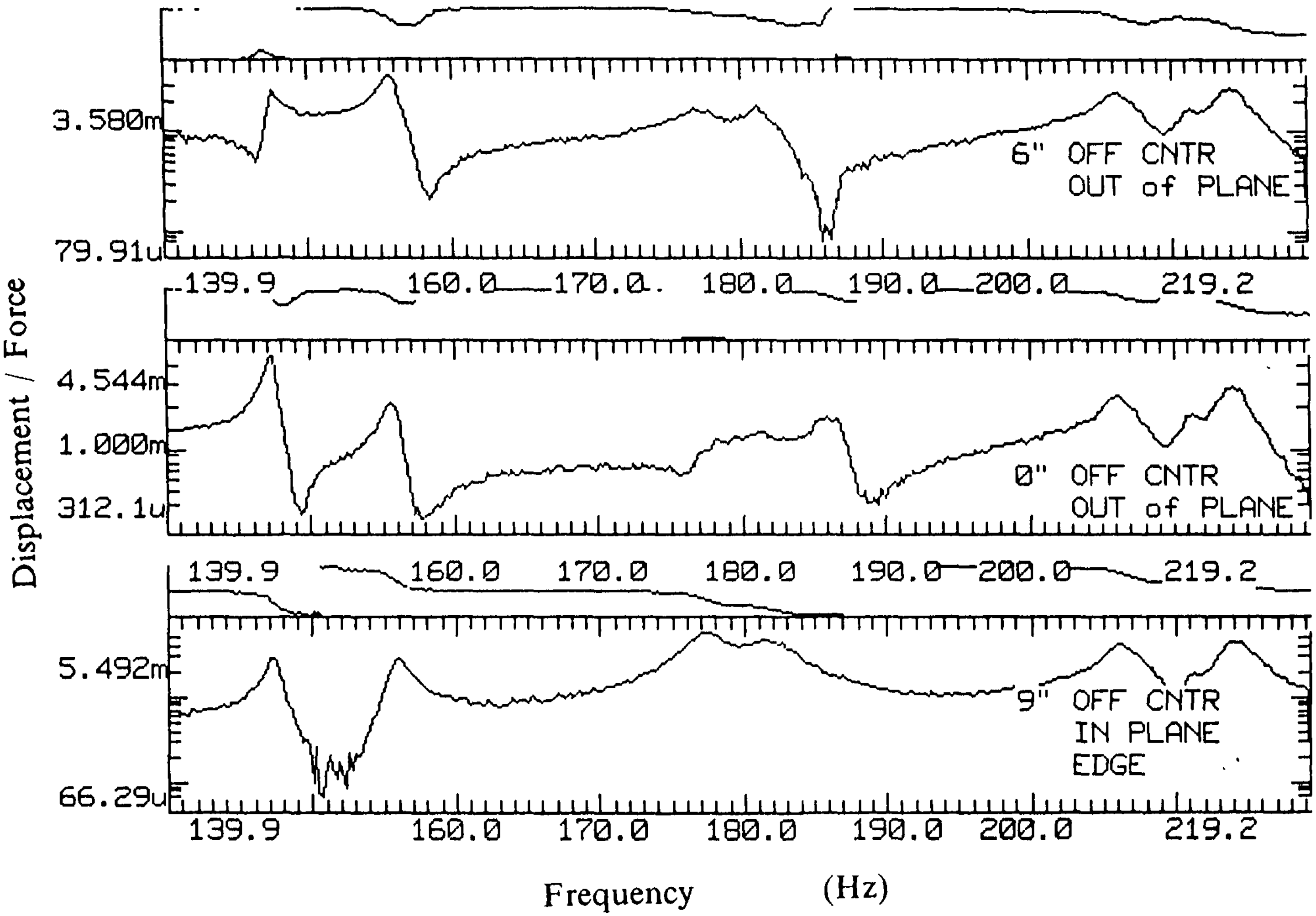

Figure 68. Channel specimen frequency response plot for lateral excitation; 140-219 Hz

C.3

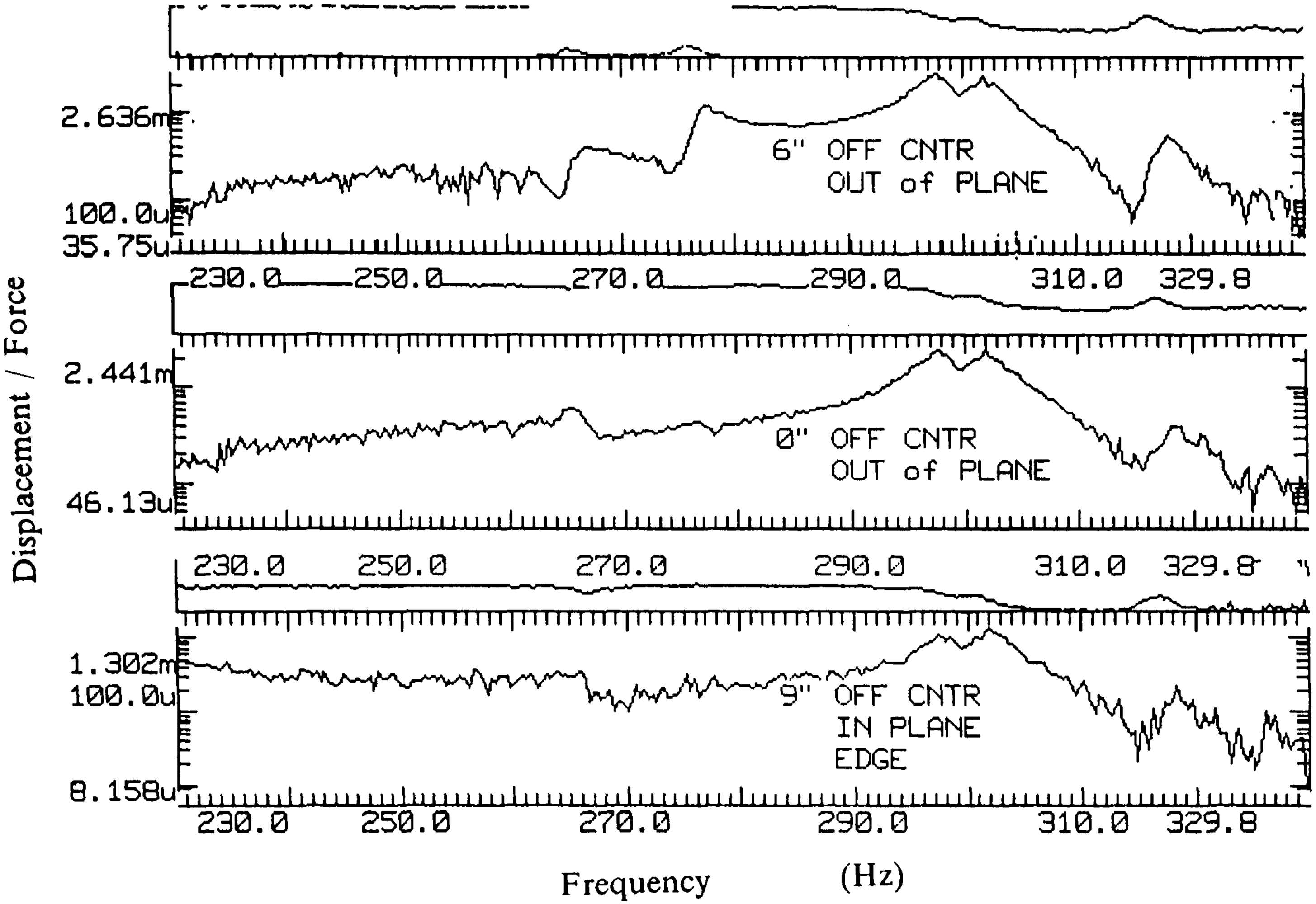

Figure 69. Channel specimen frequency response plot for lateral excitation; 230-330 Hz

Mode Shapes

This section presents the analytical mode shapes superimposed on the undeformed frame. The modes which were presented in the text are not repeated here. The experimentally located nodes are represented by dots in the figure, the undeformed frame is indicated by the solid line, and the mode shape is the broken line. Two free-free modes are presented in the first figure. The remaining modes are for the clamped-clamped case. The analytical mode shape was calculated by the finite element program discussed in Chapter 5. Two plots are presented in each figure, one for the I-specimen and one for the channel. The plots for the clamped-clamped modes are presented from top and front views. The I-specimen mode shapes consist of pure radial or pure out-of-plane motion. The channel modes are coupled and generally show motion in both views. The figures are presented without further comment.

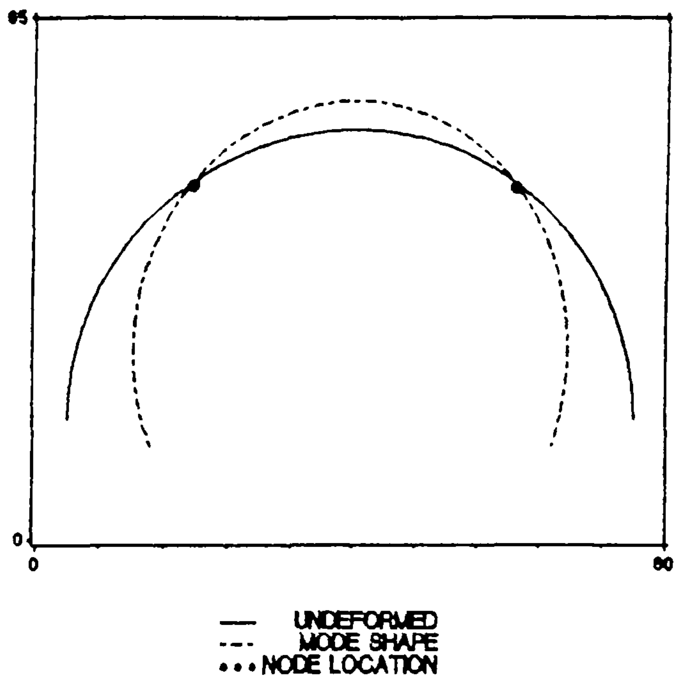

(A) TWO NODE MODE

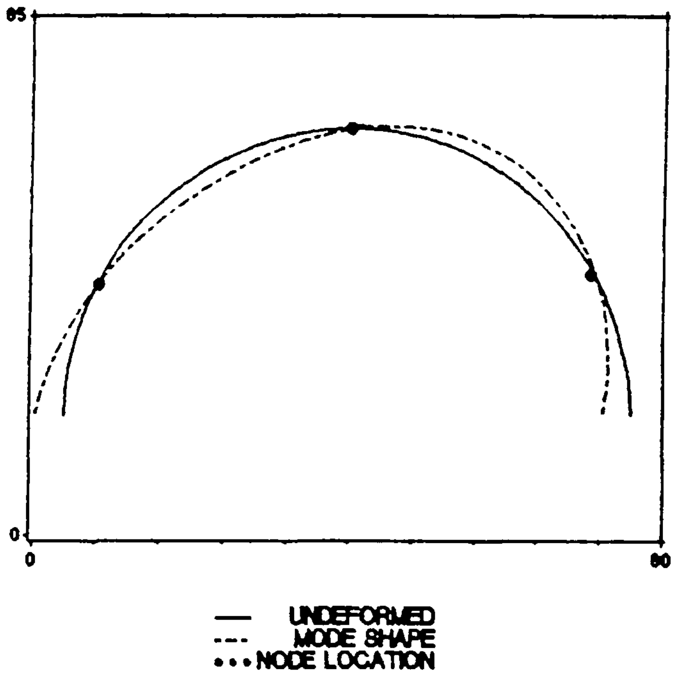

(B) THREE NODE MODE

Figure 70. Two and three noded in-plane, free-free mode shapes: Correlation between experimental data and continuum solution for the free-free in-plane modes of the I-specimen.

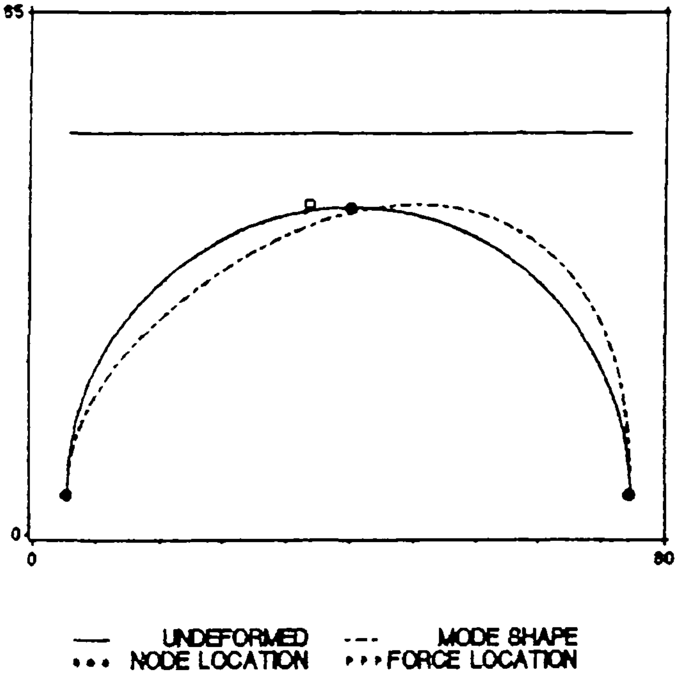

(A) I-SPECIMEN

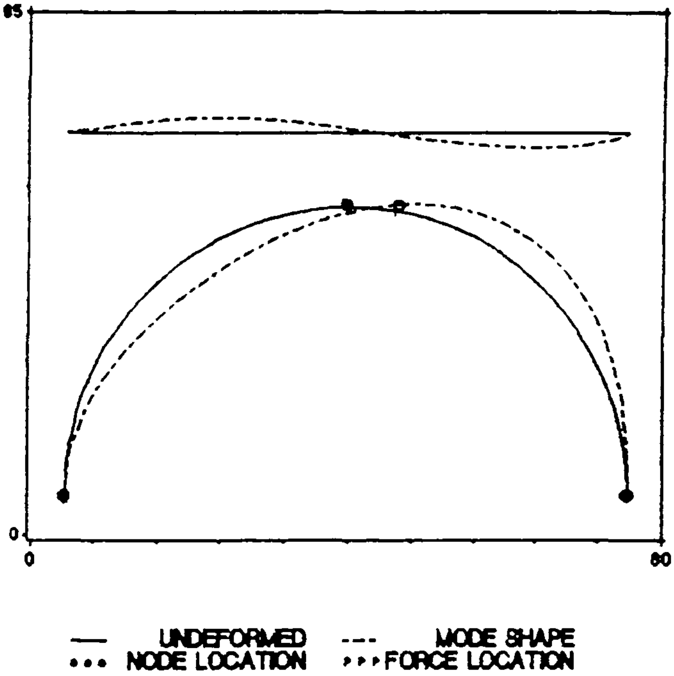

(B) CHANNEL SPECIMEN

Figure 71. Three noded in-plane, clamped-clamped modes for both specimens: The mode shapes of the three noded in-plane modes for both specimens are presented schematically.

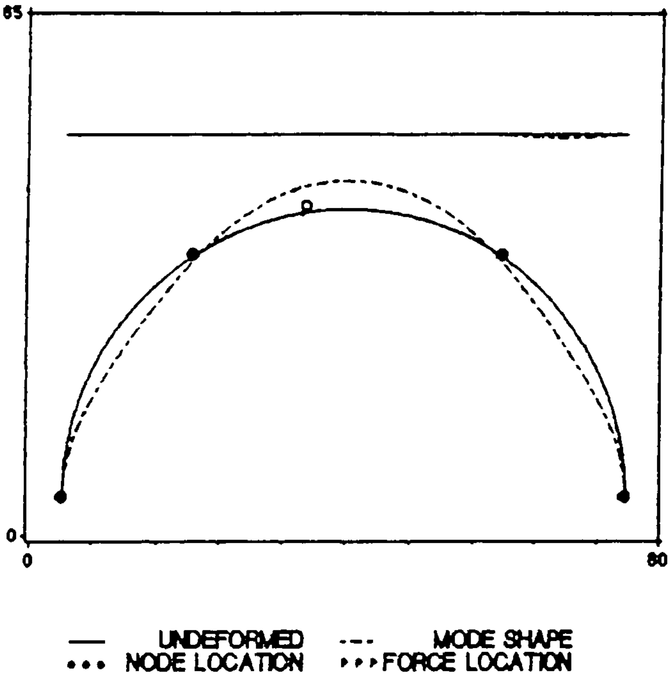
65
0
0
80
P
— UNDEFORMED
--- MODE SHAPE
••• NODE LOCATION
▸▸▸FORCE LOCATION

(A) I-SPECIMEN

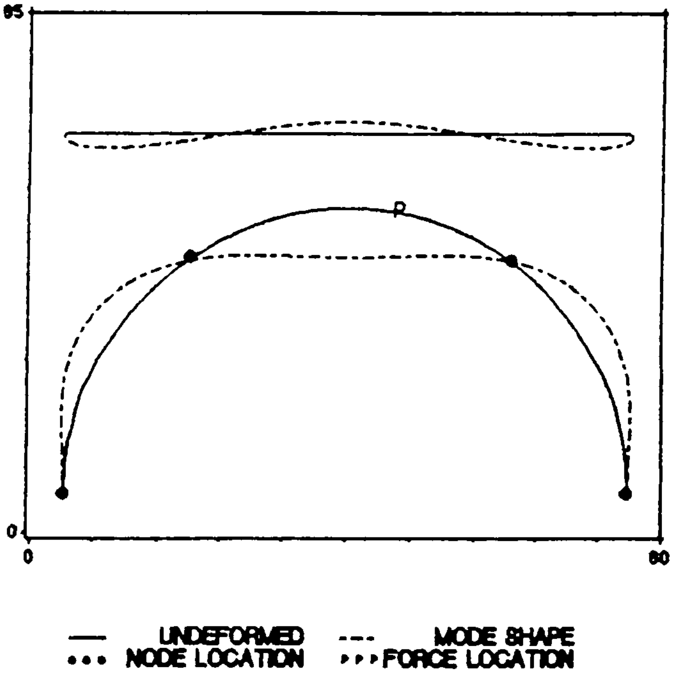
65
0
0
80
P
— UNDEFORMED
--- MODE SHAPE
••• NODE LOCATION
▸▸▸FORCE LOCATION

(B) CHANNEL SPECIMEN

Figure 72. Four noded in-plane, clamped-clamped modes for both specimens: The mode shapes of the four noded in-plane modes for both specimens are presented schematically.

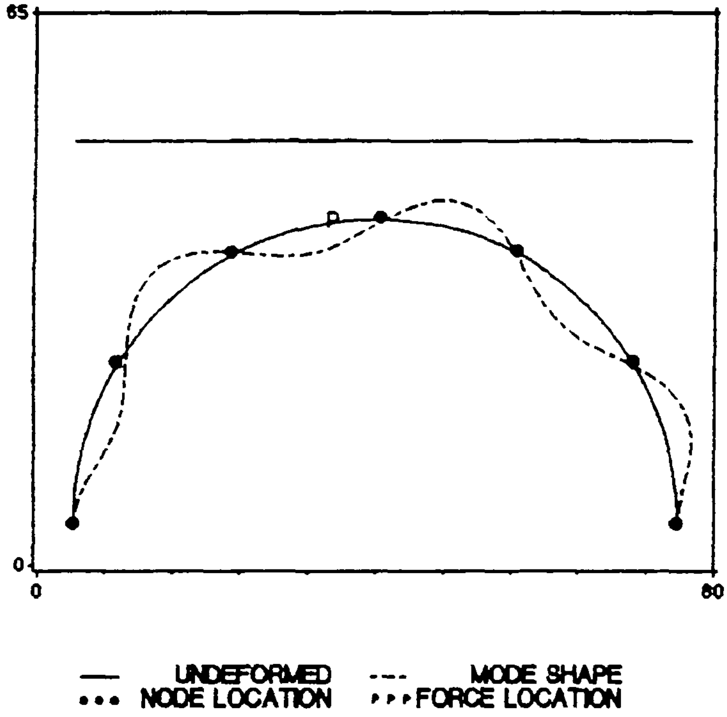

(A) I-SPECIMEN

Figure 73. Seven noded in-plane, clamped-clamped modes for the I-specimen: The mode shape of the seven noded in-plane mode for the I-specimen is presented schematically.

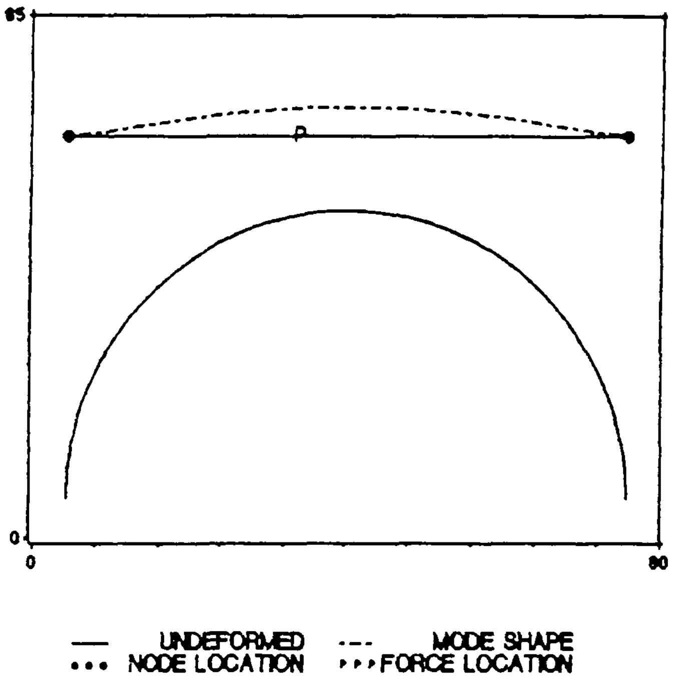

(A) I-SPECIMEN

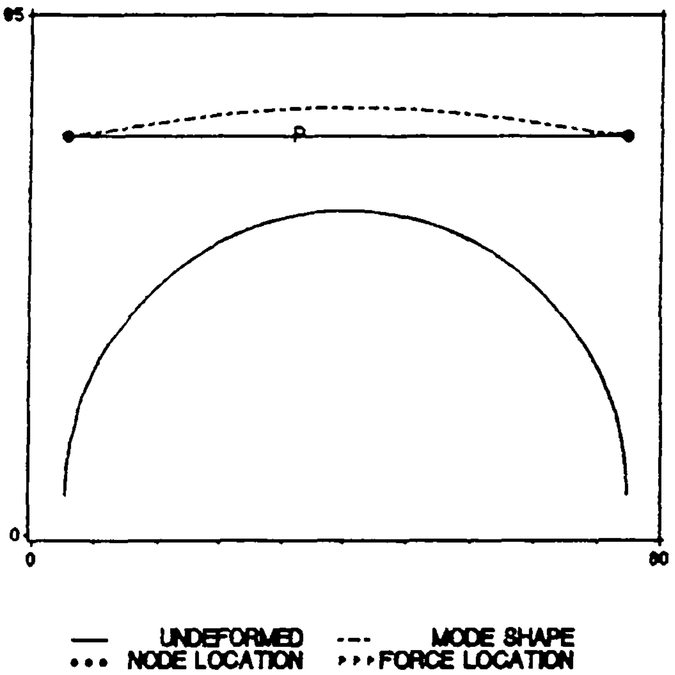

(B) CHANNEL SPECIMEN

Figure 74. Two noded out-of-plane, clamped-clamped modes for both specimens: The mode shapes of the two noded out-of-plane modes for both specimens are presented schematically.

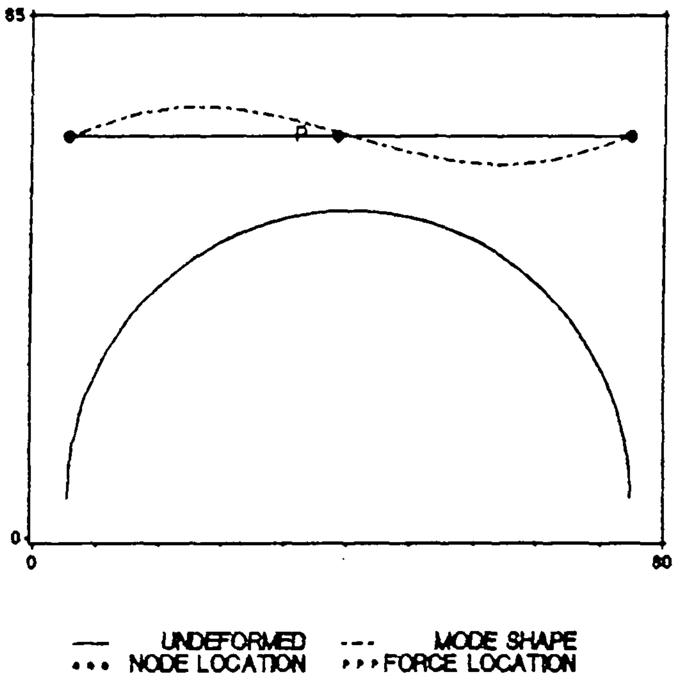

(A) I-SPECIMEN

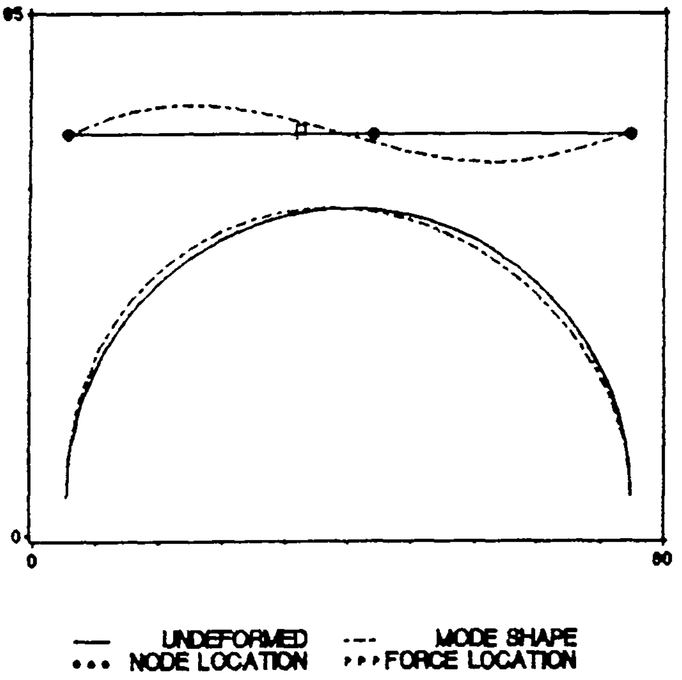

(B) CHANNEL SPECIMEN

Figure 75. Three noded out-of-plane, clamped-clamped modes for both specimens: The mode shapes of the three noded out-of-plane modes for both specimens are presented schematically.

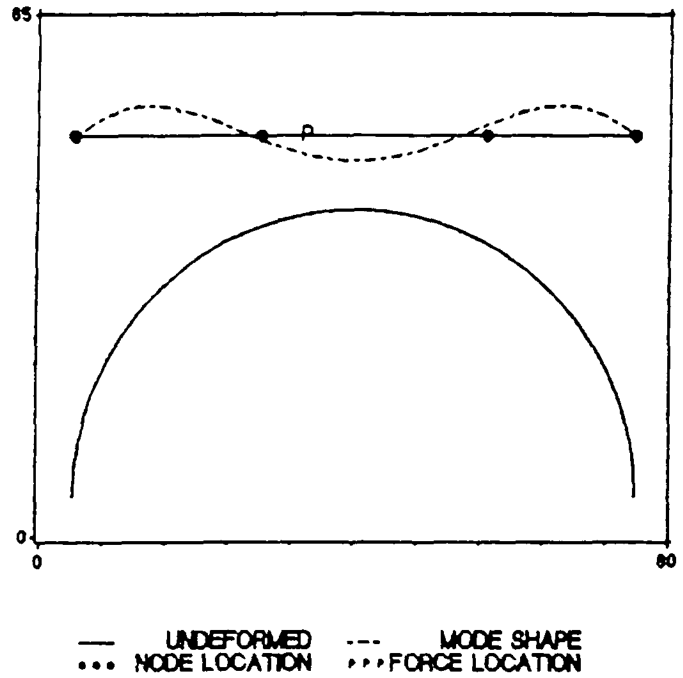
65
0
0
80
P
— UNDEFORMED
--- MODE SHAPE
••• NODE LOCATION
▸▸▸ FORCE LOCATION

(A) I-SPECIMEN

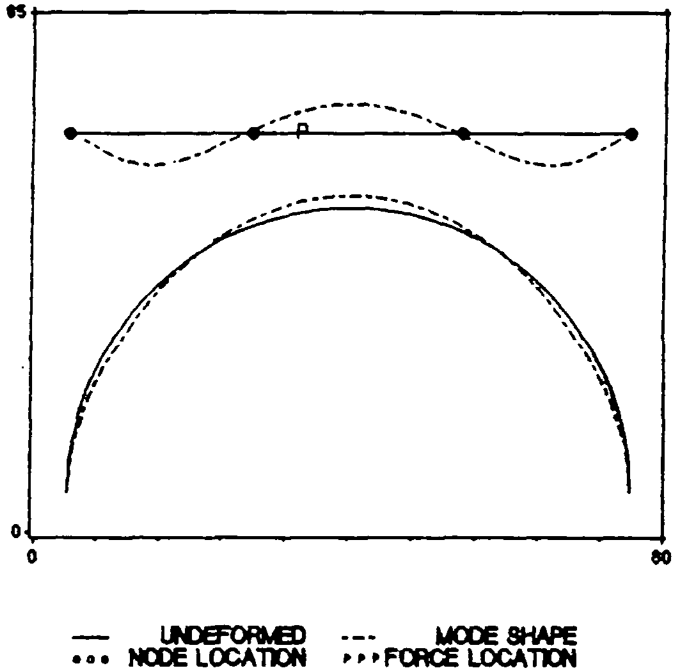
65
0
0
80
P
— UNDEFORMED
--- MODE SHAPE
••• NODE LOCATION
▸▸▸ FORCE LOCATION

(B) CHANNEL SPECIMEN

Figure 76. Four noded out-of-plane, clamped-clamped modes for both specimens: The mode shapes of the four noded out-of-plane modes for both specimens are presented schematically.

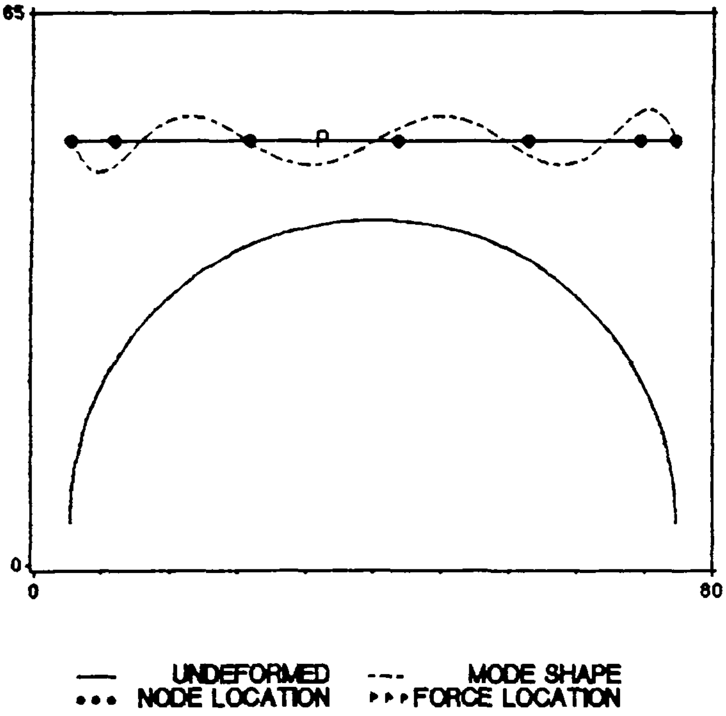

(A) I-SPECIMEN

Figure 77. Seven noded out-of-plane, clamped-clamped mode for the I-specimen: The mode shape of the seven noded out-of-plane mode for the I-specimen is presented schematically.

Appendix B
Static Test Data

This appendix contains some information on the static tests which was not covered in the text. The first section presents the reduction scheme was used to calculate the lateral and radial displacements at the centroid of the cross section at midspan. The second section presents a sample of the reduced data from the in-plane and out-of-plane tests.

Static Test Data Reduction

The data reduction scheme for the static tests used three measured displacements on the load fixture to calculate the twist, ϕ_x, of the cross section, the radial displacement, W, and the lateral displacement, V, at the centroid of the test specimen. In general, three measurements are sufficient to define the location of a body moving within a plane; hence, it is assumed that the midspan cross section does not deform circumferentially.

We assume that the load fixture and the test specimen deform as a rigid body, thus, the load fixture and test specimen can be represented by a rectangular block. A generic rectangular body is shown in Fig. 78. A Cartesian coordinate system is placed at one corner of the rectangular block with positive axis coinciding with the sides of the block. The Cartesian coordinate system is consistent with the system used in the text. With respect to the test specimen the z-axis is directed radially toward the center of the curved frame and the y-axis is perpendicular to the frame. The distances d_1, d_2, and d_3, locate the three dial indicators with respect to the origin of the coordinate system. If the distance r_c, and the angle, θ_c, locate the centroid C of the cross section with respect to point O on the load fixture, then the initial centroidal coordinates can be obtained from

$$\begin{aligned} y_c &= r_c \cos\theta_c \\ z_c &= r_c \sin\theta_c \end{aligned} \tag{B.1}$$

Since the block is a rigid body, the location of the centroid can always be located from the point O on the block. Thus, given the deformed coordinates of O, it is possible to calculate the deformed coordinates of the centroid C. The deformed state of the block is shown in Fig. 79. The deformed centroidal coordinates can be calculated from

$$\begin{aligned} y_c^* &= y_o + r_c \cos\theta_c + \phi_x \\ z_c &= z_o + r_c \sin\theta_c + \phi_x \end{aligned} \tag{B.2}$$

in which y_o and z_o are the deformed coordinates of point O, and ϕ_x is the twist.

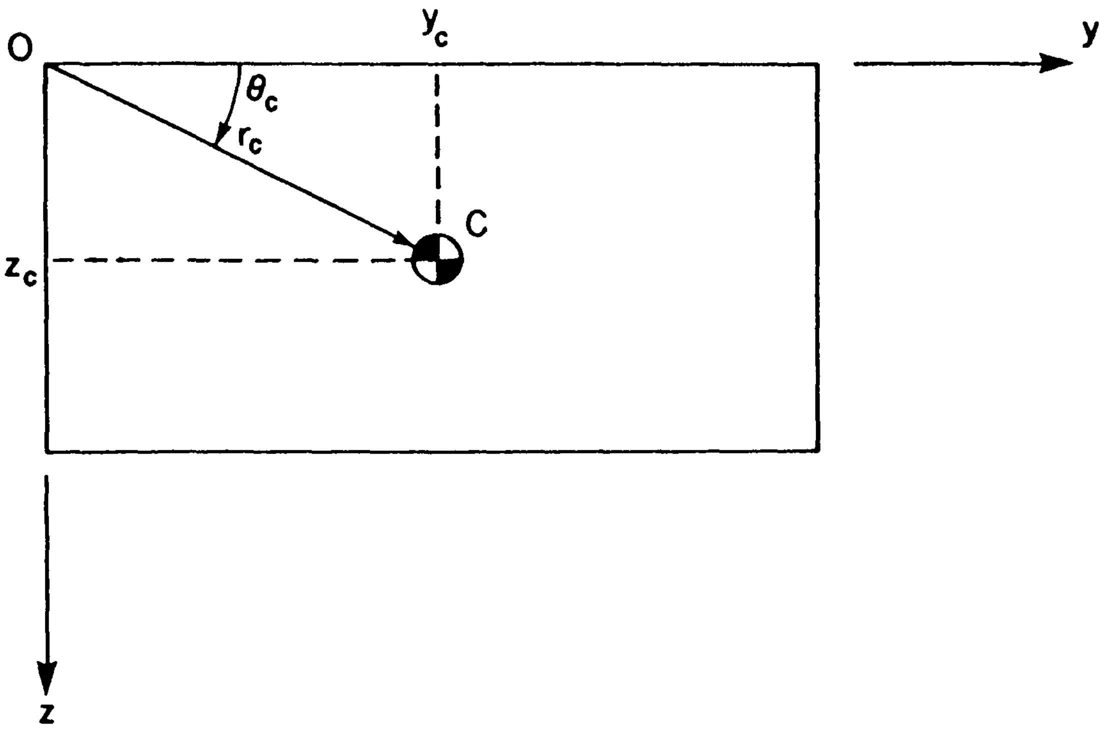

Figure 78. Schematic of rectangular block, coordinate system and dial indicators: The origin of the cartesian coordinate system coincides with point O when the block is in the undeformed position. The point C represents the centroid of the test specimen.

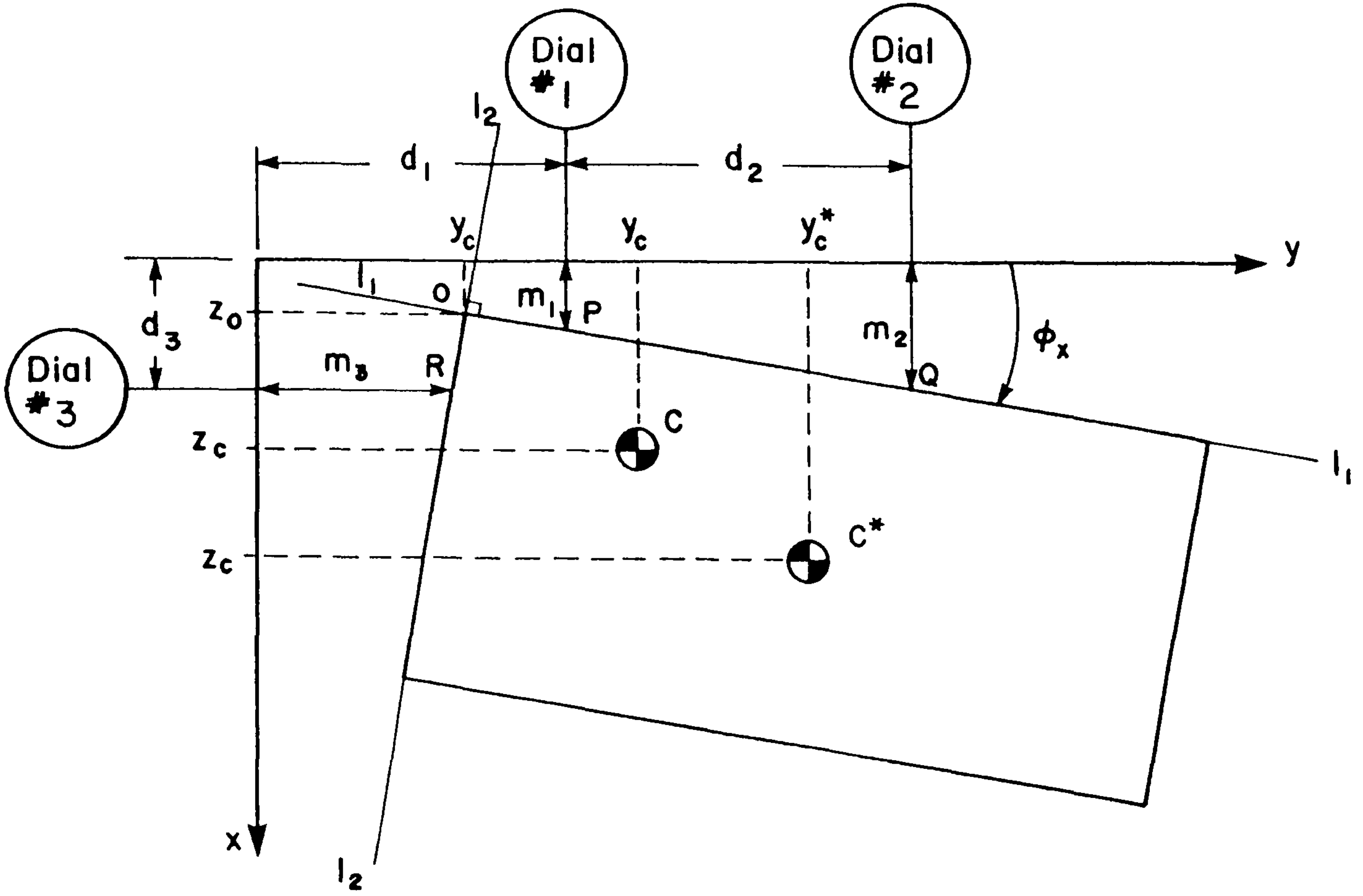
Dial #1
Dial #2
Dial #3
d_1
d_2
d_3
l_1
l_2
y_c
y_c
y_c^*
y
x
z_o
z_c
z_c
O
P
Q
R
m_1
m_2
m_3
C
C*
ϕ_x

Figure 79. Schematic of deformed cross section Since the specimen does not move with respect to the load fixture, the deformed centroidal coordinates can be calculated with respect to the deformed load fixture.

The centroidal displacements V and W are given by

$$\begin{aligned} V &= y_c^* - y_c \\ W &= z_c^* - z_c \end{aligned} \tag{B.3}$$

Thus, the unknowns necessary to calculate the centroidal displacements are ϕ_x, y_o, and z_o. The dial indicators are labelled 1, 2, and 3. The measurements from each dial indicator will be referred to as m_1, m_2, and m_3 , respectively. The points O, P, and Q lie along line l_1. The equation for line l_1 can be calculated from the coordinates of points B and C which are (d_1,m_1) and $(d_2 + d_1,m_2)$, respectively. The twist, ϕ_x; is the slope of line l_1. The equations for ϕ_x and line l_1 are

$$\begin{aligned} \phi_x &= \frac{(m_2 - m_1)}{d_2} \\ l_1: \quad z - m_2 &= \phi_x\,[y - (d_1 + d_2)] \end{aligned} \tag{B.4}$$

Since point O lies on line l_1, the coordinate y_o and z_o must satisfy Eqn. (B.4). Points O and R define a second line, l_2; which is perpendicular to line l_1, thus the slope of line l_2 is $-1/\phi_x$. A second equation for line l_2 and the coordinates y_o and z_o must satisfy this equation as well.

$$l_2: \quad z - d_3 = -\frac{1}{\phi_x}\,(y - m_3) \tag{B.5}$$

Substituting y_o and z_o into Eqn. (B.5), solving for y_o, and substituting that expression into the equation for line l_1 yields the following expressions for y_o and z_o.

$$\begin{aligned} z_o &= \{m_2 + \phi_x[\phi_x d_3 + m_3 - (d_1 + d_2)]\} \\ y_o &= \phi_x(d_3 - z_o) + m_3 \end{aligned} \tag{B.6}$$

The expressions for y_o and z_o can be used in conjunction with Eqs. (B.1-B.3) to obtain the lateral and radial displacements of the centroid. The special case where ϕ_x is zero corresponds to pure translation and the equations reduce to

$$\begin{aligned} v &= m_3 \\ w &= m_2 \end{aligned} \tag{B.7}$$

as expected.

Reduced Static Data

The tables presented in this section contain a sample of the reduced data obtained from the reduction scheme presented in the previous section. The radial and lateral displacements and the twist at midspan for both test specimens for radial loads of twenty, forty, and sixty pounds are presented in Tables 17, 18, and 19. The moment arm associated with each set of data is different for the two specimens. There is more data for the channel specimen because the response of the channel specimen was not as consistent as the response of the I-specimen. The flexibility influence coefficients were calculated from this data using the least squares method discussed in Chapter 4. The radial and lateral displacements and the twist at midspan for both specimens from the out-of-plane tests are presented in Tables 20 and 21. For the out-of-plane tests, the moment arms were the same for the two specimens but the lateral loads were different. The test data for lateral loads of 2.187 and and 1.063 pounds are presented in Table 20 for the I-specimen and channel specimen, respectively. The test data for lateral loads of 3.25 and 2.00 pounds are presented in Table 21 for the I-specimen and the channel specimen, respectively.

Table 17. Static data from in-plane tests for 20 pound radial load

I-Specimen				Channel Specimen			
Moment	Displacements			Moment	Displacements		
Arm D in	Radial W in x 10^{-3}	Lateral V in x 10^{-3}	Twist ϕ rad x 10^{-2}	Arm D in	Radial W in x 10^{-3}	Lateral V in x 10^{-3}	Twist ϕ rad x 10^{-2}
-.1458	17.14	-27.68	-.335	-.0625	28.84	-23.92	-.370
-.1250	17.10	-23.44	-.279	-.0590	28.99	-23.01	-.350
-.1042	17.06	-16.84	-.196	-.0555	29.64	-21.60	-.329
-.0833	17.04	-15.60	-.140	-.0521	29.58	-19.40	-.319
-.0625	17.27	-12.04	-.098	-.0486	29.78	-18.69	-.308
-.0417	17.25	- 5.12	-.028	-.0451	29.97	-16.74	-.298
-.0208	17.62	- 4.47	-.007	-.0417	30.27	-15.17	-.257
-.0104	17.36	- 1.23	.049	-.0347	30.66	-12.25	-.236
0.0000	17.61	1.23	.049	-.0243	31.06	- 9.09	-.216
0.0104	17.36	4.52	.105	-.0208	31.11	- 7.02	-.176
0.0208	17.49	5.92	.126	-.0139	31.72	- 6.41	-.144
0.0417	17.62	9.26	.161	-.0104	32.12	- 4.25	-.123
0.0625	17.75	11.97	.224	-.0069	32.32	- 0.04	-.113
0.0833	17.76	15.78	.265	-.0035	32.83	- 0.26	-.062
0.1042	17.67	24.11	.356	0.0000	33.14	- 0.27	-.021
0.1250	17.44	27.36	.412	0.0035	33.34	7.51	-.010
0.1458	18.22	32.23	.440	0.0069	33.55	7.47	0.000
				0.0104	33.75	8.17	0.010
				0.0139	34.31	11.49	0.051
				0.0208	34.77	14.20	0.062
				0.0243	34.72	12.90	0.072
				0.0347	35.11	16.30	0.154
				0.0382	35.32	20.25	0.165
				0.0417	36.31	22.74	0.226
				0.0451	36.02	24.19	0.236
				0.0486	35.81	23.49	0.226

Table 18. Static data from in-plane tests for 40 pound radial load

I-Specimen				Channel Specimen			
Moment	Displacements			Moment	Displacements		
Arm D in	Radial W in x 10^{-3}	Lateral V in x 10^{-3}	Twist ϕ rad x 10^{-2}	Arm D in	Radial W in x 10^{-3}	Lateral V in x 10^{-3}	Twist ϕ rad x 10^{-2}
-.1458	33.25	-56.40	-.6840	-.0625	56.94	-55.77	-.7500
-.1250	33.13	-49.39	-.5870	-.0590	57.45	-51.21	-.7090
-.1042	33.35	-36.43	-.4260	-.0555	57.69	-49.46	-.7090
-.0833	33.54	-32.09	-.3420	-.0521	58.72	-43.35	-.6270
-.0625	33.45	-22.20	-.2160	-.0486	59.30	-40.24	-.5960
-.0417	33.41	-12.18	-.1190	-.0451	60.07	-36.18	-.5550
-.0208	33.62	- 5.03	-.0000	-.0417	60.73	-31.22	-.4930
-.0104	33.62	- .99	0.0489	-.0382	61.30	-24.87	-.4630
0.0000	33.86	1.06	0.0908	-.0347	62.04	-23.86	-.4110
0.0104	33.62	7.91	0.1746	-.0243	61.99	-22.40	-.4010
0.0208	33.63	11.90	0.2304	-.0208	62.72	-17.40	-.3505
0.0417	34.02	19.10	0.2933	-.0139	64.32	-12.02	-.2160
0.0625	34.07	27.26	0.4190	-.0069	64.90	- 2.17	-.1850
0.0833	34.12	33.61	0.5028	-.0035	66.07	- 2.00	-.1130
0.1042	33.99	46.65	0.6564	0.0000	66.58	6.26	-.0620
0.1250	33.82	51.45	0.7542	0.0035	67.23	11.16	.0103
0.1458	34.83	62.77	0.8450	0.0069	67.30	14.72	.0000
				0.0104	67.98	19.13	.0720
				0.0139	68.92	24.79	.1439
				0.0208	69.42	31.01	.2056
				0.0313	70.91	37.93	.3289
				0.0347	70.63	41.63	.3392
				0.0382	71.74	46.19	.3803
				0.0417	73.12	50.26	.4729
				0.0451	73.86	57.70	.4831
				0.0486	74.00	59.81	.5148

Table 19. Static data from in-plane tests for 60 pound radial load

I-Specimen				Channel Specimen			
Moment	Displacements			Moment	Displacements		
Arm D in	Radial W in x 10^{-3}	Lateral V in x 10^{-3}	Twist ϕ rad x 10^{-2}	Arm D in	Radial W in x 10^{-3}	Lateral V in x 10^{-3}	Twist ϕ rad x 10^{-2}
-.1458	49.93	-.0908	-1.0750	-.0625	84.13	-102.00	-1.203
-.1250	49.60	-.0764	- .9080	-.0590	84.82	- 95.70	-1.162
-.1042	49.40	-.0595	- .6910	-.0555	85.34	- 91.11	-1.131
-.0833	49.26	-.0529	- .5660	-.0521	86.60	- 80.93	-1.018
-.0625	49.43	-34.93	- .3630	-.0486	88.01	- 72.14	-0.9250
-.0417	49.57	-22.52	- .1960	-.0451	89.14	- 67.45	-0.8630
-.0208	49.88	- 9.40	- .0210	-.0417	89.89	- 59.86	-0.7810
-.0104	49.99	- 5.03	.0559	-.0382	91.59	- 50.57	-0.6890
0.0000	50.11	0.98	.1047	-.0347	92.09	- 45.53	-0.6480
0.0104	50.00	11.33	.2374	-.0278	92.84	- 38.99	-0.6064
0.0208	50.90	19.38	.3282	-.0208	93.73	- 30.56	-0.4935
0.0417	50.44	26.22	.4120	-.0139	95.58	- 19.17	-0.3700
0.0625	50.21	42.93	.6285	-.0104	96.57	- 17.43	-0.3190
0.0833	50.34	53.82	.7542	-.0069	97.45	- 8.79	-0.2470
0.1042	50.61	70.26	.9777	-.0035	98.41	- 3.85	-0.1850
0.1250	49.96	82.14	1.1103	0.0000	99.37	6.83	-0.0720
0.1458	50.63	96.20	1.2573	0.0035	100.70	17.86	0.0206
				0.0069	101.39	24.00	0.0925
				0.0104	102.46	29.74	0.1953
				0.0139	103.75	39.42	0.3084
				0.0208	105.17	53.46	0.4009
				0.0313	107.57	65.69	0.5037
				0.0382	108.40	77.13	0.5654
				0.0417	110.50	86.76	0.6887
				0.0451	111.41	99.90	0.8121
				0.0486	111.68	98.45	0.8018

Table 20. Static data from out-of-plane tests

I-Specimen, Q = 2.187 lbs				Channel Specimen, Q = 1.063 lbs			
Moment	Displacements			Moment	Displacements		
Arm D in	Radial W in x 10^{-3}	Lateral V in x 10^{-3}	Twist ϕ rad x 10^{-1}	Arm D in	Radial W in x 10^{-3}	Lateral V in x 10^{-3}	Twist ϕ rad x 10^{-1}
-0.6850	2.49	232.30	0.1746	-0.6850	7.94	242.21	0.1145
-0.6294	2.29	233.24	0.1760	-0.6294	8.11	244.68	0.1152
-0.5739	2.08	235.24	0.1760	-0.5739	8.01	244.90	0.1159
-0.5183	2.36	234.93	0.1774	-0.5183	8.19	244.81	0.1180
-0.4628	2.28	236.91	0.1781	-0.4628	8.13	246.47	0.1201
-0.4072	2.37	237.79	0.1809	-0.4072	8.29	247.94	0.1208
-0.3517	2.23	238.07	0.1802	-0.3517	8.74	250.09	0.1229
-0.2961	2.44	239.74	0.1823	-0.2961	8.44	248.41	0.1215
-0.2406	2.37	240.15	0.1844	-0.2406	8.64	250.06	0.1237
-0.1850	2.49	240.68	0.1837	-0.1850	8.56	252.79	0.1244
-0.1294	2.61	243.57	0.1865	-0.1294	8.73	254.50	0.1250
-0.0739	2.64	243.01	0.1878	-0.0739	8.77	255.19	0.1264
-0.0185	2.58	241.82	0.1865	-0.0185	8.79	256.69	0.1264
0.0372	2.68	243.45	0.1893	0.0372	9.10	258.63	0.1278
0.0928	2.43	247.37	0.1913	0.0928	9.17	260.82	0.1292
0.1483	2.78	248.75	0.1941	0.1483	9.17	261.32	0.1292

Table 21. Static data from out-of-plane tests

I-Specimen, Q = 3.25 lbs				Channel Specimen, Q = 2.000 lbs			
Moment	Displacements			Moment	Displacements		
Arm D in	Radial W in x 10^{-3}	Lateral V in x 10^{-3}	Twist ϕ rad x 10^{-1}	Arm D in	Radial W in x 10^{-3}	Lateral V in x 10^{-3}	Twist ϕ rad x 10^{-1}
-0.6850	4.31	345.59	0.2612	-0.6850	13.94	434.27	0.2067
-0.6294	4.16	347.54	0.2626	-0.6294	14.02	438.02	0.2067
-0.5739	4.11	349.51	0.2633	-0.5739	13.90	436.99	0.2074
-0.5183	4.00	348.99	0.2640	-0.5183	14.15	438.40	0.2095
-0.4628	4.32	353.26	0.2696	-0.4628	14.30	443.76	0.2130
-0.4072	4.15	354.22	0.2710	-0.4072	14.20	443.48	0.2137
-0.3517	4.15	356.13	0.2730	-0.3517	14.54	446.08	0.2172
-0.2961	4.57	358.52	0.2758	-0.2961	14.71	446.80	0.2179
-0.2406	4.47	358.24	0.2765	-0.2406	14.78	447.24	0.2193
-0.1850	4.37	361.94	0.2779	-0.1850	14.98	450.37	0.2221
-0.1294	4.84	362.35	0.2800	-0.1294	15.05	453.37	0.2221
-0.0739	4.90	362.55	0.2814	-0.0739	15.21	455.25	0.2249
-0.0185	4.70	362.50	0.2828	-0.0185	15.36	458.69	0.2263
0.0372	5.18	365.07	0.2870	0.0372	15.51	459.33	0.2291
0.0928	4.99	368.50	0.2891	0.0928	15.58	462.33	0.2291
0.1483	4.87	371.20	0.2905	0.1483	15.69	464.27	0.2305

Appendix C
Cross-Sectional Properties

The modulus-weighted and geometric cross-sectional properties of the two specimens are presented in Table 22. The geometric section properties were obtained using a computer program listed in Ref. 33. The modulus-weighted section properties were obtained by modifying this computer program to evaluate the expressions for the modulus-weighted section properties presented in Chapter 5. The modulus-weighted section properties are normalized by the effective engineering moduli determined by the coupon tests discussed in Chapter 2. The mass density of the material measured to be 1465. kilograms per cubic meter.

Table 1. Cross-sectional properties of both test specimens

Section Property		I-specimen		Channel Specimen	
		M-W[a]	Geometric[b]	M-W[a]	Geometric[b]
A	m^2	0.3658×10^{-3}[c]	0.3310×10^{-3}	0.2323×10^{-3}[c]	0.2102×10^{-3}
A_y	m^2	0.3658×10^{-3}[d]	0.3310×10^{-3}	0.2323×10^{-3}[d]	0.2102×10^{-3}
A_z	m^2	0.3658×10^{-3}[d]	0.3310×10^{-3}	0.2323×10^{-3}[d]	0.2102×10^{-3}
I_{yy}	m^4	0.5339×10^{-7}[c]	0.4813×10^{-7}	0.3202×10^{-7}[c]	0.2888×10^{-7}
I_{zz}	m^4	1.6705×10^{-7}[c]	1.5114×10^{-7}	0.4844×10^{-7}[c]	0.4382×10^{-7}
I_{yz}	m^4	0.0000×10^{-7}[c]	0.000×10^{-7}	$-.1070 \times 10^{-7}$[c]	$-.9685 \times 10^{-8}$
J	m^4	0.8842×10^{-9}[d]	0.7825×10^{-9}	0.5026×10^{-9}[d]	0.4378×10^{-9}
S_ω	m^5	0.9671×10^{-7}[c]	0.8755×10^{-7}	0.1089×10^{-7}[c]	0.9860×10^{-8}
$I_{\omega y}$	m^5	$-.3217 \times 10^{-15}$[c]	$-.4539 \times 10^{-15}$	$-.6650 \times 10^{-9}$[c]	$-.6023 \times 10^{-9}$
$I_{\omega z}$	m^5	0.8114×10^{-9}[c]	0.7343×10^{-9}	0.4301×10^{-9}[c]	0.3829×10^{-9}
$I_{\omega\omega}$	m^6	0.3558×10^{-10}[c]	0.3213×10^{-10}	0.1688×10^{-10}[c]	0.1526×10^{-10}

[a] Modulus-Weighted section properties from Chapter 5

[b] Geometric section properties from Ref. 33

[c] Normalized by $E = 5.075 \times 10^{10}$ $\mathrm{Nt/m^2}$

[d] Normalized by $G = 1.953 \times 10^{10}$ $\mathrm{Nt/ m^2}$

National Aeronautics and Space Administration

Report Documentation Page

1. Report No.
NASA CR-4287

2. Government Accession No.

3. Recipient's Catalog No.

4. Title and Subtitle
Static and Free-Vibrational Response of Semi-Circular Graphite-Epoxy Frames With Thin-Walled Open Sections

5. Report Date
March 1990

6. Performing Organization Code

7. Author(s)
J. Scott Collins and
Eric R. Johnson

8. Performing Organization Report No.
VPI-E-89-19

10. Work Unit No.
505-63-01-11

9. Performing Organization Name and Address
Virginia Polytechnic Institute and State University
Dept. of Engineering Science and Mechanics
106 Norris Hall Blacksburg, VA 24061

11. Contract or Grant No.
NAG1-343

12. Sponsoring Agency Name and Address
NASA Langley Research Center
Hampton, VA 23665-5225

13. Type of Report and Period Covered
Contractor Report

14. Sponsoring Agency Code

15. Supplementary Notes

Langley Technical Monitor: Huey D. Carden

16. Abstract

Experiments were conducted to measure the three-dimensional static and free vibrational response of two graphite-epoxy, thin-walled, open section frames. The frames are semi-circular with a radius of three feet, and one specimen has an I cross section and the other has a channel cross section. The flexibility influence coefficients were measured in static tests for loads applied at midspan with the ends of the specimens clamped. Natural frequencies and modes were determined from vibrational tests for free and clamped end conditions. The experimental data is used to evaluate a new finite elements which was developed specifically for the analysis of curved, thin-walled structures. The formulation of the element is based on a Vlasov-type, thin-walled, curved beam theory.

17. Key Words (Suggested by Author(s))
Crashworthiness
Composite Materials
Graphite-Epoxy
Impact Loading
Nonlinear Response
Beam Theory
Vibration
Response

18. Distribution Statement
Unclassified - Unlimited

Subject Category: 39

19. Security Classif. (of this report)
Unclassified

20. Security Classif. (of this page)
Unclassified

21. No. of pages
208

22. Price
A10

NASA FORM 1626 OCT 86

For sale by the National Technical Information Service, Springfield, Virginia 22161-2171

NASA-Langley, 1990

National Aeronautics and
Space Administration
Code NTT-4

Washington, D.C.
20546-0001

Official Business
Penalty for Private Use, $300

SPECIAL FOURTH-CLASS RATE
POSTAGE & FEES PAID
NASA
Permit No. G-27

POSTMASTER: If Undeliverable (Section 158
Postal Manual) Do Not Return